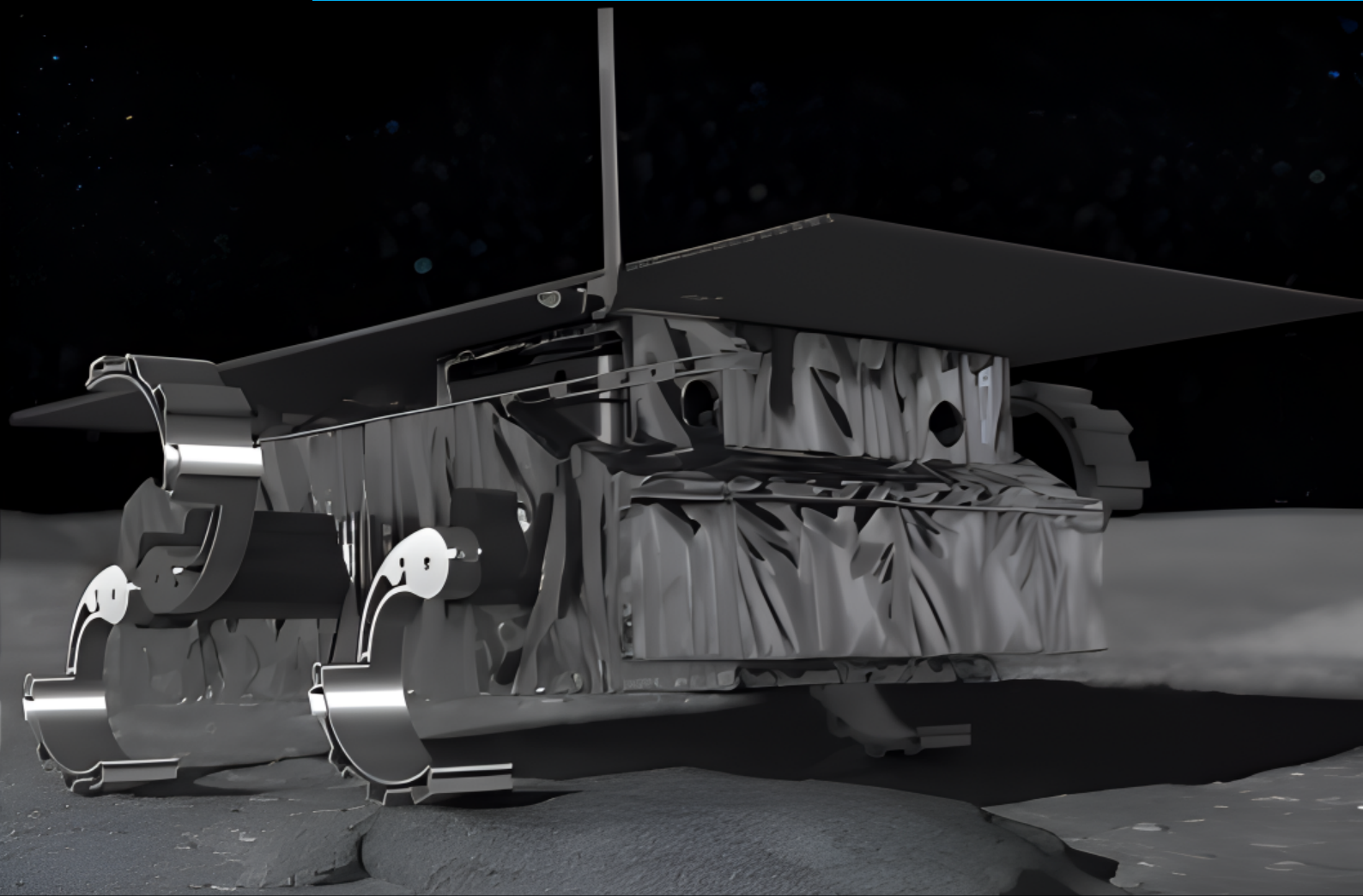


Department of Precision and Microsystems Engineering

Design and optimisation of a compliant leg module for enhanced tractive performance of a lunar nano-rover

S.X. Bloem

Report no : 2025.057
Coach : Dr. Ir. J.F.L. Goosen
Professor : Dr. Ir. J.F.L. Goosen
Specialisation : High-Tech Engineering
Type of report : Master Thesis
Date : 22 August 2025



Preface

This report is part of my Master's thesis within the department of High-Tech Engineering at the Delft University of Technology. This thesis presents a design and optimisation of a new compliant leg module for TU Delft's nano-rover, Lunar Zebro, to obtain increased tractive performance on the lunar terrain. The Lunar Zebro is depicted in the cover image [1].

During my Bachelor's studies, I developed a strong interest in robotics, applying my knowledge of structural design to create robotic hardware in multiple projects. Building on the expertise I gained in compliant structure design and analysis during my Master's studies, this thesis reflects my passion by focusing on one of the most advanced forms of robotics: the lunar rover. I am deeply grateful for the opportunity to contribute to this field, expand my understanding, and support the Lunar Zebro programme in achieving its goal of enabling the rover to walk on the Moon.

I would like to express my sincere gratitude to my supervisor, Dr. Ir. J.F.L. Goosen, for his continued support, guidance, and expertise throughout the process of conducting my Master's thesis. Finally, I would like to thank my family and friends for their support throughout this journey.

I acknowledge the utilisation of TeXGPT by Writefull for Overleaf to identify improvements in grammar and spelling of this thesis. The entirety of the text was originally personally written, after which TeXGPT was employed to identify improvements. These suggested improvements were individually evaluated and, if judged beneficial, manually incorporated. This thesis explicitly does not include any prompt-based generated text.

S.X. Bloem
Delft, August 2025

Abstract

Extra-terrestrial rovers play a vital role in the acquisition of scientific data on celestial bodies, offering a reduced risk and cost compared to human exploration. In pursuit of mapping the lunar surface, a swarm of nano-rovers can collectively form a network and cover extensive areas. The Lunar Zebro, a hexapod nano-rover, employs an innovative C-shaped leg module that combines the efficiency of a wheel with the stability and climbing capability of a leg. The current C-shaped leg module features a fully rigid design, for which tractive performance could be improved by increasing the soil contact area. Due to the extreme thermal environment on the Moon, this improvement must be achieved using compliant mechanisms and space-graded material. Consequently, the research goal is to design a compliant leg module to enhance the tractive performance of the Lunar Zebro on lunar terrain, employing an analytical optimisation model that combines compliant system behaviour with the mechanics of leg-soil interaction.

The design process employs a morphological analysis along with the ACRREx method, in which different subproblem solutions are combined into multiple concepts. The performance of these concepts is evaluated against selection criteria, leading to the creation of the final concept by integrating the design features associated with high criteria performance. The final concept is translated into an analytical model utilising Castigliano's theorem to describe the compliant behaviour and Wong's terramechanics theorem for deformable wheels to describe the leg-soil interaction. A set of design variables impacting the system's compliant behaviour is defined, for which the tractive performance is optimised while confined by constraints that ensure reliability and durability across various movements and scenarios. The optimisation process is conducted using Sequential Quadratic Programming, due to the non-linearity of the objective function and constraints. An optimal set of design variables is identified for both the middle and outer legs, resulting in not only a significant enhancement of tractive performance but also an increase in tractive efficiency and reduction of leg sinkage. Although concerns are raised about contact surface wear at the optimal set of design variables, a minimal amount of compliance, while staying in the feasible region of the design variables, enhances the tractive performance of the compliant leg compared to the original rigid leg. A final leg design is presented that incorporates modifications informed by research findings.

Contents

Preface	ii
Abstract	iii
1 Introduction	1
1.1 Lunar Zebro	1
1.2 Problem statement	2
1.3 Research scope	3
1.4 Report structure	4
2 Design process	5
2.1 Design requirements	5
2.1.1 Design assignment	5
2.1.2 Functional requirements	5
2.1.3 Non-functional requirements	6
2.2 Concept creation	6
2.2.1 Concept creation methodology	6
2.2.2 Concept designs	8
2.3 Concept selection	9
2.3.1 Concept selection methodology	9
2.3.2 Concept selection criteria	10
2.3.3 Concept selection results	10
2.3.4 Concept discussion	11
2.3.5 Final concept	12
3 Optimisation methodology	13
3.1 Objective	13
3.2 Constraints	14
3.3 Problem statement	15
3.4 Optimisation method	15
4 Terramechanics theory	17
4.1 Terramechanics model assumptions	17
4.2 Static leg-soil interaction	19
4.2.1 Static equilibrium equation	19
4.2.2 Static model solving procedure	20
4.3 Quasi-static leg-soil interaction	20
4.3.1 Soil angles	20
4.3.2 Normal stress distribution	21
4.3.3 Shear stress distribution	21
4.3.4 Leg forces	22
4.3.5 Quasi-static equilibrium equations	23
4.3.6 Tractive efficiency	23
4.3.7 Quasi-static model solving procedure	24
5 Compliance theory	25
5.1 Compliance model assumptions	25
5.1.1 Load application assumption	25
5.1.2 Compliance theorem choice	26
5.2 Castigliano's theorem	27
5.2.1 Straight flexure deflection	27
5.2.2 Curved flexure deflection	29

5.2.3 Compliance model solving procedure	31
6 Constraints theory	32
6.1 Stress limit while walking	32
6.1.1 Straight flexure stress	32
6.1.2 Curved flexure stress	33
6.1.3 Maximum stress application angle	33
6.2 Stress limit with lateral force	34
6.2.1 Straight flexure deflection	34
6.2.2 Curved flexure deflection	36
6.2.3 Loading point deflection	38
6.2.4 Straight flexure stress	38
6.2.5 Curved flexure stress	39
6.2.6 Maximum stress application angle	40
6.3 Skid steering	40
6.3.1 Lateral resistance force	40
6.3.2 Solving procedure	41
6.4 Sideways gradient	41
6.4.1 Force and moment equilibrium	42
6.4.2 Solving procedure	42
6.5 Motor torque transmission	43
6.6 End of contact surface radius for next step	43
6.7 Climbing height	44
7 System Analysis	45
7.1 Optimisation process	45
7.1.1 Middle leg	45
7.1.2 Outer leg	48
7.2 Sensitivity analysis	50
7.2.1 Forward finite difference	51
7.2.2 Central finite difference	51
7.2.3 Middle leg	51
7.2.4 Outer leg	53
8 Performance Analysis	56
8.1 Slip ratio analysis	56
8.1.1 Middle leg	56
8.1.2 Outer leg	58
8.2 Temperature range analysis	59
8.2.1 Middle leg	60
8.2.2 Outer leg	61
9 Result Evaluation	63
9.1 Design	63
9.2 Optima points	64
9.3 Contact surface wear	65
9.4 Temperature range	65
10 Discussion and recommendations	66
10.1 Design	66
10.2 Contact surface wear	66
10.3 Analytical optimisation model	67
11 Conclusion	68
Bibliography	73
A Design process supplementary	76
A.1 Function Tree	77
A.2 Morphological chart	78

A.3	ACRREx table	85
A.4	Concept designs	86
A.5	Weight factor reasoning	89
A.6	Concept selection evaluation	90
B	Terramechanics supplementary	94
B.1	Solving procedure flow charts	95
C	System analysis supplementary	96
C.1	Model parameters	97
C.2	Temperature range performance analysis	98
C.2.1	Middle leg	98
C.2.2	Thermal-resilient middle leg	100
C.2.3	Outer leg	102
C.2.4	Thermal-resilient outer leg	104
C.3	Contour plots	106
C.3.1	Middle leg	106
C.3.2	Outer leg	109
C.3.3	Thermal-resilient middle leg	112
C.3.4	Thermal-resilient outer leg	114
D	Contact surface wear optimisation	116
D.1	Contact surface wear analysis	117
D.1.1	Middle leg	117
D.1.2	Outer leg	118
E	Finite Element Analysis	119
E.1	Stress	120
E.1.1	Middle leg	120
E.1.2	Outer leg	121
E.1.3	Result discussion	123
F	Matlab Code	124
F.1	Parameters	125
F.2	Optimisation	127
F.3	Optimisation using GlobalSearch	128
F.4	Objective function	129
F.5	Analysis: Terramechanics model	130
F.6	Compliance model	136
F.6.1	Force-deflection relationship	136
F.6.2	Longitudinal force-deflection relationship	138
F.7	Constraints	140
F.7.1	Constraints definition	140
F.7.2	Stress limit while walking & motor torque transmission	141
F.7.3	Stress limit with lateral force	143
F.7.4	Sideways gradient	146
F.7.5	End of contact surface radius for next step	151
F.7.6	Climbing height	152

List of Figures

1.1	Lunar Zebro	2
1.2	Initial leg module	2
1.3	Current leg module	2
2.1	Concept designs	8
2.2	Reformulated and extended flexure concepts	11
2.3	Final concept	12
3.1	Design variable definition	14
4.1	Deformable leg on granular soil when $P_w \leq P_{cr}$	18
4.2	Static equilibrium	19
4.3	Quasi-static equilibrium	20
4.4	Longitudinal shear displacement beneath the deforming leg	22
5.1	FBD leg design	26
5.2	FBD straight flexure part	27
5.3	FBD full straight flexure	29
5.4	FBD Curved flexure	29
6.1	FBD straight flexure part	34
6.2	FBD Full straight flexure	36
6.3	FBD Curved flexure	36
6.4	Leg velocity coordinate system	40
6.5	FBD Lunar Zebro on sideways gradient	42
6.6	Effective radius definition	43
6.7	Climbing height definition	44
7.1	Contour plot middle leg drawbar pull DP, t_c vs t_s at L_{opt}	47
7.2	Contour plot middle leg drawbar pull DP, t_c vs L at $t_{s,opt}$	47
7.3	Contour plot middle leg drawbar pull DP, t_s vs L at $t_{c,opt}$	48
7.4	Contour plot outer leg drawbar pull DP, t_c vs t_s at L_{opt}	49
7.5	Contour plot outer leg drawbar pull DP, t_c vs L at $t_{s,opt}$	50
7.6	Contour plot outer leg drawbar pull DP, t_s vs L at $t_{c,opt}$	50
7.7	Middle leg curved flexure thickness t_c	52
7.8	Middle leg straight flexure thickness t_s	52
7.9	Middle leg straight flexure length L	53
7.10	Outer leg curved flexure thickness t_c	54
7.11	Outer leg straight flexure thickness t_s	54
7.12	Outer leg straight flexure length L	54
8.1	Slip ratio analysis of compliant and rigid middle leg	57
8.2	Slip ratio analysis of compliant and rigid outer leg	59
8.3	Contour plot middle leg drawbar pull DP, t_s vs L at $t_{c,100^\circ C}$, $T = 100^\circ C$	61
8.4	Contour plot middle leg drawbar pull DP, t_s vs L at $t_{c,100^\circ C}$, $T = 20^\circ C$	61
8.5	Contour plot outer leg drawbar pull DP, t_s vs L at $t_{c,100^\circ C}$, $T = 100^\circ C$	62
8.6	Contour plot outer leg drawbar pull DP, t_s vs L at $t_{c,100^\circ C}$, $T = 20^\circ C$	62
9.1	Final design middle leg	64
9.2	Final design outer leg	64

A.1	Function Tree	77
B.1	Solving procedure static model	95
B.2	Solving procedure quasi-static model	95
E.1	Maximum stress $\sigma_{s,walk}$ in straight flexure of middle leg while walking	120
E.2	Maximum stress $\sigma_{c,walk}$ in curved flexure of middle leg while walking	121
E.3	Maximum stress $\sigma_{s,side}$ in straight flexure of middle leg while climbing along a sideways gradient	121
E.4	Maximum stress $\sigma_{c,side}$ in curved flexure of middle leg while climbing along a sideways gradient	121
E.5	Maximum stress $\sigma_{s,walk}$ in straight flexure of outer leg while walking	122
E.6	Maximum stress $\sigma_{c,walk}$ in curved flexure of outer leg while walking	122
E.7	Maximum stress $\sigma_{s,side}$ in straight flexure of outer leg while climbing along a sideways gradient	123
E.8	Maximum stress $\sigma_{c,side}$ in curved flexure of outer leg while climbing along a sideways gradient	123

List of Tables

2.1	ACRREx matrix with voids	7
2.2	ACRREx matrix with new solutions	8
2.3	Concept performance ratings	9
2.4	Weight factor of criterion subject	9
2.5	Concept evaluation scores	10
4.1	Applicable normal stress at each contact section	21
7.1	Constraint performance middle leg	46
7.2	Constraint performance outer leg	48
8.1	Material properties per temperature	59
9.1	Constraint performance outer leg at $\mathbf{x}_{o,new}$	65
A.1	Morphological chart	78
A.2	ACRREx matrix with new solutions	85
A.3	Concept embodiment usage	86
A.4	Weight factor reasoning of criterion subject	89
A.5	Concept 1 evaluation chart	90
A.6	Concept 2 evaluation chart	91
A.7	Concept 3 evaluation chart	92
A.8	Concept 4 evaluation chart	93
C.1	Model parameters	97
C.2	Objective performance middle leg per temperature	98
C.3	Constraint performance middle leg per temperature	99
C.4	Objective performance thermal-resilient middle leg per temperature	100
C.5	Constraint performance thermal-resilient middle leg per temperature	101
C.6	Objective performance outer leg per temperature	102
C.7	Constraint performance outer leg per temperature	103
C.8	Objective performance thermal-resilient outer leg per temperature	104
C.9	Constraint performance thermal-resilient outer leg per temperature	105
D.1	Constraint performance middle leg optimised for contact surface wear	117
D.2	Constraint performance outer leg optimised for contact surface wear	118
E.1	Analytically derived stress values middle leg at $\mathbf{x}_{m,opt}$	120
E.2	Analytically derived stress values outer leg at $\mathbf{x}_{o,opt}$	122
E.3	FEA data	123

1

Introduction

1.1. Lunar Zebro

To gain a greater understanding of the Moon's surface, its history, and the potential for future space missions, there is a high demand for exploration and research of the lunar environment. Due to increasingly sophisticated technology of recent times, extra-terrestrial rovers play a vital role in the acquisition of scientific data, offering a reduced risk and cost compared to humans physically exploring the Moon. These rovers can be specifically designed and optimised to execute certain tasks. In pursuit of mapping the lunar surface, a swarm of nano-rovers can collectively form a network and cover extensive areas. However, these nano-rovers are likely to encounter challenges on the lunar surface, which is covered by regolith, rocks, and craters, consequently complicating mobility for smaller vehicles equipped with wheels. The Lunar Zebro presents an innovative approach to overcome such challenges.

The Lunar Zebro is a nano-rover developed by TU Delft, presented in Figure 1.1. It is a hexapod rover that uses six C-shaped legs to traverse the rough surface and steep slopes of the Moon, while also being able to climb over obstacles. Its design originates from the RHex robot, which was built to handle the complexity and diversity of natural terrain [2]. The RHex set a new standard in mobile robotics by utilising the C-shaped leg design with a single degree of freedom per leg, diverging from the traditional multi-segmented legs found in most legged robots. The design combines the stability of legged movement with the efficiency of wheels, allowing RHex to traverse rough terrain more efficiently and perform complex manoeuvres such as climbing [3]. The initial legs of the Lunar Zebro, presented in Figure 1.2, were an adaptation of the RHex leg module.

With dimensions comparable to an A4 sheet and a mass of 2.5 kg, the Lunar Zebro can be efficiently transported aboard a rocket. The chassis is characterised by a monocoque design, wherein all relevant components are integrated, and sensitive components are protected against lunar dust. The energy required to move is gained through a movable solar panel located on top of the chassis. The legs are axisymmetrically aligned to maximise stability while maintaining compactness [4]. Each leg is independently actuated by a space-graded motor, permitting adjustable contact angles and offering substantial control over the magnitude and direction of the ground contact forces [2].

The Lunar Zebro possesses the capability to employ various gaits tailored to specific tasks. This study focuses exclusively on the walking mechanism of the Lunar Zebro, which uses an alternating tripod gait. A tripod is established by two outer legs on one side and the middle leg on the other side. When one tripod establishes ground contact, the alternate tripod rotates in the air to set the next step. Due to the difference in distance between the legs and the centre of mass within the tripod, the weight in the static equilibrium of the rover is unevenly distributed over the legs. The weight distribution also varies depending on whether the rover is climbing, descending, or steering. As the Lunar Zebro remains under development, with neither the centre of mass nor the contact points of the legs definitively identified, it is assumed that the middle leg supports half the weight, whereas each outer leg supports a quarter.

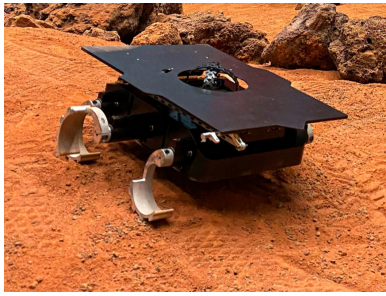


Figure 1.1: Lunar Zebro [5]

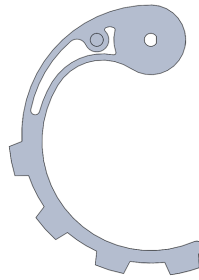


Figure 1.2: Initial leg module [6]

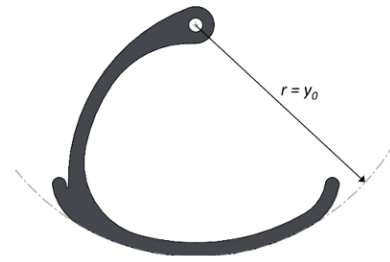


Figure 1.3: Current leg module [7]

As the initial legs of the Lunar Zebro were an adaptation from those of RHex, they are not fully optimised for the lunar surface characteristics or the Lunar Zebro itself. In a study conducted by Van Rijn [7], a system-level performance analysis was executed to improve the leg's design with respect to traction, mobility, and climbing metrics. Through a computer-aided manual optimisation process using a foundational model, it was identified that no singular optimal leg shape achieves optimal performance. Instead, it was concluded that the most effective design is dependent on the weight factors defined by the designer. An all-round performing design was developed, which is implemented as the current Lunar Zebro leg module (Figure 1.3).

The current leg features a maximised radius within the given spatial constraints to increase the contact surface area with the soil and improve traction. Furthermore, the uniform radius contributes to a smoother walking motion, reducing initial waddling behaviour and thereby improving overall energy efficiency. The climbing capability of the Lunar Zebro is supported by a hook that serves as the gripping point, enabling climbing without compromising traction or energy efficiency. The inward curling tips are designed to reduce digging in and scooping up lunar regolith.

1.2. Problem statement

The first mission of the Lunar Zebro is intended to execute a landing and traverse the lunar surface for the duration of a lunar day, equivalent to fourteen Earth days. The Lunar Zebro will operate on lunar regolith and navigate across features such as craters and dunes, requiring the legs to deliver substantial traction to maintain mobility. As the current leg design is fully rigid, only a small contact area with the soil is maintained, which limits traction and reduces movement efficiency, ultimately compromising overall system performance.

Tractive performance can be enhanced through the implementation of a deformable leg design that increases the contact area with the lunar soil. To endure the Moon's extreme thermal environment, with temperature variations ranging from average daytime highs of approximately 124°C to lows near -178°C just before lunar sunrise [8], this enhancement must be realised using compliant mechanisms and materials suitable for space. The compliant mechanism must be constrained to ensure reliability and durability across a range of movements and scenarios.

Currently, no compliant leg module has been specifically designed for the lunar environment, nor has a model been developed to analyse the influence of compliant leg characteristics on leg-soil interactions. Therefore, the following research goal is formulated:

Design a compliant leg module to enhance the tractive performance of the Lunar Zebro on lunar terrain.

To achieve this research goal, the following sub-goals can be identified:

- *Design a compliant leg concept based on the current Lunar Zebro leg module.*
- *Create a model to calculate the tractive performance of the leg concept based on terramechanics and compliance theory.*
- *Conduct an optimisation process to identify the design variables that yield optimal tractive performance.*
- *Investigate the individual influence of the design variables on the tractive performance.*
- *Present a compliant Lunar Zebro leg module based on the research findings.*

1.3. Research scope

This study focuses on the design and performance optimisation of a compliant leg module for the Lunar Zebro operating on the lunar surface. The tractive performance is solely evaluated on a flat terrain of lunar regolith, utilising the terramechanics theoretical framework. The Lunar Zebro motors are expected to deliver the required torque to facilitate the traction of the newly designed leg module. The tractive performance enhancement is assessed by comparing the tractive performance of the newly designed leg module with the currently used leg module. For the design process, a goal is set to ensure that the new leg module behaves similarly to the original rigid C-shaped leg of the Lunar Zebro, combining the efficiency of a wheel with the stability and climbing capability of a leg.

The space journey and landing survivability are excluded from the scope of this research. The study is limited to the mechanical and structural aspects of the leg, including geometric optimisation and performance evaluation. The optimisation is conducted using analytical calculations for the objective and the constraints, with assumptions detailed in the respective sections of the theoretical framework. These assumptions are accounted for by the comparative nature of the design variables that are optimised, and the optimisation limitations, such as computational constraints. Although the optimisation results in absolute optima, the primary interest lies in evaluating the design's tractive performance near its optima. This includes the determination of whether the optima are sharp or broad and whether certain design variables significantly exert a notable influence on performance. Such assessments add significance to both the obtained optima and the design's performance implications. The absolute performance of the innovative compliant leg could be compared to that of the original rigid leg, providing valuable insight towards achieving the research goal.

In this study, the tractive performance is defined in the upright leg orientation, which enables maximum tractive performance. Due to the design of the leg concept, deviations from this upright orientation result in increased stiffness, thereby decreasing the available tractive performance. The calculation of the tractive performance of the legs is performed without accounting for the multi-pass effect, signifying that any changes in the performance due to the pre-compression of lunar soil by a preceding leg are neglected.

The study focuses specifically on the utilisation of compliant features to gain traction without grousers. While the traction contribution provided by grousers can be superposed in the case of fully rigid legs [9], this is not applicable for compliant legs, as grousers would fundamentally change the stiffness of the used compliant features.

Considering its low operating speed of 5 cm/s, the Lunar Zebro is modelled as a quasi-static system, in which dynamic effects such as acceleration are considered negligible. Furthermore, the legs of the Lunar Zebro are low enough in weight to disregard rotational inertia. Nevertheless, slip effects are incorporated into the analysis.

Due to the extreme temperature variations on the lunar surface, changes in material properties may influence the compliant behaviour of the design. To minimise these effects, aluminium 7075-T6 is used exclusively, as it demonstrates relatively stable material properties over a wide temperature range. Since the mission is carried out only at specific periods on lunar day, the compliant behaviour of the design is modelled at a temperature of 20°C, independently of temperature variations. To evaluate performance under extreme operating temperatures, the final design is analysed at 100°C and -80°C. An effort is made to develop a thermal-resilient version that can be employed across a range of temperatures.

Due to the lightweight design of the Lunar Zebro, there is limited gravitational force available to deform the leg. Consequently, the thickness of the ground contact flexure is required to be small, which may pose a risk for contact surface wear due to the abrasive characteristics of lunar regolith and the presence of sharp rocks. As the goal of this research is to obtain optimal tractive performance, and since contact surface wear has uncertain variables and the first mission duration is relatively short, the analysis is performed without considering contact surface wear. However, because the material selection for this project is restricted, the optimisation results will determine whether a small ground contact flexure thickness is critical for increasing the leg's tractive performance and if soil contact wear is likely to pose an issue.

This research aims to demonstrate the potential of the compliant design to enhance traction on lunar soil. By doing so, it will establish a foundation for future testing to identify which design features, such as material selection, are required to ensure long-term viability.

1.4. Report structure

This report is structured as follows. In Chapter 2, the design process of the new compliant leg module is described, outlining the design requirements, concept design methodology, and concept selection. Chapter 3 describes the optimisation methodology used, based on the objective and constraints. The theoretical framework of this study is described in the respective Chapters 4, 5, and 6. Chapter 4 presents the theoretical framework of terramechanics, which describes the interaction between the compliant leg and the lunar soil. Chapter 5 covers the theoretical framework of compliance, detailing the relationship between applied forces and the resulting deformation of the leg. Chapter 6 addresses the constraint theory, explaining the calculations related to the constraints acting on the system. The Chapters 7, 8, and 9 form the results of the study. In Chapter 7, the optimisation is performed, showing the optimum values for the design variables, while a sensitivity analysis is conducted to evaluate the influence of the design variables on the model and the optima. In Chapter 8, the performance of the optima is analysed for each slip ratio, while further analysis explores the performance across a temperature range. The results and their physical implications are evaluated in Chapter 9. In Chapter 10, the limitations of the study are discussed and recommendations for future work are proposed. Lastly, Chapter 11 presents a conclusion drawn from the research findings.

2

Design process

This chapter describes the design process of an innovative compliant leg module. Firstly, the design assignment and requirements are identified, after which multiple concepts are created via combinations of subproblem solutions. Lastly, a final concept is selected based on the design requirements.

2.1. Design requirements

2.1.1. Design assignment

The design assignment is the objective set to improve the current product, based on the research goal. In this instance, the assignment is to design a compliant leg module to enhance the tractive performance of the Lunar Zebro on lunar terrain. The design must behave similarly to the original rigid C-shaped leg of the Lunar Zebro, combining the efficiency of a wheel with the stability and climbing capability of a leg.

2.1.2. Functional requirements

Functional requirements are criteria that the system shall meet to ensure functionality. These requirements define the intended behaviour of the system. Within these requirements exists a hierarchy structure, wherein subfunctions contribute to the primary functions. The functional requirements for the compliant Lunar Zebro leg module are specified, with a function tree visualisation as seen in Appendix A.1.

1. System shall convert motor rotation into forward motion.
 - (a) System shall generate traction to walk or brake.
 - i. System shall provide increased ground contact surface.
 - (b) System shall enable climbing over obstacles.
 - i. System shall provide a gripping point.
 - (c) System shall re-establish ground contact after each step cycle.
2. System shall support the weight of the vehicle.
 - (a) System shall provide a framework to connect flexure components.
 - (b) System shall provide a contact surface to connect flexures with the ground.
 - (c) System shall prevent excessive deflection of flexible elements.
 - (d) System shall provide a mechanical interface with the motor shaft.
3. System shall operate reliably in the lunar environment.
 - (a) System shall resist abrasive wear from lunar soil.
 - (b) System shall minimise scooping lunar regolith during operation.
 - (c) System shall prevent accumulation of lunar regolith on critical surfaces.

2.1.3. Non-functional requirements

The non-functional requirements define what the system shall be, focusing on how well it performs. These requirements form the constraints of the system and are quantifiable. The non-functional requirements for the compliant Lunar Zebro leg module are specified with their subject and corresponding specifications. These are established based on earlier Lunar Zebro design literature [6], [7], in addition to performance values of the current leg design. The deformability requirements are derived from ExoMars standards, which specify a target vertical deflection range between 10%-20% of the wheel radius and a maximum vertical deflection to the bump stop set at 24% of the wheel radius [10]. The target vertical deflection range has been broadened to 5% and 20% of the wheel radius, reflecting the physical differences between the Lunar Zebro leg module and the ExoMars wheel, alongside findings by Ishigami, which suggest improved drawbar pull at lower vertical deformation levels [11].

1. System shall be able to transmit motor torque into traction force at ground contact. (**Traction transmissibility**)
 - (a) System shall withstand a longitudinal deflection of a maximum of 5 mm during ground contact.
2. System shall be deformable on ground contact. (**Deformability**)
 - (a) System shall vertically deflect between 3-12 mm (5%-20% of the leg radius) in a smooth motion.
 - (b) System shall transition to a minimum radius of 58.5 mm at the end of the contact surface (10% of arc length) to re-establish ground contact after each step cycle.
3. System shall be durable. (**Durability**)
 - (a) System shall have a minimum lifespan of 14 Earth days.
 - i. System shall have a maximum vertical deflection of 14.4 mm (24% of leg radius).
 - ii. System shall have maximum stress levels lower than the material yield stress of 503 MPa.
 - iii. System shall be able to withstand the forces and moment along the lateral direction while skid steering or climbing along a maximum sideways gradient of 15°.
4. System shall be lightweight. (**Weight**)
 - (a) System shall have a mass less than 50 grams.
 - (b) System shall be manufactured using Aluminium 7075-T6.
5. System shall be capable of climbing over obstacles. (**Climbing ability**)
 - (a) System shall have a gripping point height higher than 55 mm.
6. System shall be feasible to manufacture. (**Manufacturability**)
 - (a) System shall have fewer than 5 parts.
 - (b) System shall be capable of being assembled in a week.
7. System shall be able to fit in the available design space. (**Size**)
 - (a) System shall have a maximum radius of 60 mm.
 - (b) System shall have a maximum width of 20 mm.

2.2. Concept creation

2.2.1. Concept creation methodology

Morphological analysis

Morphological analysis is used to create concept designs utilising sub-solutions for the functional requirements. For each subfunction, multiple design strategies are presented, from which different embodiments are derived. These embodiments are presented in a morphological chart, providing a clear overview of all identified sub-solutions. A design concept is made by combining the embodiments

of all subfunctions, thereby creating a solution to the design assignment. The process of combining embodiments is executed multiple times to generate designs with different characteristics.

The morphological analysis method is selected because its division of the problem into subfunctions creates a well-structured environment in which it becomes more manageable to find a comprehensive solution. Solutions are easier to find for subfunctions than for an entire problem. Additionally, the sub-solutions give a large amount of combinations, resulting in a high number of concepts.

The disadvantages of the morphological analysis are addressed by Van Egmond [12]. Van Egmond highlights the method's reliance on precise subfunction formulations, implying that "if the subproblems together do not span the entire main problem, then there will be gaps in created solutions". Furthermore, Van Egmond asserts that the "method leans on recombination to find new solutions" and that "the sub-solution space is usually limited by the collective knowledge of the designer(s) and therefore the chance of finding innovative solutions is limited."

ACRREx

To address the assertions made by Van Egmonds and to develop more innovative sub-solutions, the morphological analysis method is expanded with elements of the ACRREx method. The ACRREx method, created by Breedveld et al. [13], is intended to guide designers in identifying voids within the solutions obtained.

In the first phase of this method, labelled "Abstracting, Categorising and finding voids", fundamental differences between the identified sub-solutions are assessed. By categorising these differences in a table, a matrix can be generated in which the embodiments derived from the morphological analysis are integrated, thereby revealing voids. These voids lead to new solutions to the subproblems. This procedure is executed for the subfunction "System shall increase contact surface". One fundamental difference can be expressed by the design strategies, which in this case is the flexing orientation, being either in-plane or out-of-plane deformation. The other fundamental difference is the type of flexure used. A matrix table, as detailed in Table 2.1, is constructed. By filling in the already found embodiments, voids are identified, and new embodiments for this subfunction are created. The resulting matrix table is presented in Table 2.2.

Table 2.1: ACRREx matrix with voids


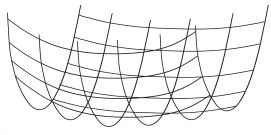



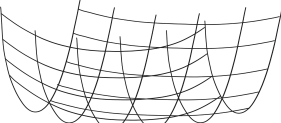
	In-plane deformation	Out-of-plane deformation
Half-circle flexures		?
Wire flexures	?	

Table 2.2: ACRREx matrix with new solutions

	In-plane deformation	Out-of-plane deformation
Half-circle flexures		
Wire flexures		

The second phase of the method, entitled "Reflecting, Reformulating and Extending", is aimed at extending the existing categorisation by examining alternatives to the fundamental differences. In this case, this approach yields additional flexure types. Next to half-circle and wire flexures, there are also straight, circle and band flexures, among others. The full ACRREx table is provided in Appendix A.3. Its findings are incorporated into the morphological chart in Appendix A.2, which presents a comprehensive overview of all sub-solutions and embodiments.

2.2.2. Concept designs

By creating combinations of the identified embodiments within the morphological chart, multiple concepts are generated. The four concepts selected for further analysis are presented in Figure 2.1, with their design specifications detailed in Appendix A.4.

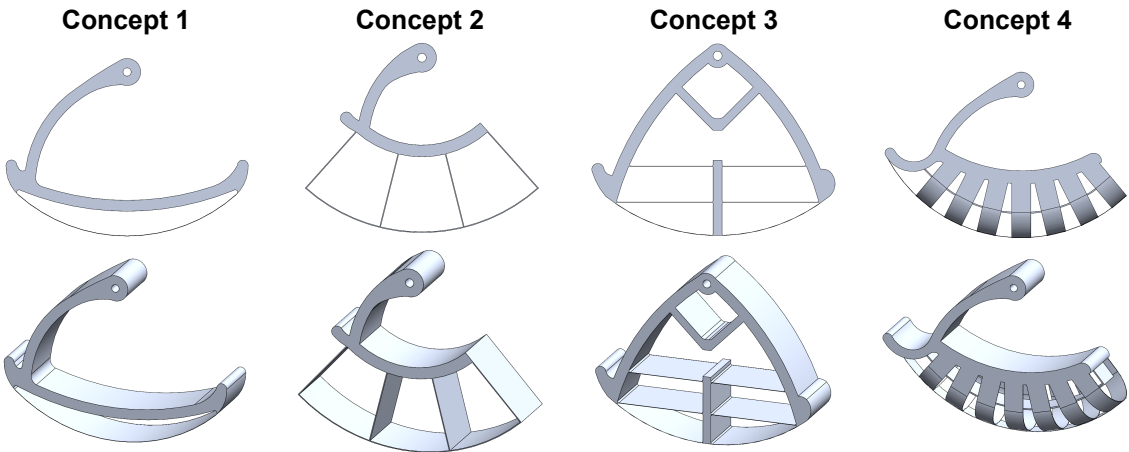


Figure 2.1: Concept designs

2.3. Concept selection

2.3.1. Concept selection methodology

In an ideal situation, the selection of a concept can be achieved by quantifying the performance of each concept against each non-functional requirement. However, it is not feasible, for instance, to ascertain the transmittable torque or longevity of a concept. Although some specifications of non-functional requirements can be determined in future design stages, a decision must be made at the current design stage with the information presently available. This is achieved by creating concept selection criteria that are a derivation of the non-functional requirement specifications. For each non-functional requirement subject, an estimation of specifications is presented to demonstrate the potential capability of a concept.

Each concept is graded based on its estimated performance on a concept selection criterion. The scores and their significance are detailed in Table 2.3. The scores corresponding to each criterion per subject are added together, divided by the total possible score and multiplied by the weight factor of that subject, as outlined in Table 2.4. The total score is calculated by summing the weighted scores for each concept. The weight factor shows which criterion subjects have the most influence on the concept's performance in achieving the design assignment. Traction transmissibility is assigned the highest weight factor, as the leg is incapable of moving the Lunar Zebro without traction transmission, whereas manufacturability is assigned the lowest weight factor, as the time consumption of custom-made production is a minor inconvenience due to the limited amount of legs required. The complete reasoning behind the weight factors is provided in Appendix A.5.

It should be recognised that the subjects may be interconnected, such as in a scenario where the flexures of a concept must be thickened to ensure torque transmission, directly resulting in reduced deformability and increased weight. In this selection process, the most important criterion subject to the spirit of a concept, as determined by the designer, is prioritised. In the mentioned example of utilising thicker flexures, the traction transmissibility was deemed the most important criterion subject. Consequently, this subject is prioritised, causing the concept to perform worse on the deformability and weight criteria.

Table 2.3: Concept performance ratings

Performance rating	Score	Symbol
Good	5	++
Decent	4	+
Mediocre	3	0
Bad	2	-
Terrible	1	--

Table 2.4: Weight factor of criterion subject

Criterion subject	Weight factor
Traction transmissibility	30
Deformability	20
Durability	20
Weight	15
Climbing ability	10
Manufacturability	5
Total	100

2.3.2. Concept selection criteria

Based on the non-functional requirements and specifications provided in Section 2.1.3, the concept selection criteria are determined. The subjects with their respective concept selection criteria are presented below. The subject of size is not taken into account, as it is expected that every concept fits in the available design space.

- **Traction transmissibility**

- Capability to transmit moment from the motor axis to leg contact.
- Capability to transmit moment at leg contact to forward movement.

- **Deformability**

- Capability to deform in a range of 3-12 mm.
- Capability to do a smooth deformation motion and transition.

- **Durability**

- Capability to counter over-deflection.
- Capability to have low stress levels.
- Capability to withstand forces and moments along the lateral direction.

- **Weight**

- Capability to be low weight.

- **Climbing ability**

- Capability to have a high gripping point.

- **Manufacturability**

- Capability to manufacture with minimum parts.
- Capability to manufacture in a sufficient time frame.

2.3.3. Concept selection results

The four concepts are evaluated on the selection criteria. The performance of a concept on each criterion is explained in Appendix A.6. The overall scores are provided in Table 2.5. It is evident that Concept 1 performs the best. This is largely due to its high performance in traction transmissibility, while also scoring well on less important criteria such as climbing ability and manufacturability. The downside of Concept 1 is its deformability, due to the stiff design and non-smooth deformation motion.

Concept 2 scores second best, with its flaw being traction transmissibility, due to the long radial flexure design. However, this design ensures good deformability performance. Concept 4 is rated third best. Although the concept scores well in traction transmissibility and deformability, the number of flexures needed increases the weight and makes it difficult to manufacture. Concept 3 performs the worst, as the number of parallel flexures causes the concept to deform poorly if reasonable flexure thicknesses are considered.

Table 2.5: Concept evaluation scores

Criteria	Weight factor	Concept 1		Concept 2		Concept 3		Concept 4	
		Score	Weighted	Score	Weighted	Score	Weighted	Score	Weighted
Traction transmissibility	30	9/10	27	6/10	18	9/10	27	8/10	24
Deformability	20	5/10	10	9/10	16	2/10	4	8/10	16
Durability	20	10/15	13.3	11/15	14.7	12/15	16	10/15	13.3
Weight	15	4/5	12	5/5	15	3/5	9	2/5	6
Climbing ability	10	5/5	10	3/5	6	5/5	10	5/5	10
Manufacturability	5	10/10	5	8/10	4	6/10	3	4/10	2
Total	100		77.3		75.7		69.0		71.3

2.3.4. Concept discussion

Although Concept 1 has the best performance on the concept selection criteria, it does not imply that this concept is the perfect design for the assignment. It is more valuable to analyse why a design performs better in certain areas, to understand the influence of a design aspect. This design phase can be called a second "Reflecting, Reformulating and Extending" phase.

Reflecting the performance of the concepts on their most important criteria, it can be seen that Concept 1 has a high traction transmissibility performance, due to the ground contact flexure being connected to the frame at two points, and the small distance between the ground contact flexure and the frame. Meanwhile, Concepts 2 and 4 have high deformability performance because the ground contact flexure is connected to the frame by other flexures, which creates the possibility to deflect in additional directions than just radially. The deformation performance of Concept 2 is especially high as the design's traction contributes to flexure deformation, which is beneficial as the available gravitational force is low.

When the design task is reformulated, one could question how the leg design could combine the traction transmissibility performance of Concept 1 with the deformability performance of Concept 2. In which the answer is given in the combination of the strengths of the concepts. This leads to a design in which the ground contact flexure is connected to the frame on the side that makes initial ground contact, creating good traction transmissibility. The other end of the ground contact flexure is connected to another flexure, which lets the ground contact flexure deflect in both the radial and longitudinal directions. A reformulated concept of the combination of Concepts 1 and 2 is created and presented as the radial flexure concept in Figure 2.2. If this reformulation is extended, different types of flexures can be used to create the deformation of the ground contact flexure, for example, using a single half-circle flexure, an X-flexure or a double-sided X-flexure, as respectively presented in Figure 2.2.

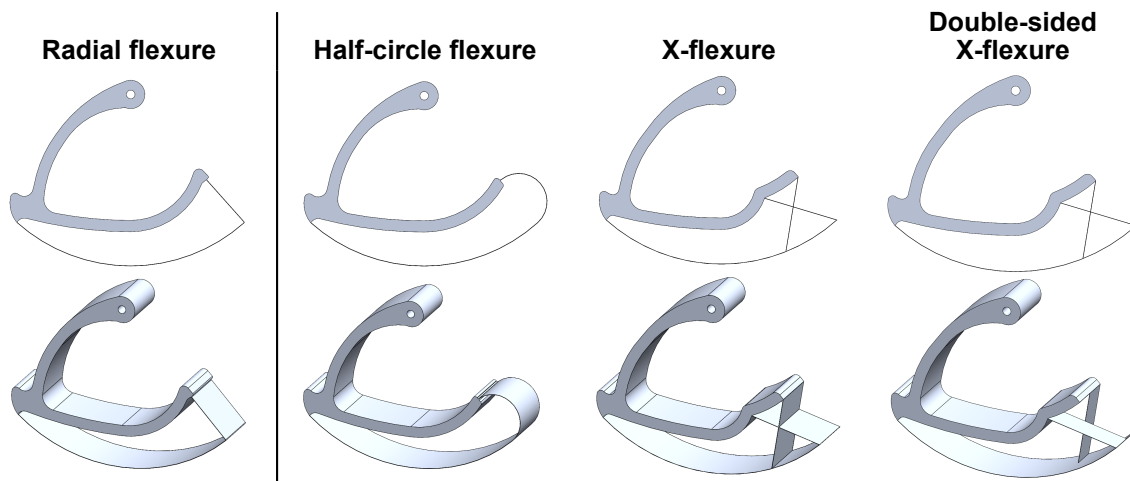


Figure 2.2: Reformulated and extended flexure concepts

The final concept is chosen between the reformulated and extended flexure concepts. Based on the reformulated design task, the end of the ground contact flexure must be able to deflect both in the radial and longitudinal directions. The radial flexure concept is expected to have the highest radial and longitudinal deflection capability. Additionally, its movement is also predictable, and enough stiffness can be created at the end of the contact surface to achieve a smooth transition to the next step. The extended flexure designs with half-circle flexure and double-sided X-flexure are presumed to have the capability to nearly, if not match, the radial flexure performance. However, potential concerns are raised about these concepts. The half-circle flexure concept could be vulnerable to rotational instability around its vertical axis, whereas the double-sided X-flexure concept could be vulnerable to rotational instability around its longitudinal axis. These concerns could limit the performance range of these concepts. Consequently, they were not selected for this study. Nevertheless, further research is recommended on these concepts. The single X-flexure is expected to be too stiff to obtain the required rotatory motion around its central axis to let the ground contact flexure deflect in the longitudinal direction and obtain enough vertical deflection.

2.3.5. Final concept

The final concept is presented in Figure 2.3. The frame of the leg is made out of a smaller C-shape with an extension to form an uncoupled hook. This uncoupled hook gives the design a high gripping point, while also creating a rigid segment to ensure traction transmission. It has a flexure that consists of a curved segment and a straight segment, while being fixed to the frame at both ends. The straight segment is placed radially on the curved segment, increasing stiffness when the leg is at the end of its step and needs to let the next leg make contact with the ground. The flexure design deflects under the influence of gravity and traction force. Due to the low mass of the Lunar Zebro and corresponding low gravitational force, a design that deflects solely under gravity is expected to require such a small flexure thickness that the design becomes infeasible to operate. The design has a single ground contact flexure, guaranteeing a large ground contact surface to transmit traction. The design prevents over-deflection of the ground contact flexure utilising a bump stop created by the base frame. The frame is connected to the motor axis by a set screw.

Multiple design choices are aimed at helping the leg survive in the lunar environment. The system minimises scooping up lunar regolith by increasing the design's contact area to minimise sinkage, while all edges are made with fillets to prevent lunar regolith from accumulating on these edges. No protection against soil contact wear is created, as the mission duration is just fourteen Earth days and a coating layer is expected to make the flexure behaviour less predictable.

As a final remark, the final concept will undergo optimisation for tractive performance on lunar terrain. Should this study identify areas where objective performance or constraint satisfaction can be improved through design modifications, such recommendations will be presented in the design discussion of Section 9.1.

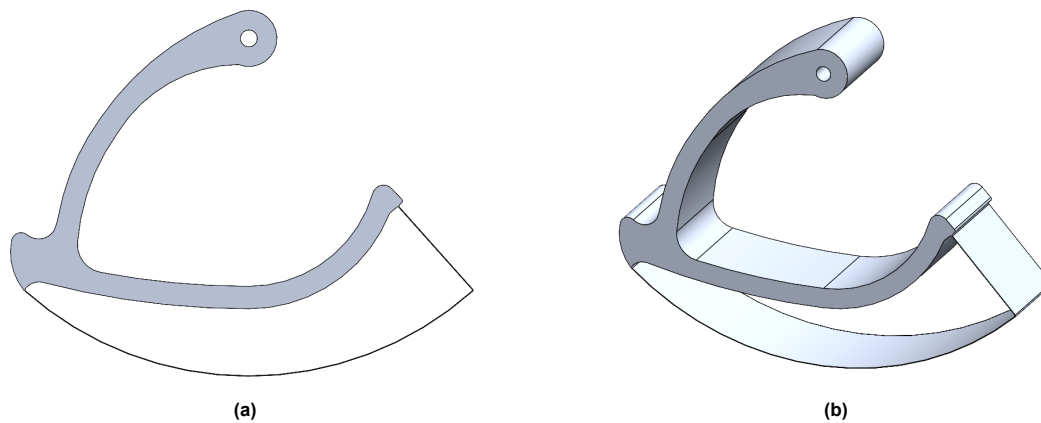


Figure 2.3: Final concept

Optimisation methodology

This chapter describes the methodology of the optimisation process. First, the research goal is translated to an optimisation objective, in which three design variables are identified. Subsequently, the constraints in the optimisation process are presented, and the optimisation method is argued and explained.

3.1. Objective

The research goal is to design a compliant leg module to enhance the tractive performance of the Lunar Zebro on lunar terrain. Based on the proposed design, an analytical optimisation model is created that combines terramechanics and compliance theory. An optimisation process is performed to maximise the tractive performance, expressed by the maximum drawbar pull. The deformation of the leg is not constant, as it varies depending on the orientation of the leg relative to the ground contact point, which consequently affects the drawbar pull. In this research, the drawbar pull is defined at its maximum, obtained in the leg orientation presented in Figure 2.3, which means that the ground contact flexure makes full contact with the available soil, and the vertical deformation of the leg is also approximately at its maximum. As the optimisation is performed in the scaled negative null form, the maximum of the objective is found by finding the minimum of the negative objective. The objective function $f(\mathbf{x})$ is given in the scaled negative null form as:

$$\min_{\mathbf{x}} f(\mathbf{x}) = -DP(\mathbf{x}), \quad (3.1)$$

in which DP is the drawbar pull and \mathbf{x} are the design variables that are optimised, defined as the curved flexure thickness t_c , straight flexure thickness t_s , and straight flexure length L . These variables influence the compliant behaviour of the leg and, consequently, the leg-soil interaction.

$$x_1 = t_c, \quad (3.2a)$$

$$x_2 = t_s, \quad (3.2b)$$

$$x_3 = L. \quad (3.2c)$$

As the middle and outer legs are subject to different gravitational forces, the respective legs have different combinations of design variables that yield optimal tractive performance. Consequently, the optimisation process and result analysis are performed separately for both.

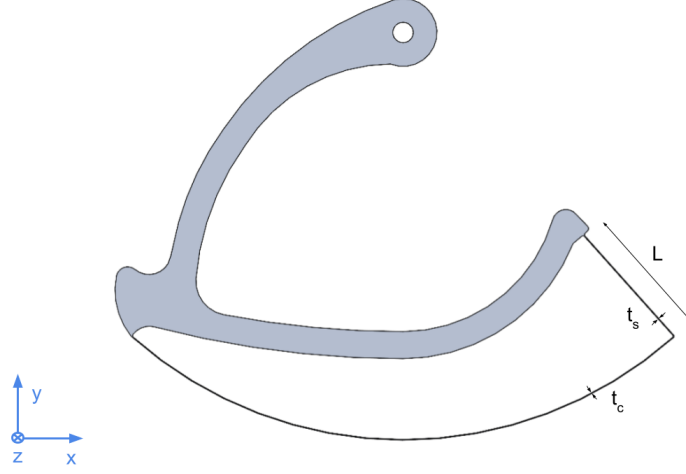


Figure 3.1: Design variable definition

3.2. Constraints

The optimum of the objective is bounded by six non-linear inequality constraints, which are identified based on the non-functional requirements, described in Section 2.1.3.

The Lunar Zebro shall be able to walk without failing, meaning that the maximum stress obtained in the flexure cannot exceed the yield strength σ_y :

$$c_1(\mathbf{x}) = \sigma_{max,walk}(\mathbf{x}) - \sigma_y \leq 0. \quad (3.3)$$

The Lunar Zebro shall be able to skid steer at a single location. During skid steering, a lateral force is exerted on the leg, which increases the stress in the ground contact flexure. The maximum stress in the flexure while skid steering cannot exceed the yield strength σ_y :

$$c_2(\mathbf{x}) = \sigma_{max,skid}(\mathbf{x}) - \sigma_y \leq 0. \quad (3.4)$$

The Lunar Zebro shall be able to climb along a maximum sideways gradient of 15° . While climbing along the sideways gradient, the force equilibrium over the legs changes, increasing the stress in the ground contact flexure on one side. The maximum stress in the flexure while climbing along a sideways gradient cannot exceed the yield strength σ_y :

$$c_3(\mathbf{x}) = \sigma_{max,side}(\mathbf{x}) - \sigma_y \leq 0. \quad (3.5)$$

The Lunar Zebro shall transmit the motor torque to a ground contact force. The longitudinal displacement of the force loading point δ_x cannot exceed the longitudinal displacement threshold $\delta_{x,max}$ of 5 mm:

$$c_4(\mathbf{x}) = \delta_x(\mathbf{x}) - \delta_{x,max} \leq 0. \quad (3.6)$$

The Lunar Zebro shall have a minimum radius at the end of the contact surface to ensure that the next leg can continue the walking motion. With the used gait by the Lunar Zebro, the first 10% of the second leg makes ground contact at the same time as the last 10% of the first leg. The effective remaining radius R_{eff} at the last 10% of the contact surface shall exceed the radius threshold $R_{eff,min}$ of 58.5 mm:

$$c_5(\mathbf{x}) = R_{eff,min} - R_{eff}(\mathbf{x}) \leq 0. \quad (3.7)$$

The Lunar Zebro shall be able to climb over obstacles. The climbing height y_c shall exceed the climbing threshold $y_{c,min}$ of 55 mm:

$$c_6(\mathbf{x}) = y_{c,min} - y_c(\mathbf{x}) \leq 0. \quad (3.8)$$

The design variables are also constrained. The flexure thicknesses are bounded at a minimum of 0.10 mm due to the feasibility of the design and sustained soil contact wear, and at a maximum

of 0.40 mm. Flexure length L was initially bounded to 25 mm, due to the feasibility of the design. However, this was later increased to 40 mm, as the original bound limited the optimal objective value, and potential design adjustments could accommodate the longer length. At the combined upper bound of the flexure thicknesses and lower bound of the flexure length, the leg can be considered rigid.

$$0.10 \leq t_c \leq 0.40 \text{ mm}, \quad (3.9a)$$

$$0.10 \leq t_s \leq 0.40 \text{ mm}, \quad (3.9b)$$

$$10 \leq L \leq 40 \text{ mm}. \quad (3.9c)$$

Due to the lightweight design of the Lunar Zebro, only a limited amount of gravitational force is available to deform the leg. The design compensates for this by utilising its traction force to get additional deformation. However, the defined bounds are necessary to ensure deflection. Nevertheless, the curved flexure thickness can potentially pose a risk for soil contact wear, given the abrasive nature of lunar regolith and the presence of sharp rocks. Based on the reasoning in Section 1.3, the analysis is performed using the defined bounds.

3.3. Problem statement

The full optimisation problem in the scaled negative null form is presented below. On the stress constraints, a safety factor SF is introduced, with a value of 1.5, representing the ultimate factor of safety (FOS_{ULT}) used in aircraft and spacecraft [14]. The safety factor is applied to the stress constraints given the importance of the survivability of the leg in space and the possibility of unaccounted stress spikes due to made assumptions, external factors or unaccounted loads. An example of a made assumption is the neglect of the warping effect, despite its potential to increase stress. An example of an unaccounted load is the Lunar Zebro doing small skid steering manoeuvres while climbing along a sideways gradient. It will not perform full skid steering rotations as expressed by the skid steering constraint, but small lateral forces will be encountered in the manoeuvres. The extra stress this causes is incorporated in the safety factor.

The constraints for torque transmission and end of contact surface radius have no safety factor, due to already strict estimated constraint values ($\delta_{x,max}$ and $R_{eff,min}$). Due to the designed curled climbing hook making initial ground contact when setting a step, the minimum effective radius required at the end of the contact surface is 55.4 mm. However, to create a smooth walking motion, the constraint threshold $R_{eff,min}$ is set at 58.5 mm. The climbing height constraint has no safety factor, as it is expected that the concept design ensures good climbing performance.

$$\begin{aligned} \min_{t_s, t_c, L} \quad & f(t_c, t_s, L) = -DP(t_c, t_s, L) \\ \text{s.t.} \quad & SF \cdot \frac{\sigma_{max, walk}(t_c, t_s, L)}{\sigma_y} - 1 \leq 0, \\ & SF \cdot \frac{\sigma_{max, skid}(t_c, t_s, L)}{\sigma_y} - 1 \leq 0, \\ & SF \cdot \frac{\sigma_{max, side}(t_c, t_s, L)}{\sigma_y} - 1 \leq 0, \\ & \frac{\delta_x(t_c, t_s, L)}{\delta_{x, max}} - 1 \leq 0, \\ & 1 - \frac{R_{eff}(t_c, t_s, L)}{R_{eff, min}} \leq 0, \\ & 1 - \frac{y_c(t_c, t_s, L)}{y_{c, min}} \leq 0, \\ & 0.10 \leq t_c \leq 0.40 \text{ mm}, \\ & 0.10 \leq t_s \leq 0.40 \text{ mm}, \\ & 10 \leq L \leq 40 \text{ mm}. \end{aligned} \quad (3.10)$$

3.4. Optimisation method

The optimisation method applied in this research is Sequential Quadratic Programming (SQP), due to its accuracy and robustness with non-linear problems. This choice is substantiated by Gill et al. [15] stating that "SQP methods have proved highly effective for solving constrained optimisation problems with smooth non-linear functions in the objective and constraints", and by Gould and Toint [16] suggesting that "it is now reasonable to accept the widely-held view that SQP methods really are best".

SQP is a Newton-based iterative method that can incorporate both equality and inequality constraints. As detailed in Equation 3.10, only inequality constraints are used in this study, resulting in the

problem being of the form:

$$\begin{aligned} \min_{\mathbf{x}} \quad & f(\mathbf{x}) \\ \text{s.t.} \quad & g_i(\mathbf{x}) \leq 0, \quad i = 1, \dots, m, \\ & l_{\mathbf{x}} \leq \mathbf{x} \leq u_{\mathbf{x}}. \end{aligned} \quad (3.11)$$

SQP finds a solution to this problem by solving a sequence of Quadratic Programming (QP) subproblems based on a quadratic approximation of the Lagrangian:

$$\mathcal{L}(\mathbf{x}, \lambda) = f(\mathbf{x}) + \sum_{i=1}^m \lambda_i g_i(\mathbf{x}). \quad (3.12)$$

The initial problem is simplified by assuming that the bound constraints are expressed as inequality constraints. The QP subproblems then become of the form:

$$\begin{aligned} \min_{\mathbf{x}} \quad & \frac{1}{2} d^T H_k d + \nabla f(x_k)^T d \\ \text{s.t.} \quad & g_i(x_k) + \nabla g_i(x_k)^T d \leq 0, \quad i = 1, \dots, m. \end{aligned} \quad (3.13)$$

The result of SQP using *fmincon* is found using the following solving algorithm [17]:

1. Input the initial point \mathbf{x}_0 , with *fmincon* then initialising Lagrange multiplier λ_0 and Hessian H_0 estimates.
2. The QP subproblem of Eq. 3.13 is formulated at iteration k and the matrices are set up.
3. The QP subproblem of Eq. 3.13 is solved for search direction d_k and estimated Lagrange multipliers λ_{k+1} .
4. A line search procedure is performed to find the step length parameter α_k , so that a sufficient decrease in the merit function is obtained. The merit function used is a simplified version of the one used by Han [18] and Powell [19], without the influence of equality constraints:

$$\Psi(\mathbf{x}) = f(\mathbf{x}) + \sum_{i=1}^m r_i \max[0, g_i(\mathbf{x})]. \quad (3.14)$$

This function penalises a constraint violation, with r_i being the penalty parameter.

5. If the step is accepted, the new iterate is found to be:

$$x_{k+1} = x_k + \alpha_k d_k, \quad (3.15)$$

while the Hessian H_K and Lagrange multiplier λ_k are updated.

6. This process repeats itself from step 2 until the convergence criteria are reached and a feasible point fulfilling all constraints is found. The default convergence tolerances are applied, with a function and constraint tolerance of 10^{-6} , and step size tolerance of 10^{-10} .

Since *fmincon* is a local optimisation solver dependent on the initial point of the analysis, it does not necessarily find the global optimum. To increase the likelihood of identifying the global minimum, an additional optimisation procedure is performed, in which *fmincon* is combined with a global search method that conducts a scatter search across promising regions of the design space.

4

Terramechanics theory

This chapter describes the terramechanics theory used in the optimisation model. First, the terramechanics model with its assumptions is argued. Subsequently, the used theorem is explained.

4.1. Terramechanics model assumptions

Terramechanics is the theoretical framework that describes the interactions between wheels and soil. Its foundations were introduced by Bekker [9], enabling the computation of wheel tractive performance on granular soil through semi-empirical equations. Wong and Reece [20] expanded upon this theorem by integrating the effects of slippage and the semi-elliptical distribution of stresses beneath the wheel. Bekker's model is used to calculate the tractive performance of the current rigid Lunar Zebro leg module by Van Rijn [7].

This study focuses on the development of a deformable leg, indicating that an altered theoretical framework is required to model the interaction of the designed deforming leg with lunar regolith. Given that the designed leg has a limited contact patch and variable stiffness dependent on leg orientation, the maximum tractive performance is obtained when the leg is in an upright position with the load application near the centre of the flexure. In this orientation, the leg establishes full contact with the soil, which makes the theoretical framework for deformable wheels applicable in this context. The tractive performance is expected to be less in other leg orientations.

The theoretical framework for deformable wheels on granular terrain is described by Wong [21]. It assumes that if the average ground pressure P_w is lower than the critical pressure P_{cr} , part of the wheel flattens against the terrain, as depicted in Figure 4.1. In the static state, the normal stress on this flattened surface equals the average ground pressure P_w . The theorem divides the wheel-soil contact into three sections: soil entry section AB, flattened section BC and soil elastic exit section CD. It is assumed that sections AB and CD keep the original radius, thereby replicating the behaviour of a rigid wheel.

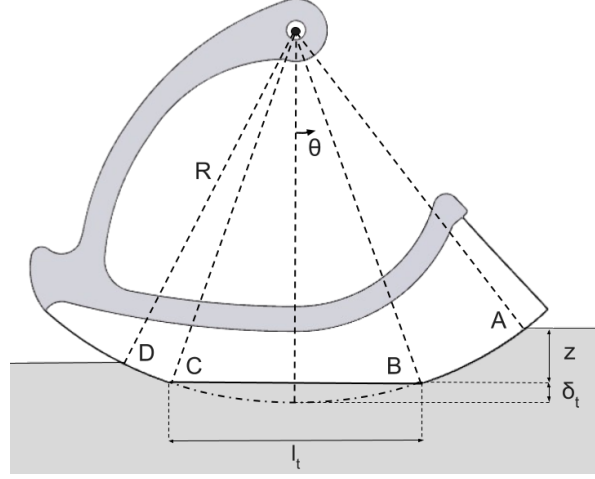


Figure 4.1: Deformable leg on granular soil when $P_w \leq P_{cr}$ [11]

Based on Wong's description, Ishigami [11] developed a terramechanics model that assesses the tractive performance of both flexible and rigid wheels traversing on deformable soil. Within this model, static sinkage and wheel deflection are computed based on the equilibrium between the wheel load and the pressure distribution on the soil in the static state. Subsequently, the vertical and longitudinal force equilibria are obtained for a driving wheel in quasi-static state, assuming the size of the flattened section BC in quasi-static state remains the same as in the static state. Using the equilibrium equations, the tractive performance of the wheel is calculated.

Ishigami introduced two additional assumptions in his model. Firstly, the normal stress beneath the flattened section is uniformly distributed. Secondly, the normal stress beneath the entire contact patch (including non-deformed sections) in the lateral direction is uniformly distributed. Ishigami verified the reliability of the first assumption through experimental evidence provided by Narita et al. [22], who demonstrated uniform normal stress on the flattened section of a lunar rover wheel composed of metal leaf flexures and operating on lunar regolith. Should the ground become more rigid or the mechanical behaviour of the deformable leg become non-linear, the theorem is expected to lose accuracy.

This study employs a modified version of Ishigami's model to calculate the tractive performance of the designed deformable leg. Modifications include the coupling with the compliance theory of the leg module defined in Chapter 5, an altered sinkage definition and static leg-soil interaction, adopting a similar approach to Zhu [23], and adjustments to the deformation resistance, incorporating the equation proposed by Bekker and Semonin [24]. The entire model is explained in successive sections.

As stated, the objective of the calculation is to find the maximum tractive performance, expressed by the maximum drawbar pull:

$$DP = H - R_t, \quad (4.1)$$

where H is the thrust and R_t is the total external resistance. To let the Lunar Zebro move, the thrust must exceed the total external resistance, requiring a positive drawbar pull. A large drawbar pull on a horizontal surface is desirable, as it indicates sufficient thrust to accommodate additional resistance, such as overcoming a slope or an obstacle on the lunar surface.

4.2. Static leg-soil interaction

4.2.1. Static equilibrium equation

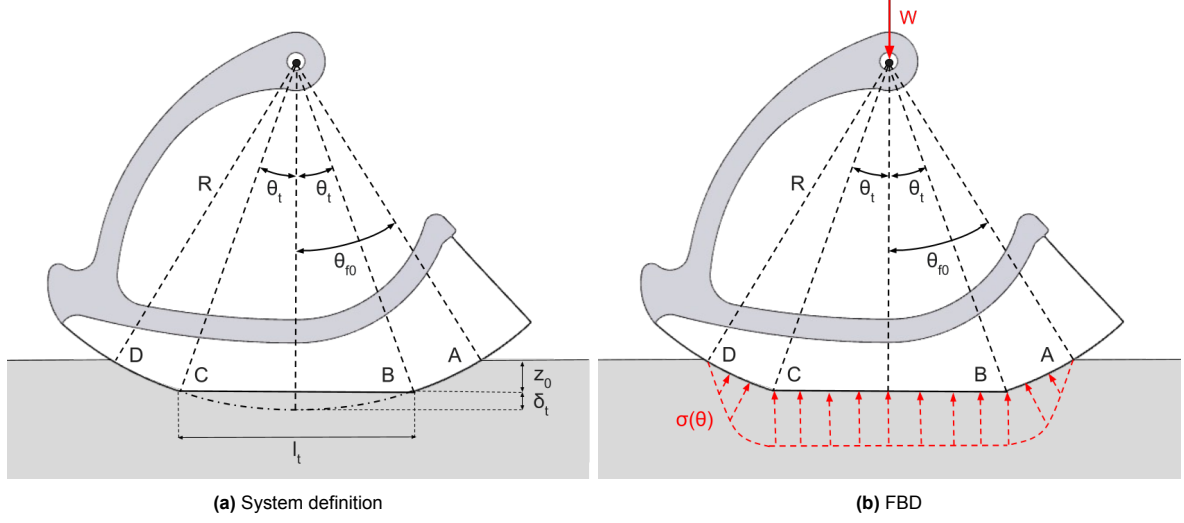


Figure 4.2: Static equilibrium

In the static state, there is a vertical force equilibrium, which balances the gravitational force on a single leg W with a summation of the ground reaction forces F_{y0} of the flattened section BC (F_y) and the non-deformed sections AB and CD ($2F_s$):

$$F_{y0} = F_y + 2F_s. \quad (4.2)$$

The length of the flattened section l_t is defined as:

$$l_t = 2\sqrt{\delta_t(2R - \delta_t)}, \quad (4.3)$$

where δ_t is the vertical deflection and R is the leg radius. The average ground pressure P_w at the flattened section can be obtained using:

$$P_w = \frac{F_y}{wl_t}, \quad (4.4)$$

where w is the leg width. The static sinkage of the leg is expressed as:

$$z_0 = \begin{cases} \left(\frac{P_w}{\frac{k_c}{l_t} + k_\phi} \right)^{\frac{1}{n}} & \text{if } l_t < w, \\ \left(\frac{P_w}{\frac{k_c}{w} + k_\phi} \right)^{\frac{1}{n}} & \text{if } l_t \geq w, \end{cases} \quad (4.5)$$

where k_c is the cohesive soil deformation modulus, k_ϕ is the frictional soil deformation modulus, and n is the exponent of soil deformation.

The normal stress along the non-deformed sections AB and CD can be expressed using the equation:

$$\sigma(\theta) = \left(\frac{k_c}{w} + k_\phi \right) R^n (\cos \theta - \cos \theta_{f0})^n \quad \text{if } \theta_t \leq \theta \leq \theta_{f0}, \quad (4.6)$$

where the initial soil entry angle θ_{f0} and soil flattening angle θ_t can be calculated using the relations:

$$\theta_{f0} = \arccos \left(1 - \frac{z_0 + \delta_t}{R} \right), \quad (4.7)$$

$$\theta_t = \arcsin \left(\frac{l_t}{2R} \right). \quad (4.8)$$

By integrating the vertical component of the normal stress over the arced contact area, the ground reaction force of the non-deformed sections can be obtained:

$$F_s = R w \int_{\theta_t}^{\theta_{f0}} \sigma(\theta) \cos \theta d\theta. \quad (4.9)$$

4.2.2. Static model solving procedure

The vertical deflection δ_t of the leg is calculated in an iteration process. The initial value for δ_t is the vertical deflection obtained when no vertical force is yet acting on the leg. As leg deflection depends on both the vertical and longitudinal forces acting on the flexure, the initial value of δ_t in the static state is the calculated vertical deflection caused by only a longitudinal force acting on the leg. This longitudinal force should estimate the drawbar pull. This might sound counterintuitive, but if the longitudinal force is not taken into account in the static state, the assumption of the flattened section size staying the same in the quasi-static state would be incorrect. The calculation procedure is detailed in Section 5.2.3.

Starting the iteration process, the vertical deflection value δ_t is substituted in the force-displacement relationship of the leg design, described in Chapter 5, to calculate F_y , and in Eq. 4.3 to calculate l_t . These values can subsequently be substituted in Eq. 4.4 and Eq. 4.5 to obtain the average ground pressure P_w and the static sinkage z_0 . Further obtaining the soil angles θ_{f0} and θ_t , the vertical ground reaction force F_s of the non-deformed sections can be identified. Using Eq. 4.2, the total ground reaction force F_{y0} can be calculated. If F_{y0} equals the vertical load W , the correct value of δ_t is determined. If not, alternative values of δ_t are explored until the correct value is obtained. This process is accelerated by making δ_t dependent on the size of the error between F_{y0} and W . A flow chart of the static model solving procedure is presented in Figure B.1.

4.3. Quasi-static leg-soil interaction

4.3.1. Soil angles

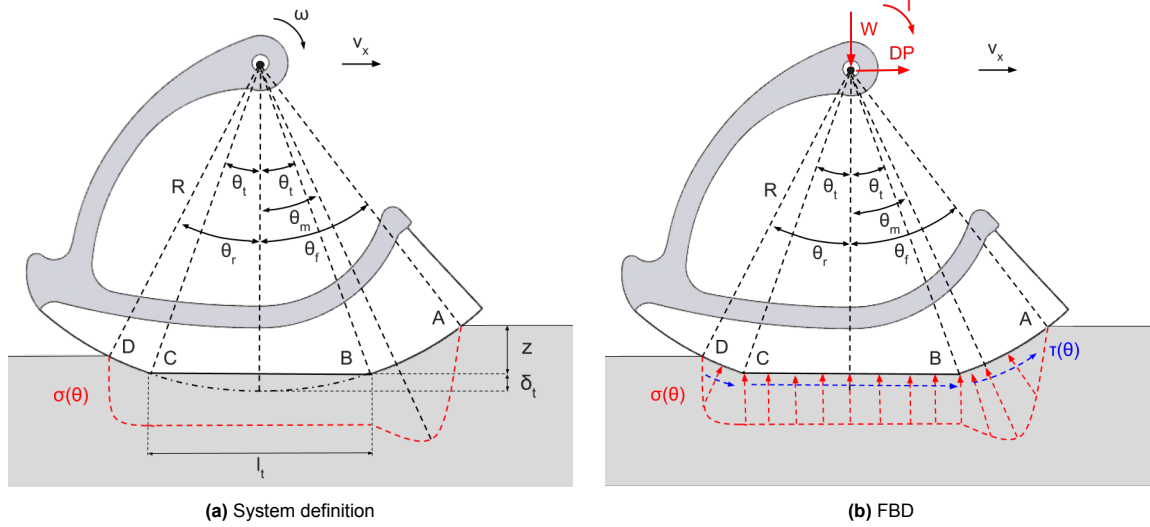


Figure 4.3: Quasi-static equilibrium

When the Lunar Zebro walks, the leg can be described as being in quasi-static interaction with the soil. In the quasi-static interaction, the soil entry angle θ_f and soil exit angle θ_r change due to the movement of regolith. The entry angle θ_f increases due to regolith gathering in front of the leg. The soil entry angle θ_f and soil exit angle θ_r can be defined with the relations:

$$\theta_f = \arccos \left(1 - \frac{z + \delta_t}{R} \right), \quad (4.10)$$

$$\theta_r = \arccos \left(1 - \frac{\lambda(z + \delta_t)}{R} \right), \quad (4.11)$$

where z is the leg sinkage and λ is the terrain reboundness due to soil elasticity. As the length of the flattened section in the quasi-static state is assumed to stay the same as in the static state, the soil flattening angle θ_t also stays the same and can be determined using Eq. 4.8. The angle of the maximum normal stress θ_m can be determined using [20]:

$$\theta_m = (c_1 + c_2 s) \theta_f, \quad (4.12)$$

where c_1 and c_2 are wheel-soil interaction coefficients, typically assumed to be $c_1 \approx 0.4$ and $0 \leq c_2 \leq 0.3$ [11]. In this study, c_2 is assumed to be equal to 0.15. The slip ratio s while walking ($|v_x| \leq |v_t|$) can be determined using:

$$\begin{aligned} s &= 1 - \frac{v_x}{v_t}, \\ &= 1 - \frac{v_x}{R\omega}, \end{aligned} \quad (4.13)$$

where v_x , v_t and ω are respectively the forward, theoretical and angular velocity of the leg.

4.3.2. Normal stress distribution

The normal stress distribution in the quasi-static state differs between contact sections. The normal stress distribution can be obtained using:

$$\sigma(\theta) = \begin{cases} \sigma_f = (k_c/w + k_\phi) R^n (\cos \theta - \cos \theta_f)^n, \\ \sigma_t = \begin{cases} (k_c/l_t + k_\phi) z^n & \text{if } l_t < w, \\ (k_c/w + k_\phi) z^n & \text{if } l_t \geq w, \end{cases} \\ \sigma_r = (k_c/w + k_\phi) R^n (\cos(\theta_f - \frac{\theta - \theta_r}{\theta_m - \theta_r}(\theta_f - \theta_m)) - \cos \theta_f)^n. \end{cases} \quad (4.14)$$

The applicable normal stress equation for the different contact sections is obtained using Table 4.1 and is dependent on the angle of the maximum normal stress θ_m .

Table 4.1: Applicable normal stress at each contact section [11]

$\sigma(\theta)$	If $\theta_m > \theta_t$	If $\theta_m \leq \theta_t$
σ_f	$\theta_m \leq \theta \leq \theta_f$	$\theta_t \leq \theta \leq \theta_f$
σ_t	$-\theta_t \leq \theta < \theta_t$	$-\theta_t \leq \theta < \theta_t$
σ_r	$\theta_t \leq \theta < \theta_m$ $\theta_r \leq \theta < -\theta_t$	$\theta_r \leq \theta < -\theta_t$

4.3.3. Shear stress distribution

In the quasi-static state, the influence of the shear stress is taken into account. The shear stress $\tau(\theta)$ can be determined using the equation of Janosi and Hanamoto [25]:

$$\tau(\theta) = (c + \sigma(\theta) \tan \phi) \left(1 - e^{-\frac{j(\theta)}{\kappa}} \right), \quad (4.15)$$

where c is the soil cohesion, ϕ is the internal friction angle, κ is the shear deformation modulus, and j is the longitudinal shear displacement. The longitudinal shear displacement j for the non-deformed contact sections in the case of positive slip ratios ($s \geq 0$) is:

$$j(\theta) = R(\theta_f - \theta - (1 - s)(\sin \theta_f - \sin \theta)) \quad \text{if } |\theta| \geq |\theta_t|. \quad (4.16)$$

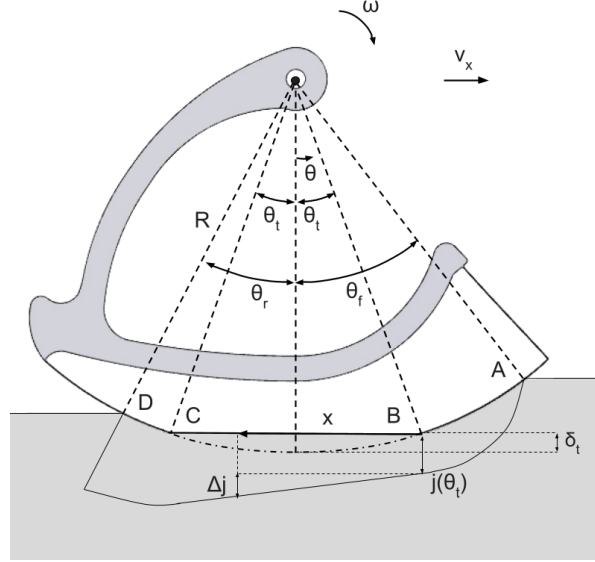


Figure 4.4: Longitudinal shear displacement beneath the deforming leg

In the case of the flattened section BC, the slip velocity is considered constant, which means that this section has a similar behaviour under a rigid track. Because of this, the shear displacement j along BC increases proportionally to both the slip ratio s and the distance x from point B [21]:

$$\Delta j = sx. \quad (4.17)$$

The longitudinal shear displacement j for the flattened section in the case of a positive slip ratio ($s \geq 0$) can then be calculated using:

$$\begin{aligned} j(\theta) &= j(\theta_t) + \Delta j, \\ &= j(\theta_t) + sx, \\ &= j(\theta_t) + s(R \sin \theta_t - (R - \delta_t) \tan \theta) \quad \text{if } |\theta| < |\theta_t|. \end{aligned} \quad (4.18)$$

4.3.4. Leg forces

The total vertical soil reaction force is defined as the summation of the vertical soil reaction forces of the different contact patches. This is done by integrating over the vertical effects of the normal stress and shear stress distributions of the entry and exit regions. However, if the flattening angle is larger than the exit angle, the influence of the exit region is ignored. The vertical reaction force of the flattened section is only dependent on the normal stress distributions, as the shear stress is perpendicular to the vertical direction. The vertical reaction force at this section is constant and calculated by multiplying the normal stress by the contact patch area. The total vertical ground reaction force is:

$$\begin{aligned} F &= F_{AB} + F_{BC} + F_{CD}, \\ &= Rw \int_{\theta_t}^{\theta_f} (\sigma(\theta) \cos \theta + \tau(\theta) \sin \theta) d\theta + l_t w \sigma_t + Rw \int_{\theta_r}^{-\theta_t} (\sigma(\theta) \cos \theta + \tau(\theta) \sin \theta) d\theta. \end{aligned} \quad (4.19)$$

The thrust H of the leg is calculated by a summation of the positive longitudinal soil reaction forces of the different contact patches. The entire shear stress below the flattened section contributes to the drawbar pull, showing the positive impact a compliant leg has on tractive performance compared to a rigid leg, for which the shear stress is tangential to the circular shape of the contact surface. It is also evident that the normal stress at the exit section contributes to the thrust. However, it is negatively defined in the equation because the exit-section angles are also negatively defined. This results in the following equation:

$$\begin{aligned} H &= H_{AB} + H_{BC} + H_{CD}, \\ &= Rw \int_{\theta_t}^{\theta_f} \tau(\theta) \cos \theta d\theta + (R - \delta_t)w \int_{-\theta_t}^{\theta_t} \frac{\tau(\theta)}{\cos^2 \theta} d\theta + Rw \int_{\theta_r}^{-\theta_t} (\tau(\theta) \cos \theta - \sigma(\theta) \sin \theta) d\theta. \end{aligned} \quad (4.20)$$

The external resistance force R_t acting on the leg is calculated by a summation of the longitudinal resistance force acting on the entry contact patch due to soil compaction and the leg deformation resistance R_d . The bulldozing resistance is neglected, as the expected leg sinkage is less than a third of the wheel radius, which is the threshold at which it begins to significantly increase according to Petritsenko and Sell [26]. The resistance force R_t is given by the equation:

$$\begin{aligned} R_t &= R_{AB} + R_d, \\ &= R w \int_{\theta_t}^{\theta_f} \sigma(\theta) \sin \theta d\theta + R_d. \end{aligned} \quad (4.21)$$

Due to the externally induced elastic deformation in the leg, energy is dissipated in internal losses, causing additional resistance. This resistance depends on the design, construction, material and operating conditions of a wheel or C-shaped leg and is often obtained experimentally. Using a proposed equation by Bekker and Semonin, an estimation of the deformation resistance can be made [24]:

$$R_d = \frac{3.581 w (2R)^2 P_w \epsilon (0.0349 \theta_t - \sin 2\theta_t)}{\theta_t (2R - 2\delta_t)}, \quad (4.22a)$$

$$\epsilon = 1 - \exp\left(\frac{-k_e \delta_t}{h}\right), \quad (4.22b)$$

where h is the deformable section height and k_e is a parameter related to the wheel/leg construction. As denoted by Bekker, the value of k_e is assumed to be 7, and the soil flattening angle θ_t in Eq. 4.22a is expressed in degrees [24].

4.3.5. Quasi-static equilibrium equations

The vertical equilibrium of the deformable leg can be described by equating the gravitational force W acting on the leg and the vertical ground reaction force F :

$$\begin{aligned} W &= F, \\ &= R w \int_{\theta_t}^{\theta_f} (\sigma(\theta) \cos \theta + \tau(\theta) \sin \theta) d\theta + l_t w \sigma_t + R w \int_{\theta_r}^{-\theta_t} (\sigma(\theta) \cos \theta + \tau(\theta) \sin \theta) d\theta. \end{aligned} \quad (4.23)$$

With the longitudinal equilibrium, the performance metric of the leg can be calculated, the drawbar pull. As mentioned in Eq. 4.1, it can be obtained by subtracting the total external resistance R_t from the thrust H :

$$\begin{aligned} DP &= H - R_t, \\ &= R w \int_{\theta_t}^{\theta_f} (\tau(\theta) \cos \theta - \sigma(\theta) \sin \theta) d\theta + (R - \delta_t) w \int_{-\theta_t}^{\theta_t} \frac{\tau(\theta)}{\cos^2 \theta} d\theta \\ &\quad + R w \int_{\theta_r}^{-\theta_t} (\tau(\theta) \cos \theta - \sigma(\theta) \sin \theta) d\theta - R_d. \end{aligned} \quad (4.24)$$

4.3.6. Tractive efficiency

The resistance torque T of the deformable leg is obtained by the summation of the shear stress acting around the leg:

$$\begin{aligned} T &= T_{AB} + T_{BC} + T_{CD}, \\ &= R^2 w \int_{\theta_t}^{\theta_f} \tau(\theta) d\theta + (R - \delta_t)^2 w \int_{-\theta_t}^{\theta_t} \frac{\tau(\theta) + \sigma_t \tan \theta}{\cos^2 \theta} d\theta + R^2 w \int_{\theta_r}^{-\theta_t} \tau(\theta) d\theta. \end{aligned} \quad (4.25)$$

The resistance torque opposes the rotary motion, equalling the input torque of the motor axis in the static state. The input torque must be greater than the resistance torque to obtain rotary motion. Using

the torque, the tractive efficiency η can be identified, which is used to describe the capability to transform the input torque to output power, being the net traction force or drawbar pull:

$$\eta = \frac{DP(1-s)R}{T}. \quad (4.26)$$

4.3.7. Quasi-static model solving procedure

The drawbar pull and tractive efficiency can be calculated in a numerical simulation. First, the gravitational force W acting on the leg and the slip ratio s must be entered. Second, the leg deflection δ_t and soil flattening angle θ_t must be obtained using the process described in Section 4.2.2. The leg sinkage z in quasi-static state can be calculated using an iteration process focused on the vertical equilibrium of the total ground reaction force F and the gravitational force W acting on the leg. In this process, the vertical deflection δ_t is the initial input of the leg sinkage. Given the sinkage iteration value, the soil entry angle θ_f , soil exit angle θ_r and angle of maximum normal stress θ_m can be determined using Eq. 4.10, Eq. 4.11 and Eq. 4.12, respectively. Using these angles, the normal stress and shear stress can be calculated with Eq. 4.14 and Eq. 4.15. The total ground reaction force F can now be derived from Eq. 4.19. If the ground reaction force F is unequal to the gravitational force W acting on the leg, the next step in the iteration process is taken with an increased value of the leg sinkage, until the point where the ground reaction force F equals the gravitational force W acting on the leg. When this point is obtained, the values of the leg sinkage, soil angles, shear stress and normal stress can be used in further calculations.

Using respectively Eq. 4.20 and Eq. 4.21, the thrust H and total external resistance R_t can be calculated. Whereas the drawbar pull DP can be obtained with Eq. 4.24. Finally, the resistance torque T can be derived with Eq. 4.25 and the tractive efficiency η with Eq. 4.26. A flow chart of the quasi-static model solving procedure is presented in Figure B.2.

5

Compliance theory

This chapter describes the compliance theory used in the optimisation model. First, the compliance model with its assumptions is argued. Subsequently, the used theorem is explained.

5.1. Compliance model assumptions

5.1.1. Load application assumption

To calculate the tractive performance of the innovative leg module in the optimisation process, an analytical calculation of the force-deflection relationship of the leg module is essential. Within the terramechanics model, this force-deflection relationship is utilised to calculate the force required for a certain iterated vertical deflection value. It is expected that the true behaviour of the leg can be most accurately characterised by a non-linear contact load on granular soil. However, modelling the deformation of the leg upon non-linear contact on granular soil is difficult. As the load on the leg increases, the contact patch of the flexure with the soil increases, resulting in variations in both contact pressure and deflection shape. Deformation modelling is further complicated by the dynamics of the Lunar Zebro leg traversing over lunar regolith, as the granular soil particles constantly rearrange, thereby altering the normal and shear stress distributions at various deformation locations. A possible assumption could be the analytical description of non-linear deflection due to a contact pressure load at the flattened section of the leg. However, this method is expected to be challenging to model and computationally demanding. Instead, the load application is modelled as a single point, which can be combined by linear and non-linear descriptions of the flexure behaviour.

The assumption of the forces being applied at a single point serves as a simplification of reality and is most reasonable for small displacements. However, if high loads are applied and the deflection is large, the accuracy of the results might be compromised. The assumption is believed to be justified by the comparative nature of the design variables in finding a combination that yields optimal drawbar pull. The assumption also ensures compatibility with the compliance theorem. The force-deflection relationship of the flexure with a singular load application point is characterised as statically indeterminate.

The definition of the load application is visualised in Figure 5.1a. Force F_x represents the longitudinal force applied to the leg, which is equal to the drawbar pull accommodated by the available force arising from the interaction of the leg and the lunar soil. Force F_y represents the vertical ground reaction force that leads to flexure deflection, as previously mentioned in Section 4.2.1. This force is accommodated by the gravitational force of the Lunar Zebro mass acting on a single leg. Due to the tripod walking motion, the gravitational force W acting on the leg is defined as:

$$W = \frac{mg}{N}, \quad (5.1)$$

where m is the Lunar Zebro mass, g is the gravitational acceleration, and N is the leg load factor:

$$N = \begin{cases} 2 & \text{if middle leg,} \\ 4 & \text{if outer leg.} \end{cases} \quad (5.2)$$

The leg flexure is divided into two distinct cantilever flexures in Figure 5.1b: a straight flexure and a curved flexure. These distinct flexures are used in the calculation procedure. The intermediate forces acting on the ends of these flexures are the radial force $F_{B,r}$, the tangential force $F_{B,\theta}$ and the moment about the z-axis $M_{B,z}$. The goal of this calculation procedure is to obtain the deflection and angular displacement at point C, in the direction of the radial force $F_{C,r}$, tangential force $F_{C,\theta}$, and moment $M_{C,z}$.

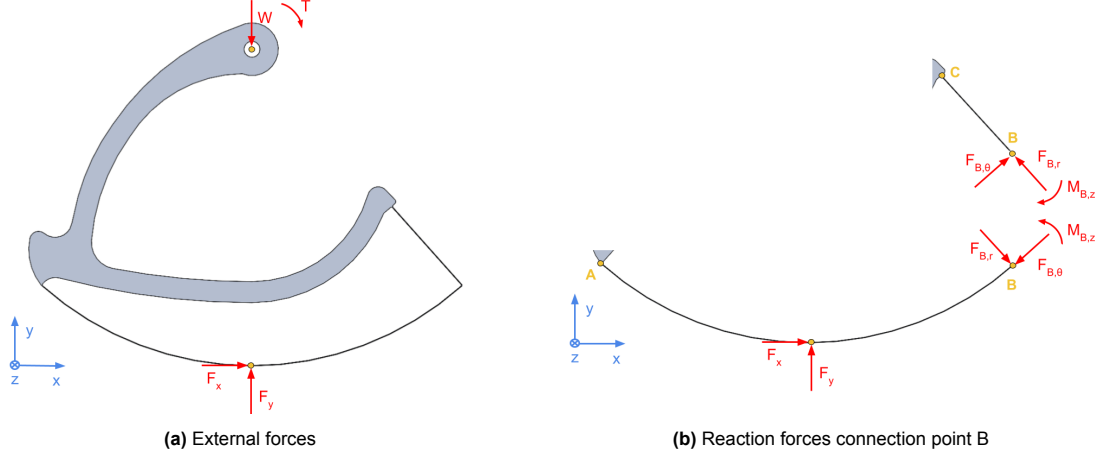


Figure 5.1: FBD leg design

5.1.2. Compliance theorem choice

The singular load application point can be combined with both a linear and a non-linear description of the flexure behaviour. Although non-linear methods offer a better description of large displacements, they are inherently more complex. The non-linear Pseudo-Rigid Body Modelling (PRBM) method can be applied to a leg flexure. Galloway [27] presents such an application in which a compliant C-shape leg is modelled as an initially curved cantilever beam. However, the flexure of the concept design in this study is characterised by a double connection to the frame and a combination of applied forces at the ground contact point, making the flexure statically indeterminate and preventing it from being modelled as one of the use-cases described in [28]. Instead, the 3R-model for a combined force and moment end load, wherein a flexure is divided into three distinct flexures with relative motion, is considered a more appropriate option. The 3R-model was originally developed by Su [29] and subsequently refined by Chen et al. [30] to enhance the accuracy of deflection modelling for a straight flexure, with the trade-off of increased complexity [28]. Venkiteswaran's research [31] further advanced this 3R-model to describe initially curved cantilever beams with a uniform cross-section. To determine the force-deflection relationship using Venkiteswaran's 3R-model, a non-linear optimisation routine is employed to minimise the residual energy, defined as the difference between the energy input and the strain energy within the system.

The implementation of a non-linear optimisation routine to obtain the system's force-deflection relationship requires conducting an optimisation within the existing optimisation process aimed at identifying the optimal drawbar pull, consequently demanding significant computing power. Considering this and the complexity of the 3R-model, a decision was made to use the linear Castigliano's theorem instead of the 3R-model. Castigliano's theorem offers computational efficiency for simpler geometries compared to numerical methods, as it is anticipated that the strain energy can easily be expressed in terms of external forces. Furthermore, the extent to which a non-linear method might more accurately describe the compliant leg's true behaviour is highly uncertain, as its primary benefit may lie in enhancing the accuracy of the deflection size based on the assumptions made. When assuming a singular load application point, the ability of either a linear or non-linear method to accurately estimate the non-linear contact load on granular soil remains unknown.

Using Castigliano's theorem implies an assumption of linear deformations, which limits the accuracy of the assumption-based force-deflection relationship as deformations increase. The choice to utilise a linear method is deemed reasonable given the goal to compare the tractive performance of different design variables, the described complexity of using non-linear analytical methods, and the

acknowledged uncertainty of estimating the true compliant behaviour. A linear approximation provides valuable insight into the influence of different design variables. To verify that the compliance model behaves as expected, a Finite Element Analysis (FEA) is performed in Appendix E.

5.2. Castigliano's theorem

Castigliano's theorem is an energy-based deflection analysis method to calculate linear elastic compliance. It is used to determine the force-deflection relationship of a linear-elastic beam, using the partial derivatives of a point in the beam with respect to the external forces on that point [32]. The deflection of a loading point δ_i can be obtained by the derivative of the total strain energy U with respect to an arbitrary force F_i :

$$\delta_i = \frac{\partial U}{\partial F_i}. \quad (5.3)$$

The angular displacement of a loading point ϕ_i can be obtained by the derivative of the total strain energy U with respect to an arbitrary moment M_i :

$$\phi_i = \frac{\partial U}{\partial M_i}. \quad (5.4)$$

5.2.1. Straight flexure deflection

Force and moment equilibrium

Considering the goal of this calculation procedure to obtain the deflection and angular displacement at point C, in the direction of the radial force $F_{C,r}$, tangential force $F_{C,\theta}$, and moment $M_{C,z}$, the Free Body Diagram (FBD) of a straight flexure part is presented in Figure 6.1, where r is the radial coordinate.

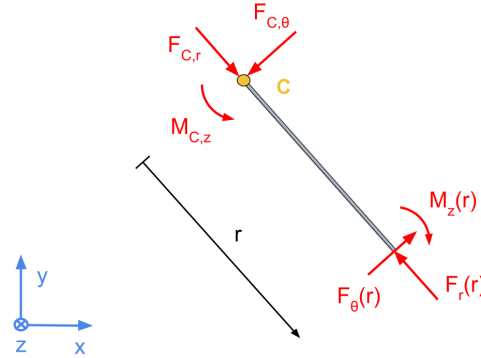


Figure 5.2: FBD straight flexure part

The force equilibria at the cross-section in the straight flexure are given as:

$$F_r(r) = F_{C,r}, \quad (5.5a)$$

$$F_\theta(r) = F_{C,\theta}. \quad (5.5b)$$

The moment equilibrium at the cross-section in the straight flexure is given as:

$$M_z(r) = F_{C,\theta}r + M_{C,z}. \quad (5.6)$$

Strain energy

The strain energy for axial, bending, and shear loading is obtained by the respective equations:

$$U_{axial} = \int \frac{N^2 dr}{2EA}, \quad (5.7a)$$

$$U_{bending} = \int \frac{M^2 dr}{2EI}, \quad (5.7b)$$

$$U_{shear} = \int \frac{\mu V^2 dr}{2GA}, \quad (5.7c)$$

where N is an axial force, M is a bending moment, V is a shear force, E is the Young's modulus, G is the shear modulus, and μ is the shear constant. The shear load influence can be neglected at the following length-thickness threshold,

$$\frac{L}{t_s} > 10. \quad (5.8)$$

As the length-thickness ratio is expected to be much higher than ten, the influence of the shear load $F_\theta(r)$ is neglected. Subsequently, the total strain energy in the straight flexure is:

$$U_s = \int_0^L \frac{F_r(r)^2 dr}{2EA_s} + \int_0^L \frac{M_z(r)^2 dr}{2EI_{s,z}}, \quad (5.9)$$

where A_s is the cross-sectional area and $I_{s,z}$ the moment of inertia about the z -axis of the straight flexure, which are respectively expressed by the following equations:

$$A_s = wt_s, \quad (5.10a)$$

$$I_{s,z} = \frac{wt_s^3}{12}. \quad (5.10b)$$

Deflection

Given Eq. 5.3, the deflection δ_i of the straight flexure in the direction of the force F_i for the axial, bending and shear load can be obtained using the respective equations:

$$\delta_{axial,i} = \frac{1}{EA} \int N \frac{\partial N}{\partial F_i} dr, \quad (5.11a)$$

$$\delta_{bending,i} = \frac{1}{EI} \int M \frac{\partial M}{\partial F_i} dr, \quad (5.11b)$$

$$\delta_{shear,i} = \frac{1}{GA} \int \mu V \frac{\partial V}{\partial F_i} dr. \quad (5.11c)$$

The deflection $\delta_{C,r}$ of the straight flexure in the r -direction at point C, resulting from the axial load $F_r(r)$ is obtained by the equation:

$$\begin{aligned} \delta_{C,r} &= \frac{1}{EA_s} \int_0^L F_r(r) \frac{\partial F_r(r)}{\partial F_{C,r}} dr, \\ &= \frac{F_{C,r}L}{EA_s}. \end{aligned} \quad (5.12)$$

The deflection $\delta_{C,\theta}$ of the straight flexure in the θ -direction at point C, resulting from the bending moment $M_z(r)$, is obtained by the equation:

$$\begin{aligned} \delta_{C,\theta} &= \frac{1}{EI_{s,z}} \int_0^L M_z(r) \frac{\partial M_z(r)}{\partial F_{C,\theta}} dr, \\ &= \frac{M_{C,z}L^2}{2EI_{s,z}} + \frac{F_{C,\theta}L^3}{3EI_{s,z}}. \end{aligned} \quad (5.13)$$

Angular displacement

Given Eq. 5.4, the angular displacement ϕ_i of the straight flexure in the direction of the moment M_i for the bending load is obtained using the equation:

$$\phi_{bending,i} = \frac{1}{EI} \int M \frac{\partial M}{\partial M_i} dr. \quad (5.14)$$

The angular displacement $\phi_{C,z}$ of the straight flexure about the z -axis at point C, resulting from the bending moment $M_z(r)$, is obtained by the equation:

$$\begin{aligned} \phi_{C,z} &= \frac{1}{EI_{s,z}} \int_0^L M_z(r) \frac{\partial M_z(r)}{\partial M_{C,z}} dr, \\ &= \frac{M_{C,z}L}{EI_{s,z}} + \frac{F_{C,z}L^2}{2EI_{s,z}}. \end{aligned} \quad (5.15)$$

5.2.2. Curved flexure deflection

In Figures 5.3 and 5.4, the FBDs of the straight and curved flexure are respectively presented, where θ is the leg angle, α is the load application angle, and β is the leg flexure angle. The load application angle α is dependent on the leg orientation. Note that in compliance theory, the leg angle θ is defined from the straight flexure onward (see Figure 5.4), whereas in terramechanics theory, the leg angle θ is defined from the centre of the flattened section.

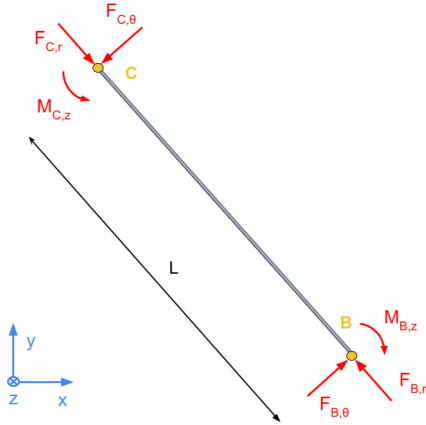


Figure 5.3: FBD full straight flexure

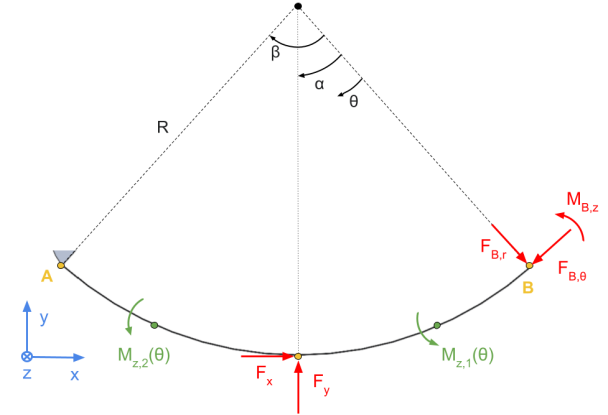


Figure 5.4: FBD Curved flexure

Force and moment equilibrium

As the goal is to obtain the total displacement at point C, the reaction forces and moment at point B can be expressed by those at point C, using the straight flexure equilibrium equations. Note that the direction of the forces and moments at point C is equal to that of point B on the curved flexure. The force equilibria in the full straight flexure are given as:

$$F_{B,r} = F_{C,r}, \quad (5.16a)$$

$$F_{B,\theta} = F_{C,\theta}. \quad (5.16b)$$

The moment equilibrium in the full straight flexure is given as:

$$M_{B,z} = F_{C,\theta}L + M_{C,z}. \quad (5.17)$$

The internal moments in the curved flexure before the external forces are applied $M_{z,1}(\theta)$, and after the external forces are applied $M_{z,2}(\theta)$, are obtained by the equation:

$$M_{z,1}(\theta) = F_{B,\theta}R(1 - \cos(\theta)) + F_{B,r}R\sin(\theta) - M_{B,z} \quad \text{if } 0 \leq \theta < \alpha, \quad (5.18a)$$

$$M_{z,2}(\theta) = M_{z,1}(\theta) - F_xR(1 - \cos(\theta - \alpha)) - F_yR\sin(\theta - \alpha) \quad \text{if } \alpha \leq \theta \leq \beta. \quad (5.18b)$$

Strain energy

The strain energy of a curved beam can be expressed by the equation [32]:

$$U_c = \int \frac{M^2 R d\theta}{2AeE} + \int \frac{F_\theta^2 R d\theta}{2AE} + \int \frac{CF_R^2 R d\theta}{2AG} - \int \frac{MF_\theta d\theta}{AE}, \quad (5.19)$$

where M is the total bending moment, F_θ is the tangential force, F_R is the radial force, e is the eccentricity, and C is a correction factor. Angle $d\theta$ is defined as:

$$d\theta = \frac{dl}{R}, \quad (5.20)$$

where l is the arc length. When the radius R of the curved beam is more than ten times greater than the thickness t_c of the curved flexure,

$$\frac{R}{t_c} > 10, \quad (5.21)$$

the strain energy in a curved beam of Eq. 5.19 can be approximated by:

$$U_c \simeq \int \frac{M^2 R d\theta}{2EI}. \quad (5.22)$$

This results in the strain energy of the curved flexure:

$$U_c \simeq \int_0^\alpha \frac{M_{z,1}^2(\theta) R d\theta}{2EI_{c,z}} + \int_\alpha^\beta \frac{M_{z,2}^2(\theta) R d\theta}{2EI_{c,z}}, \quad (5.23)$$

where $I_{c,z}$ is the moment of inertia about the z -axis of the curved flexure, given by:

$$I_{c,z} = \frac{wt_c^3}{12}. \quad (5.24)$$

Deflection

Given Eq. 5.3, the deflection δ_i of the curved flexure in the direction of the force F_i for the bending load can be obtained using the equation:

$$\delta_{bending,i} = \frac{1}{EI} \int M \frac{\partial M}{\partial F_i} R d\theta. \quad (5.25)$$

The deflection $\delta_{B,r}$ of the curved flexure in the r -direction at point B, resulting from the bending moment $M_z(\theta)$, is obtained by the equation:

$$\delta_{B,r} = \frac{1}{EI_{c,z}} \left(\int_0^\alpha M_{z,1}(\theta) \frac{\partial M_{z,1}(\theta)}{\partial F_{C,r}} R d\theta + \int_\alpha^\beta M_{z,2}(\theta) \frac{\partial M_{z,2}(\theta)}{\partial F_{C,r}} R d\theta \right). \quad (5.26)$$

The deflection $\delta_{B,\theta}$ of the curved flexure in the θ -direction at point B, resulting from the bending moment $M_z(\theta)$, is obtained by the equation:

$$\delta_{B,\theta} = \frac{1}{EI_{c,z}} \left(\int_0^\alpha M_{z,1}(\theta) \frac{\partial M_{z,1}(\theta)}{\partial F_{C,\theta}} R d\theta + \int_\alpha^\beta M_{z,2}(\theta) \frac{\partial M_{z,2}(\theta)}{\partial F_{C,\theta}} R d\theta \right). \quad (5.27)$$

Angular displacement

Given Eq. 5.4, the angular displacement ϕ_i of the curved flexure in the direction of the moment M_i for the bending load can be obtained using the equation:

$$\phi_{bending,i} = \frac{1}{EI} \int M \frac{\partial M}{\partial M_i} R d\theta. \quad (5.28)$$

The angular displacement $\phi_{B,z}$ of the curved flexure about the z -axis at point B, resulting from the bending moment $M_z(\theta)$, is obtained by the equation:

$$\phi_{B,z} = \frac{1}{EI_{c,z}} \left(\int_0^\alpha M_{z,1}(\theta) \frac{\partial M_{z,1}(\theta)}{\partial M_{C,z}} R d\theta + \int_\alpha^\beta M_{z,2}(\theta) \frac{\partial M_{z,2}(\theta)}{\partial M_{C,z}} R d\theta \right). \quad (5.29)$$

5.2.3. Compliance model solving procedure

The leg flexure, consisting of the straight and curved flexure, is fixed at point C. The boundary conditions are defined as the summation of the total deflection and the angular displacement in every direction at point C being equal to zero:

$$\delta_{B,r} + \delta_{C,r} = 0, \quad (5.30a)$$

$$\delta_{B,\theta} + \delta_{C,\theta} = 0, \quad (5.30b)$$

$$\phi_{B,z} + \phi_{C,z} = 0. \quad (5.30c)$$

As mentioned in Section 4.2.2, the iteration value of the vertical deflection δ_t is implemented in the compliance calculation to return the force F_y required for this deflection. The vertical deflection of the loading point δ_y can be calculated using the equation:

$$\delta_y = \frac{1}{EI_{c,z}} \left(\int_0^\alpha M_{z,1}(\theta) \frac{\partial M_{z,1}(\theta)}{\partial F_y} R d\theta + \int_\alpha^\beta M_{z,2}(\theta) \frac{\partial M_{z,2}(\theta)}{\partial F_y} R d\theta \right). \quad (5.31)$$

Given that the vertical deflections δ_t and δ_y must be equal, the boundary condition is the following:

$$\delta_t - \delta_y = 0. \quad (5.32)$$

Using these boundary conditions, four equations can be identified with five unknown variables, the vertical deflection δ_t , the vertical ground reaction force of the flattened section F_y , and the intermediate forces and moment acting at point C: $F_{C,r}$, $F_{C,\theta}$, and $M_{C,z}$. The vertical deflection δ_t is iterated in the process described in Section 4.2.2. Initially, the longitudinal force F_x is also unknown, as it should define the drawbar pull. However, an initial estimated value is used for both the middle and outer legs. These values are altered by a manual iteration, in which the values are changed based on the outcome of the calculation, until the estimated values are close to the final optimised drawbar pull.

Solving the four boundary equations gives the value of F_y . This process is performed for every iteration value δ_t until a static vertical force equilibrium is obtained in the terramechanics calculation, and the final value for δ_t is identified. The initial value of δ_t in the iteration process is determined when the vertical force F_y is equal to zero, and only the longitudinal force F_x influences the deflection of the flexure. This initial deflection must be used to ensure that the terramechanics calculation is not compromised.

6

Constraints theory

This chapter describes the theory of the different constraints applied in the optimisation model. First, the material stress while walking is obtained, after which this theory is expanded by introducing a lateral force for skid steering and climbing along a sideways gradient. This is followed by descriptions of the motor torque transmission, end of contact surface radius for the next step, and climbing height constraints, respectively.

6.1. Stress limit while walking

The Lunar Zebro shall be able to walk without failing, meaning that the maximum stress obtained in the flexure cannot exceed the yield strength. The stress in the flexure is calculated, with the stress tensor considering general plane stress defined as

$$\boldsymbol{\sigma} = \begin{bmatrix} \sigma_r & \tau_{r\theta} \\ \tau_{\theta r} & \sigma_\theta \end{bmatrix}.$$

6.1.1. Straight flexure stress

The maximum stress in the straight flexure is obtained at the fixed end, at point C. The normal stress $\sigma_{s,r}$ in the r -direction is subject to the influence of the axial load $F_{B,r}$, and bending moment $M_{C,z}$:

$$\sigma_{s,r1} = \frac{F_{B,r}}{wt_s}, \quad (6.1a)$$

$$\sigma_{s,r2} = \frac{M_{C,z}c_z}{I_{s,z}} = \frac{(M_{B,z} - F_{B,\theta}L)c_z}{I_{s,z}}, \quad (6.1b)$$

leading to the equation:

$$\sigma_{s,r} = \frac{F_{B,r}}{wt_s} + \frac{(M_{B,z} - F_{B,\theta}L)c_z}{I_{s,z}}. \quad (6.2)$$

The shear stresses $\tau_{s,r\theta}$ and $\tau_{s,\theta r}$ are subject to bending stress due to shear force $F_{B,\theta}$:

$$\tau_{s,r\theta} = \tau_{s,\theta r} = \frac{3F_{B,\theta}}{2wt_s}. \quad (6.3)$$

Given that aluminium is a ductile material, the von Mises stress criterion can be used to predict yielding [33]. The general plane von Mises stress $\sigma_{s,vm}$ in the straight flexure is given by:

$$\sigma_{s,vm} = \sqrt{\sigma_{s,r}^2 + 3\tau_{s,r\theta}^2}. \quad (6.4)$$

The stress in the straight flexure while walking $\sigma_{s,walk}$ is obtained using this equation.

6.1.2. Curved flexure stress

The maximum stress in the curved flexure is obtained at the fixed end, at point A. The normal stress $\sigma_{c,\theta}$ in the θ -direction is subject to the influence of the axial load $F_{B,\theta}$, and bending moment $M_{z,2}(\beta)$:

$$\sigma_{c,\theta 1} = \frac{F_{B,\theta}}{wt_c}, \quad (6.5a)$$

$$\sigma_{c,\theta 2} = \frac{M_{z,2}(\beta)(R^* - R)}{wt_c R(\bar{R} - R^*)}, \quad (6.5b)$$

where the distance between the centre of curvature and the neutral axis R^* , and the distance between the centre of curvature and the centroid of the cross-section \bar{R} are given as, respectively:

$$R^* = \frac{t_c}{\ln \frac{R}{R-t_c}}, \quad (6.6a)$$

$$\bar{R} = \frac{R + (R - t_c)}{2}. \quad (6.6b)$$

This leads to the total normal stress equation:

$$\sigma_{c,\theta} = \frac{F_{B,\theta}}{wt_c} + \frac{M_{z,2}(\beta)(R^* - R)}{wt_c R(\bar{R} - R^*)}. \quad (6.7)$$

The shear stresses $\tau_{c,r\theta}$ and $\tau_{c,\theta r}$ are subject to bending stress due to shear force $F_{B,r}$:

$$\tau_{c,r\theta} = \tau_{c,\theta r} = \frac{3F_{B,r}}{2wt_c}. \quad (6.8)$$

The general plane von Mises stress $\sigma_{c,vm}$ in the curved flexure is given by:

$$\sigma_{c,vm} = \sqrt{\sigma_{c,\theta}^2 + 3\tau_{c,r\theta}^2}. \quad (6.9)$$

The stress in the curved flexure while walking $\sigma_{c,walk}$ is obtained using this equation.

6.1.3. Maximum stress application angle

The deformation of the leg flexure is constrained by the maximum stress. In terramechanics and compliance theory, it is assumed that the leg orientation is upright, with the load application point located at the centre of the flexure (Figure 5.1a). However, it is expected that the stress is greater in alternative leg orientations. Given that the load application point, at which the maximum stress is obtained, is dependent on the applied load and the design variables t_c , t_s and L , there exists no fixed point from which the maximum stress can be computed. The maximum stress in either the straight or curved flexure is also obtained at different load application points. Consequently, the intermediate forces and moment acting at point C: $F_{C,r}$, $F_{C,\theta}$, and $M_{C,z}$, are calculated for each load application angle α and utilised to obtain the respective stress. The maximum stress $\sigma_{max,walk}$ obtained at one of these load application angles of either the straight flexure $\sigma_{s,walk}$ or curved flexure $\sigma_{c,walk}$ is used to form the constraint.

As the deformable leg has a limited contact patch with the soil and varying stiffness at different load application points, it is expected that the maximum drawbar pull is not obtained at points outside the centre of the flexure. Nonetheless, it is assumed that the maximum drawbar pull is exerted at all these load application points, given the complexity and the computing power required to calculate the drawbar pull at each leg orientation. For similar reasons, it is also assumed that the ground reaction force applied at the load application point is equal to the entire gravitational force acting on the leg. This assumption contrasts with the terramechanics theorem, which asserts that the ground reaction forces are divided into three sections, with only the flattened section force contributing to the deformation of the leg. As the flattened section force is unattainable at each leg orientation, the entire gravitational force on the leg represents the most viable alternative assumption.

The assumptions of the maximum drawbar pull and the entire gravitational force on the leg acting as the ground reaction force on the load application point form a more stringent constraint, ensuring that the found optimum satisfies the constraints in reality. Consequently, the ground loading point forces

necessary to calculate the intermediate forces in the calculation procedure of Section 5.2 while walking are:

$$F_x = DP, \quad (6.10a)$$

$$F_y = W. \quad (6.10b)$$

Given that the vertical force F_y is known, only the boundary conditions of Eq. 5.30 are used to calculate the intermediate forces and moment required for the stress equations.

6.2. Stress limit with lateral force

In the event of the Lunar Zebro skid steering or climbing along a sideways gradient, a lateral force F_z acts on the leg. The intermediate force and moment equilibria change, consequently altering the stress levels in the flexure, which must be analysed in 3D. The lateral force F_z applied while skid steering is derived in Section 6.3 and while climbing along a sideways gradient in Section 6.4. The load application points are assumed to be in the centre of the flexure width. The goal of this calculation procedure is to obtain the deformation and angular displacement at point C, to derive the intermediate forces and moments in the system that are required to calculate the stress in the flexure.

In this calculation, the warping effects of the flexure are neglected. Although warping is expected to increase both deflection and stress levels, its impact is beyond the scope of this study and is assumed to be covered by the safety factor. To verify that the compliance model behaves as expected, a Finite Element Analysis (FEA) is performed in Appendix E.

6.2.1. Straight flexure deflection

Force and moment equilibrium

The FBD of a straight flexure part is presented in Figure 6.1. Due to the lateral resistance force F_z , the reaction force in the lateral direction $F_z(r)$ and the moments about the radial and tangential direction, $M_r(r)$ and $M_\theta(r)$, are introduced.

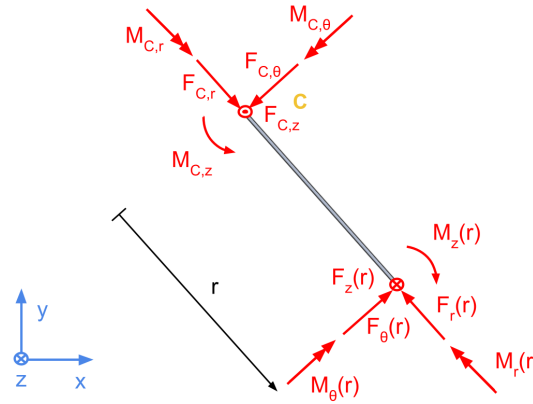


Figure 6.1: FBD straight flexure part

The force equilibria in the straight flexure are given as:

$$F_r(r) = F_{C,r}, \quad (6.11a)$$

$$F_\theta(r) = F_{C,\theta}, \quad (6.11b)$$

$$F_z(r) = F_{C,z}. \quad (6.11c)$$

The moment equilibria in the straight flexure are given as:

$$M_r(r) = M_{C,r}, \quad (6.12a)$$

$$M_\theta(r) = F_{C,z}r + M_{C,\theta}, \quad (6.12b)$$

$$M_z(r) = F_{C,\theta}r + M_{C,z}. \quad (6.12c)$$

Strain energy

In addition to the equations of the straight flexure strain energy for axial, bending, and shear loading of Eq. 5.7, the strain energy for torsion loading is obtained by:

$$U_{torsion} = \int \frac{T^2 dr}{2GJ}, \quad (6.13)$$

where T is a torsion moment. The total strain energy in the straight flexure is then obtained by:

$$U_s = \int_0^L \frac{F_r(r)^2 dr}{2EA_s} + \int_0^L \frac{M_z(r)^2 dr}{2EI_{s,z}} + \int_0^L \frac{M_\theta(r)^2 dr}{2EI_{s,\theta}} + \int_0^L \frac{M_r(r)^2 dr}{2GJ_s} + \int_0^L \frac{\mu F_z(r)^2 dr}{2GA_s}, \quad (6.14)$$

where the moment of inertia $I_{s,\theta}$ about the θ -axis and the polar moment of inertia J_s of the straight flexure are given by the respective equations:

$$I_{s,\theta} = \frac{t_s w^3}{12}, \quad (6.15a)$$

$$J_s = \frac{wt_s(w^2 + t_s^2)}{12}. \quad (6.15b)$$

In contrast to the influence of shear load $F_\theta(r)$, the influence of shear load $F_z(r)$ is not neglected because the length-width ratio is expected to be smaller than 10. The length-width threshold at which the shear load influence can be neglected is

$$\frac{L}{w} > 10. \quad (6.16)$$

The shear constant μ for a rectangular cross-section is equal to 1.2.

Deflection

Given Eq. 5.3, the deflection δ_i of the straight flexure in the direction of the force F_i for the torsion load can be found using the equation:

$$\delta_{torsion,i} = \frac{1}{GJ_s} \int T \frac{\partial T}{\partial F_i} dr. \quad (6.17)$$

The load application point C is considered to be in the centre of the flexure width, meaning that the torsion load does not influence the deflection of the straight flexure at point C. The deflection $\delta_{C,z}$ of the straight flexure in the z -direction at point C, resulting from the bending moment $M_\theta(r)$ and the shear force $F_z(r)$ is obtained by the equation:

$$\begin{aligned} \delta_{C,z} &= \frac{1}{EI_{s,\theta}} \int_0^L M_\theta(r) \frac{\partial M_\theta(r)}{\partial F_{C,z}} dr + \frac{1}{GA_s} \int_0^L \mu F_z(r) \frac{\partial F_z(r)}{\partial F_{C,z}} dr, \\ &= \frac{M_{C,\theta} L^2}{2EI_{s,\theta}} + \frac{F_{C,z} L^3}{3EI_{s,\theta}} + \frac{\mu F_{C,z} L}{GA_s}. \end{aligned} \quad (6.18)$$

Angular displacement

Given Eq. 5.4, the angular displacement ϕ_i of the straight flexure in the direction of the moment M_i for the torsion load can be found using the equation:

$$\phi_{torsion,i} = \frac{1}{GJ_s} \int T \frac{\partial T}{\partial M_i} dr. \quad (6.19)$$

The angular displacement $\phi_{C,\theta}$ of the straight flexure about the θ -axis at point C, resulting from the bending moment $M_\theta(r)$ is obtained by the equation:

$$\begin{aligned} \phi_{C,\theta} &= \frac{1}{EI_{s,\theta}} \int_0^L M_\theta(r) \frac{\partial M_\theta(r)}{\partial M_{C,\theta}} dr, \\ &= \frac{M_{C,\theta} L}{EI_{s,\theta}} + \frac{F_{C,z} L^2}{2EI_{s,\theta}}. \end{aligned} \quad (6.20)$$

The angular displacement $\phi_{C,r}$ of the straight flexure about the r -axis at point C, resulting from the bending moment $M_r(r)$ is obtained by the equation:

$$\begin{aligned}\phi_{C,r} &= \frac{1}{GJ_s} \int_0^L M_r(r) \frac{\partial M_r(r)}{\partial M_{C,r}} dr, \\ &= \frac{M_{C,r}L}{GJ_s}.\end{aligned}\quad (6.21)$$

6.2.2. Curved flexure deflection

Force and moment equilibrium

The FBDs of the straight and curved flexure are presented in Figures 6.2 and 6.3, respectively.

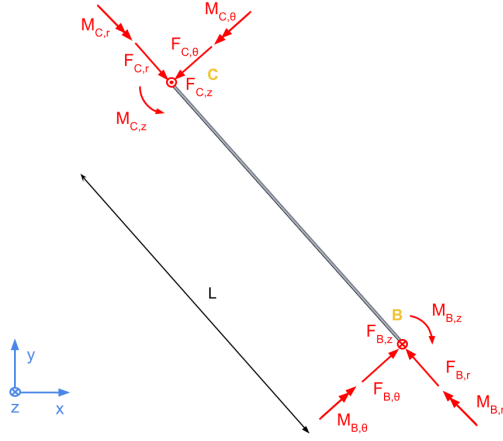


Figure 6.2: FBD Full straight flexure

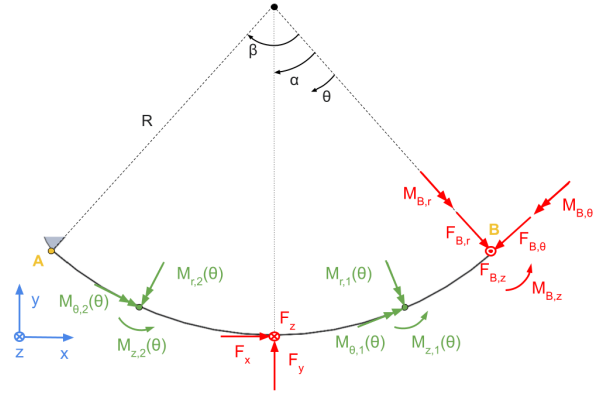


Figure 6.3: FBD Curved flexure

As the goal is to obtain the total displacement at point C, the reaction forces and moment at point B can be expressed by those at point C using the straight flexure equilibrium equations. The force equilibria in the straight flexure are given as:

$$F_{B,r} = F_{C,r}, \quad (6.22a)$$

$$F_{B,\theta} = F_{C,\theta}, \quad (6.22b)$$

$$F_{B,z} = F_{C,z}. \quad (6.22c)$$

The moment equilibria in the straight flexure are given as:

$$M_{B,r} = M_{C,r}, \quad (6.23a)$$

$$M_{B,\theta} = F_{C,z}L + M_{C,\theta}, \quad (6.23b)$$

$$M_{B,z} = F_{C,\theta}L + M_{C,z}. \quad (6.23c)$$

The internal moment in the curved flexure before the external forces are applied $M_{r,1}(\theta)$, $M_{\theta,1}(\theta)$ and $M_{z,1}(\theta)$, and after the external forces are applied $M_{r,2}(\theta)$, $M_{\theta,2}(\theta)$ and $M_{z,2}(\theta)$ around the respective r , θ and z -axes, are given by the equations:

$$M_{r,1}(\theta) = -F_{B,z}R \sin(\theta) + M_{B,r} \cos(\theta) + M_{B,\theta} \sin(\theta) \quad \text{if } 0 \leq \theta < \alpha, \quad (6.24a)$$

$$M_{r,2}(\theta) = M_{r,1}(\theta) + F_z R \sin(\theta - \alpha) \quad \text{if } \alpha \leq \theta \leq \beta, \quad (6.24b)$$

$$M_{\theta,1}(\theta) = -F_{B,z}R(1 - \cos(\theta)) + M_{B,r} \sin(\theta) - M_{B,\theta} \cos(\theta) \quad \text{if } 0 \leq \theta < \alpha, \quad (6.25a)$$

$$M_{\theta,2}(\theta) = M_{\theta,1}(\theta) + F_z R(1 - \cos(\theta - \alpha)) \quad \text{if } \alpha \leq \theta \leq \beta, \quad (6.25b)$$

$$M_{z,1}(\theta) = F_{B,\theta}R(1 - \cos(\theta)) + F_{B,r}R\sin(\theta) - M_{B,z} \quad \text{if } 0 \leq \theta < \alpha, \quad (6.26a)$$

$$M_{z,2}(\theta) = M_{z,1}(\theta) - F_xR(1 - \cos(\theta - \alpha)) - F_yR\sin(\theta - \alpha) \quad \text{if } \alpha \leq \theta \leq \beta. \quad (6.26b)$$

Strain energy

In addition to the equations of the curved flexure strain energy for bending Eq. 5.22, the strain energy for torsion loading is given by:

$$U_{torsion} = \int \frac{T^2 R d\theta}{2GJ}. \quad (6.27)$$

The total strain energy in the curved flexure then becomes:

$$\begin{aligned} U_c = & \int_0^\alpha \frac{M_{r,1}(\theta)^2 R d\theta}{2EI_{c,r}} + \int_\alpha^\beta \frac{M_{r,2}(\theta)^2 R d\theta}{2EI_{c,r}} + \int_0^\alpha \frac{M_{\theta,1}(\theta)^2 R d\theta}{2GJ_c} \\ & + \int_\alpha^\beta \frac{M_{\theta,2}(\theta)^2 R d\theta}{2GJ_c} + \int_0^\alpha \frac{M_{z,1}(\theta)^2 R d\theta}{2EI_{c,z}} + \int_\alpha^\beta \frac{M_{z,2}(\theta)^2 R d\theta}{2EI_{c,z}}, \end{aligned} \quad (6.28)$$

where the moment of inertia $I_{c,r}$ about the r -axis and the polar moment of inertia J_c of the curved flexure are given by the respective equations:

$$I_{c,r} = \frac{t_c w^3}{12}, \quad (6.29a)$$

$$J_c = \frac{wt_c(w^2 + t_c^2)}{12}. \quad (6.29b)$$

Deflection

Given Eq. 5.3, the deflection δ_i of the curved flexure in the direction of the force F_i for the torsion load can be found using the equation:

$$\delta_{torsion,i} = \frac{1}{GJ} \int T \frac{\partial T}{\partial F_i} R d\theta. \quad (6.30)$$

The deflection $\delta_{B,z}$ of the curved flexure in the z -direction at point B, resulting from the bending moment $M_r(\theta)$ and torsion moment $M_\theta(\theta)$ is obtained by the equation:

$$\begin{aligned} \delta_{B,z} = & \frac{1}{EI_{c,r}} \left(\int_0^\alpha M_{r,1}(\theta) \frac{\partial M_{r,1}(\theta)}{\partial F_{C,z}} R d\theta + \int_\alpha^\beta M_{r,2}(\theta) \frac{\partial M_{r,2}(\theta)}{\partial F_{C,z}} R d\theta \right) \\ & + \frac{1}{GJ_c} \left(\int_0^\alpha M_{\theta,1}(\theta) \frac{\partial M_{\theta,1}(\theta)}{\partial F_{C,z}} R d\theta + \int_\alpha^\beta M_{\theta,2}(\theta) \frac{\partial M_{\theta,2}(\theta)}{\partial F_{C,z}} R d\theta \right). \end{aligned} \quad (6.31)$$

Angular displacement

Given Eq. 5.4, the angular displacement ϕ_i of the curved flexure in the direction of the moment M_i for the torsion load can be found using the equation:

$$\phi_{torsion,i} = \frac{1}{GJ} \int T \frac{\partial T}{\partial M_i} R d\theta. \quad (6.32)$$

The angular displacement $\phi_{B,r}$ of the curved flexure about the r -axis at point B, resulting from the bending moment $M_r(\theta)$ and torsion moment $M_\theta(\theta)$ is obtained by the equation:

$$\begin{aligned} \phi_{B,r} = & \frac{1}{EI_{c,r}} \left(\int_0^\alpha M_{r,1}(\theta) \frac{\partial M_{r,1}(\theta)}{\partial M_{C,r}} R d\theta + \int_\alpha^\beta M_{r,2}(\theta) \frac{\partial M_{r,2}(\theta)}{\partial M_{C,r}} R d\theta \right) \\ & + \frac{1}{GJ_c} \left(\int_0^\alpha M_{\theta,1}(\theta) \frac{\partial M_{\theta,1}(\theta)}{\partial M_{C,r}} R d\theta + \int_\alpha^\beta M_{\theta,2}(\theta) \frac{\partial M_{\theta,2}(\theta)}{\partial M_{C,r}} R d\theta \right). \end{aligned} \quad (6.33)$$

The angular displacement $\phi_{B,\theta}$ of the curved flexure about the θ -axis at point B, resulting from the bending moment $M_r(\theta)$ and torsion moment $M_\theta(\theta)$ is obtained by the equation:

$$\begin{aligned} \phi_{B,\theta} = & \frac{1}{EI_{C,r}} \left(\int_0^\alpha M_{r,1}(\theta) \frac{\partial M_{r,1}(\theta)}{\partial M_{C,\theta}} R d\theta + \int_\alpha^\beta M_{r,2}(\theta) \frac{\partial M_{r,2}(\theta)}{\partial M_{C,\theta}} R d\theta \right) \\ & + \frac{1}{GJ_c} \left(\int_0^\alpha M_{\theta,1}(\theta) \frac{\partial M_{\theta,1}(\theta)}{\partial M_{C,\theta}} R d\theta + \int_\alpha^\beta M_{\theta,2}(\theta) \frac{\partial M_{\theta,2}(\theta)}{\partial M_{C,\theta}} R d\theta \right). \end{aligned} \quad (6.34)$$

6.2.3. Loading point deflection

The leg flexure, consisting of the straight and curved flexure, is fixed at point C. The boundary conditions are defined as the summation of the total deflection and the angular displacement in every direction at point C being equal to zero:

$$\delta_{B,r} + \delta_{C,r} = 0, \quad (6.35a)$$

$$\delta_{B,\theta} + \delta_{C,\theta} = 0, \quad (6.35b)$$

$$\delta_{B,z} + \delta_{C,z} = 0, \quad (6.35c)$$

$$\phi_{B,r} + \phi_{C,r} = 0, \quad (6.35d)$$

$$\phi_{B,\theta} + \phi_{C,\theta} = 0, \quad (6.35e)$$

$$\phi_{B,z} + \phi_{C,z} = 0. \quad (6.35f)$$

Using these boundary conditions, six equations can be identified with six unknown variables, being the intermediate forces and moments acting at point C: $F_{C,r}$, $F_{C,\theta}$, $F_{C,z}$, $M_{C,r}$, $M_{C,\theta}$ and $M_{C,z}$. Solving these equations gives the values of the intermediate forces and moments acting at point C, which are used to calculate the displacements at the load application point and the stress in the flexure.

The lateral deflection δ_z in the direction of the load application force F_z can be found using the equation:

$$\begin{aligned} \delta_z = & \frac{1}{EI_{C,r}} \left(\int_0^\alpha M_{r,1}(\theta) \frac{\partial M_{r,1}(\theta)}{\partial F_z} R d\theta + \int_\alpha^\beta M_{r,2}(\theta) \frac{\partial M_{r,2}(\theta)}{\partial F_z} R d\theta \right) \\ & + \frac{1}{GJ_c} \left(\int_0^\alpha M_{\theta,1}(\theta) \frac{\partial M_{\theta,1}(\theta)}{\partial F_z} R d\theta + \int_\alpha^\beta M_{\theta,2}(\theta) \frac{\partial M_{\theta,2}(\theta)}{\partial F_z} R d\theta \right). \end{aligned} \quad (6.36)$$

6.2.4. Straight flexure stress

The stress tensor is defined as

$$\boldsymbol{\sigma} = \begin{bmatrix} \sigma_r & \tau_{r\theta} & \tau_{rz} \\ \tau_{\theta r} & \sigma_\theta & \tau_{\theta z} \\ \tau_{zr} & \tau_{z\theta} & \sigma_z \end{bmatrix}.$$

The maximum stress in the straight flexure is obtained at the fixed end, at point C. The normal stress $\sigma_{s,r}$ in the r -direction is subject to the influence of the axial load $F_{B,r}$, and the bending moments $M_{C,\theta}$ and $M_{C,z}$:

$$\sigma_{s,r1} = \frac{F_{B,r}}{wt_s}, \quad (6.37a)$$

$$\sigma_{s,r2} = \frac{M_{C,z}c_z}{I_{s,z}} = \frac{(M_{B,z} - F_{B,\theta}L)c_z}{I_{s,z}}, \quad (6.37b)$$

$$\sigma_{s,r3} = \frac{M_{C,\theta}c_\theta}{I_{s,\theta}} = \frac{(M_{B,\theta} - F_{B,z}L)c_\theta}{I_{s,\theta}}, \quad (6.37c)$$

leading to the equation:

$$\sigma_{s,r} = \frac{F_{B,r}}{wt_s} + \frac{(M_{B,z} - F_{B,\theta}L)c_z}{I_{s,z}} + \frac{(M_{B,\theta} - F_{B,z}L)c_\theta}{I_{s,\theta}}, \quad (6.38)$$

where c_z and c_θ are the distances from the respective neutral axes z and θ . The shear stresses $\tau_{s,r\theta}$ and $\tau_{s,\theta r}$ are subject to bending stress due to shear force $F_{B,\theta}$:

$$\tau_{s,r\theta} = \tau_{s,\theta r} = \frac{3F_{B,\theta}}{2wt_s}, \quad (6.39)$$

whereas $\tau_{s,rz}$ and $\tau_{s,zr}$ are subject to bending stress due to shear force $F_{B,z}$:

$$\tau_{s,rz} = \tau_{s,zr} = \frac{3F_{B,z}}{2Lt_s}. \quad (6.40)$$

The shear stresses $\tau_{s,\theta z}$ and $\tau_{s,z\theta}$ are subject to torsion stress due to torsion moment $M_{C,r}$:

$$\tau_{s,\theta z} = \tau_{s,z\theta} = \frac{3M_{C,r}}{wt_s^2} = \frac{3M_{B,r}}{wt_s^2}. \quad (6.41)$$

The von Mises stress $\sigma_{s,vm}$ in the straight flexure is given by:

$$\sigma_{s,vm} = \sqrt{\sigma_{s,r}^2 + 3(\tau_{s,r\theta}^2 + \tau_{s,\theta z}^2 + \tau_{s,zr}^2)}. \quad (6.42)$$

The stress in the straight flexure while skid steering $\sigma_{s,skid}$ and climbing along a sideways gradient $\sigma_{s,side}$ are obtained using this equation.

6.2.5. Curved flexure stress

The maximum stress in the curved flexure is obtained at the fixed end, at point A. The normal stress $\sigma_{c,\theta}$ in the θ -direction is subject to the influence of the axial load $F_{B,\theta}$, and bending moments $M_{r,2}(\beta)$ and $M_{z,2}(\beta)$:

$$\sigma_{c,\theta 1} = \frac{F_{B,\theta}}{wt_c}, \quad (6.43a)$$

$$\sigma_{c,\theta 2} = \frac{M_{z,2}(\beta)(R^* - R)}{wt_c R(\bar{R} - R^*)}, \quad (6.43b)$$

$$\sigma_{c,\theta 3} = \frac{M_{r,2}(\beta)c_r}{I_{c,r}}, \quad (6.43c)$$

where c_r is the distance from the respective neutral axis r . Using β , the bending moments of the entire curved flexure are calculated at point A. The total normal stress is then given as the equation:

$$\sigma_{c,r} = \frac{F_{B,\theta}}{wt_c} + \frac{M_{z,2}(\beta)(R^* - R)}{wt_c R(\bar{R} - R^*)} + \frac{M_{r,2}(\beta)c_r}{I_{c,r}}. \quad (6.44)$$

The shear stresses $\tau_{c,r\theta}$ and $\tau_{c,\theta r}$ are subject to bending stress due to shear force $F_{B,r}$:

$$\tau_{c,r\theta} = \tau_{c,\theta r} = \frac{3F_{B,r}}{2wt_c}, \quad (6.45)$$

whereas $\tau_{c,\theta z}$ and $\tau_{c,z\theta}$ are subject to bending stress due to shear force $F_{B,z}$:

$$\tau_{c,\theta z} = \tau_{c,z\theta} = \frac{3F_{B,z}}{2\beta Rt_c}. \quad (6.46)$$

The shear stresses $\tau_{c,rz}$ and $\tau_{c,zr}$ are subject to torsion stress due to torsion moment $M_{\theta,2}(\beta)$:

$$\tau_{c,rz} = \tau_{c,zr} = \frac{3M_{\theta,2}(\beta)}{wt_c^2}. \quad (6.47)$$

The von Mises stress $\sigma_{c,vm}$ in the curved flexure is given by:

$$\sigma_{c,vm} = \sqrt{\sigma_{c,\theta}^2 + 3(\tau_{c,r\theta}^2 + \tau_{c,\theta z}^2 + \tau_{c,zr}^2)}. \quad (6.48)$$

The stress in the curved flexure while skid steering $\sigma_{c,skid}$ and climbing along a sideways gradient $\sigma_{c,side}$ are obtained using this equation.

6.2.6. Maximum stress application angle

In addition to the variables mentioned in Section 6.1.3, the lateral force influences the load application point from which the maximum stress is calculated. To find the maximum stress obtained when a lateral force is applied, the intermediate forces and moments acting at point C: $F_{C,r}$, $F_{C,\theta}$, $F_{C,z}$, $M_{C,r}$, $M_{C,\theta}$, and $M_{C,z}$, are computed for every load application angle α and used to calculate the respective stress. The maximum stress value obtained at one of the load application angles is used to form the constraint. The same assumptions are made as in Section 6.1.3, using the maximum drawbar pull and entire gravitational force on the leg as ground reaction force at the load application point, to form a more stringent constraint, ensuring that the found optimum satisfies the constraints in reality.

6.3. Skid steering

The Lunar Zebro shall be able to skid steer at a single location. During skid steering, the legs on one side of the Lunar Zebro move forward, while the legs on the other side move backwards, resulting in a lateral force being exerted on the legs, which increases the stress in the ground contact flexures. For the concept leg design, the forward-moving legs endure the highest stress load, which therefore forms the constraint. The maximum stress during skid steering cannot exceed the yield strength. The lateral force is determined by evaluating the soil resistance.

6.3.1. Lateral resistance force

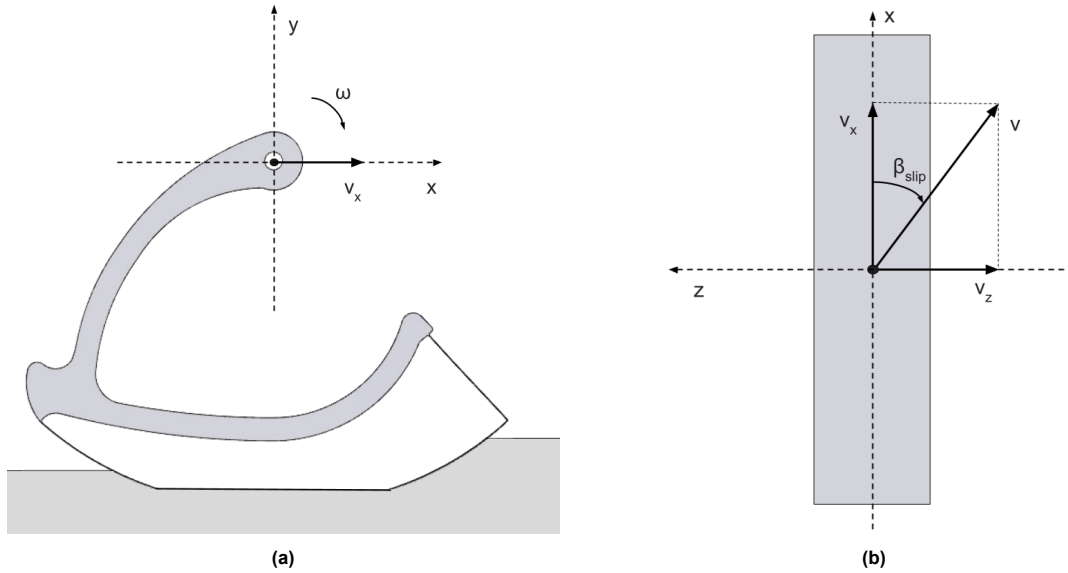


Figure 6.4: Leg velocity coordinate system

The lateral resistance force R_z acting on the leg consists of two types of resistance, the soil compaction resistance $R_{z,c}$ exerted by the shear stress that develops at the ground contact between the leg and the lunar soil, and the bulldozing resistance $R_{z,b}$ exerted by the sidewall of the leg bulldozing in the lunar soil [34]. As the created leg design makes ground contact via a flexure, the size of the sidewall is minimal. Consequently, the bulldozing resistance is neglected, and the lateral resistance force is computed based solely on the soil compaction resistance:

$$R_z = R_{z,c}. \quad (6.49)$$

The shear stress in the lateral direction is derived using the equation [25]:

$$\tau_z(\theta) = (c + \sigma(\theta) \tan \phi) \left(1 - e^{-\frac{j_z(\theta)}{\kappa_z}} \right), \quad (6.50)$$

where κ_z is the lateral shear deformation modulus, and j_z is the lateral shear displacement:

$$j_z(\theta) = r(1 - s)(\theta_f - \theta) \tan \beta_{slip}. \quad (6.51)$$

The slip angle β_{slip} is defined by the equation:

$$\beta_{slip} = \tan^{-1} \left(\frac{v_z}{v_x} \right), \quad (6.52)$$

where v_x is the forward velocity and v_z the lateral velocity. When skid steering perfectly, the leg only has a lateral velocity v_z , whereas the forward velocity v_x is equal to zero. In this case, the slip angle equals 90° . Using Eq. 4.13, the slip ratio when v_x is zero becomes equal to one. Implementing this value in Eq. 6.51 results in a total lateral shear stress of zero.

In a more realistic scenario, there is still a small forward velocity, resulting in a slip angle that approaches but does not reach 90° , and a slip ratio that approaches but does not reach one. Consequently, the tangent of β_{slip} becomes an exceptionally high number, which implies that the lateral shear stress of Eq. 6.50 can be simplified to represent the maximum obtainable lateral shear stress:

$$\tau_{z,max}(\theta) = c + \sigma(\theta) \tan \phi. \quad (6.53)$$

This maximum lateral shear stress is used to find the maximum lateral resistance, which is the value at which the maximum stress in the leg flexure is obtained, forming the constraint. The total lateral resistance R_z of the deformable leg during skid steering can be calculated using:

$$\begin{aligned} R_z &= R_{z,AB} + R_{z,BC} + R_{z,CD}, \\ &= R_w \int_{\theta_t}^{\theta_f} \tau_z(\theta) d\theta + (R - \delta_t)w \int_{-\theta_t}^{\theta_t} \frac{\tau_z(\theta)}{\cos^2 \theta} d\theta + R_w \int_{\theta_r}^{-\theta_t} \tau_z(\theta) d\theta. \end{aligned} \quad (6.54)$$

The maximum total lateral resistance force $R_{z,max}$ is obtained using $\tau_{z,max}$ in Eq. 6.54.

6.3.2. Solving procedure

To calculate the stress during skid steering, the following ground loading point forces F_x , F_y , and F_z are used in the calculation procedure described in Section 6.2:

$$F_x = DP, \quad (6.55a)$$

$$F_y = W, \quad (6.55b)$$

$$F_z = R_{z,max}. \quad (6.55c)$$

The calculation will result in the maximum stress in the straight flexure $\sigma_{s,skid}$ and in the curved flexure $\sigma_{c,skid}$, from which the highest value forms the constraint $\sigma_{max,skid}$.

6.4. Sideways gradient

The Lunar Zebro shall be able to climb along a maximum sideways gradient of 15° . During this, the force equilibrium over the legs changes, with higher forces applied at the lower leg(s), consequently increasing the stress in the ground contact flexure. The maximum stress in the flexure while climbing along a sideways gradient cannot exceed the yield strength.

The distance between the centre of gravity and the legs varies between the middle and outer legs, as the middle leg is located farther outward. However, since the Lunar Zebro is still in its design phase, the exact location of the centre of gravity is yet unknown. As a result, it is assumed that these distances are equal, with their estimated value and that of the height of the centre of gravity detailed in Table C.1. It is also assumed that the Lunar Zebro uses small rotations to steer and does not perform full skid steering rotations while climbing along a sideways gradient.

6.4.1. Force and moment equilibrium

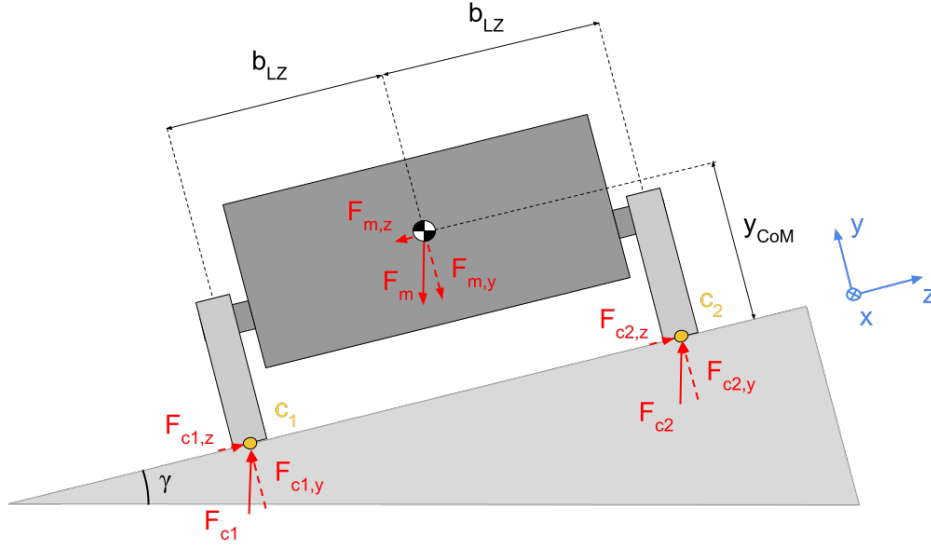


Figure 6.5: FBD Lunar Zebro on sideways gradient

The total gravitational force of the Lunar Zebro exerted on the centre of mass is given by:

$$F_m = mg. \quad (6.56)$$

Due to the sideways gradient γ , the gravitational force is divided into the normal and lateral direction of the body:

$$F_{m,z} = F_m \sin \gamma, \quad (6.57a)$$

$$F_{m,y} = F_m \cos \gamma. \quad (6.57b)$$

The highest load is applied at the lower leg(s), making forces $F_{c1,y}$ and $F_{c1,z}$ of interest. Using the moment around point c_2 at the higher leg(s), an equation for $F_{c1,y}$ is derived:

$$F_{c1,y} = \frac{F_{m,z} y_{com} + F_{m,y} b_{LZ}}{2b_{LZ}}, \quad (6.58)$$

where y_{com} is the height of the CoM and b_{LZ} is the lateral distance between the CoM and the load application points of the legs at ground contact. Lateral force $F_{c1,z}$ is then given as:

$$F_{c1,z} = F_{c1,y} \tan \gamma. \quad (6.59)$$

6.4.2. Solving procedure

Due to the load distribution on the legs while climbing along a sideways gradient, the flexure deformation and consequently the drawbar pull of the leg have changed. The drawbar pull of the critical leg DP_{c1} is calculated by defining the vertical force causing leg deformation as the normal force on the critical leg (Eq. 6.60b) in the terramechanics model of Chapter 4. As explained in Section 5.2.3, the longitudinal force F_x , defined as the drawbar pull, is initially unknown. However, an initial estimated value is implemented for both the middle and outer legs, which is altered by manual iteration until the estimated values are close to the final optimised drawbar pull.

To calculate the stress in the flexure while climbing along a sideways gradient, the following ground loading point forces F_x , F_y , and F_z are used in the theorem described in Section 6.2:

$$F_x = DP_{c1}, \quad (6.60a)$$

$$F_y = \frac{2F_{c1,y}}{N}, \quad (6.60b)$$

$$F_z = \frac{2F_{c1,z}}{N}, \quad (6.60c)$$

where N is the leg load factor, which is used to define the number of legs on the critical side: one middle or two outer legs. Using the defined ground loading point forces, the resulting intermediate flexure forces, deformations, and stress can be calculated by the procedure described in Section 6.2. The calculation will result in the maximum stress in the straight flexure $\sigma_{s,side}$ and in the curved flexure $\sigma_{c,side}$, from which the highest value forms the constraint $\sigma_{max,side}$.

6.5. Motor torque transmission

The Lunar Zebro shall transmit the motor torque to ground contact force. Therefore, the leg flexure shall have a certain stiffness in the longitudinal direction, which is represented in the longitudinal displacement of the force loading point being restricted from excessively deforming and, consequently, being constrained by a longitudinal displacement threshold. Using the compliance model described in Chapter 5, the intermediate forces and moment acting at point C: $F_{C,r}$, $F_{C,\theta}$, and $M_{C,z}$, can be calculated. Using these variables, the longitudinal deflection δ_x is obtained using the equation:

$$\delta_x = \frac{1}{EI_{c,z}} \left(\int_0^\alpha M_{z,1}(\theta) \frac{\partial M_{z,1}(\theta)}{\partial F_x} R d\theta + \int_\alpha^\beta M_{z,2}(\theta) \frac{\partial M_{z,2}(\theta)}{\partial F_x} R d\theta \right), \quad (6.61)$$

where F_x equals the drawbar pull DP . The longitudinal displacement is calculated at every leg orientation, and the maximum longitudinal displacement obtained is used to form the constraint.

6.6. End of contact surface radius for next step

The Lunar Zebro shall have a minimum radius at the end of the contact surface to ensure that the next leg can continue the walking motion. With the used gait by the Lunar Zebro, the first 10% of the second leg makes ground contact at the same time as the last 10% of the first leg. The effective remaining radius at the last 10% of the contact surface shall exceed the radius threshold.

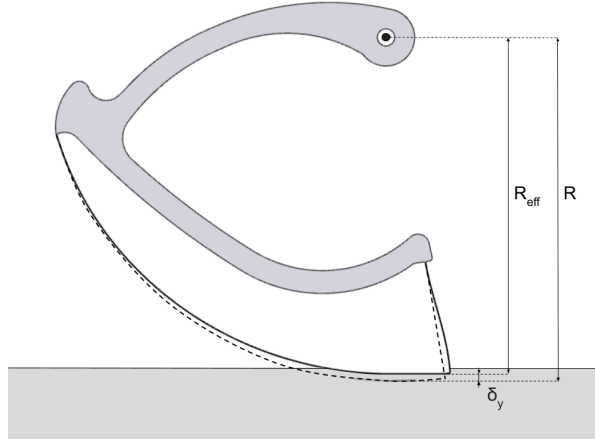


Figure 6.6: Effective radius definition

The angle of the load application point at the last 10% of the is calculated using:

$$\alpha_{end} = 0.10\beta. \quad (6.62)$$

Using α_{end} in the compliance calculation described in Chapter 5, the intermediate forces and moment acting at point C: $F_{C,r}$, $F_{C,\theta}$, and $M_{C,z}$ can be calculated when the leg stands on the last 10% of its contact surface. Using these values, the vertical deflection δ_y can be obtained using the equation:

$$\delta_y = \frac{1}{EI_{c,z}} \left(\int_0^{\alpha_{end}} M_{z,1}(\theta) \frac{\partial M_{z,1}(\theta)}{\partial F_y} R d\theta + \int_{\alpha_{end}}^\beta M_{z,2}(\theta) \frac{\partial M_{z,2}(\theta)}{\partial F_y} R d\theta \right). \quad (6.63)$$

Due to the limited contact surface between the leg and the soil when it sets itself up for the next step, it is assumed that the ground reaction force F_y is equal to the entire gravitational force W acting on the

leg at the load application point. As in all other constraints, the maximum drawbar pull DP is assumed to act as F_x at the load application point. In reality, this maximum drawbar pull is not reached due to the higher stiffness at the end of the contact surface and the limited contact surface between the leg and the soil. The remaining effective radius R_{eff} at the last 10% of the contact surface is then given as:

$$R_{eff} = R - \delta_y. \quad (6.64)$$

The impact of sinkage is excluded in this formulation, as it is anticipated that the leg will experience comparable sinkage at the initiation of the contact surface in the following steps, combined with the decreased radius the leg has at the initiation, due to the curled tip. To prevent unforeseen outcomes and address potential waddling motion, the minimum radius threshold $R_{eff,min}$, designated for the effective radius R_{eff} , is strictly defined.

6.7. Climbing height

The Lunar Zebro shall be able to climb over obstacles, and therefore its climbing height y_c shall exceed a climbing threshold. In this study, the climbing height of the Lunar Zebro is defined as the height at which the gripping point can make contact with an elevated object when the leg is maximally deformed. The climbing height y_c is obtained using the equation:

$$y_c = R + y_g - z - \delta_t, \quad (6.65)$$

where y_g is the vertical distance between the leg axle and the gripping point.

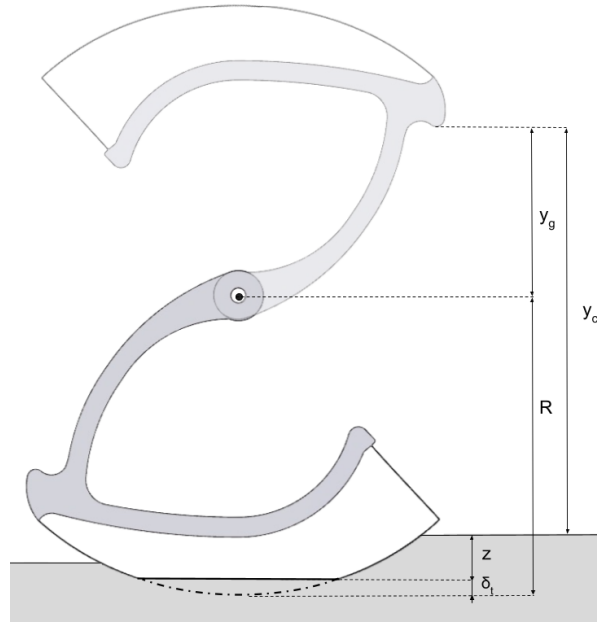


Figure 6.7: Climbing height definition

It is assumed that the available normal force at the contact point is sufficient to climb. However, the climbing performance is more unpredictable in practice, attributed to factors such as the difference in shape and texture of obstacles, the used gait, the leg orientation with respect to the obstacle, and the combination of tractive force and slippage of the legs [7]. As this research focuses on the comparison of design variables that make the leg deformable and increase tractive performance, combined with the fact that the climbing definition is the same for all variables, the climbing height measurement is assumed to be sufficient.

7

System Analysis

This chapter describes the results of the performed optimisation process for both the middle and outer leg. First, the optima are presented, after which the objective and constraint behaviour is analysed to understand the sharpness of the found optima in the design space. Lastly, a sensitivity analysis is performed to acknowledge the individual influence of the design variables on the objective function near the optima.

7.1. Optimisation process

The tractive performance optimisation of the designed compliant leg module is conducted. The optimal solutions were initially identified utilising the SQP algorithm and *fmincon* from the initial point \mathbf{x}_0 , after which the global search strategy was applied to expand the exploration of the design space. However, the global search strategy did not result in improved optima, signifying there is a clear optimum in the design space. The initial point \mathbf{x}_0 is defined as:

$$\mathbf{x}_0 = \begin{bmatrix} t_c \\ t_s \\ L \end{bmatrix} = \begin{bmatrix} 0.150 \\ 0.300 \\ 30.0 \end{bmatrix} \text{ mm},$$

with the parameter values used in the model are detailed in Table C.1. The slip ratio is assumed to be equal to one, for which the maximum drawbar pull can be obtained. A separate analysis on the performance of the optimal legs per slip ratio is performed in Section 8.1.

The optima are presented together with their objective and constraint performance in rounded figures. However, the optimisation process locates exact optima in higher significant figures, which are presented in Appendix C.2. These values are mathematical optima that cannot be translated to reality with such precision due to the assumptions made in the analytical model and the physical challenges in production. Nonetheless, as explained in the scope of this study, the absolute performance at the optima of the innovative compliant leg is compared to that of the original rigid leg in Section 8.1 to provide valuable insight into achieving the research goal.

7.1.1. Middle leg

The point at which the middle leg achieves optimal tractive performance is:

$$\mathbf{x}_{m,opt} = \begin{bmatrix} t_c \\ t_s \\ L \end{bmatrix} = \begin{bmatrix} 0.139 \\ 0.308 \\ 33.2 \end{bmatrix} \text{ mm}.$$

The value of the objective function, the drawbar pull, at this point is equal to 1.81 N. The leg vertically deforms 10.6 mm at the load application point, resulting in a flattened section length that measures 68.1 mm. The critical constraints are c_3 and c_4 , corresponding to the maximum stress in the flexure

while climbing along a sideways gradient and the maximum longitudinal displacement required to ensure torque transmission. The constraint values at the optimum point are detailed in Table 7.1. The constraint on the minimum radius at the end of the contact surface (c_5) is close to its limiting value, whereas the minimum climbing height constraint (c_6) has negligible influence. Similarly, the stress constraint while walking (c_1) and skid steering (c_2) are also inactive compared to the stress constraint while climbing along a sideways gradient, which is a predictable outcome, given the load encountered at the specific legs.

Table 7.1: Constraint performance middle leg

Constraint	Value	Value with safety factor (1.5)	Limiting value
c_1	307 MPa	461 MPa	≤ 503 MPa
c_2	313 MPa	470 MPa	≤ 503 MPa
c_3	335 MPa	503 MPa	≤ 503 MPa
c_4	5.00 mm	-	≤ 5.00 mm
c_5	59.1 mm	-	≥ 58.5 mm
c_6	82.3 mm	-	≥ 55.0 mm

The contour plots in Figures 7.1, 7.2, and 7.3 illustrate the visual representations of the design space at the optimum value of the remaining design variable. Enlarged versions of the contour plots are presented in Appendix C.3. The constraints are visualised together with their infeasible region (IR). The plots show a dominant gradient direction, where the drawbar pull increases as either t_c or t_s decreases, or L increases. Figures 7.1 and 7.2 illustrate contour lines with double curvatures, indicating that the objective function experiences non-linear local sensitivity. By analysing the spacing between the contour lines of one design variable while keeping the other variable constant at its optimum value, an insight is offered into the individual linearity of the local sensitivities of design variables near the optimum. In the case of t_c , the spacing becomes larger at higher values in both Figures 7.1 and 7.2, meaning that the local sensitivity of t_c becomes non-linear at higher values. For t_s and L , the spacing in the respective Figures 7.1 and 7.2 remains relatively similar, which means that the local sensitivities of these design variables are more linear. The latter is reaffirmed in Figure 7.3, as illustrated by the fact that the contour lines of t_s and L at $t_{c,opt}$ are diagonal, parallel, and evenly spaced below the constraint lines, indicating that the local normalised sensitivity of t_s and L at $t_{c,opt}$ are similar, relatively high and relatively linear.

Figures 7.1 and 7.2 also illustrate relatively small critical constraint intersection angles, indicating that in directions involving t_c , the feasible region near the optimum is moderately narrow and small movements away from the optimum violate constraints or decrease objective performance. The critical constraint lines near the optimum in Figure 7.3 are almost parallel to each other and the objective contour lines, which means that the feasible region near the optimum is wide and the optimum is flat in the direction along the critical constraint lines. The latter indicates that multiple combinations of t_s and L could yield similar tractive performance as the optimum at the fixed $t_{c,opt}$. However, the tightly spaced contour lines perpendicular to the critical constraint lines are an indication of a sharp optimum. Consequently, if the values of t_s and L move away from the critical constraint lines, objective performance quickly degrades.

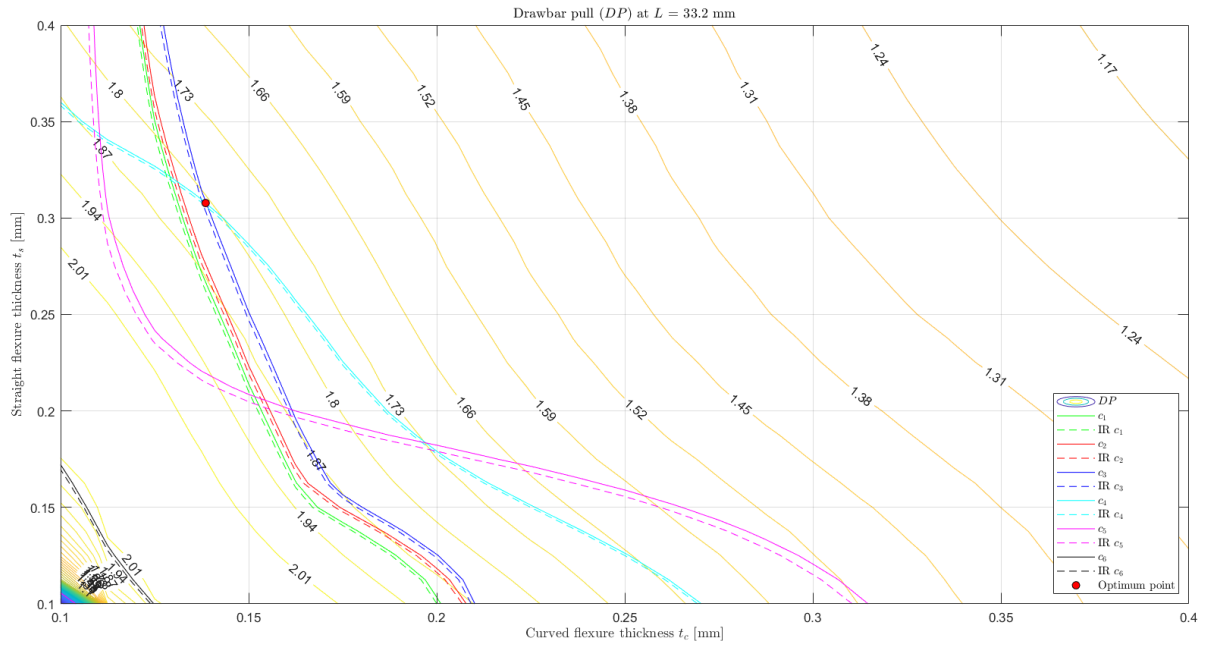


Figure 7.1: Contour plot middle leg drawbar pull DP , t_c vs t_s at L_{opt}

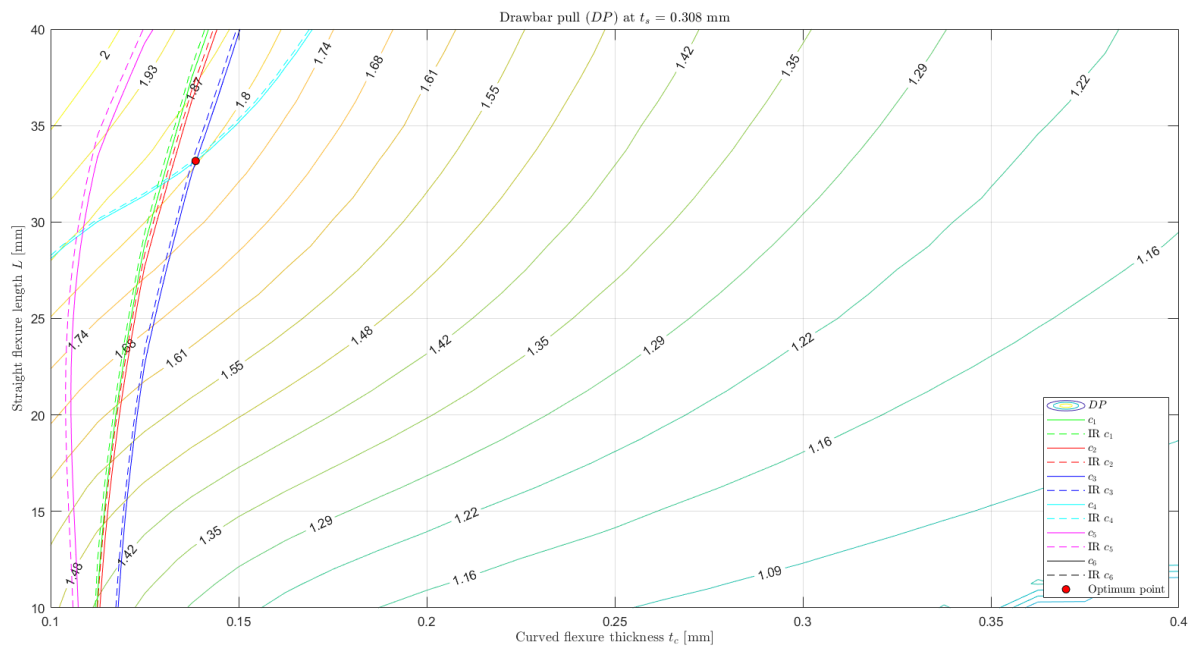


Figure 7.2: Contour plot middle leg drawbar pull DP , t_c vs L at $t_{s,opt}$

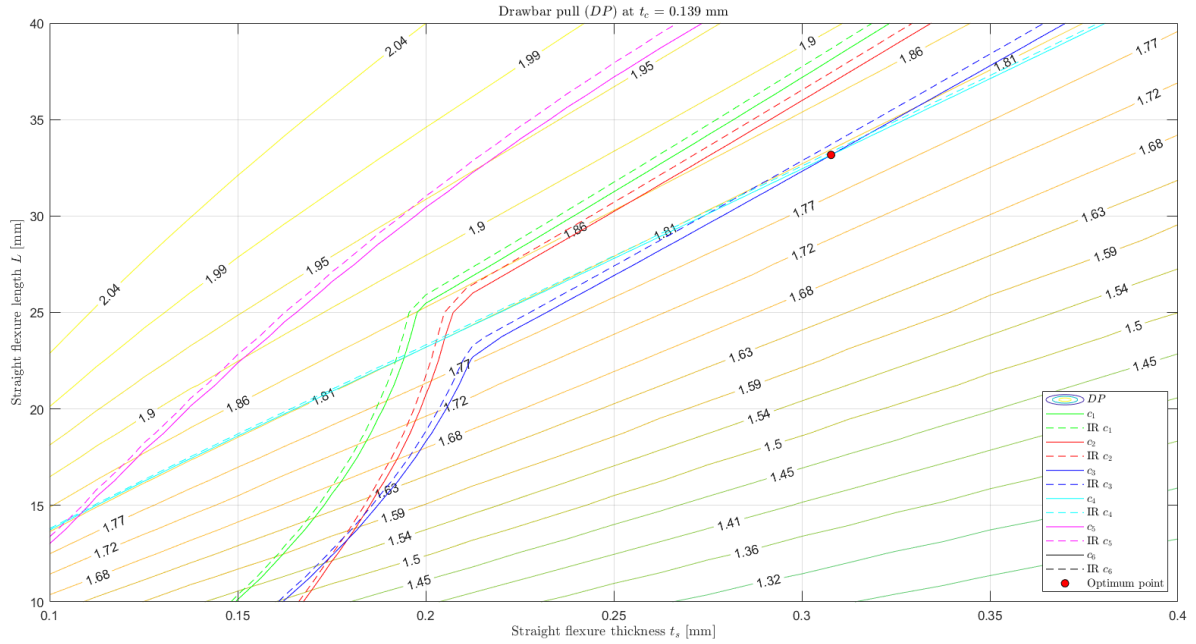


Figure 7.3: Contour plot middle leg drawbar pull DP , t_s vs L at $t_{c,opt}$

7.1.2. Outer leg

The point at which the outer leg achieves optimal tractive performance is:

$$\mathbf{x}_{o,opt} = \begin{bmatrix} t_c \\ t_s \\ L \end{bmatrix} = \begin{bmatrix} 0.100 \\ 0.157 \\ 19.8 \end{bmatrix} \text{ mm.}$$

The value of the objective function, the drawbar pull, at this point is equal to 1.17 N. The leg vertically deforms 11.0 mm at the load application point, resulting in a flattened section length that measures 69.4 mm, which slightly exceeds that of the middle leg. The critical constraints are again c_3 and c_4 , but in this case, these are accompanied by the lower bound of t_c . This indicates that the minimum curved flexure thickness limits the drawbar pull.

The constraint values at the optimum point are detailed in Table 7.2. Almost all constraints behave similarly to those of the middle leg, except for the stress encountered during skid steering. The value has changed from the middle leg value, whereas the stress values encountered while walking and climbing along a sideways gradient have negligible or no changes. This difference can be explained by the sideways compaction force acting on the leg during skid steering. As the load on the leg varies between the middle and outer legs, this compaction force changes indirectly, much like the drawbar pull. Both these load changes cause a stress variation. In contrast, for walking and sideways gradient climbing, the load distribution is the only thing changing, which happens at the same rate for both constraints.

Table 7.2: Constraint performance outer leg

Constraint	Value	Value with safety factor (1.5)	Limiting value
c_1	309 MPa	463 MPa	≤ 503 MPa
c_2	330 MPa	495 MPa	≤ 503 MPa
c_3	335 MPa	503 MPa	≤ 503 MPa
c_4	5.00 mm	-	≤ 5.00 mm
c_5	59.2 mm	-	≥ 58.5 mm
c_6	82.6 mm	-	≥ 55.0 mm

The contour plots in Figures 7.4, 7.5, and 7.6 illustrate the visual representations of the design space at the optimum value of the remaining design variable. The contour plots have changed significantly from the middle leg. Firstly, the constraints and the optimum are located within a narrow region of the design space, due to the decrease in normal load on the leg. Secondly, the spacing between the contour lines enlarges for all design variables, indicating that the non-linearity of their respective sensitivities has increased. Lastly, the behaviour of the critical constraints to variations in t_s and L differs significantly. At the fixed $t_{c,opt}$ used for the middle leg in Figure 7.3, the critical constraint lines are nearly coincident with each other and parallel to the objective's contour lines near the optimum. This alignment means that a variation in t_s and L along one of the critical constraint lines results in only a slight decrease in objective performance, whereas both constraint values remain nearly unchanged. In contrast, Figure 7.6 shows that the critical constraint lines for the outer leg are not closely aligned. For values of t_s and L greater than the optimum, c_4 remains as the critical constraint, whereas the initial critical constraint c_3 and constraints c_1 and c_2 become less restrictive. Since c_4 is nearly parallel to the objective's contour lines, this leads to a region of points with similar drawbar pull to the optimum, but less stress obtained in the flexure while walking, skid steering, or climbing along a sideways gradient.

In Figure 7.6, it is illustrated that the feasible area near the optimum has become narrower in contrast to Figure 7.3 of the middle leg, while the optimum remains flat in the direction along the constraint line c_4 from approximately $t_s = 0.21$ mm and $L = 22$ mm onwards. The closely spaced contour lines cause the optimum to be sharp in directions perpendicular to the constraint lines. Figures 7.4 and 7.5 show that the feasible area near the optimum is moderately narrow in their respective planes by the lower bound of t_c . Although the critical constraint lines of c_3 and c_4 in Figure 7.4 are relatively similar to the constraint lines near the optimum, the difference between the two and the closely spaced contour lines show that different value combinations of t_c and t_s cause a loss in objective performance, indicating a relatively sharp optimum in multiple directions of this plane. The latter is also true for the optimum in the plane of Figure 7.5, but this is mainly attributed to the difference in shape between the constraint line c_4 and the contour lines.

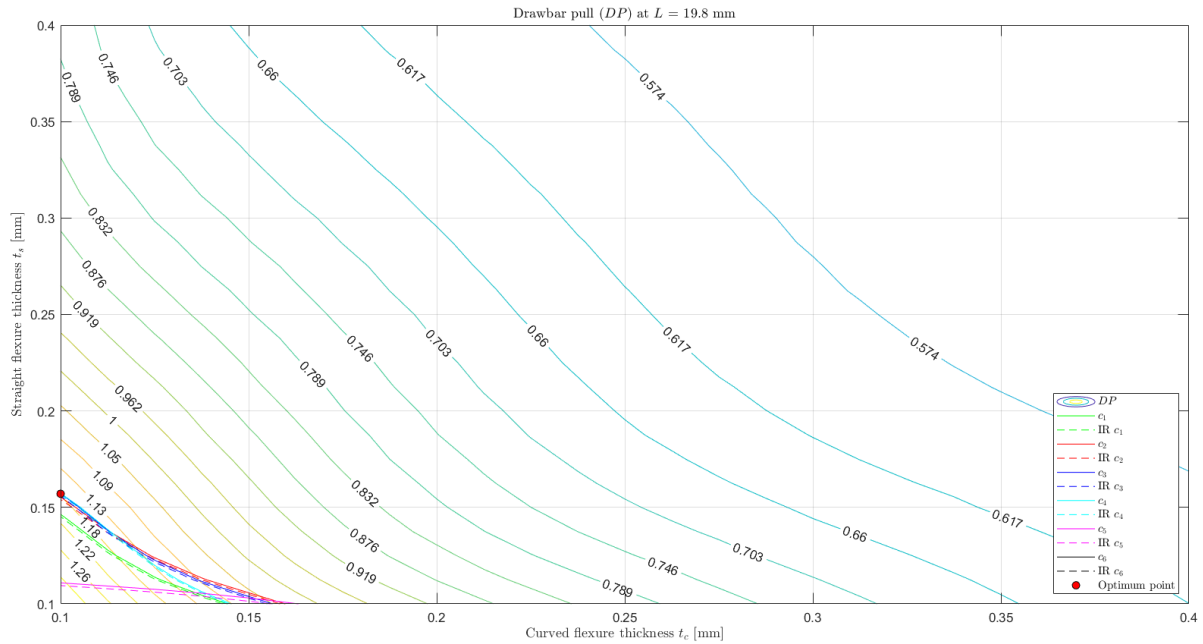


Figure 7.4: Contour plot outer leg drawbar pull DP , t_c vs t_s at L_{opt}

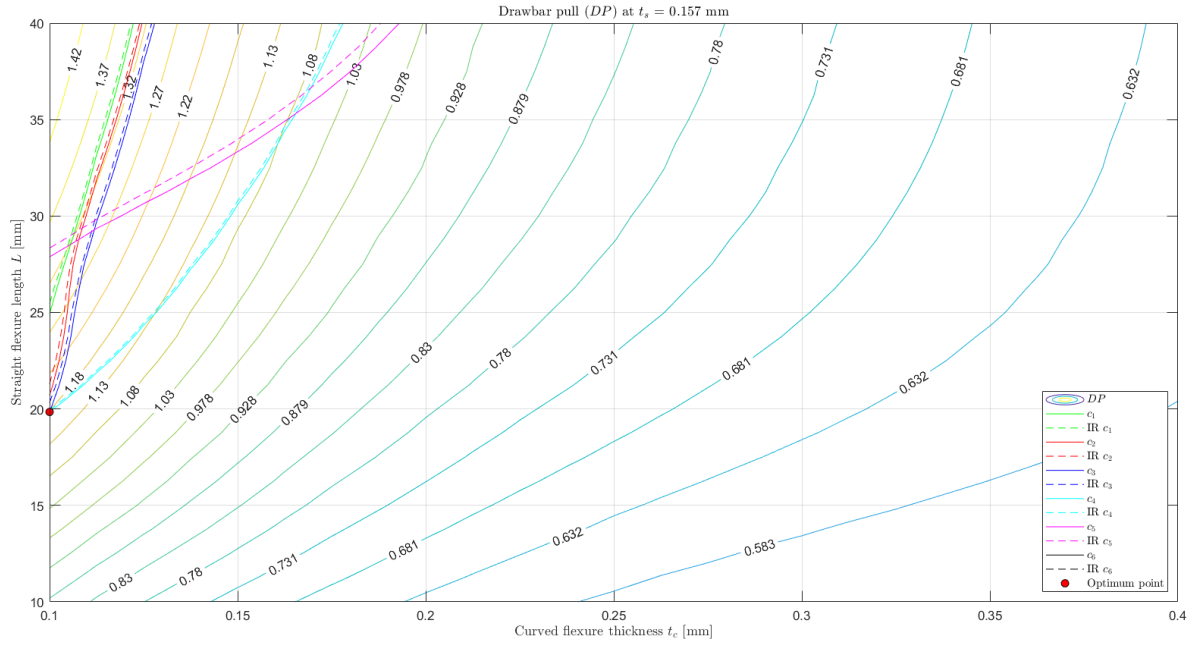


Figure 7.5: Contour plot outer leg drawbar pull DP , t_c vs L at $t_{s,opt}$

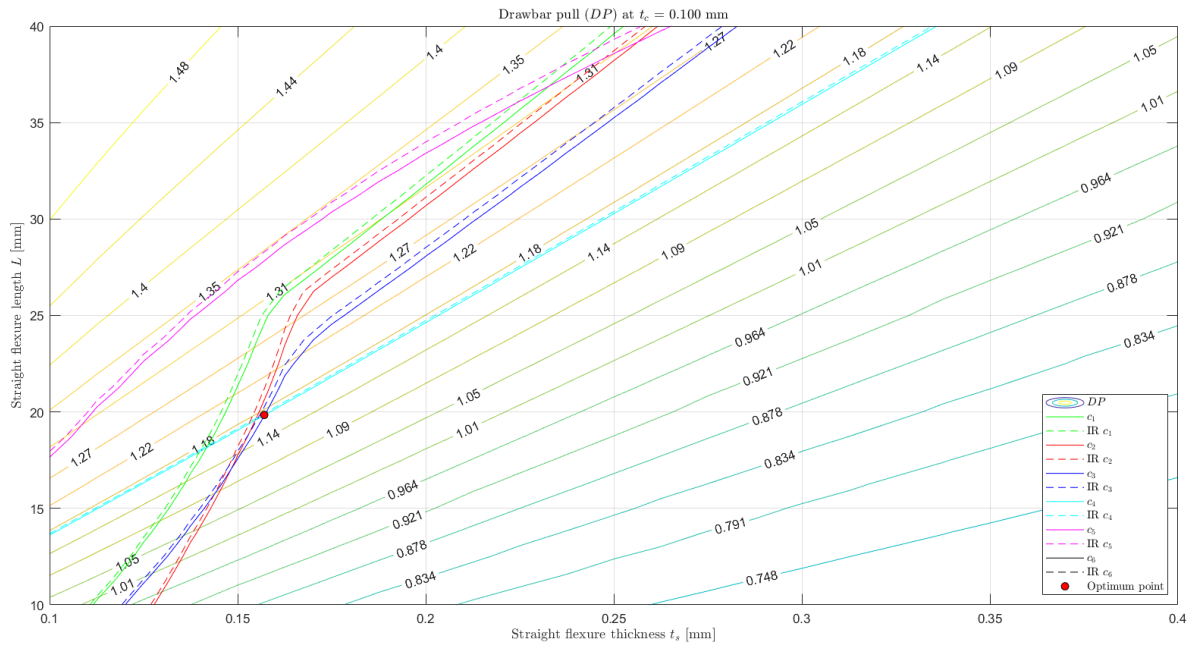


Figure 7.6: Contour plot outer leg drawbar pull DP , t_s vs L at $t_{c,opt}$

7.2. Sensitivity analysis

Although the previous section provided an initial understanding of the sensitivities of the design variables, a numerical sensitivity analysis is conducted at the optimal points \mathbf{x}_{opt} to comprehend the influence of these variables on the objective function near these points. The sensitivity indicates the degree to which the output of the objective function varies in response to changes in the input variables. This analysis will ascertain which variable exerts the greatest influence and should thus be prioritised, as well as identify variables whose contribution is negligible. Furthermore, sensitivity analysis contributes to the evaluation of the robustness of the system by detecting its linearity, potential instability, and noise. Due to the complexity of the calculations, it is not feasible to compute the analytical sensitivity.

Instead, the local sensitivity is estimated using finite difference methods. The central finite difference method is used for the design variables t_s and L , given its high accuracy due to the symmetric evaluation about the analysis point. This high accuracy comes at the cost of being computationally more expensive. However, this approach is unsuitable for the design variable t_c because the optimal points are positioned near, or in the case of the outer leg, precisely on the lower boundary of the design space. The perturbations are defined to obey the bounds of the design space, similar to the SQP algorithm in *fmincon* [35]. When the lower boundary constrains the design variable, only the forward finite difference method is applicable.

It is crucial to exercise caution when using finite difference sensitivities in iterative models. Due to the iterative nature of the solution procedures and the associated residuals, additional inaccuracies arise [36], which could introduce noise that distorts the true sensitivities. However, these effects were found to be minimal in this model.

7.2.1. Forward finite difference

The forward finite difference sensitivity $S_{x_i,FFD}$ for a design variable x_i is calculated using the equation:

$$S_{x_i,FFD} = \frac{\partial f}{\partial x_i} \approx \frac{f(x_i + \Delta x_i) - f(x_i)}{\Delta x_i}, \quad (7.1)$$

where Δx_i is the perturbation size. As the design variables have different magnitudes, the sensitivities are not directly comparable. To enable a consistent and dimensionless comparison, the sensitivities are normalised using the expression:

$$\hat{S}_{x_i,FFD} = S_{x_i,FFD} \cdot \frac{x_i}{f(\mathbf{x})}. \quad (7.2)$$

Given the design variable bounds and the optimal points \mathbf{x}_{opt} , the maximum perturbation size of the FFD method is assumed to be 0.10×10^{-3} m.

7.2.2. Central finite difference

The central finite difference sensitivity $S_{x_i,CFD}$ for a design variable x_i is calculated using the equation:

$$S_{x_i,CFD} = \frac{\partial f}{\partial x_i} \approx \frac{f(x_i + \Delta x_i) - f(x_i - \Delta x_i)}{2\Delta x_i}, \quad (7.3)$$

whereas the normalised central finite difference sensitivity is given by the expression:

$$\hat{S}_{x_i,CFD} = S_{x_i,CFD} \cdot \frac{x_i}{f(\mathbf{x})}. \quad (7.4)$$

The maximum perturbation sizes $\Delta t_{s,max}$ and ΔL_{max} of the CFD method to stay within the design space bounds are calculated using the equations:

$$\Delta t_{s,max} = \begin{cases} u_{t_s} - t_{s,opt} & \text{if } t_{s,opt} \geq 0.25 \times 10^{-3} \text{ m,} \\ t_{s,opt} - l_{t_s} & \text{if } t_{s,opt} < 0.25 \times 10^{-3} \text{ m,} \end{cases} \quad (7.5a)$$

$$\Delta L_{max} = \begin{cases} u_L - L_{opt} & \text{if } t_{s,opt} \geq 25 \times 10^{-3} \text{ m,} \\ L_{opt} - l_L & \text{if } t_{s,opt} < 25 \times 10^{-3} \text{ m,} \end{cases} \quad (7.5b)$$

where u_{x_i} and l_{x_i} are the respective upper and lower bounds of the design variables x_i .

7.2.3. Middle leg

According to Figures 7.7a and 7.8a, the normalised sensitivities of the curved flexure thickness \hat{S}_{t_c} and the straight flexure thickness \hat{S}_{t_s} remain stable throughout the perturbation range, registering values of -0.33 and -0.29, respectively. This indicates that a local increase in these design variables corresponds to a decrease in drawbar pull, which is supported by Figures 7.7b and 7.8b. The drawbar pull decreases at a higher rate for t_c than for t_s . As noted in Figure 7.9a, the normalised sensitivity of the straight flexure length \hat{S}_L maintains a relatively constant value of 0.32 until 5.0×10^{-4} m, indicating that the drawbar pull

increases along with L . For perturbations below 4.0×10^{-7} m, small fluctuations are observed in \hat{S}_L , attributable to light round-off error noise. The increase of \hat{S}_L at perturbations higher than 5.0×10^{-4} m can be attributed to the subtle non-linear relationship between L and the drawbar pull beyond optimal values, which is evident in Figure 7.9b. These values are obtained for larger perturbation magnitudes, consequently increasing the sensitivity. The non-linearity in the relationship between the drawbar pull and t_c , as well as t_s , does not appear in the normalised sensitivity plots because the corresponding high perturbations have not been reached due to the maximum perturbation sizes.

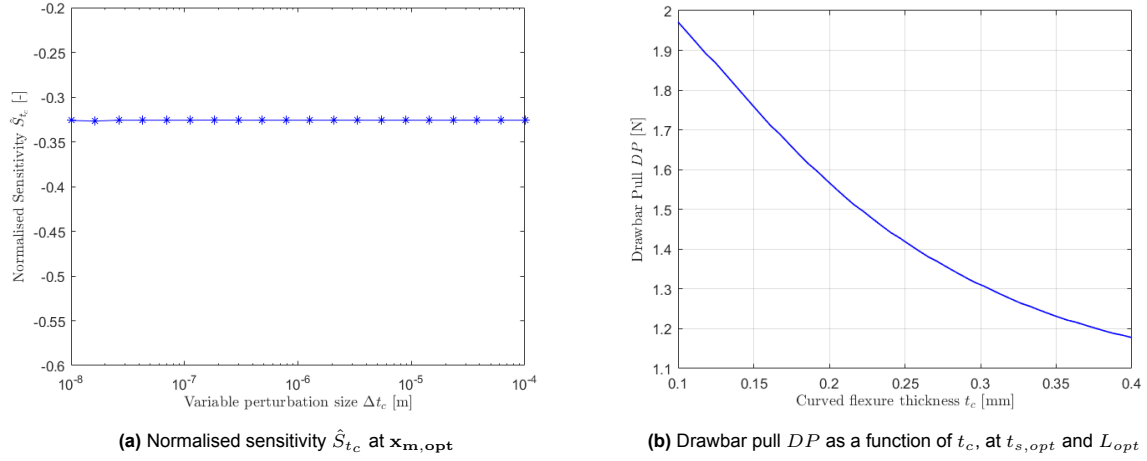


Figure 7.7: Middle leg curved flexure thickness t_c

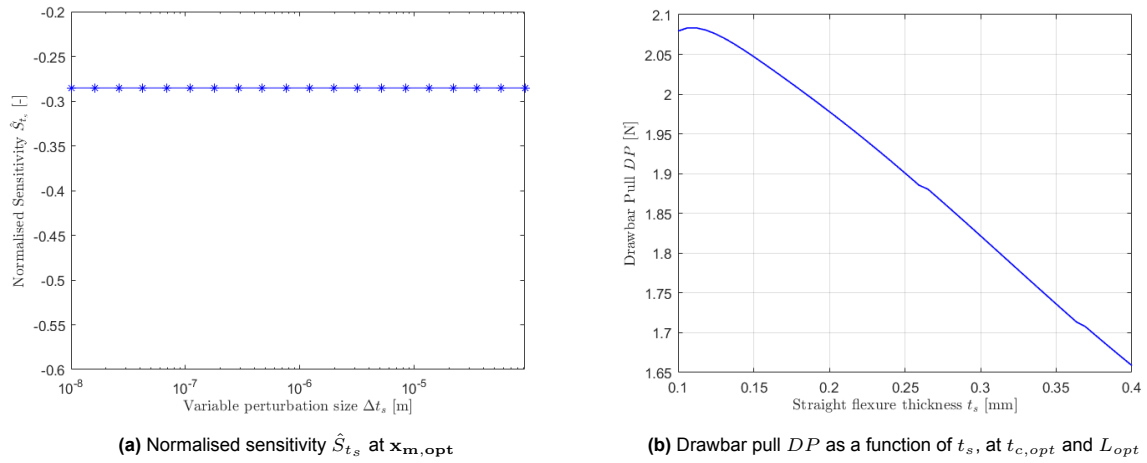
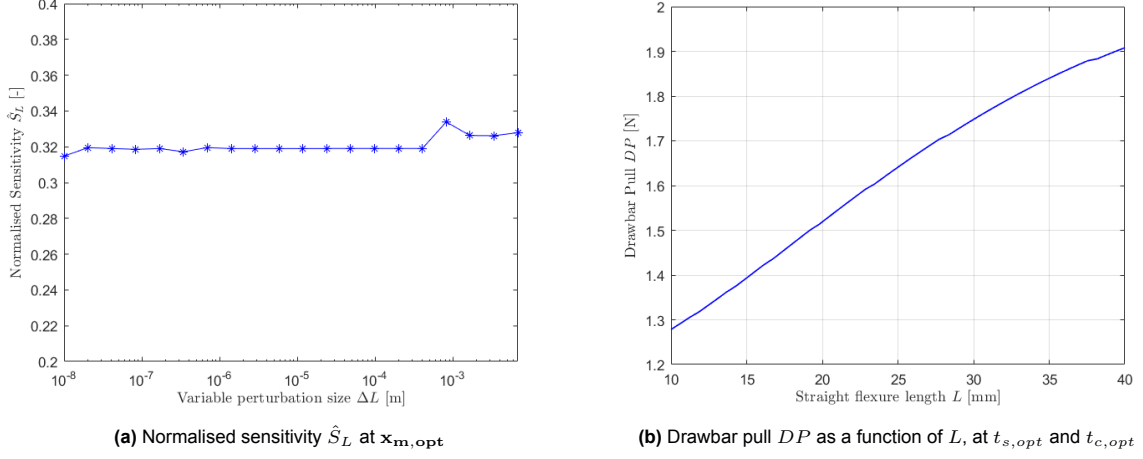


Figure 7.8: Middle leg straight flexure thickness t_s

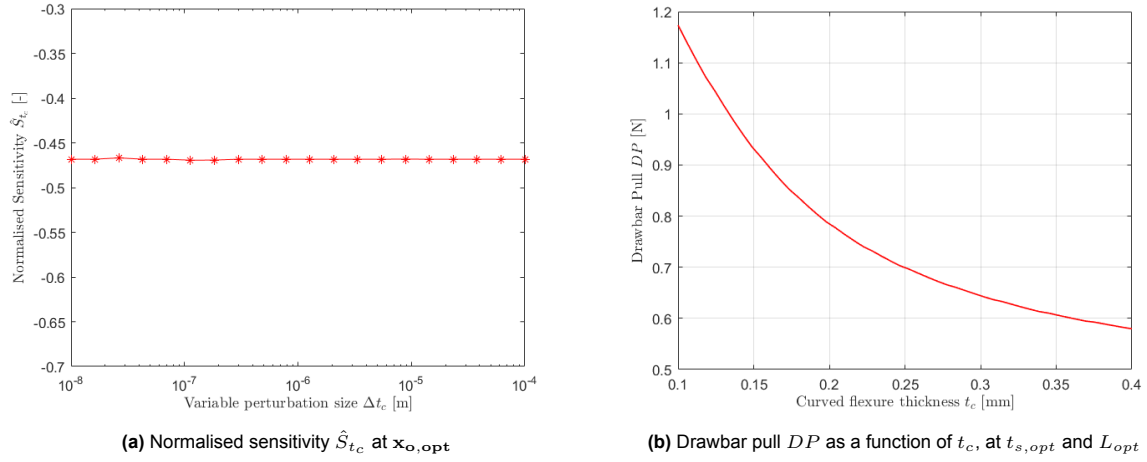
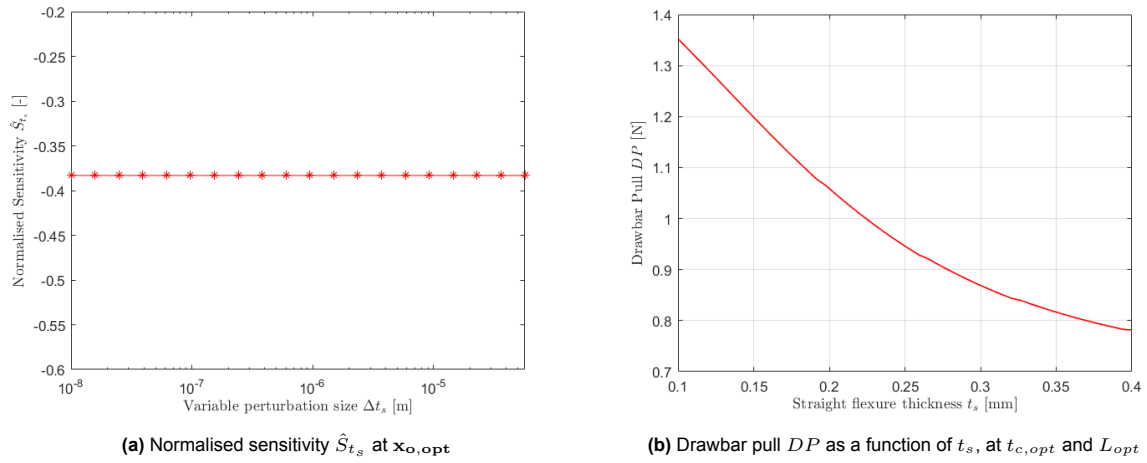
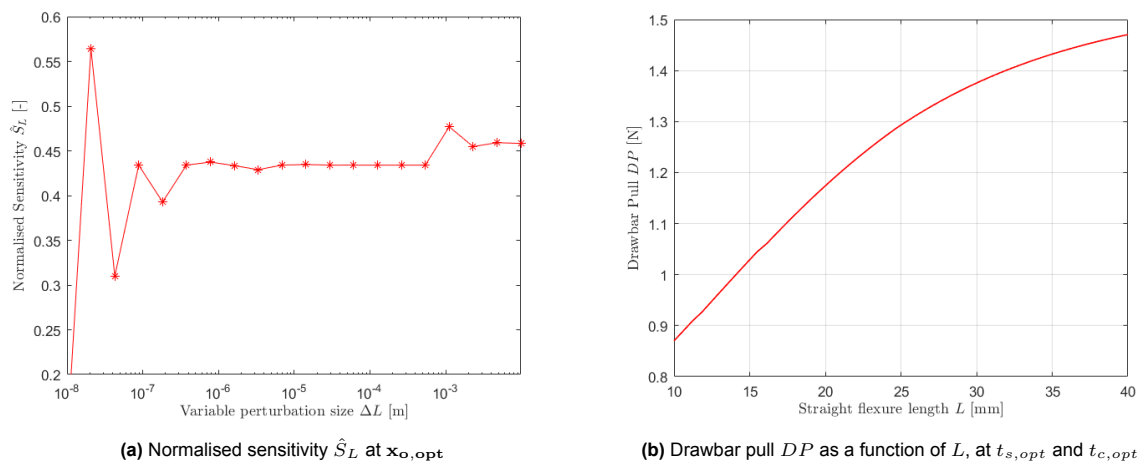
Figure 7.9: Middle leg straight flexure length L

Given the absolute values of the sensitivities at the stable perturbation regions, it is evident that t_c has the most influence on the drawbar pull near the optimum, closely followed by L and t_s . However, the difference between the absolute normalised sensitivities is too small to consider one design variable dominant. Instead, it can be concluded that all design variables have a similar influence near the optimum of the middle leg.

7.2.4. Outer leg

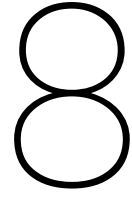
Similarly to the middle leg, Figures 7.10a and 7.11a demonstrate that the normalised sensitivities of both the outer leg curved flexure thickness \hat{S}_{t_c} and straight flexure thickness \hat{S}_{t_s} remain stable throughout the perturbation range, registering values of -0.47 and -0.38, respectively. As noted in Figure 7.12a, the normalised sensitivity of the straight flexure length \hat{S}_L within the perturbation range of 4.0×10^{-7} – 5.0×10^{-4} m maintains a stable value of 0.43. The region of perturbations below 4.0×10^{-7} m is characterised by instability, which can be attributed to the presence of round-off error noise, as illustrated by the absence of disruptions in Figure 7.12b. The round-off error noise is much more defined than for the middle leg, likely attributable to $t_{c,opt}$ being located at its lower bound, limiting the system's response freedom. The other design variables are interdependent, causing $t_{c,opt}$ to indirectly distort the reaction of the objective drawbar pull on the other design variables, increasing their round-off error noise. However, this round-off error noise is only visible for \hat{S}_L , which can be explained by the difference in magnitude of L with respect to t_c and t_s . Perturbations of 10^{-8} m are much smaller for L , that can range 10–40 mm, than for t_c and t_s , that can range 0.10–0.40 mm. For perturbations lower than 10^{-8} m, the noise becomes also visible for t_c and t_s , but these perturbations are too small to be of interest.

According to Figure 7.12a, \hat{S}_L exhibits an increase at perturbations surpassing 5.0×10^{-4} m, comparable to that observed of \hat{S}_L of the middle leg. Again, this peak likely results from the subtle non-linear interaction between L and the drawbar pull at values exceeding the optimum, as depicted in Figure 7.12b, whereas the non-linear interactions of the drawbar pull with t_c and t_s are not evident in the normalised sensitivity plots, given that such high perturbations are not achieved due to the maximum perturbation size.

Figure 7.10: Outer leg curved flexure thickness t_c Figure 7.11: Outer leg straight flexure thickness t_s Figure 7.12: Outer leg straight flexure length L

Based on the absolute values of the sensitivities within the stable perturbation regions, it can be concluded that the hierarchy of influence among the design variables near the optimum is equal to

that of the middle leg. However, the absolute normalised sensitivities have increased compared to the middle leg system, indicating that the outer leg system demonstrates heightened sensitivity to variations in design variables. This increase broadens the disparity between the absolute normalised sensitivities, resulting in a clearer distinction of the influence of each design variable. Consequently, for the outer leg drawbar pull, t_c emerges as the most influential design variable near the optimum, closely followed by L , while t_s has the least influence. To optimise computational efficiency, the design variable that exerts the least influence could be stabilised in the optimisation process. However, given that the absolute normalised sensitivities remain close to each other and considering the optimisation process involving three variables is computationally feasible, this approach has not been pursued.



Performance Analysis

This chapter describes the performance of the optimised compliant leg module. First, a slip ratio analysis is performed, in which the drawbar pull, sinkage, resistance torque, and tractive efficiency are reviewed over a range of slip ratios and compared to those of the original rigid leg. Subsequently, an analysis is conducted on the performance at the extreme temperatures encountered on the Moon.

8.1. Slip ratio analysis

In the optimisation model, the slip ratio is assumed to be equal to one, as this value provides the maximum drawbar pull. However, a slip ratio of one implies that the forward velocity v_x is nullified, and consequently the rover remains stationary. The slip ratio at which the rover will operate is logically lower and is influenced by the combination of torque input and soil properties. By defining the leg performance as a function of the slip ratio, the leg performance can be obtained at a certain operating slip ratio. The analysis is conducted for both the optimised compliant leg and the original rigid leg to present the enhanced performance of the compliant leg, as a result of this research. The performance enhancement is defined at the maximum achievable value in this study, at a slip ratio of one. The true performance enhancement depends on the slip ratio at which the rover will operate.

8.1.1. Middle leg

The compliant middle leg generates a maximum drawbar pull of 1.81 N, in contrast to the rigid leg, which achieves a maximum drawbar pull of 0.836 N, representing a 116% enhancement in performance. A leg with lower compliance than the optimum, visualised by the contour lines in Figures 7.1, 7.2 and 7.3, still reaches higher drawbar pull than the rigid leg, from which can be concluded that the introduction of a minimal amount of compliance to the leg, while staying in the feasible region of the design variables, enhances its tractive performance.

At a slip ratio of zero, the interaction between the leg and the soil is free of slip. As visible in Figure 8.1a, the drawbar pull becomes negative for both legs at slip ratios approaching zero, indicating that the resistance generated by the legs is greater than the thrust. This phenomenon can be attributed to the dependence of the thrust on the slip ratio via shear stress, whereas the resistance remains largely unaffected. Instead, the resistance is predominantly dependent on the normal stress at the soil entry section. Hence, the drawbar pull is more negatively affected for the rigid leg, as its soil entry section is larger compared to that of a compliant leg. In contrast, the compliant leg has a large flattened section that is subjected solely to positive thrust. When using the optimal design variables, the deformation resistance has the highest impact on the drawbar pull of the compliant leg.

The obtained sinkage of the compliant middle leg is approximately 1.64 mm, whereas the sinkage of the rigid leg varies between 6.51 and 7.21 mm, representing an average decrease of 76%. The reduction in sinkage of the compliant leg compared to the rigid leg can be explained by the lower average normal stress experienced by the compliant leg due to the increased contact patch with the soil. The rigid leg sinkage increases with the slip ratio, while the compliant leg sinkage remains constant. Ishigami explains this difference, asserting that "the sinkage of deforming wheels is almost constant regardless of the slip ratio since the flattened section of the wheel mostly supports the vertical load of

the wheel,” in contrast to the sinkage of most rigid wheels, which increases with rising slip ratios “due to the fact that the shear deformation of a wheel increases with increasing the slip ratio” [11]. These assertions are validated by the model results, with the relationship between shear deformation and slip ratio detailed in Eq. 4.16. The reduction in sinkage experienced by the compliant leg increases its climbing capability and positively influences its drawbar pull due to the decreased compaction resistance.

The maximum resistance torque for the compliant middle leg is 0.0963 Nm, in contrast to the rigid leg’s 0.0742 Nm, reflecting a 30% increase. The flattened section of the compliant leg experiences higher normal and shear stresses, thereby not only enhancing the drawbar pull but also contributing to an increased resistance torque. As a result, the rotary motion of the compliant leg requires a greater input torque to overcome the increased resistance torque.

The maximum tractive efficiency of the compliant middle leg is 82.2%, significantly exceeding that of the rigid leg, which is 30.2%. Tractive efficiency denotes the capability to convert input torque into output power, which is the drawbar pull. Higher tractive efficiency indicates that less input torque is required to traverse a given distance, thereby raising the energy efficiency of the leg. The compliant leg has a higher tractive efficiency than the rigid leg across all slip ratios, indicating superior energy efficiency. However, the energy losses induced by the waddling motion of the compliant leg are not taken into account. Consequently, the real energy efficiency of the compliant leg is expected to be lower than the calculated value. As demonstrated in Figure 8.1d, the maximum tractive efficiency for the compliant and rigid legs occurs at different slip ratios. For optimal energy efficiency, the compliant leg should operate at the slip ratio corresponding to this maximum, which is 0.151. It should be noted that this optimal energy efficiency operation reduces the output drawbar pull to approximately 0.549 N.

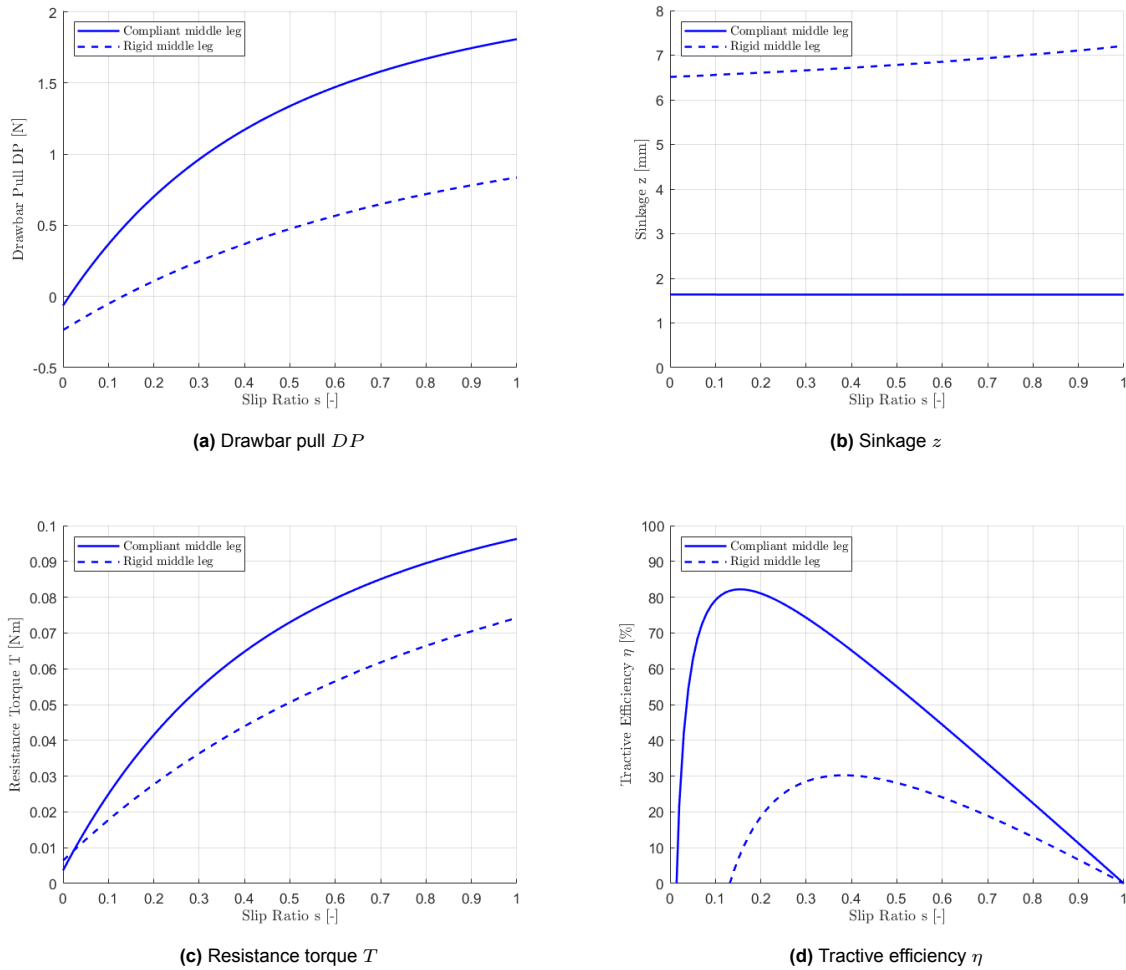


Figure 8.1: Slip ratio analysis of compliant and rigid middle leg

8.1.2. Outer leg

The results of the conducted analysis of the compliant outer leg reveal that it demonstrates a greater performance enhancement compared to the middle leg. The compliant outer leg generates a maximum drawbar pull of 1.17 N, in contrast to the rigid leg, which achieves only 0.448 N. This represents a 206% improvement in performance, whereas the middle leg exhibited only a 116% improvement. Furthermore, the resistance torque of the outer leg has also increased, achieving a maximum value of 0.0607 Nm, compared to 0.0364 Nm of the rigid leg. This corresponds to an increase of 67%, as opposed to a 30% increase for the middle leg.

The difference in performance enhancement can be attributed to the reduced dependency of the traction force on the normal load, as opposed to the resistance force. Due to distinct optimisations of the middle and outer legs, they possess different stiffness characteristics, resulting in similar vertical deflection and consequently a similar contact area. The traction force is generated by the shear stress beneath the contact area, with the contact area exerting a substantial influence on shear stress, whereas that of the normal stress is small. Consequently, the increase in the shear stress of the middle leg compared to that of the rigid leg is less than that of the outer leg. At maximum drawbar pull, there is a 106% increase in traction for the outer leg, compared to a 60% increase for the middle leg.

The resistance force is predominantly dependent on the normal stress. An increase in normal stress directly amplifies resistance. The middle leg, subjected to a higher load, consequently experiences greater normal stress and resistance force than the outer leg. However, given the similar vertical deflection and contact area between the middle and outer legs, the resistance forces of both decrease at a similar rate as those of the rigid legs. At maximum drawbar pull, the resistance force is reduced by 63% for the outer leg, whereas it is reduced by 57% for the middle leg.

As a result, the increase in traction force of the middle leg proceeds at a slower rate relative to the rigid leg than that of the outer leg, while both legs experience a comparable rate of reduction in resistance force. Consequently, the overall drawbar pull of the middle leg increases at a slower rate than that of the outer leg. It is thus concluded that if wheel deformation is similar, the compliant leg's advantage increases at lower loads.

Not all performance metrics of the outer leg reflect a substantial relative difference when compared to those of the middle leg. The sinkage of the compliant outer leg is approximately 0.808 mm, whereas the sinkage of the rigid leg varies between 4.08 and 4.56 mm. On average, this is a reduction of 81%, which is similar to the reduction of 76% observed for the middle leg. Again, the similar contact area under their respective loads causes a similar relative difference with the rigid leg for both the middle and outer compliant legs.

The maximum tractive efficiency of the compliant outer leg is 87.9%, which is significantly higher than the 34.1% of the rigid leg. However, as mentioned earlier, the real energy efficiency of the compliant leg is expected to be lower than the calculated value, because of the induced waddling motion of the compliant leg module. The maximum tractive efficiency occurs at a slip ratio of 0.141, which is the slip ratio at which the compliant outer leg achieves optimal energy efficiency. Meanwhile, the drawbar pull decreases to approximately 0.334 N.

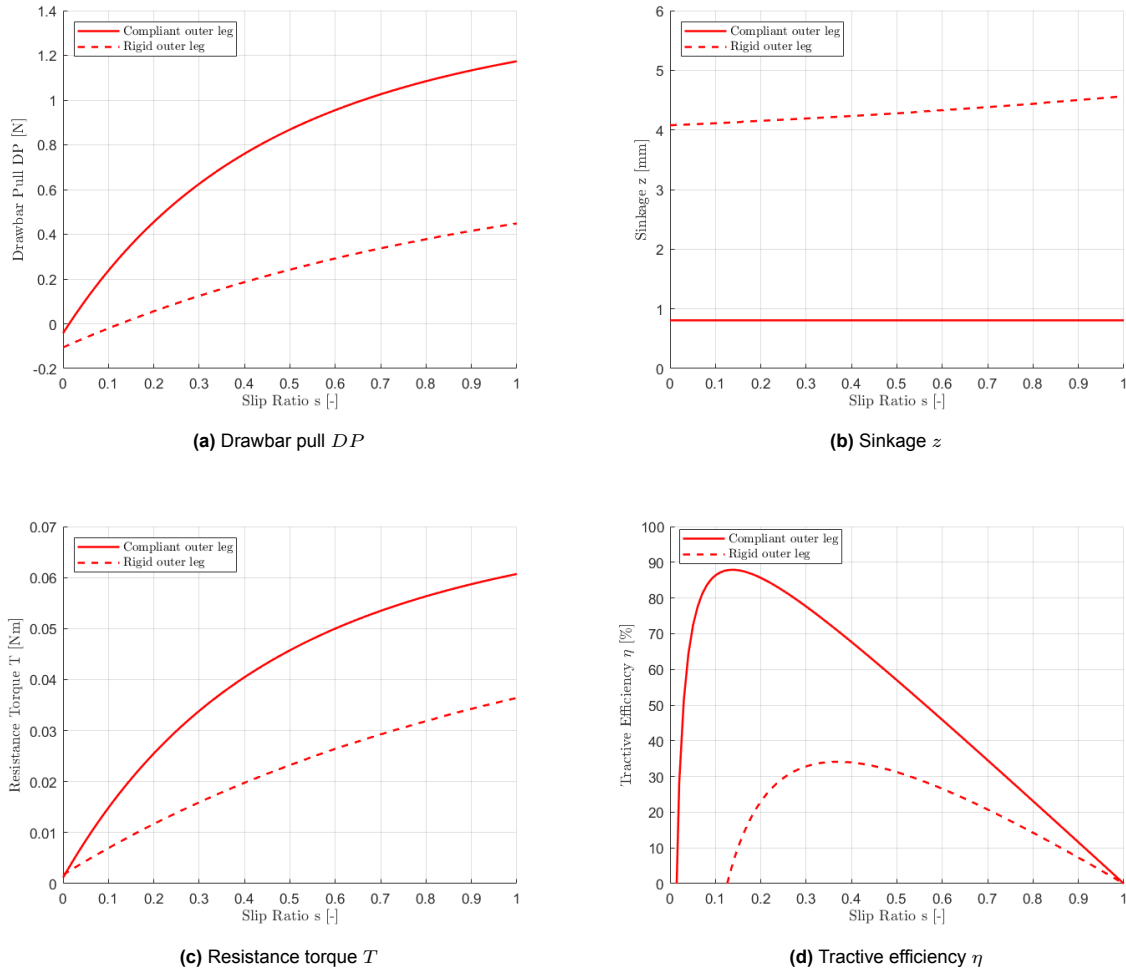


Figure 8.2: Slip ratio analysis of compliant and rigid outer leg

8.2. Temperature range analysis

Despite the extreme temperature fluctuations experienced on the Moon and possible heat accumulation caused by friction, it is assumed that the legs will operate at a temperature of 20°C. Consequently, the legs are optimised for operation at this nominal temperature. Although Aluminium 7075-T6 is generally robust against these extreme temperature fluctuations, the performance of thin leg flexures can be sensitive to small changes in material properties. To account for this, the optimal legs are analysed at extreme temperatures of 100°C and -80°C. The corresponding material properties at these temperatures are provided in Table 8.1.

Table 8.1: Material properties per temperature [37]

Symbol	Description	Value	Unit
T = 100°C			
σ_y	Yield strength	448	MPa
E	Young's modulus	68.3	GPa
G	Shear modulus	25.7	GPa
T = -80°C			
σ_y	Yield strength	545	MPa
E	Young's modulus	73.8	GPa
G	Shear modulus	27.7	GPa

The objective and constraint performance of the optimal designs at extreme temperatures are presented in Appendix C.2. The variations in drawbar pull and constraint values are minimal, which can be explained by the marginal difference in the Young's and shear moduli of the material. In contrast, the material yield strength is significantly influenced by temperature, directly affecting constraint limits. As the temperature rises, the yield strength decreases, leading to more stringent stress constraints. At 100°C, while the stress remains within constraint limits, the safety factor is compromised. The opposite behaviour is observed at lower temperatures, where a decrease in temperature results in increased yield strength and, consequently, less restrictive stress constraints. At -80°C, stress levels remain substantially below the constraint limits, even when considering the safety factor, indicating the potential for enhanced performance.

The legs optimised for 20°C continue operational viability at lower temperatures. However, elevated temperatures pose an increased risk due to violation of the stress safety factor. To achieve functionality across the entire temperature range, the legs should be optimised for maximum temperature conditions. Although this approach ensures safe operation, it results in peak tractive performance occurring at the maximum temperature, compromising tractive performance at lower temperatures. The following subsections present an optimisation of the middle and outer leg to determine the optimal tractive performance at the extreme temperature of 100°C, creating a thermal-resilient design that ensures functionality across the temperature range. The same optimisation procedure and settings are used as for the legs optimised at 20°C. However, the design space for this analysis has an increased upper bound for L :

$$0.10 \leq t_c \leq 0.40 \text{ mm}, \quad (8.1a)$$

$$0.10 \leq t_s \leq 0.40 \text{ mm}, \quad (8.1b)$$

$$10 \leq L \leq 50 \text{ mm}. \quad (8.1c)$$

8.2.1. Middle leg

The point at which the middle leg achieves optimal tractive performance at 100°C is:

$$\mathbf{x}_{m,100^\circ\text{C}} = \begin{bmatrix} t_c \\ t_s \\ L \end{bmatrix} = \begin{bmatrix} 0.150 \\ 0.380 \\ 40.9 \end{bmatrix} \text{ mm}.$$

The thermal-resilient middle leg generates a maximum drawbar pull of 1.79 N at 100°C. At the standard operating temperature of 20°C, the maximum drawbar pull achieved is 1.77 N, which represents a slight reduction compared to the design specifically optimised for 20°C, with optimal design variables at 100°C differing substantially from those at 20°C. In Figure 8.3, it is observed that the 100°C-optimum exists at the intersection point of critical constraints c_3 and c_4 , similar to the 20°C-optimum. Plotting the 100°C-optimum at 20°C in Figure 8.4, it becomes evident that the stress constraints are more reluctant at 20°C, and the drawbar pull of the 100°C-optimum has decreased. The decreased drawbar pull can be attributed to the increased Young's and shear moduli at 20°C. The 100°C-optimum had lower Young's and shear moduli, resulting in reduced stiffness of the leg. This reduction is compensated for by increasing the values of the design variables, ensuring a similar deflection and contact area that is necessary for optimal drawbar pull. At 20°C, the increase in Young's and shear moduli raises the overall stiffness of the 100°C-optimised leg, consequently decreasing the deflection and drawbar pull. Figure 8.4 further shows that the torque transmission constraint (c_4) alters at a similar rate as the drawbar pull, as both depend similarly on the changes in Young's and shear moduli.

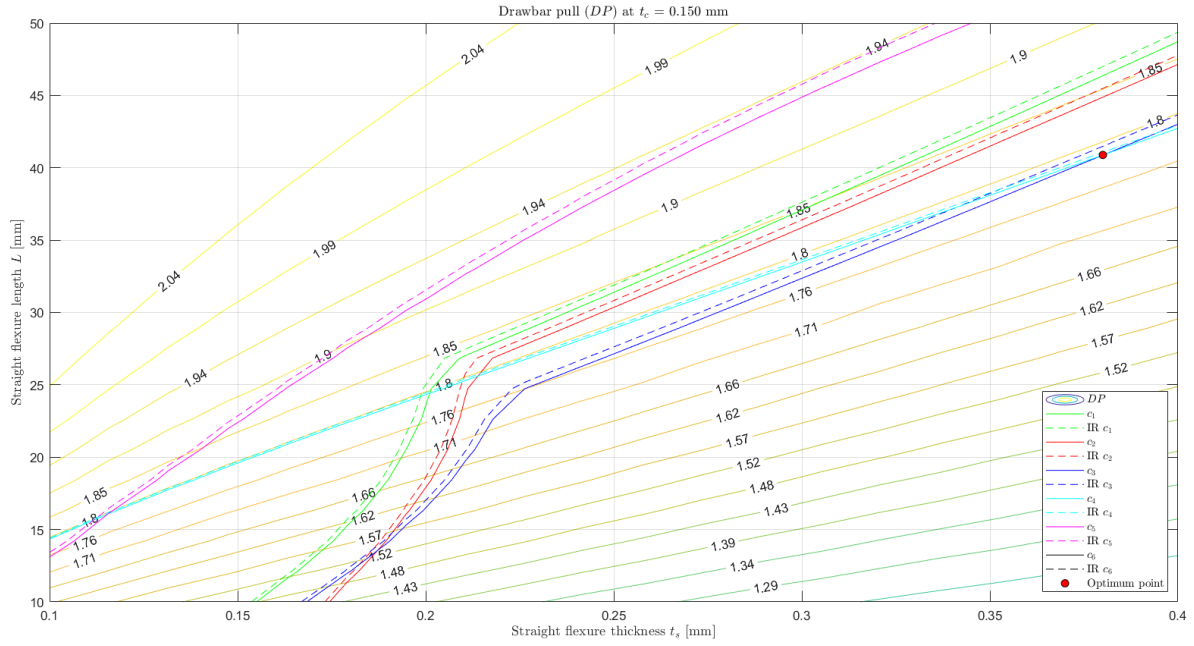


Figure 8.3: Contour plot middle leg drawbar pull DP , t_s vs L at $t_{c,100^\circ C}$, $T = 100^\circ C$

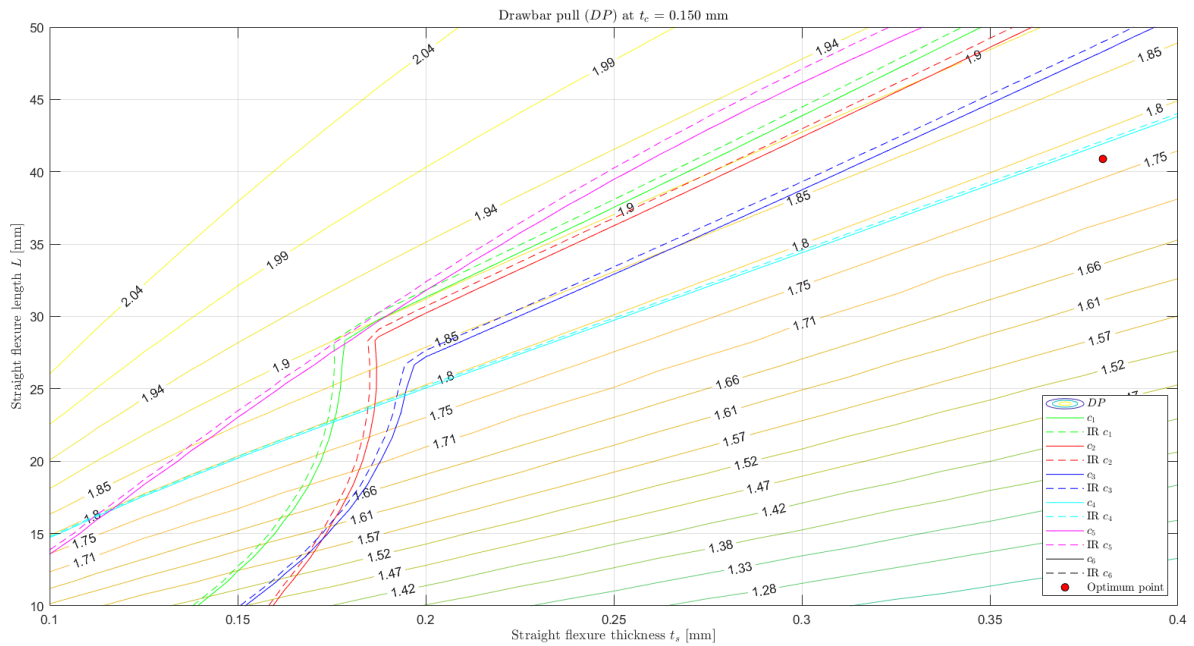


Figure 8.4: Contour plot middle leg drawbar pull DP , t_s vs L at $t_{c,100^\circ C}$, $T = 20^\circ C$

8.2.2. Outer leg

The point at which the outer leg achieves optimal tractive performance at $100^\circ C$ is:

$$\mathbf{x}_{o,100^\circ C} = \begin{bmatrix} t_c \\ t_s \\ L \end{bmatrix} = \begin{bmatrix} 0.102 \\ 0.234 \\ 28.1 \end{bmatrix} \text{ mm.}$$

The thermal-resilient outer leg generates a maximum drawbar pull of 1.17 N at $100^\circ C$. At the standard operating temperature of $20^\circ C$, the drawbar pull is equal to 1.15 N, which is again a slight reduction compared to the design optimised specifically for $20^\circ C$. The system reacts similarly to the outer leg as

to the middle leg. However, this time the optimal value of t_c at 100°C is nearly identical to the optimal value at 20°C. As discussed in Section 7.1.2, at the 20°C-optimum value of t_c , the constraint line of c_4 is parallel to the contour line of the drawbar pull, and the constraint line of c_3 is much less critical for higher values of t_s and L , indicating that similar drawbar pull values can be achieved by varying t_s and L , while simultaneously reducing the stress in the flexure. Although due to the decreased yield strength at 100°C, the constraint line of c_3 has moved on top of that of c_4 , which creates the optimum point, as visible in Figure 8.5. In contrast, Figure 8.6 illustrates that at 20°C, the 100°C critical constraint lines have moved away from each other, and the 100°C-optimum has a decreased drawbar pull.

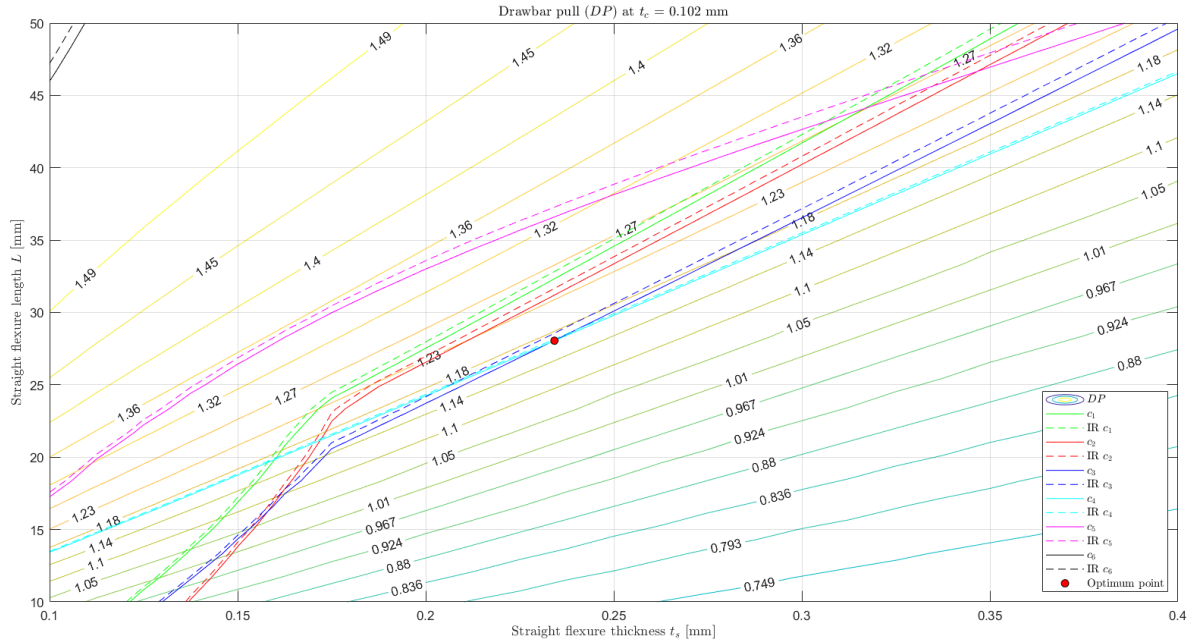


Figure 8.5: Contour plot outer leg drawbar pull DP , t_s vs L at $t_{c,100^\circ C}$, $T = 100^\circ C$

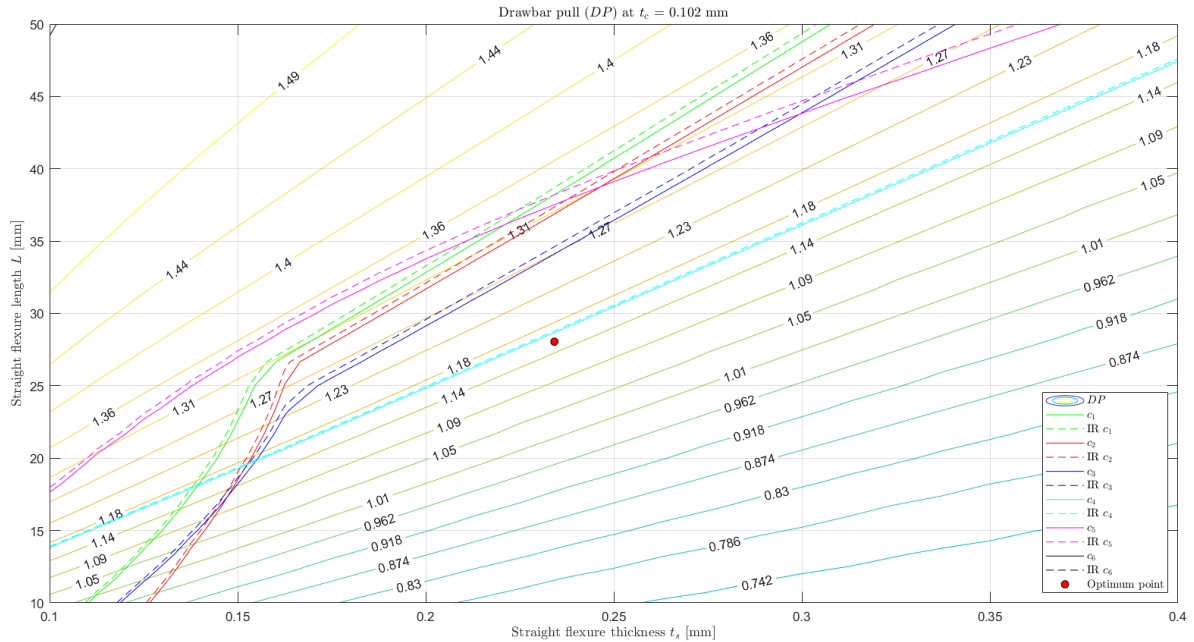


Figure 8.6: Contour plot outer leg drawbar pull DP , t_s vs L at $t_{c,100^\circ C}$, $T = 20^\circ C$

9

Result Evaluation

This chapter describes an evaluation of the research findings. The study has yielded optima that satisfy all constraints and significantly enhance tractive performance, thereby achieving the research goal. However, the scope of the study extends beyond solely creating a design and obtaining the optimal tractive performance. The aim is to comprehend the implications of these results for the design's physical performance. The emphasis is placed on investigating potential design modifications informed by research findings, examining potential variations of the optimum design variables, and understanding the physical consequences of these results.

9.1. Design

As mentioned at the start of the optimisation process, the final concept is subject to design modifications as the optimisation study highlights areas where enhancements in objective performance or constraint satisfaction are achievable. The final designs of the middle and outer legs at their respective optima are presented in Figures 9.1 and 9.2, respectively. The modifications made to create the final designs are detailed.

Initially, it was determined that the optimal straight flexure length was excessively large for the final concept's feasibility. To accommodate this, its connection point to the frame has been altered to connect directly with the leg hub. Furthermore, the end of contact surface radius constraint was identified as approaching critical status, showing the importance of a bump stop that covers the entire contact surface with the ground. To integrate this bump stop, the frame has been modified into a triangular shape. This modification would increase not only the bump stop coverage of the ground contact flexure but also that of the straight flexure, if it is deflected into the frame when the leg rotates backwards during skid steering or encounters unforeseen forces. The bump stop restricts maximum vertical deflections of the ground contact flexure at 20% of the leg radius. Within the triangular frame, the connection of the straight flexure with the leg hub structurally supports the forces at the point of flexure connection, thereby reducing the structural reliance on the bump stop in the final concept. Consequently, a reduction in bump stop thickness could result in weight savings. The final designs in the presented configuration, without weight and structural optimisation, have a mass of approximately 48 grams.

One of the critical constraints of the optimisation is the stress encountered while climbing along a sideways gradient. In the middle leg, the maximum stress is located near the connection point of the curved flexure with the frame, whereas in the outer leg, it is near the connection point with the straight flexure and the frame. These respective locations are consistent across all stress constraints. An additional bump stop has been incorporated on the outer side of the straight flexure to stop over-deflection and reduce fracture risk. The size of the bump stop depends on the optimised length of the straight flexure.

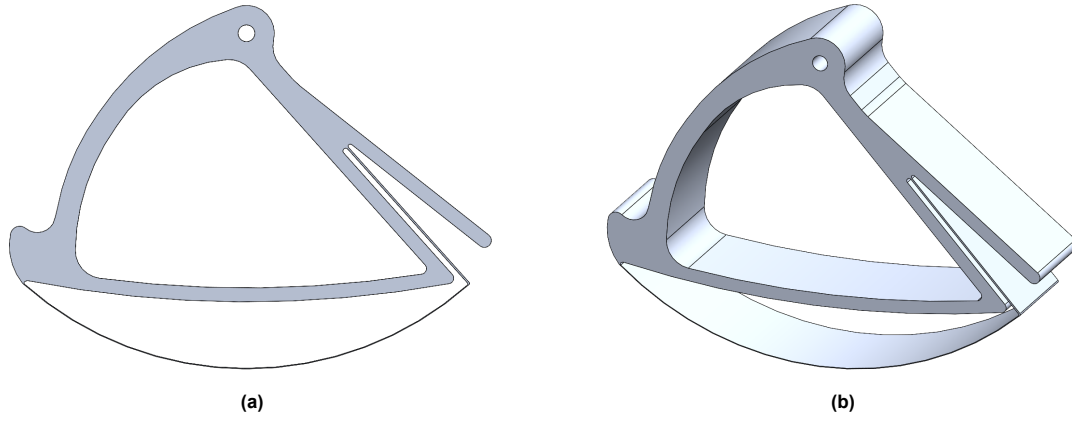


Figure 9.1: Final design middle leg

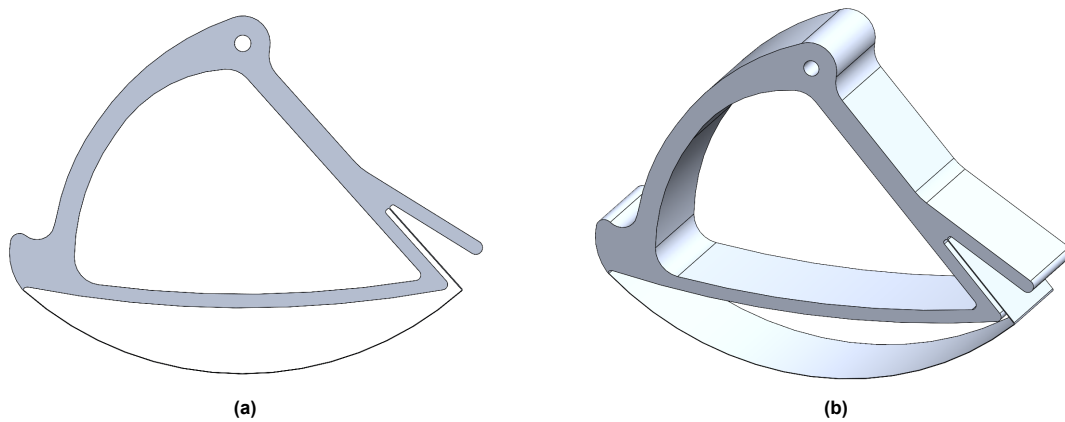


Figure 9.2: Final design outer leg

9.2. Optima points

The sharpness of the feasible region near the optima is examined to explore potential variations of design variables. Although the sensitivities of the design variables for the middle leg are notably similar, the narrowness of the feasible region in directions that involve t_c indicates that minimal adjustments to the optimum value of t_c can be made without decreasing objective performance. However, the feasible region near the optimum in the t_s - L plane visible in Figure 7.3 is wide, and the optimum is flat in the direction along the critical constraint lines. The latter suggests that various combinations of t_s and L could yield tractive performance comparable to the optimum at the fixed $t_{c,opt}$. Nevertheless, these combinations must lie on the critical constraint lines, as the sharp optimum in the direction perpendicular to these lines results in objective performance degradation. The combination of values for t_s ranges approximately 0.22-0.38 mm, while for L , it ranges approximately 23-40 mm. Changes in the values of t_s and L could be justified when constraint performance improves with the altered values. As the critical constraint lines are almost coincident, there is no substantial basis to modify the optimum values for the middle leg. However, for the outer leg, changes in the values of t_s and L could yield improved constraint performance. While the optimum in the t_s - L plane visible in Figure 7.3 is located at the intersection point of two critical constraint lines, the optimum is flat in the direction along a single critical constraint line. The other initial critical constraint, the stress in the flexure while climbing along a sideways gradient, is demonstrated to become less restrictive, alongside the stress constraints while walking and skid steering. For the middle leg, combinations of values of t_s and L must lie on the critical constraint line, as deviations in the direction perpendicular to the critical constraint lines lead to objective performance degradation due to the sharp optimum in this direction. The combination of values usable for t_s ranges approximately 0.16-0.34 mm, whereas for L , it ranges approximately 20-40 mm. An example of a point

on the critical constraint line is:

$$\mathbf{x}_{o,new} = \begin{bmatrix} t_c \\ t_s \\ L \end{bmatrix} = \begin{bmatrix} 0.100 \\ 0.230 \\ 28.0 \end{bmatrix} \text{ mm.}$$

The value of the objective function, the drawbar pull, at this point is equal to 1.17 N. The constraint values at this point are presented in Table 9.1. If these values are compared to the constraint values of the outer leg optimum in Table 7.2, it can be concluded that all constraints, excluding the critical constraint c_4 , are further away from their limiting value, showing increased performance.

Table 9.1: Constraint performance outer leg at $\mathbf{x}_{o,new}$

Constraint	Value	Value with safety factor (1.5)	Limiting value
c_1	283 MPa	424 MPa	$\leq 503 \text{ MPa}$
c_2	289 MPa	433 MPa	$\leq 503 \text{ MPa}$
c_3	304 MPa	462 MPa	$\leq 503 \text{ MPa}$
c_4	5.00 mm	-	$\leq 5.00 \text{ mm}$
c_5	59.0 mm	-	$\geq 58.5 \text{ mm}$
c_6	82.7 mm	-	$\geq 55.0 \text{ mm}$

9.3. Contact surface wear

The physical impact of the optima is not only positive. The findings indicate that the thickness of the ground contact (curved) flexure is small near the optima, raising concerns regarding potential performance losses and failures induced by contact surface wear. The abrasive nature of lunar regolith and the presence of sharp rocks can cause substantial damage to the flexure, while metal fatigue poses a potential issue in future, longer missions. Increasing the ground contact flexure thickness could offer a viable solution, but it is shown to significantly decrease tractive performance. Nonetheless, even a slight increase in compliance added to the leg demonstrates an improvement in tractive performance compared to the original rigid leg. An additional optimisation process incorporating an increased minimum curved flexure thickness is presented in Appendix D.1.

9.4. Temperature range

The temperature range analysis revealed that the optima obtained at the standard operating temperature of 20°C failed to satisfy the constraints under elevated temperatures, which may arise due to increased ambient temperatures or heat accumulation caused by friction. Consequently, an effort was made to obtain a thermal-resilient leg by optimising at 100°C. This process resulted in optima with a slight reduction in drawbar pull of 0.04 N and 0.02 N for the respective middle and outer leg at the standard operating temperature, in comparison to those optimised at the standard operating temperature. However, the stress experienced in the flexure is significantly reduced. This observation, combined with the capability of the thermal-resilient leg to ensure functionality across the entire temperature range, provides a reason to use the thermal-resilient design that is optimised at maximum temperature conditions. It is also no coincidence that the newly proposed outer leg point $\mathbf{x}_{o,new}$ is very similar to the optimum of the thermal-resilient design. The fine margins between the design variable values, although the respective drawbar pull at the standard operating temperature of 20°C differs by 0.02 N, do show the sensitivity of the system.

Discussion and recommendations

This chapter discusses the results and methodology of the study. Limitations for the design and optimisation model are identified, and recommendations are proposed for future work.

10.1. Design

The presented design is not yet a final product, leaving opportunities for improvement in future work. The performance of the design could be improved by ensuring comprehensive bump stop coverage over displacements causing significant stress peaks, for which the entire flexure's deflection across all locations must be analysed. Additionally, a weight and structural optimisation can be performed to limit the total weight of the design. Furthermore, potential failure methods that affect the longevity of the design should be analysed, such as contact surface wear and wear experienced due to contact between the flexure and the bump stop. Based on these analyses, conclusions can be drawn about the feasibility of the design. Future studies may also focus on making the design fault-tolerant. In the scenario where the flexure may fail unexpectedly, the bump stop could potentially preserve the leg's functionality. This likelihood is enhanced if future studies explore increasing the bump stop curvature.

The created designs are the result of an extensive design and optimisation process aimed at increasing tractive performance on lunar terrain. Although performance has improved, an optimal solution remains unattainable due to designer bias in the design process. A limitation inherent to the created design is the induced waddling motion, attributable to variations in vertical stiffness dependent on leg orientation, that causes extra energy losses. Future work may explore alternative design solutions to further improve performance. A design could be created with a uniform optimal stiffness that enhances not only energy efficiency but also ensures a consistent optimised drawbar pull over the entire contact surface, instead of the maximum drawbar pull obtained solely in the upright orientation, as is the case in this study. The achievement of uniform stiffness is complicated by the torque transmission and climbing height constraints. However, the climbing height has proven to be the least critical constraint, as it comfortably reaches the benchmark due to the design created. Although it is positive that the design excels in this area, if a different design objective is adopted, such as decreasing the waddling motion, the position of the climbing hook could be modified.

As demonstrated in this study, the tractive performance of a leg on lunar terrain improves with a compliant, uniform contact surface. However, most extra-terrestrial rover wheels have integrated grousers, which enhance tractive performance by providing additional thrust due to the shearing action of the vertical surfaces in the granular lunar soil [21]. Future work could incorporate grousers into the design and analytical optimisation model to further improve tractive performance, while significantly impacting the leg's compliant behaviour.

10.2. Contact surface wear

Contact surface wear is the most significant vulnerability of the design, induced by the small thickness of the ground contact (curved) flexure near the optima. Consequently, future work must analyse the influence of contact surface wear on the longevity of the design. To achieve optimal tractive performance without concerns of contact surface wear, future work may focus on creating designs with a

larger ground contact flexure thickness that maintain the design's deformability in the radial direction and stiffness in the longitudinal direction. A solution to still utilise the made design is employing alternative materials. Such materials should have a high strain-to-failure ratio, allowing them to deflect without fracturing. Nitinol may serve as such a material due to its testing by NASA for use on rover wheels. Because nitinol is a shape memory alloy, it "provides enhanced control over the effective stiffness as a function of the deformation, providing increased design versatility" [38]. Additionally, an alternative material could also address other challenges associated with low flexure thickness, such as manufacturing complexity and space journey survivability (which is not in the scope of this study).

10.3. Analytical optimisation model

In the constructed model, several assumptions and simplifications have been applied, which result in the model calculating an estimation of the true performance, whereas the optima of the tractive performance are presented with significant precision. The majority of these assumptions and simplifications are accounted for by the comparative nature of the design variables in this study and the optimisation limitations, such as computational constraints. To validate the performance of the developed design and the theoretical model, experimental evaluations must be conducted.

To increase the model's accuracy in representing reality, some assumptions require modifications. Most importantly, the assumption of linear deflections and a single load application point might cause the model to inaccurately describe the performance of the compliant design compared to the rigid design. Instead of presuming linear deflections and a single load application point, the flexure should be characterised by non-linear deflections and granular contact load. Achieving this analytically is challenging, but it may be accomplished using simulation software. A potentially analytically achievable method is the assumption of non-linear deflections due to a single contact pressure load, which is likely more accurate than the current assumption. However, it could be challenging to model and computationally demanding. To ensure easy handling of the model in future use cases, the manual iteration of the longitudinal force F_x can be converted into a computed iteration.

The terramechanics model can have multiple improvements. Firstly, the assumption that the flattened section length remains constant between static and quasi-static interactions, and that the curved parts retain the original radius, is debatable, as the deflection created by the radial flexure is not incorporated outside the force-deflection relationship. Although the analytical terramechanics framework using compliant parts is limited, a study could explore applying the substitute-circle approach of Bekker [9] and Schmid [39], which assumes that the deformed wheel or leg retains a residual radius. Secondly, the normal stress equation is based on the assumption that the contact surface between the wheel and the soil can be modelled as a flat plate. This assumption loses accuracy for smaller wheels, or in this case, legs. A study by Meirion-Griffith and Spenko [40] developed a normal stress equation incorporating the influence of wheel diameter. However, this model is currently based on a limited set of experimental results, which should be improved and extended for applications involving lunar regolith in future work. Thirdly, the proposed deformation resistance equation is typically employed to model pneumatic tire deformation. Although the analytical model contains the same parameter assumptions as Ishigami's study [11], it is recommended for future work to obtain another deformation resistance equation that is more suitable for the design. Lastly, the multi-pass effect can be incorporated, taking into account the changes in tractive performance due to the pre-compression of lunar soil by a preceding leg.

To ensure that a future design is not at risk of contact surface wear, a constraint must be implemented based on the properties of the lunar soil and the mission duration. However, this is complicated by the uncertainty of encountered obstacles and their unknown effect on wear. Furthermore, the definition of the climbing height could be improved. The current definition expects that if the gripping point makes contact with an obstacle, the Lunar Zebro will be able to climb over it, whereas in reality, factors such as the shape and texture of obstacles, the gait, the leg orientation with respect to the obstacle and the combination of tractive force and slippage of the legs play significant roles. Other constraint definitions that could be improved are those of torque transmission and end of contact surface radius. In this study, it is assumed that these constraints limit walking, whereas they could instead limit climbing along a sideways gradient, as the legs on one side of the Lunar Zebro will experience larger normal forces than when walking. However, these constraints are not as critical as a stress constraint, given that it is not necessarily the case that the torque cannot be transmitted or the next step cannot be set if these constraints are slightly violated, due to the limiting values of the constraints being very strict.

11

Conclusion

This paper presents an effort to design a compliant leg module to enhance the tractive performance of the Lunar Zebro on lunar terrain. To achieve this research goal, different sub-goals were identified and reached, each resulting in new insights.

Firstly, a conceptual compliant leg module for the Lunar Zebro was developed. Given the limitations imposed by the exclusive use of aluminium 7075-T6, the minimal mass of the Lunar Zebro, and its associated low gravitational force on the Moon, a design that deflects purely under the influence of gravity was found to require unfeasibly small flexure thicknesses. Consequently, a flexure design is employed that deflects under both gravitational and traction forces.

Secondly, a model was created to calculate the tractive performance of the leg concept based on terramechanics and compliance theory. The model directly combines the compliant behaviour of the leg concept with the mechanics of the interaction between lunar soil and the leg to calculate the tractive performance. It was observed that accurately creating an analytical model of the compliant behaviour of the flexure was challenging due to the non-linear contact load on granular soil, leading to an approximation of compliance behaviour by applying a point load and assuming linear deflections. The model is capable of estimating tractive performance for different materials, dimensions and surfaces.

Thirdly, an optimisation process was conducted to identify the design variables that yield optimal tractive performance for the created compliant leg module, while being limited by constraints. The optimisation process yielded sets of design variables that result in an optimal drawbar pull of 1.81 N for the middle leg and 1.17 N for the outer leg, marking respective improvements of 116% and 206% over the original rigid legs. The legs experience significantly reduced sinkage and demonstrate an improved capability to convert the torque input into tractive output, thereby enhancing the energy efficiency of the Lunar Zebro. It was determined that constraints related to the maximum stress while climbing along a sideways gradient and the torque transmission were critical for both the middle and outer legs.

An analysis aimed at the sharpness of the feasible region near the optima revealed an alternative set of design variables for the outer leg that offers tractive performance similar to the optimum while improving constraint performance. Additionally, a performance analysis was conducted to create a thermal-resilient design capable of operating at temperatures up to 100°C, resulting in sets of design variables with a drawbar pull of 1.77 N for the middle leg and 1.15 N for the outer leg at the standard operating temperature of 20°C. Furthermore, the stress in the flexure is significantly reduced compared to the leg optimised at the standard operating temperature.

Fourthly, the individual influence of each compliant variable on the tractive performance was investigated. The sensitivity of the design variables for the middle leg was observed to be similar, indicating equal influence on tractive performance. However, the design variables for the outer leg exhibited greater and more distinct sensitivities, demonstrating significant changes when the design variables are varied, with the curved flexure thickness exerting greater influence on tractive performance compared to other variables. In the optimal design variable set, the curved flexure is thin and any increase in thickness results in a notable decrease in tractive performance. As the curved flexure makes contact with the soil, its minimal thickness raises concerns regarding contact surface wear, increasing the risk of failure and limiting potential mission duration.

Ultimately, an innovative compliant Lunar Zebro leg with enhanced tractive performance on the lunar terrain is presented. The improvement in performance at the determined optima is significant. Although concerns are raised about contact surface wear at the optima and the reduction in tractive performance that results from an increase in curved flexure thickness, the introduction of a minimal amount of compliance to the leg, while staying in the feasible region of the design variables, enhances its tractive performance compared to the original rigid design, highlighting the concept's potential. Experiments will ascertain whether the design's performance aligns with expectations and if concerns regarding contact surface wear are warranted. The outcome will inform a strategy for future work, potentially involving alternative material choices.

Abbreviations

FOS_{ULT} Ultimate factor of safety in aircraft and spacecraft.

CFD Central Finite Difference.

CoM Centre of Mass.

CoR Centre of Rotation.

FACT Freedom and Constraint Topology.

FBD Free Body Diagram.

FEA Finite Element Analysis.

FFD Forward Finite Difference.

IR Infeasible Region.

PRBM Pseudo-Rigid Body Modelling.

SQP Sequential Quadratic Programming.

Nomenclature

α	Load application angle	$\sigma_{s,vm}$	Straight flexure von Mises stress
β	Leg flexure angle	$\sigma_{s,walk}$	Straight flexure stress while walking
β_{slip}	Slip angle	τ	Longitudinal soil shear stress
Δx_i	Perturbation size	τ_z	Lateral soil shear stress
δ_i	Deflection of loading point in i-direction	$\tau_{c,ij}$	Curved flexure shear stress in i,j-surface
δ_t	Vertical deflection	$\tau_{s,ij}$	Straight flexure shear stress in i,j-surface
$\delta_{B,i}$	Deflection of curved flexure at point B in the i-direction	θ	Leg angle
$\delta_{C,i}$	Deflection of straight flexure at point C in the i-direction	θ	Tangential coordinate
η	Tractive efficiency	θ_f	Soil entry angle
γ	Sideways gradient angle	θ_m	Angle of the maximum normal stress
$\hat{S}_{x_i,CFD}$	Normalised sensitivity CFD	θ_r	Soil exit angle
$\hat{S}_{x_i,FFD}$	Normalised sensitivity FFD	θ_t	Soil flattening angle
κ	Longitudinal shear deformation modulus	θ_{f0}	Initial soil entry angle
κ_z	Lateral shear deformation modulus	A_c	Curved flexure surface area
λ	Terrain reboundness due to soil elasticity	A_s	Straight flexure surface area
\mathbf{X}	Design variable vector	b_{LZ}	Width between outer legs and CoM
\mathbf{X}_0	Initial point	c	Soil cohesion
$\mathbf{X}_{m,100^\circ C}$	Optimal point middle leg at 100°C	c_1	Wheel soil interaction coefficient
$\mathbf{X}_{m,opt}$	Optimal point middle leg	c_2	Wheel soil interaction coefficient
$\mathbf{X}_{o,100^\circ C}$	Optimal point outer leg at 100°C	c_i	Distance from neutral axis i
$\mathbf{X}_{o,new}$	New point outer leg	c_j	Constraints
$\mathbf{X}_{o,opt}$	Optimal point outer leg	DP	Drawbar pull
μ	Shear constant	E	Young's modulus
ω	Angular velocity	e	Eccentricity
\bar{R}	Distance between the centre of curvature and the centroid of the cross-section	F	Vertical ground reaction force
ϕ	Coulombian internal friction angle	f	Objective
ϕ_i	Angular displacement of loading point in i-direction	F_i	Force at deflection point in i-direction
$\phi_{B,i}$	Angular displacement of curved flexure at point B in the i-direction	F_m	Total Lunar Zebro gravitational force
$\phi_{C,i}$	Angular displacement of straight flexure at point C in the i-direction	$F_{B,i}$	Force at point B in i-direction
σ	Soil normal stress	$F_{C,i}$	Force at point C in i-direction
σ_y	Tensile yield strength	$F_{c,i}$	Force on leg in i-direction
$\sigma_{c,i}$	Curved flexure normal stress in i-direction	$F_{m,i}$	Total Lunar Zebro gravitational force in i-direction
$\sigma_{c,side}$	Curved flexure stress while climbing along a sideways gradient	G	Shear modulus
$\sigma_{c,skid}$	Curved flexure stress while skid steering	g	Gravitational acceleration
$\sigma_{c,vm}$	Curved flexure von Mises stress	H	Soil thrust
$\sigma_{c,walk}$	Curved flexure stress while walking	h	Deformable section height
σ_{max}	Maximum von Mises stress	$I_{c,i}$	Curved flexure moment of inertia about the i-axis
$\sigma_{s,i}$	Straight flexure normal stress in i-direction	$I_{s,i}$	Straight flexure moment of inertia about the i-axis
$\sigma_{s,side}$	Straight flexure stress while climbing along a sideways gradient	j	Longitudinal shear displacement
$\sigma_{s,skid}$	Straight flexure stress while skid steering	J_c	Curved flexure polar moment of inertia
		J_s	Straight flexure polar moment of inertia
		j_z	Lateral shear displacement
		k_ϕ	Frictional soil deformation modulus
		k_c	Cohesive soil deformation modulus
		k_e	Parameter related to the wheel/leg construction

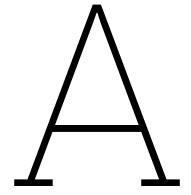
L	Straight flexure length	$S_{x_i,FFD}$	Sensitivity FFD
l	Arc length	SF	Safety factor
l_t	Flat contact section length	T	Resistance torque
l_{x_i}	Lower bound of design variable x_i	T	Temperature
M	Total bending moment	T	Torsion moment
m	Lunar Zebro mass	t_c	Curved flexure thickness
M_i	Moment in flexure around i-direction	t_s	Straight flexure thickness
$M_{B,i}$	Moment at point B around i-axis	U	Strain energy
$M_{C,i}$	Moment at point C around i-axis	u_{x_i}	Upper bound of design variable x_i
N	Axial load	V	Shear load
N	Leg load factor	v_t	Theoretical velocity
n	Exponent of soil deformation	v_x	Forward velocity
P_w	Average ground pressure flattened surface	v_z	Lateral velocity
P_{cr}	Critical ground pressure	W	Gravitational force on axle
R	Leg radius	w	Leg width
r	Radial coordinate	x	Longitudinal coordinate
R^*	Distance between the centre of curvature and the neutral axis	x_i	Design variable
R_d	Deformation resistance	$x_{i,opt}$	Optimal design variable value
R_t	Total external resistance force	y	Vertical coordinate
R_z	Lateral resistance force	y_c	Climbing height
R_{eff}	Effective remaining radius	y_g	Distance between gripping point and axle
$R_{z,c}$	Lateral compaction resistance force	y_{com}	Height of CoM
s	Slip ratio	y_{min}	Minimal climbing height
$S_{x_i,CFD}$	Sensitivity CFD	z	Lateral coordinate
		z	Leg sinkage
		z_0	Static leg sinkage

Bibliography

- [1] TU Delft. *Lunar Zebro Project*. <https://zebro.tudelft.nl/>. Accessed: 2025-05-09. 2025.
- [2] Uluc Saranli, Martin Buehler, and Daniel E Koditschek. "RHex: A simple and highly mobile hexapod robot". In: *The International Journal of Robotics Research* 20.7 (2001), pp. 616–631.
- [3] Piotr Burzyński et al. "Kinematic Analysis and Application to Control Logic Development for RHex Robot Locomotion". In: *Sensors* 24.5 (2024), p. 1636.
- [4] Lunar Zebro Team. *Moon Mission*. Accessed: 2025-05-16. 2025. URL: https://zebro.tudelft.nl/?page_id=679.
- [5] Lunar Zebro. *Lunar Zebro while testing*. 2022. URL: <https://zebro.space/science/> (visited on 09/05/2024).
- [6] Elke Solot. "Improving the Traction of a Legged Rover: A Biomimetic Approach". MA thesis. Delft University of Technology, 2022. URL: <https://resolver.tudelft.nl/uuid:3ded2b01-eba4-4ad2-936c-c610d7cbd2b2>.
- [7] J. van Rijn and J. F. L. Goosen. "A system level performance analysis method for the design of a C-shape hexapod leg operating on compactive terrain". In: *MDPI* (2022).
- [8] J-P. Williams et al. "The global surface temperatures of the Moon as measured by the Diviner Lunar Radiometer Experiment". In: *Icarus* 283 (2017), pp. 300–325.
- [9] Mieczyslaw Gregory Bekker. *Theory of land locomotion: the mechanics of vehicle mobility*. University of Michigan press Ann Arbor, MI, 1956.
- [10] Christian Grimm. "Concept development and design of a flexible metallic wheel with an adaptive mechanism for soft planetary soils". PhD thesis. Luleå University of Technology, 2011.
- [11] Genya Ishigami et al. "Modeling of flexible and rigid wheels for exploration rover on rough terrain". In: *the 28th International Symposium on Space Technology and Science, Okinawa, Japan, 5-12 June*. 2011.
- [12] Stan van Egmond. "Comparing Design Synthesis Methods". MA thesis. Delft University of Technology, 2023.
- [13] Paul Breedveld, Just L. Herder, and Tetsuo Tomiyama. "Teaching creativity in mechanical design". In: *4th World Conference on Design Research (IASDR2011)*. 2011, pp. 1–10.
- [14] John J. Zipay, Clarence T. Modlin, and Curtis E. Larsen. "The ultimate factor of safety for aircraft and spacecraft-its history, applications and misconceptions". In: *57th AIAA/ASCE/AHS/ASC Structures, Structural Dynamics, and Materials Conference*. 2016, p. 1715.
- [15] Philip E. Gill, Walter Murray, and Michael A. Saunders. "SNOPT: An SQP algorithm for large-scale constrained optimization". In: *SIAM review* 47.1 (2005), pp. 99–131.
- [16] Nicholas I. M. Gould and Philippe L. Toint. "SQP methods for large-scale nonlinear programming". In: *IFIP Conference on System Modeling and Optimization*. Springer. 1999, pp. 149–178.
- [17] MathWorks. *Constrained Nonlinear Optimization Algorithms*. Accessed: 2025-04-15. 2025. URL: <https://nl.mathworks.com/help/optim/ug/constrained-nonlinear-optimization-algorithms.html>.
- [18] Shih-Ping Han. "A globally convergent method for nonlinear programming". In: *Journal of optimization theory and applications* 22.3 (1977), pp. 297–309.
- [19] Michael J. D. Powell. "A fast algorithm for nonlinearly constrained optimization calculations". In: *Numerical Analysis: Proceedings of the Biennial Conference Held at Dundee, June 28–July 1, 1977*. Springer. 2006, pp. 144–157.

- [20] Jo Yung Wong and A. R. Reece. "Prediction of rigid wheel performance based on the analysis of soil-wheel stresses part I. Performance of driven rigid wheels". In: *Journal of Terramechanics* 4.1 (1967), pp. 81–98.
- [21] Jo Yung Wong. *Theory of Ground Vehicles*. 3rd ed. New York: John Wiley & Sons, 2001.
- [22] Shinichiro Narita et al. "Terramechanics evaluation of low-pressure wheel on deformable terrain". In: *2011 IEEE International Conference on Robotics and Automation*. IEEE. 2011, pp. 1–4.
- [23] Jianzhong Zhu et al. "Modeling of flexible metal wheel for pressurized lunar rover and traction performance prediction". In: *Journal of Field Robotics* 40.8 (2023), pp. 2030–2041.
- [24] M. G. Bekker and E. V. SEMONIN. "Motion resistance of pneumatic tyres". In: *Journal of Automotive Engineering* 6.2 (1975).
- [25] Z. Janosi and B. Hanamoto. "The analytical determination of drawbar pull as a function of slip for tracked vehicles in deformable soils". In: *International Society for Terrain-Vehicle Systems, 1st Int. Conf.* Vol. 707. 1961.
- [26] A. Petritsenko and R. Sell. "Wheel motion Resistance and soil thrust traction of mobile robot". In: *8th International DAAAM Baltic Conference, Industrial Engineering*. 2012, pp. 19–21.
- [27] Kevin C. Galloway, Jonathan E. Clark, and Daniel E. Koditschek. "Design of a multi-directional variable stiffness leg for dynamic running". In: *ASME International Mechanical Engineering Congress and Exposition*. Vol. 43041. 2007, pp. 73–80.
- [28] Craig Lusk. "Using Pseudo-Rigid Body Models". In: *Handbook of Compliant Mechanisms* (2013), pp. 55–76.
- [29] Hai-Jun Su. "A pseudorigid-body 3R model for determining large deflection of cantilever beams subject to tip loads". In: *Journal of Mechanisms and Robotics* (2009).
- [30] Guimin Chen, Botao Xiong, and Xinbo Huang. "Finding the optimal characteristic parameters for 3R pseudo-rigid-body model using an improved particle swarm optimizer". In: *Precision Engineering* 35.3 (2011), pp. 505–511.
- [31] Venkatasubramanian Kalpathy Venkiteswaran and Hai-Jun Su. "A versatile 3R pseudo-rigid-body model for initially curved and straight compliant beams of uniform cross section". In: *Journal of Mechanical Design* 140.9 (2018), p. 092305.
- [32] Yasemin O. Aydın et al. "Modeling the compliance of a variable stiffness C-shaped leg using Castigliano's theorem". In: *International Design Engineering Technical Conferences and Computers and Information in Engineering Conference*. Vol. 44106. 2010, pp. 705–713.
- [33] John W. Pepi. *Opto-Structural Analysis*. SPIE Press, 2018, pp. 1–29. ISBN: 9781510619340. URL: <https://www.spiedigitallibrary.org/ebooks/PM/Opto-structural-Analysis/eISBN-9781510619340/10.1117/3.2317988>.
- [34] Genya Ishigami et al. "Terramechanics-based model for steering maneuver of planetary exploration rovers on loose soil". In: *Journal of Field robotics* 24.3 (2007), pp. 233–250.
- [35] MathWorks. *fmincon - Find minimum of constrained nonlinear multivariable function*. Accessed: 2025-06-20. 2024. URL: <https://nl.mathworks.com/help/optim/ug/fmincon.html>.
- [36] Pablo A. Muñoz-Rojas, Jun S. O. Fonseca, and Guillermo J. Creus. "An Efficient Finite Difference Sensitivity Analysis Method Allowing Remeshing In Large Deformation Problems." In: *Mecánica Computacional* 1 (2002), pp. 2712–2731.
- [37] J. Sessler and V. Weiss. *Materials data handbook, aluminum alloy 7075*. Tech. rep. NASA, 1966.
- [38] NASA Glenn Research Center. *Superelastic Tire (LEW-TOPS-99)*. <https://technology.nasa.gov/patent/LEW-TOPS-99>. Case Nos. LEW-18729-1, LEW-19444-1, LEW-19444-2. 2021.
- [39] Ingobert C. Schmid. "Interaction of vehicle and terrain results from 10 years research at IKK". In: *Journal of terramechanics* 32.1 (1995), pp. 3–26.
- [40] Gareth Meirion-Griffith and Matthew Spenko. "A modified pressure–sinkage model for small, rigid wheels on deformable terrains". In: *Journal of Terramechanics* 48.2 (2011), pp. 149–155.
- [41] Nildeep Patel, Richard Slade, and Jim Clemmet. "The ExoMars rover locomotion subsystem". In: *Journal of Terramechanics* 47.4 (2010), pp. 227–242.

- [42] Ravivat Rugsaj and Chakrit Suvanjumrat. "Revolutionizing tire engineering: Finite element analysis and design of an X-shaped spoke structure for non-pneumatic military tires". In: *Alexandria Engineering Journal* 99 (2024), pp. 303–318.
- [43] Tachadol Suthisomboon, Stephane Bonardi, and Genya Ishigami. "Design and development of jamming-based stiffness-adjustable wheel on soft terrain". In: *Journal of Terramechanics* 117 (2025), p. 101014.
- [44] Vivake Asnani, Damon Delap, and Colin Creager. "The development of wheels for the Lunar Roving Vehicle". In: *Journal of Terramechanics* 46.3 (2009), pp. 89–103.
- [45] Valerie L. Wiesner et al. *Protective Coatings for Lunar Dust Tolerance*. NASA Technical Memorandum NASA/TM–20230003195. NASA Langley Research Center and National Institute of Aerospace, 2023. URL: <https://ntrs.nasa.gov/citations/20230003195>.
- [46] L. Adams and D. Aliya. "Properties and selection: Nonferrous alloys and special-purpose materials". In: *ASM Metals Handbook ASM International* 210 (1990), pp. 1770–1782.
- [47] Zu Qun Li and Lee K. Bingham. *Terramechanics for LTV Modeling and Simulation*. NASA White Paper Document ID 20220010732. NASA Johnson Space Center, 2022. URL: <https://ntrs.nasa.gov/citations/20220010732>.
- [48] Grant H. Heiken, David T. Vaniman, and Bevan M. French. *Lunar sourcebook: A user's guide to the Moon*. 1259. Cup Archive, 1991.
- [49] Arturo Rankin et al. "Assessing Mars Curiosity rover wheel damage". In: *2022 IEEE Aerospace Conference (AERO)*. IEEE. 2022, pp. 1–19.
- [50] *Premature Wear of the MSL Wheels*. NASA Jet Propulsion Laboratory. Sept. 26, 2017. URL: <https://llis.nasa.gov/lesson/22401> (visited on 04/06/2025).
- [51] Gábor Kalácska et al. "The Abrasive Effect of Moon and Mars Regolith Simulants on Stainless Steel Rotating Shaft and Polytetrafluoroethylene Sealing Material Pairs". In: *Materials* 17.17 (2024), p. 4240.



Design process supplementary

A.1. Function Tree

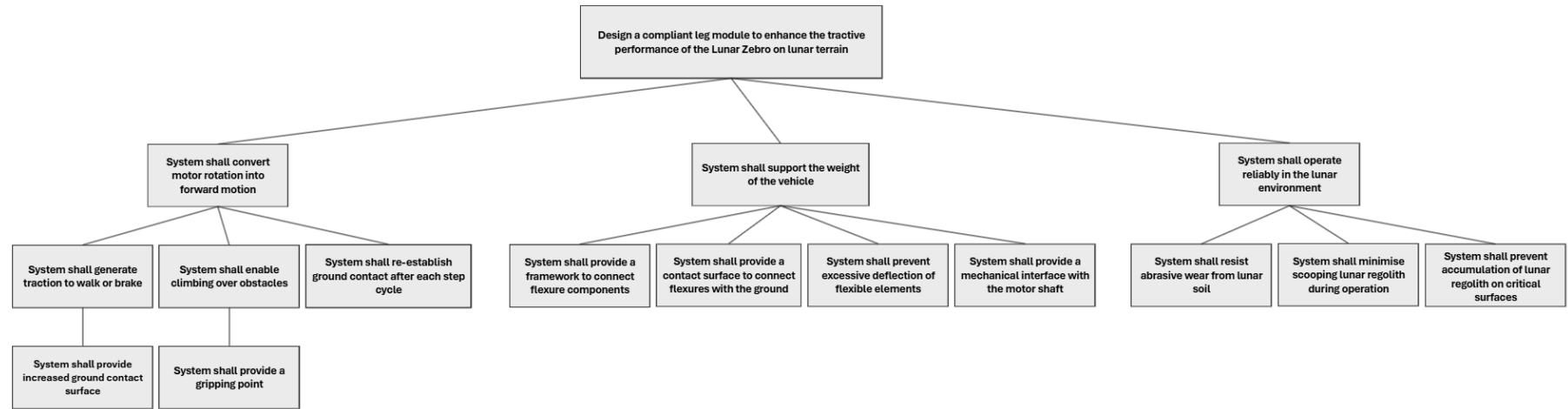

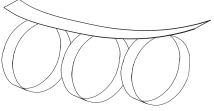
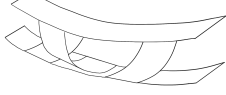

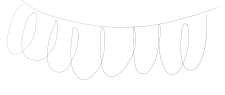
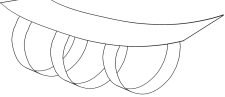

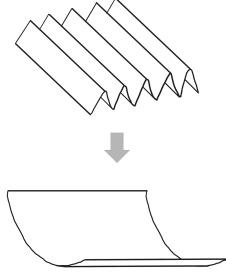

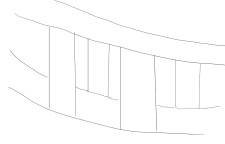
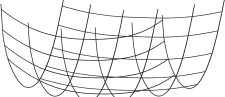

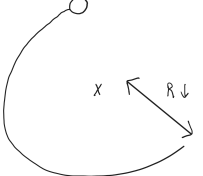
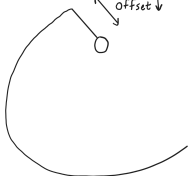
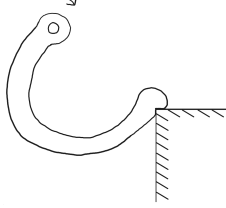


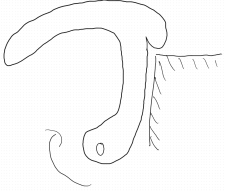
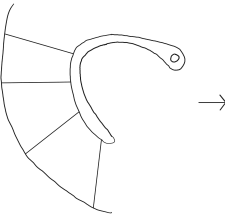
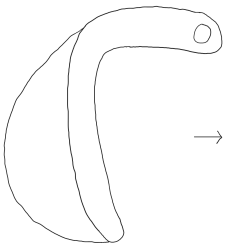
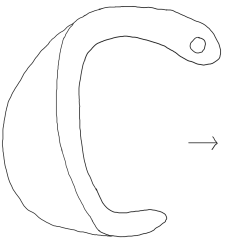
Figure A.1: Function Tree

A.2. Morphological chart

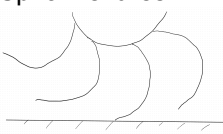

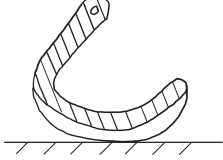
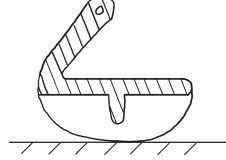
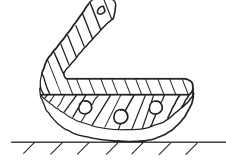
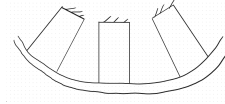
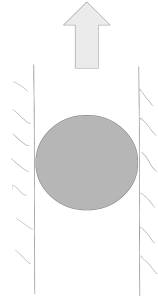
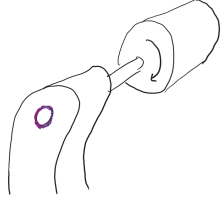
Table A.1: Morphological chart

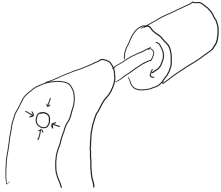
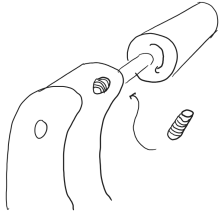
Functional requirement	Strategy	Embodiments				
1. System shall convert motor rotation into forward motion						
System shall provide increased ground contact surface	In-plane deformation	Single ground contact flexure	C-flexure	Cylinder flexure	Double sided curved flexures	Double sided X-flexure
		Flexure band double [41]	Half-circle flexure	Honeycomb	Origami	Springs
		Straight radial flexures	Wire carcass	X-flexure [42]	Compliant linear guide	Double half-circle flexures
		Horizontal flexures	Leaf spring suspension	Single linear guided ground flexure attached to springs	Spiral flexures	

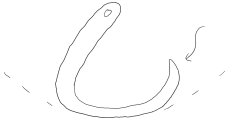
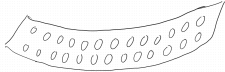


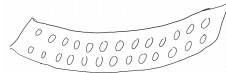
Functional requirement	Strategy	Embodiments				
	Out-of-plane deformation	C-flexures 	Cylinder flexures 	Double sided curved flexures 	Double sided X-flexure 	Flexure band 
		Half-circle flexures 	Honeycomb 	Origami 	Springs 	Straight flexures 
		Wire carcass 	X-flexure 			
System shall provide a gripping point	Leg tip point	Minimise radius [7] 	Minimise CoR offset [7] 	Tip hooking point 		

Functional requirement	Strategy	Embodiments	
	Uncoupled gripping point	Uncoupled hook [7] 	
System shall re-establish ground contact after each step cycle	Tip radial on flexure	Standard flexure tip 	
	Tip radial on framework	Standard framework tip 	Curved framework tip 

Functional requirement	Strategy	Embodiments				
2. System shall support the weight of the vehicle						
System shall provide a framework to connect flexure components	Aluminium frame	Sharp angle	C-shape	Triangle	C-shape with cylinder	G-shape
		Cylinder	Mirrored Z-shape	Double C-shape connection	Half-circle	
System shall provide a contact surface to connect flexures with the ground	Single flexure	Single flexure connected to frame	Single flexure connected to flexures	Cross pattern flexure		
	Non-flexure materials	Blocks directly connected to flexures	Blocks connected to central flexure [43]	Traction pads on central flexure	Plates connected with hinges	




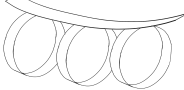

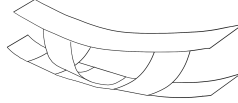
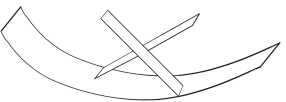
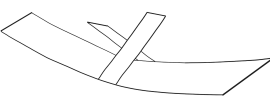



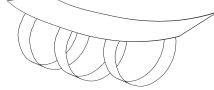
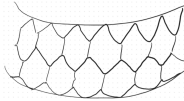
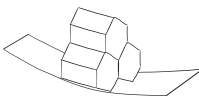
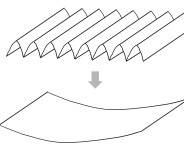
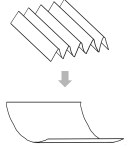
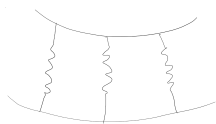


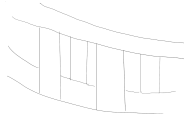



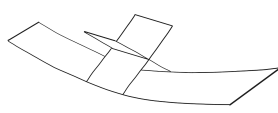
Functional requirement	Strategy	Embodiments				
	No contact surface (Flexure to ground contact)	Spiral flexures 	T flexures 			
System shall prevent excessive deflection of flexible elements	Contact	Structural bump stop 	Outpointing bump stop 	Sheet bump stop (Exomars) [41] 	Stiff inner frame (LRV) [44] 	Linear guide 
	Dimensions	Thin flexures	Combination of thick flexures			
System shall provide a mechanical interface with the motor shaft	Weld	Welded to motor axis 				

Functional requirement	Strategy	Embodiments	
	Clamped	Clamped on motor axis 	
	Set screw	Screwed to motor axis 	

Functional requirement	Strategy	Embodiments			
3. System shall operate reliably in the lunar environment					
System shall resist abrasive wear from lunar soil	Material contact	Flexure contact			
	Material layer	Nylon textile [43]			
	Coating layer	APS Al2O3-TiO2 coating [45]			Cr3C2-NiCr coating [45]
System shall minimise scooping lunar regolith during operation	Minimise sinkage	Increased contact surface			
	Resistant coating layer	APS Al2O3-TiO2 coating [45]			Cr3C2-NiCr coating [45]
	Inward curling tip	Curled end tip [7]			
					
	Perforated structure	Perforated ground contact flexure			
					
System shall prevent accumulation of lunar regolith on critical surfaces	Resistant coating layer	APS Al2O3-TiO2 coating [45]			Cr3C2-NiCr coating [45]
	Resistant shape	Fillet edges			Chamfered edges
					

A.3. ACRREx table

Table A.2: ACRREx matrix with new solutions, new sub-solutions implemented in voids are indicated with *

	In-plane deformation	Out-of-plane deformation
C-flexures		 *
Cylinder flexures		
Double sided curved flexures		 *
Double sided X-flexures	 *	
Flexure bands		 *
Half-circle flexures		 *
Honeycomb		 *
Origami		 *
Springs		 *
Straight flexures		 *
Wire flexures	 *	
X-flexures		 *

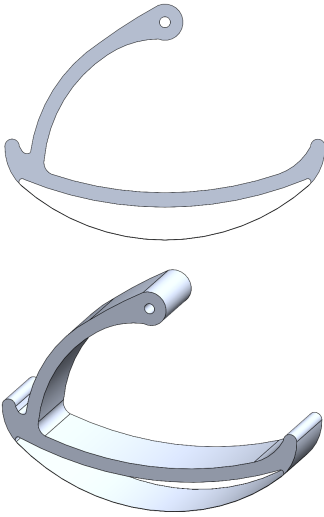
A.4. Concept designs

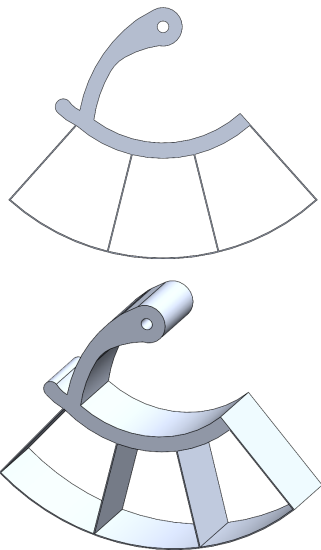
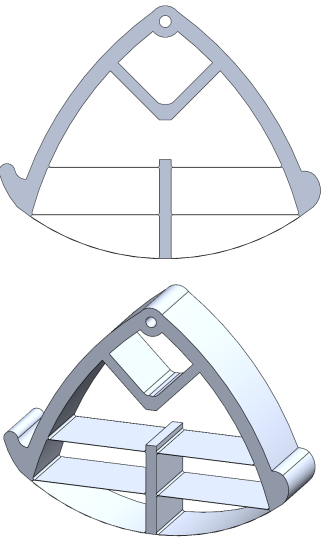
Every concept design consists of a combination of functional requirement embodiments from the morphological chart in Appendix A.2. In Table A.3, an overview is given of the used embodiments per concept, coupled to the functional requirements below:

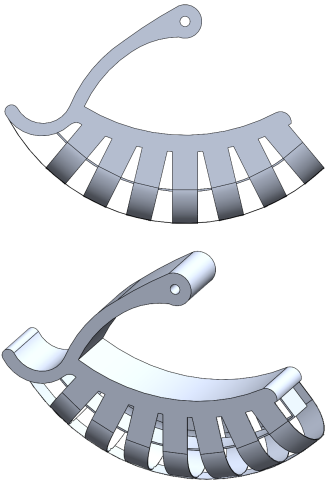
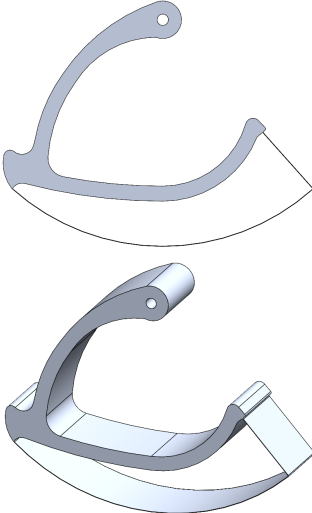
- 1. System shall convert motor rotation into forward motion.
 - (a) System shall provide increased ground contact surface.
 - (b) System shall provide a gripping point.
 - (c) System shall re-establish ground contact after each step cycle.
- 2. System shall support the weight of the vehicle.
 - (a) System shall provide a framework to connect flexure components.
 - (b) System shall provide a contact surface to connect flexures with the ground.
 - (c) System shall prevent excessive deflection of flexible elements.
 - (d) System shall provide a mechanical interface with the motor shaft.
- 3. System shall operate reliably in the lunar environment.
 - (a) System shall resist abrasive wear from lunar soil.
 - (b) System shall minimise scooping lunar regolith during operation.
 - (c) System shall prevent accumulation of lunar regolith on critical surfaces.

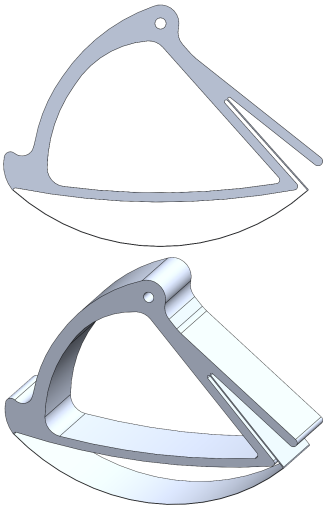
It is worth noting that for certain functional requirements, all concepts use the same embodiment. In some cases, this is due to that embodiment simply being the best applicable, such as the fillet edges used to prevent lunar regolith from accumulating on flexure edges. In other cases, the embodiment choice results from the Lunar Zebro design team. It became clear that the design team preferred to connect the system to the motor axis using a set screw and that the aluminium flexure does not get additional soil contact protection. These preferences are applied to the different concepts.

Table A.3: Concept embodiment usage

Embodiment usage	
Concept 1	
	<ul style="list-style-type: none">1. System shall convert motor rotation into forward motion.<ul style="list-style-type: none">(a) Single ground contact flexure(b) Uncoupled hook(c) Curved framework tip2. System shall support the weight of the vehicle.<ul style="list-style-type: none">(a) C-shape frame(b) Single ground contact flexure connected to frame(c) Structural bump stop(d) Set screw3. System shall operate reliably in the lunar environment.<ul style="list-style-type: none">(a) Aluminium flexure contact(b) Increased contact surface and inward curling tips(c) Fillet edges

Embodiment usage	
Concept 2	
	<ol style="list-style-type: none">1. System shall convert motor rotation into forward motion.<ol style="list-style-type: none">(a) Straight radial flexures(b) Uncoupled hook(c) Standard flexure tip2. System shall support the weight of the vehicle.<ol style="list-style-type: none">(a) C-shape frame(b) Single ground contact flexure connected to flexures(c) Combination of flexures(d) Set screw3. System shall operate reliably in the lunar environment.<ol style="list-style-type: none">(a) Aluminium flexure contact(b) Increased contact surface(c) Fillet edges
Concept 3	
	<ol style="list-style-type: none">1. System shall convert motor rotation into forward motion.<ol style="list-style-type: none">(a) Horizontal flexures(b) Uncoupled hook(c) Standard framework tip2. System shall support the weight of the vehicle.<ol style="list-style-type: none">(a) Half-circle frame(b) Single ground contact flexure connected to frame and flexures(c) Outpointing bump stop(d) Set screw3. System shall operate reliably in the lunar environment.<ol style="list-style-type: none">(a) Aluminium flexure contact(b) Increased contact surface(c) Fillet edges

Embodiment usage	
Concept 4	
	<ol style="list-style-type: none">1. System shall convert motor rotation into forward motion.<ol style="list-style-type: none">(a) Half-circle flexures (Out-of-plane deformation)(b) Uncoupled hook(c) Standard flexure tip2. System shall support the weight of the vehicle.<ol style="list-style-type: none">(a) C-shape frame(b) Single ground contact flexure connected to frame and flexures(c) Stiff inner frame(d) Set screw3. System shall operate reliably in the lunar environment.<ol style="list-style-type: none">(a) Aluminium flexure contact(b) Increased contact surface and perforated ground contact flexure(c) Fillet edges and perforated ground contact flexure
Final concept	
	<ol style="list-style-type: none">1. System shall convert motor rotation into forward motion.<ol style="list-style-type: none">(a) Straight radial flexure(b) Uncoupled hook(c) Standard flexure tip2. System shall support the weight of the vehicle.<ol style="list-style-type: none">(a) C-shape frame(b) Single ground contact flexure connected to frame and flexure(c) Structural bump stop(d) Set screw3. System shall operate reliably in the lunar environment.<ol style="list-style-type: none">(a) Aluminium flexure contact(b) Increased contact surface(c) Fillet edges

Embodiment usage	
Final design	
	<ol style="list-style-type: none"> System shall convert motor rotation into forward motion. <ol style="list-style-type: none"> Straight radial flexure Uncoupled hook Standard flexure tip System shall support the weight of the vehicle. <ol style="list-style-type: none"> Triangular-shape frame Single ground contact flexure connected to frame and flexure Structural bump stop Set screw System shall operate reliably in the lunar environment. <ol style="list-style-type: none"> Aluminium flexure contact Increased contact surface Fillet edges

A.5. Weight factor reasoning

Table A.4: Weight factor reasoning of criterion subject

Criterion subject	Weight	Reasoning
Traction transmissibility	30	The leg is incapable of moving the Lunar Zebro without traction transmission.
Deformability	20	The research focus is on improving the tractive performance of the leg module using deformation, making it necessary that the design is capable of doing so.
Durability	20	The leg module cannot be repaired on the Moon and thus must be durable.
Weight	15	Low weight decreases the cost needed to get the Lunar Zebro to the Moon, but the leg module weight is not expected to drastically increase relative to the old solid design.
Climbing ability	10	The research focus is on improving the tractive performance of the leg module, but the leg module needs to be able to climb a certain height to ensure functionality on the Moon surface.
Manufacturability	5	The time consumption of custom-made production is a minor inconvenience, as a limited number of legs are needed.
Total	100	

A.6. Concept selection evaluation

Table A.5: Concept 1 evaluation chart, main subject indicated with *

Concept 1			
Subject	Concept selection criteria	Score	Reasoning
Traction transmissibility *	Capability to transmit moment from the motor axis to leg contact.	++	Concept 1 is expected to be capable of transmitting the moment from the motor axis to leg contact, due to the small distance between the stiff frame and the ground contact flexure.
	Capability to transmit moment at leg contact to forward movement.	+	Concept 1 is expected to be decently capable of transmitting the force at leg contact to forward movement, due to the full contact surface. The contact surface is enlarged by radial deformation, but this deformation is expected to be small.
Deformability	Capability to deform in a range of 3-12 mm.	o	Concept 1 is expected to perform mediocre at vertically deforming in a range of 3-12 mm, due to the limited gravitational force available and the fixed connections of the ground contact flexure, leading to an increase in stiffness.
	Capability to do a smooth deformation motion and transition.	-	Concept 1 is expected to have a wobbling, non-smooth motion, due to the fixed connections not giving space for deformation. Because of the high stiffness at the end of the contact surface, the transition to the next leg is expected to succeed.
Durability	Capability to counter over-deflection.	+	Concept 1 is expected to be decently capable of countering vertical over-deflection, due to the bump stop created by the frame. Horizontal over-deflection is limited due to the ends of the flexure being connected to the frame. This does mean that the stress level of this flexure is expected to be higher.
	Capability to have low stress levels.	-	
	Capability to withstand forces and moments along the lateral direction.	+	Concept 1 is expected to be decently capable of withstanding forces and moments along the lateral direction, due to both ends being connected to the frame and the small distance between these connections and the ground contact flexure.
Weight	Capability to be low weight.	+	Concept 1 is expected to be of a decently low weight, due to the normal-sized frame and the single flexure.
Climbing ability	Capability to climb by having a high gripping point.	++	Concept 1 is expected to perform well at climbing due to the uncoupled gripping point at radius distance.
Manufacturability	Capability to manufacture with minimum parts.	++	Concept 1 is expected to be capable of being manufactured with minimal parts in a sufficient time frame, due to its single flexure design.
	Capability to manufacture in a sufficient time frame.	++	

Table A.6: Concept 2 evaluation chart, main subject indicated with *

Concept 2			
Subject	Concept selection criteria	Score	Reasoning
Traction transmissibility	Capability to transmit moment from the motor axis to leg contact.	-	Concept 2 is not expected to be capable of transmitting the moment from the motor axis to leg contact, due to the large distance between the stiff frame and the ground contact flexure. To get the desired traction transmission, the flexure needs to have an increase in stiffness, leading to a performance decrease of other concept selection criteria, such as the deformability and weight.
	Capability to transmit moment at leg contact to forward movement.	+	Concept 2 is expected to be capable of transmitting the force at leg contact to forward movement, due to the full contact surface. The contact surface is enlarged by radial and longitudinal deformation. This deformation is expected to be large.
Deformability *	Capability to deform in a range of 3-12 mm.	++	Concept 2 is expected to be capable of vertically deforming in a range of 3-12 mm, due to the large flexures and the ground contact flexure being capable of deflecting horizontally at the end connections. The traction force contributes to the deflection.
	Capability to do a smooth deformation motion and transition.	+	Concept 2 is expected to be decently capable of creating a smooth deformation motion, with the ground flexure having enough room to deflect. However, the high radial stiffness of the middle flexures may take away some of the smoothness. Because of the radial flexure at the end of the contact surface, the transition to the next leg is expected to succeed.
Durability	Capability to counter over-deflection.	0	Concept 2 is expected to perform mediocre at countering both vertical and horizontal over-deflection, due to not having a bump stop but instead relying on the stiffness of the multiple flexures.
	Capability to have low stress levels.	++	Concept 2 is expected to have low stress levels due to the length of the flexures.
	Capability to withstand forces and moments along the lateral direction.	0	Concept 2 is expected to perform mediocre at withstanding forces and moments along the lateral direction, due to long flexures with a large distance between the frame and the ground contact flexure. The use of multiple flexures does give an increase in lateral stiffness.
Weight	Capability to be low weight.	++	Concept 2 is expected to be low weight, due to the small frame size and multiple lightweight flexures.
Climbing ability	Capability to climb by having a high gripping point.	0	Concept 2 is expected to perform mediocre at climbing due to the uncoupled gripping point at approximately half radius distance.
Manufacturability	Capability to manufacture with minimum parts.	+	Concept 2 is expected to be decently capable of being manufactured with minimal parts in a sufficient time frame, due to the ease of the flexure connections and multiple flexure parts.
	Capability to manufacture in a sufficient time frame.	+	

Table A.7: Concept 3 evaluation chart, main subject indicated with *

Concept 3			
Subject	Concept selection criteria	Score	Reasoning
Traction transmissibility *	Capability to transmit moment from the motor axis to leg contact.	++	Concept 3 is expected to perform well at transmitting the moment from the motor axis to leg contact, due to the small distance between the stiff frame and the ground contact flexure.
	Capability to transmit moment at leg contact to forward movement.	+	Concept 3 is expected to be decently capable of transmitting the force at leg contact to forward movement, due to the full contact surface. The contact surface is enlarged by radial deformation, but this deformation is expected to be small.
Deformability	Capability to deform in a range of 3-12 mm.	--	Concept 3 is expected to perform badly at vertically deforming in a range of 3-12 mm, due to the limited gravitational force available and the multiple flexures used to counter the deformation in other directions. The flexures are expected to be very thin to be able to get the desired deformation, making the structure vulnerable to wear and difficult to manufacture.
	Capability to do a smooth deformation motion and transition.	--	Concept 3 is not expected to have smooth deformation, due to the ground flexure having three fixed points to the frame. Because of the high stiffness at the end of the contact surface, the transition to the next leg is expected to succeed.
Durability	Capability to counter over-deflection.	++	Concept 3 is expected to perform well at countering both vertical and horizontal over-deflection, due to the bump stop and the FACT-design limiting movements in other directions.
	Capability to have low stress levels.	-	Concept 3 is expected to have decently high stress levels due to the flexures not being able to be as thin as needed to get the desired deformation.
	Capability to withstand forces and moments along the lateral direction.	++	Concept 3 is expected to perform well at withstanding forces and moments along the lateral direction, due to the FACT-design limiting movements in other directions.
Weight	Capability to be low weight.	o	Concept 3 is expected to be of mediocre weight, due to the larger frame and multiple lightweight flexures.
Climbing ability	Capability to climb by having a high gripping point.	++	Concept 3 is expected to perform well at climbing due to the uncoupled gripping point at radius distance.
Manufacturability	Capability to manufacture with minimum parts.	o	Concept 3 is expected to perform mediocre at being capable of manufacturing with minimal parts in a sufficient time frame, due to the multiple very thin flexures needed.
	Capability to manufacture in a sufficient time frame.	o	

Table A.8: Concept 4 evaluation chart, main subject indicated with *

Concept 4			
Subject	Concept selection criteria	Score	Reasoning
Traction transmissibility	Capability to transmit moment from the motor axis to leg contact.	+	Concept 4 is expected to be decently capable of transmitting the moment from the motor axis to leg contact, due to the large amount of flexures used to create a structure that is stiff in the direction of walking.
	Capability to transmit moment at leg contact to forward movement.	+	Concept 4 is expected to be decently capable of transmitting the force at leg contact to forward movement, due to the contact surface being enlarged by both out-of-plane deformation. Though the contact surface is made smaller by the perforated ground contact flexure.
Deformability *	Capability to deform in a range of 3-12 mm.	+	Concept 4 is expected to perform decently at vertically deforming in a range of 3-12 mm, due to the flexures being able to deflect in radial and lateral directions. A consideration needs to be made of the amount of flexures required to create traction in the direction of walking, while also leaving enough room for vertical deformation. However, a problem could occur when the flexures deform too much in the lateral direction, as they would go outside the design volume, potentially coming in contact with other legs, depending on the gait used.
	Capability to do a smooth deformation motion and transition.	+	Concept 4 is expected to have a smooth deformation motion, due to the ground flexure being connected to other flexures, while the transition to the next leg is expected to succeed due to the smaller cylinder flexures with higher stiffness at the end of the contact surface.
Durability	Capability to counter over-deflection.	+	Concept 4 is expected to perform decently at countering both vertical and horizontal over-deflection, due to the stiff inner frame.
	Capability to have low stress levels.	o	Concept 4 is expected to have mediocre stress levels due to the length of the flexures.
	Capability to withstand forces and moments along the lateral direction.	o	Concept 4 is expected to perform mediocre at withstanding forces and moments along the lateral direction, due to the half-circle flexures having a low stiffness in the lateral direction.
Weight	Capability to be low weight.	-	Concept 4 is expected to be of decently high weight, due to the larger frame and the large amount of flexures.
Climbing ability	Capability to climb by having a high gripping point.	++	Concept 4 is expected to perform well at climbing due to the uncoupled gripping point at radius distance.
Manufacturability	Capability to manufacture with minimum parts.	-	Concept 4 is expected to be difficult to manufacture with minimum parts in a sufficient time frame, due to the large amount of flexures needed and the difficulty of the connections.
	Capability to manufacture in a sufficient time frame.	-	

B

Terramechanics supplementary

B.1. Solving procedure flow charts

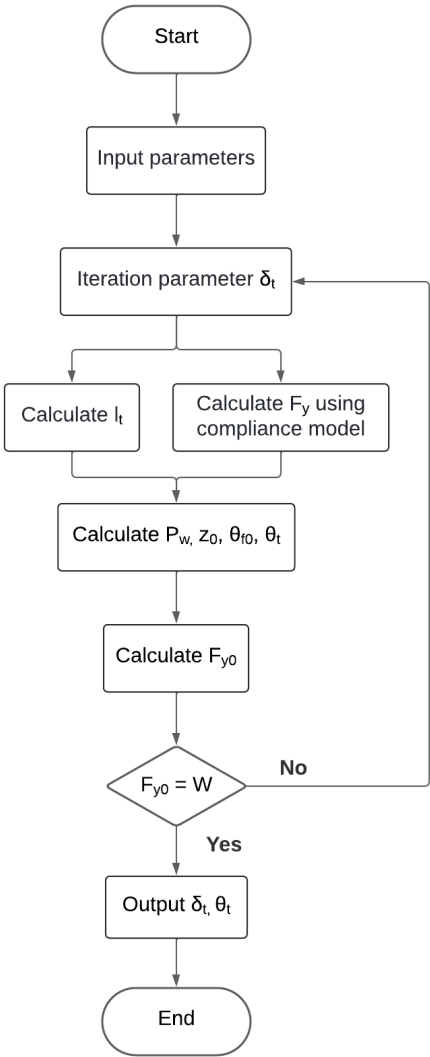


Figure B.1: Solving procedure static model

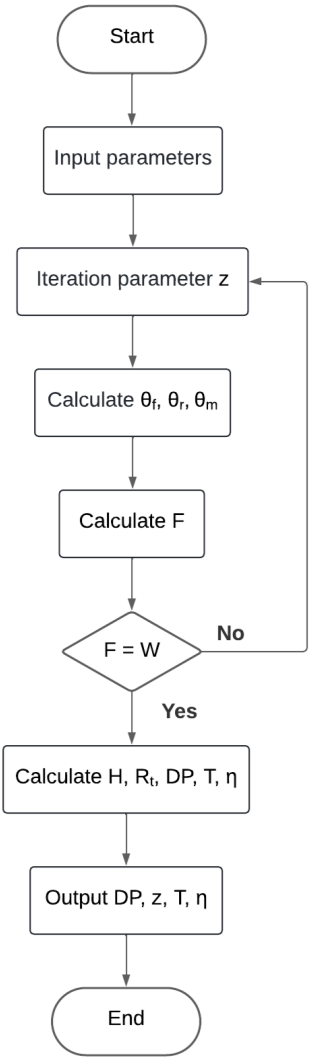


Figure B.2: Solving procedure quasi-static model

C

System analysis supplementary

C.1. Model parameters

Table C.1: Model parameters

Symbol	Description	Value	Unit
Material properties			
E	Young's modulus	71.7 ¹	GPa
G	Shear modulus	26.9 ¹	GPa
SF	Stress safety factor	1.5	–
Terramechanics			
κ	Shear deformation modulus	0.018 ²	m
λ	Terrain reboundness	0.1 ³	–
ϕ	Internal friction angle	42 ⁴	°
c	Soil cohesion coefficient	0.52 ⁴	kPa
g	Gravitational acceleration	1.62 ⁴	m/s ²
h	Deformable section height of leg	0.020	m
k_c	Cohesion modulus of soil deformation	1.4 ²	kPa/m ¹⁻ⁿ
k_e	Leg construction parameter	7 ³	–
k_ϕ	Friction modulus of soil deformation	820 ²	kPa/m ⁿ
m	Lunar rover mass	2.5	kg
n	Exponent of soil deformation	1	–
N	Leg load factor (Middle / Outer leg)	2 / 4	–
s	Slip ratio	1	–
Force-deflection relationship			
α	Load application angle	41.8	°
β	Leg flexure angle	83.6	°
R	Leg radius	0.060	m
w	Leg width	0.020	m
Skid steering constraint			
μ	Shear constant (rectangle)	1.2	–
Sideways gradient constraint			
γ	Soil gradient angle	15	°
b_{LZ}	Width between outer legs and CoM	0.125	m
y_{com}	Height of CoM	0.06	m
Climbing height constraint			
y_g	Height between gripping point and axle	0.034	m

¹ At 20°C, data from [46]

² Data from [47]

³ Data from [11]

⁴ Data from [48]

C.2. Temperature range performance analysis

The optima of the standard (20°C-optimised) and the thermal-resilient (100°C-optimised) designs are presented with their objective and constraint performance. The values are presented in high significant figures as a result of the exact optimum location obtained in the optimisation process. These values are mathematical optima that cannot be translated to reality with such precision due to the assumptions made in the analytical optimisation model and the physical challenges in production. When using slightly altered or rounded values of the optima, the objective and constraint performance results change accordingly.

C.2.1. Middle leg

The point at which the middle leg achieves optimal tractive performance at 20°C is:

$$\mathbf{x}_{m,opt} = \begin{bmatrix} t_c \\ t_s \\ L \end{bmatrix} = \begin{bmatrix} 0.13857 \\ 0.30778 \\ 33.16760 \end{bmatrix} \text{ mm.}$$

The objective and constraint performances for this optimum point at various temperatures are detailed in Table C.2 and Table C.3, respectively.

Table C.2: Objective performance middle leg per temperature

Objective	Value
T = 100°C (Constraints violated)	
Drawbar pull DP	1.8268 N
Thrust H	1.9696 N
Total external resistance R_t	0.1428 N
Sinkage z	1.6010 mm
Vertical deformation δ_t	11.1568 mm
T = 20°C	
Drawbar pull DP	1.8085 N
Thrust H	1.9471 N
Total external resistance R_t	0.1387 N
Sinkage z	1.6351 mm
Vertical deformation δ_t	10.6091 mm
T = -80°C	
Drawbar pull DP	1.7975 N
Thrust H	1.9339 N
Total external resistance R_t	0.1363 N
Sinkage z	1.6557 mm
Vertical deformation δ_t	10.2951 mm

Table C.3: Constraint performance middle leg per temperature

Constraint	Value	Value with safety factor (x1.5)	Limiting value
T = 100°C (Constraints violated)			
c_1	308 MPa	462 MPa	≤ 448 MPa
c_2	314 MPa	471 MPa	≤ 448 MPa
c_3	336 MPa	504 MPa	≤ 448 MPa
c_4	5.27 mm	-	≤ 5.00 mm
c_5	59.0 mm	-	≥ 58.5 mm
c_6	81.7 mm	-	≥ 55.0 mm
T = 20°C			
c_1	307 MPa	461 MPa	≤ 503 MPa
c_2	314 MPa	470 MPa	≤ 503 MPa
c_3	335 MPa	503 MPa	≤ 503 MPa
c_4	5.00 mm	-	≤ 5.00 mm
c_5	59.1 mm	-	≥ 58.5 mm
c_6	82.3 mm	-	≥ 55.0 mm
T = -80°C			
c_1	307 MPa	460 MPa	≤ 545 MPa
c_2	313 MPa	469 MPa	≤ 545 MPa
c_3	335 MPa	502 MPa	≤ 545 MPa
c_4	4.84 mm	-	≤ 5.00 mm
c_5	59.1 mm	-	≥ 58.5 mm
c_6	82.5 mm	-	≥ 55.0 mm

C.2.2. Thermal-resilient middle leg

The point at which the middle leg achieves optimal tractive performance at 100°C is:

$$\mathbf{x}_{m,100^\circ\text{C}} = \begin{bmatrix} t_c \\ t_s \\ L \end{bmatrix} = \begin{bmatrix} 0.14981 \\ 0.38005 \\ 40.88794 \end{bmatrix} \text{ mm.}$$

The objective and constraint performances for this optimum point at various temperatures are detailed in Table C.4 and Table C.5, respectively.

Table C.4: Objective performance thermal-resilient middle leg per temperature

Objective	Value
T = 100°C	
Drawbar pull DP	1.7915 N
Thrust H	1.9265 N
Total external resistance R_t	0.1351 N
Sinkage z	1.6672 mm
Vertical deformation δ_t	10.1254 mm
T = 20°C	
Drawbar pull DP	1.7731 N
Thrust H	1.9045 N
Total external resistance R_t	0.1314 N
Sinkage z	1.7028 mm
Vertical deformation δ_t	9.6260 mm
T = -80°C	
Drawbar pull DP	1.7621 N
Thrust H	1.8915 N
Total external resistance R_t	0.1293 N
Sinkage z	1.7244 mm
Vertical deformation δ_t	9.3401 mm

Table C.5: Constraint performance thermal-resilient middle leg per temperature

Constraint	Value	Value with safety factor (x1.5)	Limiting value
T = 100°C			
c_1	273 MPa	410 MPa	≤ 448 MPa
c_2	280 MPa	419 MPa	≤ 448 MPa
c_3	299 MPa	448 MPa	≤ 448 MPa
c_4	5.00 mm	-	≤ 5.00 mm
c_5	59.1 mm	-	≥ 58.5 mm
c_6	82.7 mm	-	≥ 55.0 mm
T = 20°C			
c_1	273 MPa	409 MPa	≤ 503 MPa
c_2	279 MPa	418 MPa	≤ 503 MPa
c_3	298 MPa	447 MPa	≤ 503 MPa
c_4	4.74 mm	-	≤ 5.00 mm
c_5	59.1 mm	-	≥ 58.5 mm
c_6	83.2 mm	-	≥ 55.0 mm
T = -80°C			
c_1	272 MPa	409 MPa	≤ 503 MPa
c_2	279 MPa	418 MPa	≤ 503 MPa
c_3	298 MPa	447 MPa	≤ 503 MPa
c_4	4.59 mm	-	≤ 5.00 mm
c_5	59.1 mm	-	≥ 58.5 mm
c_6	83.4 mm	-	≥ 55.0 mm

C.2.3. Outer leg

The point at which the outer leg achieves optimal tractive performance at 20°C is:

$$\mathbf{x}_{o,opt} = \begin{bmatrix} t_c \\ t_s \\ L \end{bmatrix} = \begin{bmatrix} 0.10000 \\ 0.15707 \\ 19.84535 \end{bmatrix} \text{ mm.}$$

The objective and constraint performances for this optimum point at various temperatures are detailed in Table C.6 and Table C.7, respectively.

Table C.6: Objective performance outer leg per temperature

Objective	Value
T = 100°C (Constraints violated)	
Drawbar pull DP	1.1908 N
Thrust H	1.2589 N
Total external resistance R_t	0.0682 N
Sinkage z	0.7909 mm
Vertical deformation δ_t	11.6040 mm
T = 20°C	
Drawbar pull DP	1.1735 N
Thrust H	1.2394 N
Total external resistance R_t	0.0659 N
Sinkage z	0.8077 mm
Vertical deformation δ_t	11.0444 mm
T = -80°C	
Drawbar pull DP	1.1633 N
Thrust H	1.2278 N
Total external resistance R_t	0.0645 N
Sinkage z	0.8179 mm
Vertical deformation δ_t	10.7242 mm

Table C.7: Constraint performance outer leg per temperature

Constraint	Value	Value with safety factor (x1.5)	Limiting value
T = 100°C (Constraints violated)			
c_1	310 MPa	465 MPa	≤ 448 MPa
c_2	332 MPa	499 MPa	≤ 448 MPa
c_3	337 MPa	506 MPa	≤ 448 MPa
c_4	5.29 mm	-	≤ 5.00 mm
c_5	59.1 mm	-	≥ 58.5 mm
c_6	82.1 mm	-	≥ 55.0 mm
T = 20°C			
c_1	309 MPa	463 MPa	≤ 503 MPa
c_2	330 MPa	495 MPa	≤ 503 MPa
c_3	335 MPa	503 MPa	≤ 503 MPa
c_4	5.00 mm	-	≤ 5.00 mm
c_5	59.2 mm	-	≥ 58.5 mm
c_6	82.6 mm	-	≥ 55.0 mm
T = -80°C			
c_1	307 MPa	461 MPa	≤ 545 MPa
c_2	329 MPa	493 MPa	≤ 545 MPa
c_3	334 MPa	501 MPa	≤ 545 MPa
c_4	4.83 mm	-	≤ 5.00 mm
c_5	59.2 mm	-	≥ 58.5 mm
c_6	83.0 mm	-	≥ 55.0 mm

C.2.4. Thermal-resilient outer leg

The point at which the outer leg achieves optimal tractive performance at 100°C is:

$$\mathbf{x}_{o,100^\circ\text{C}} = \begin{bmatrix} t_c \\ t_s \\ L \end{bmatrix} = \begin{bmatrix} 0.10150 \\ 0.23422 \\ 28.05035 \end{bmatrix} \text{ mm.}$$

The objective and constraint performances for this optimum point at various temperatures are detailed in Table C.8 and Table C.9, respectively.

Table C.8: Objective performance thermal-resilient outer leg per temperature

Objective	Value
T = 100°C	
Drawbar pull DP	1.1710 N
Thrust H	1.2366 N
Total external resistance R_t	0.0655 N
Sinkage z	0.8102 mm
Vertical deformation δ_t	10.9657 mm
T = 20°C	
Drawbar pull DP	1.1539 N
Thrust H	1.2172 N
Total external resistance R_t	0.0634 N
Sinkage z	0.8275 mm
Vertical deformation δ_t	10.4361 mm
T = -80°C	
Drawbar pull DP	1.1438 N
Thrust H	1.2059 N
Total external resistance R_t	0.0621 N
Sinkage z	0.8380 mm
Vertical deformation δ_t	10.1336 mm

Table C.9: Constraint performance thermal-resilient outer leg per temperature

Constraint	Value	Value with safety factor (x1.5)	Limiting value
T = 100°C			
c_1	274 MPa	411 MPa	≤ 448 MPa
c_2	280 MPa	420 MPa	≤ 448 MPa
c_3	299 MPa	448 MPa	≤ 448 MPa
c_4	5.00 mm	-	≤ 5.00 mm
c_5	59.0 mm	-	≥ 58.5 mm
c_6	82.7 mm	-	≥ 55.0 mm
T = 20°C			
c_1	273 MPa	410 MPa	≤ 503 MPa
c_2	279 MPa	418 MPa	≤ 503 MPa
c_3	298 MPa	446 MPa	≤ 503 MPa
c_4	4.72 mm	-	≤ 5.00 mm
c_5	59.1 mm	-	≥ 58.5 mm
c_6	83.2 mm	-	≥ 55.0 mm
T = -80°C			
c_1	273 MPa	409 MPa	≤ 503 MPa
c_2	278 MPa	417 MPa	≤ 503 MPa
c_3	297 MPa	445 MPa	≤ 503 MPa
c_4	4.56 mm	-	≤ 5.00 mm
c_5	59.1 mm	-	≥ 58.5 mm
c_6	83.5 mm	-	≥ 55.0 mm

C.3. Contour plots

C.3.1. Middle leg

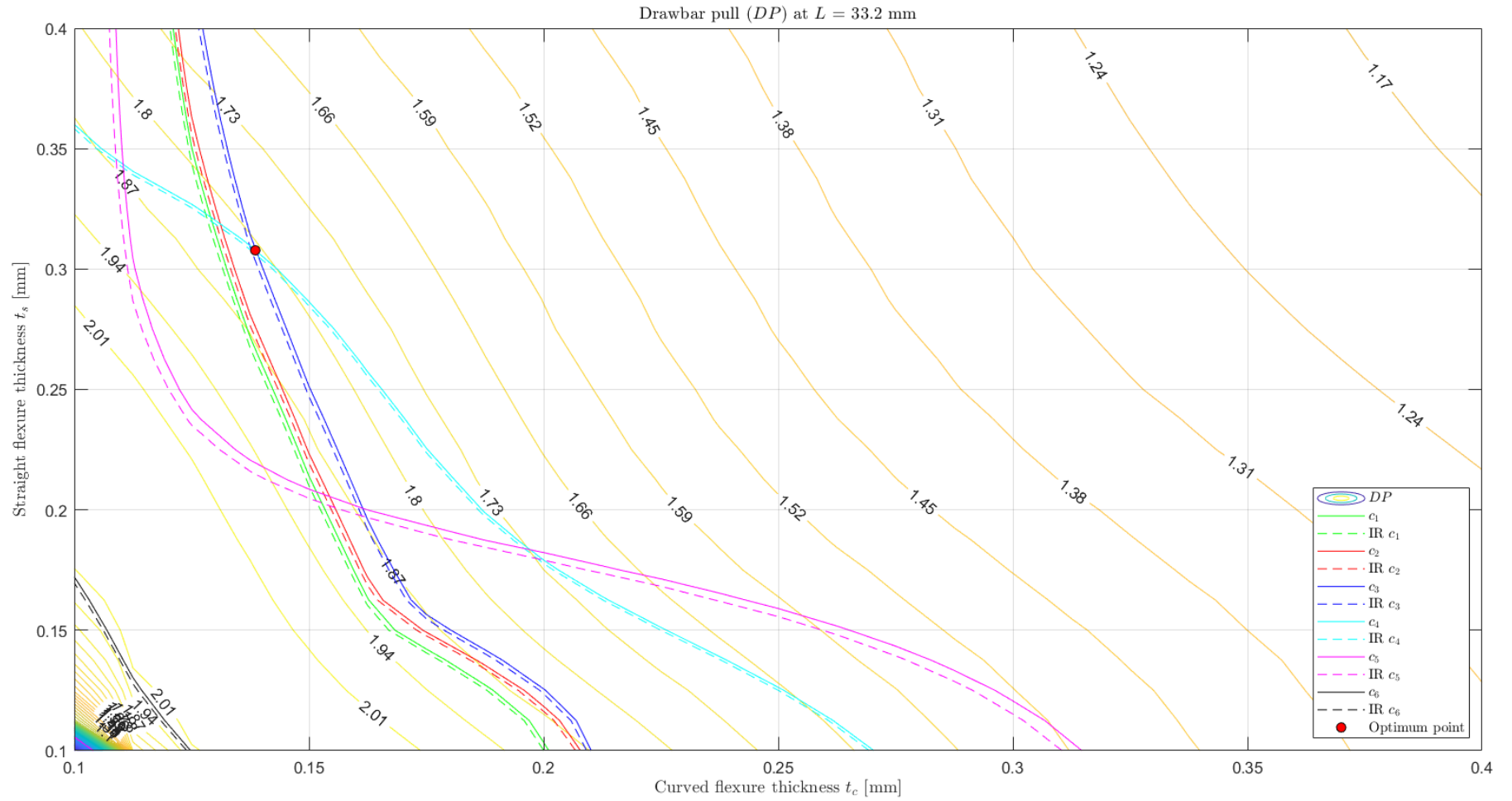


Figure 7.1: Contour plot middle leg drawbar pull DP , t_c vs t_s at L_{opt}

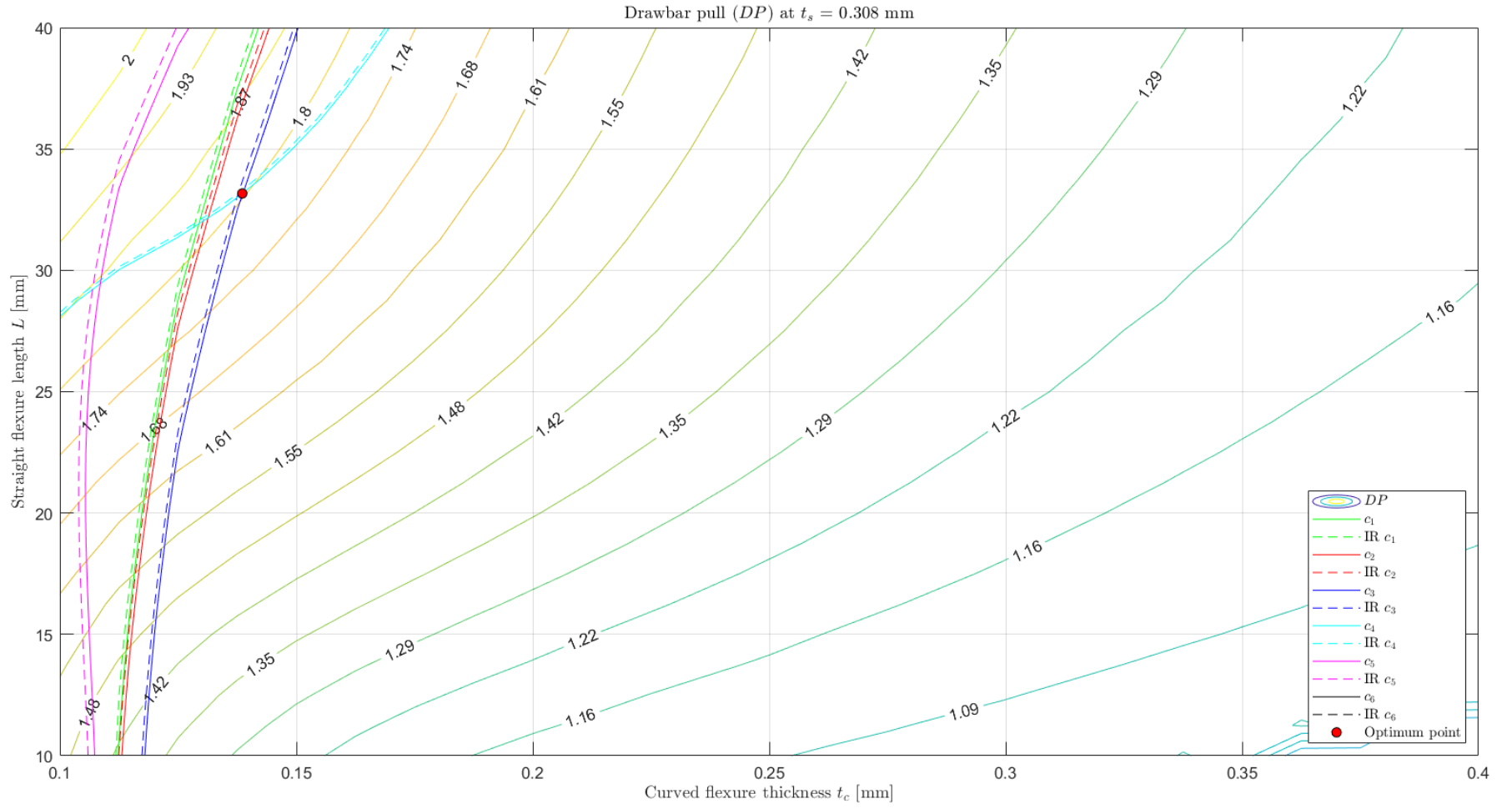


Figure 7.2: Contour plot middle leg drawbar pull DP , t_c vs L at $t_{s,opt}$

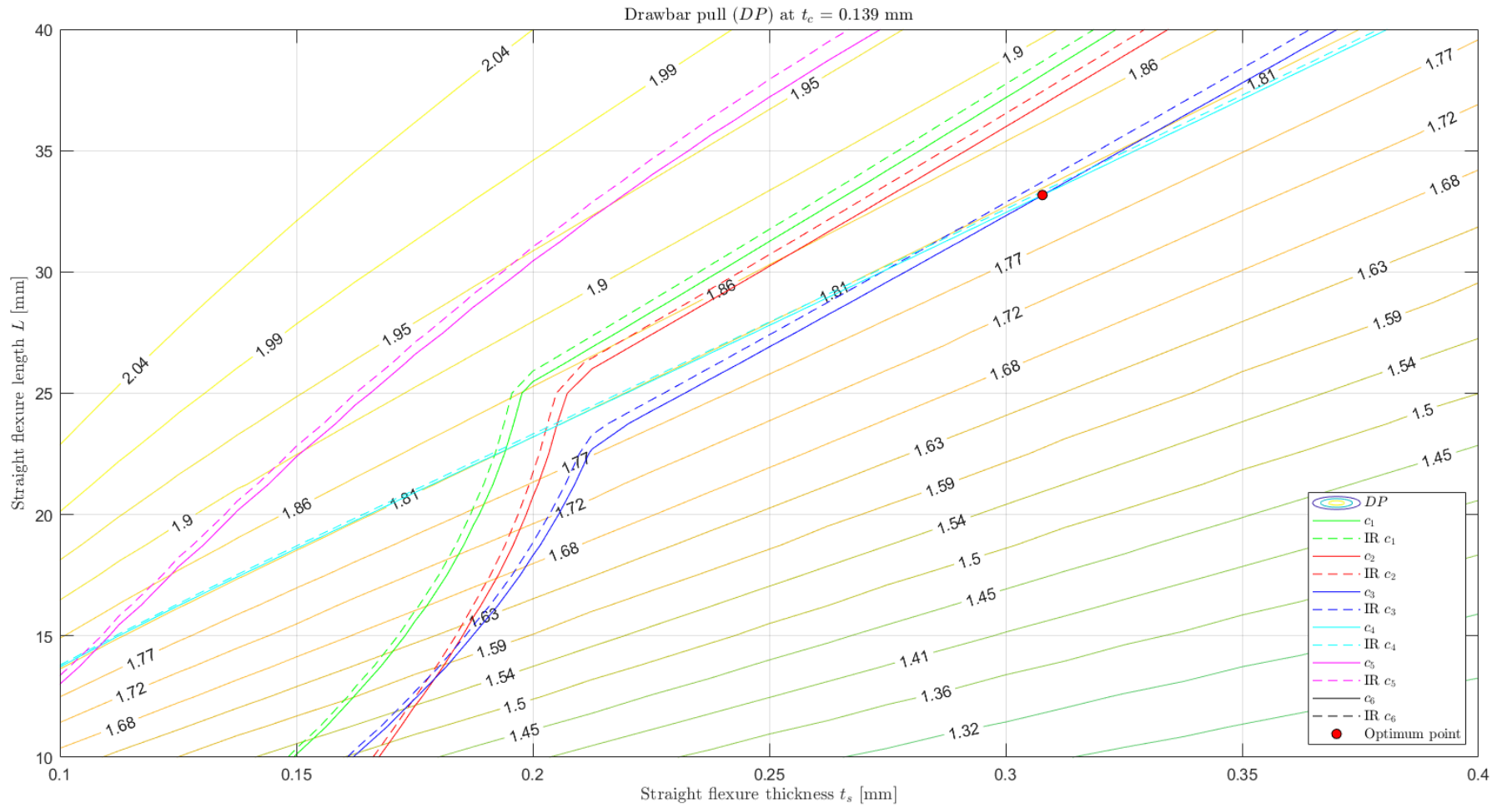
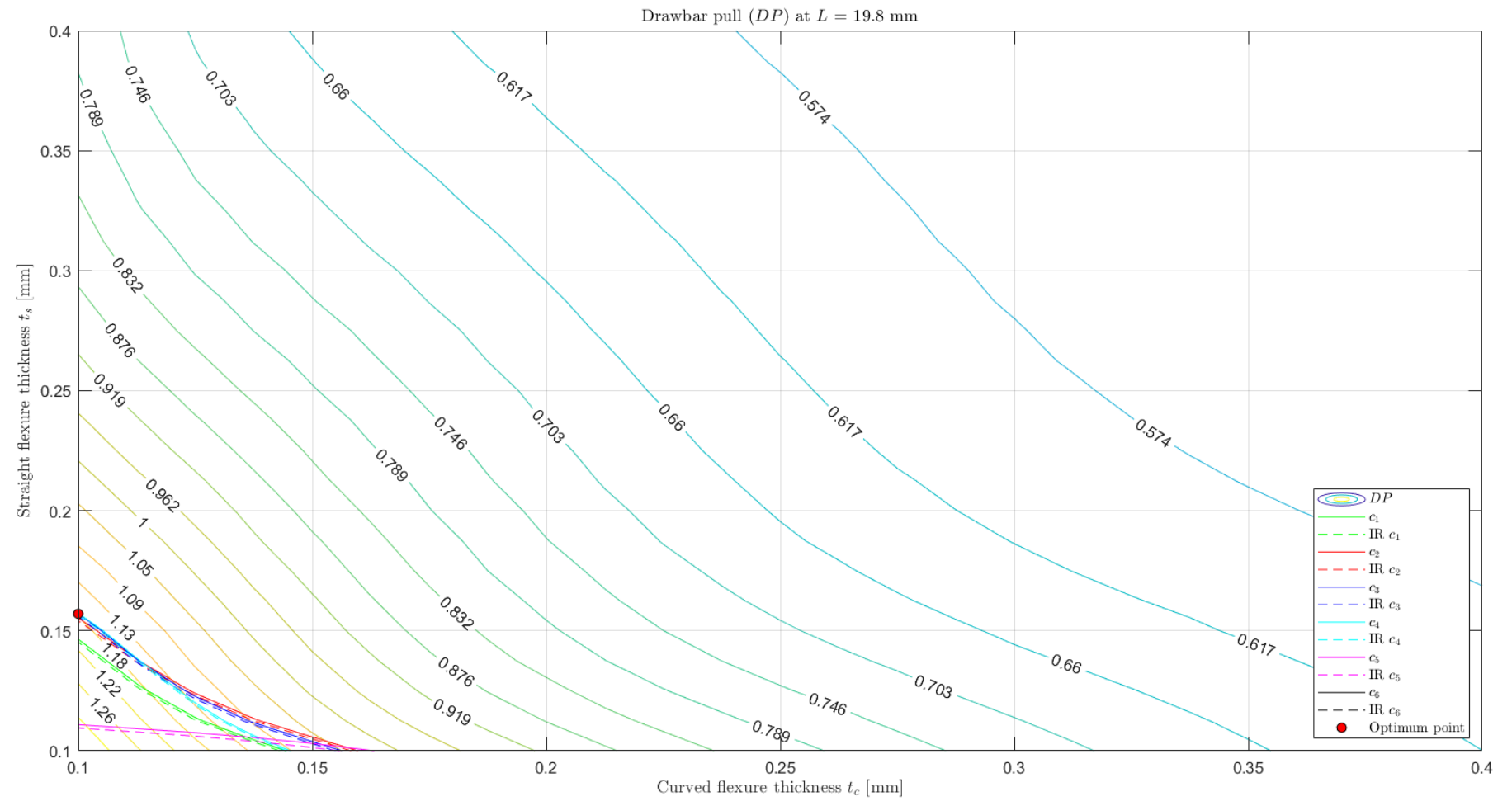


Figure 7.3: Contour plot middle leg drawbar pull DP , t_s vs L at $t_{c,opt}$

C.3.2. Outer leg

Figure 7.4: Contour plot outer leg drawbar pull DP , t_c vs t_s at L_{opt}

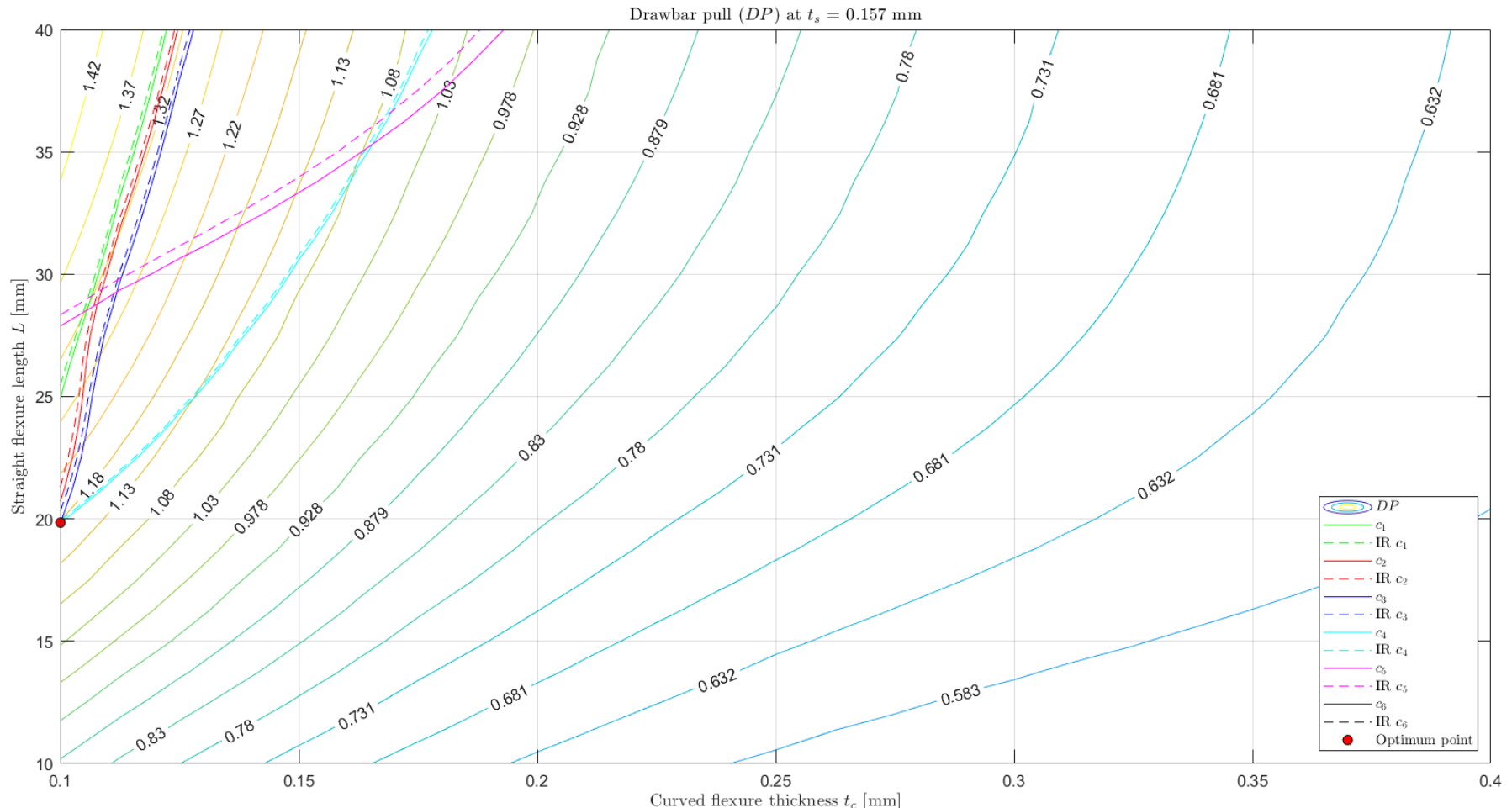


Figure 7.5: Contour plot outer leg drawbar pull DP , t_c vs L at $t_{s,opt}$

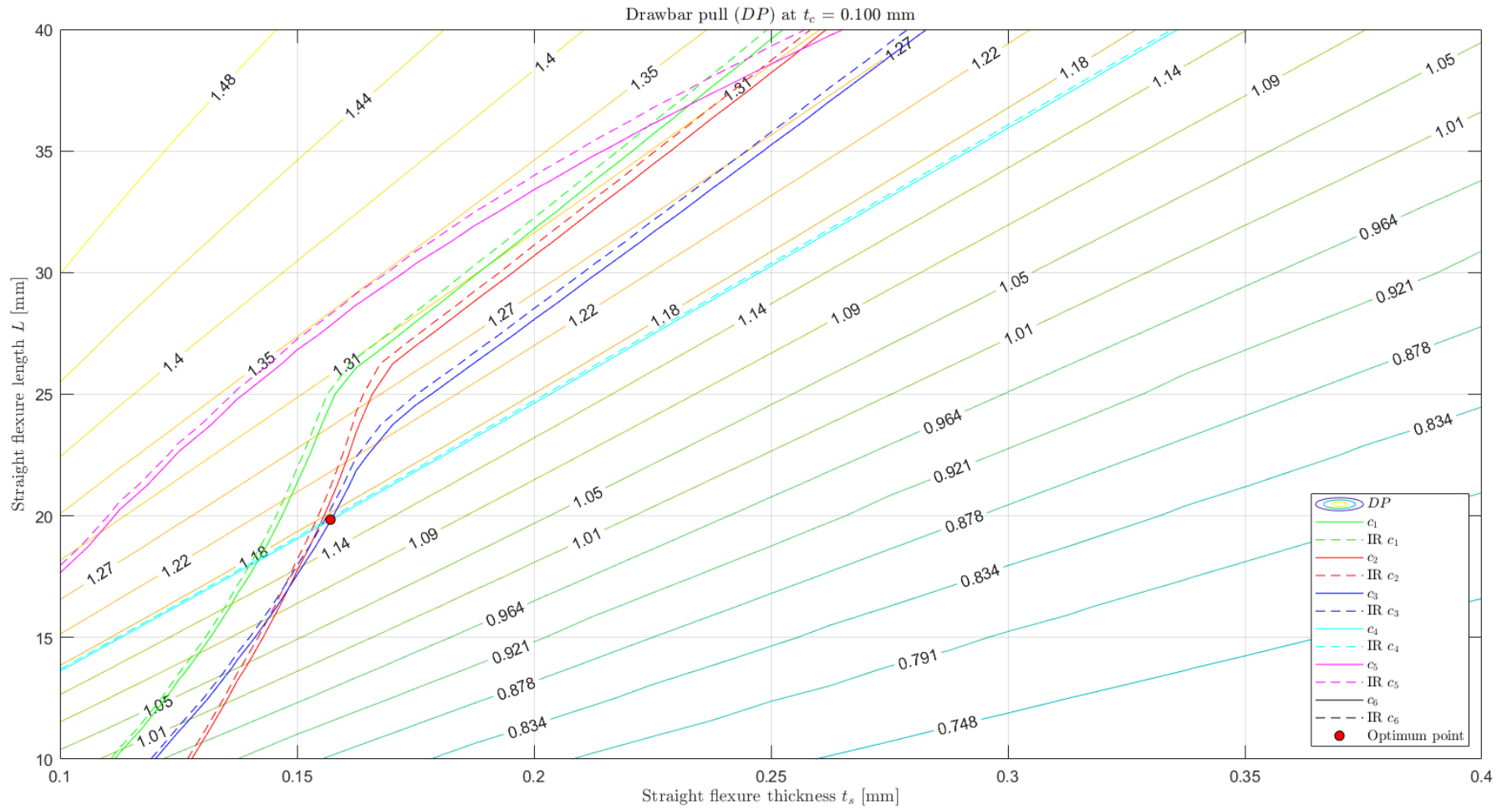


Figure 7.6: Contour plot outer leg drawbar pull DP , t_s vs L at $t_{c,opt}$

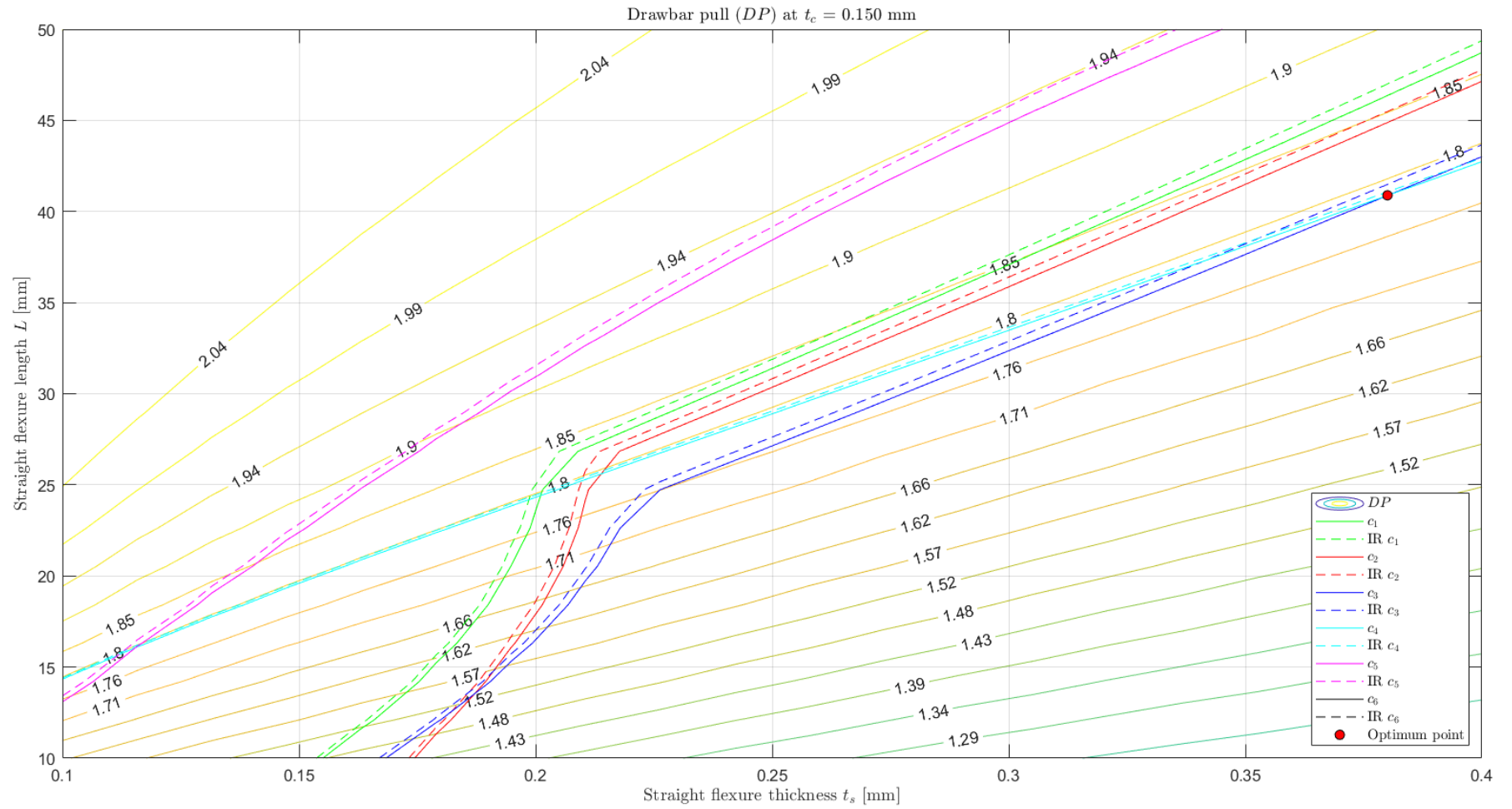


Figure 8.3: Contour plot middle leg drawbar pull DP , t_s vs L at $t_c, 100^\circ C$, $T = 100^\circ C$

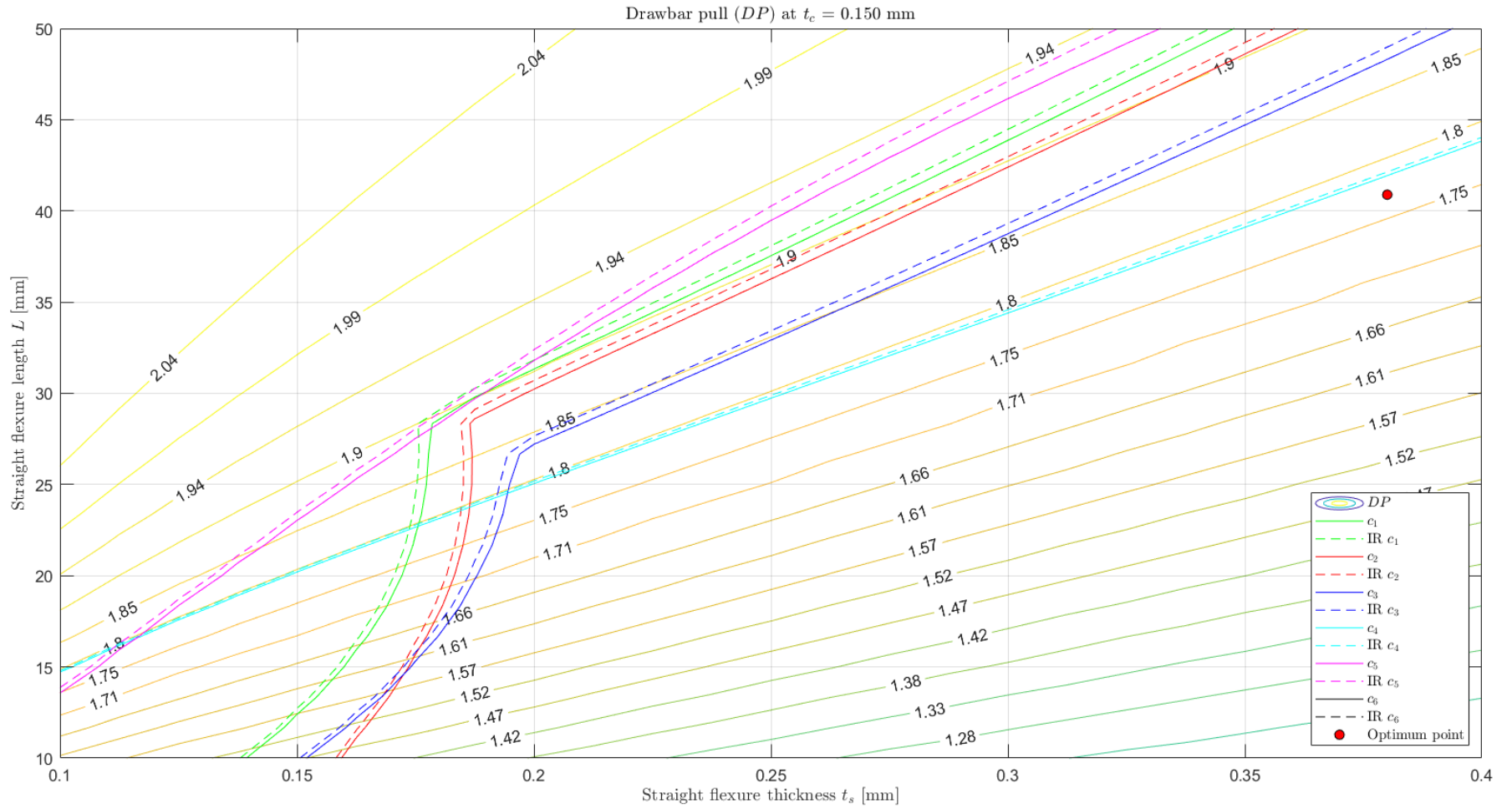


Figure 8.4: Contour plot middle leg drawbar pull DP , t_s vs L at $t_{c,100^\circ C}$, $T = 20^\circ C$

C.3.4. Thermal-resilient outer leg

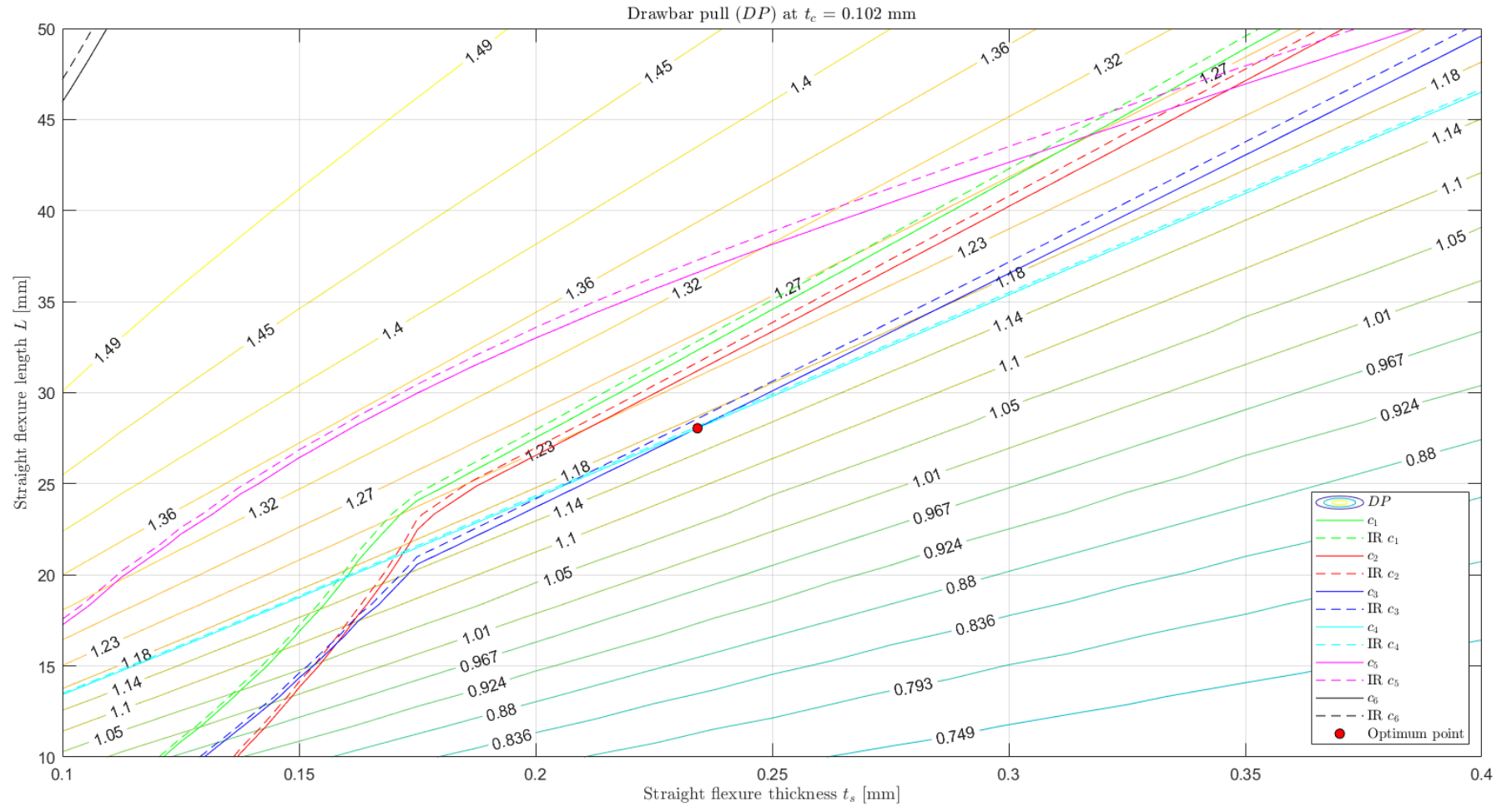


Figure 8.5: Contour plot outer leg drawbar pull DP , t_s vs L at $t_c, 100^\circ\text{C}$, $T = 100^\circ\text{C}$

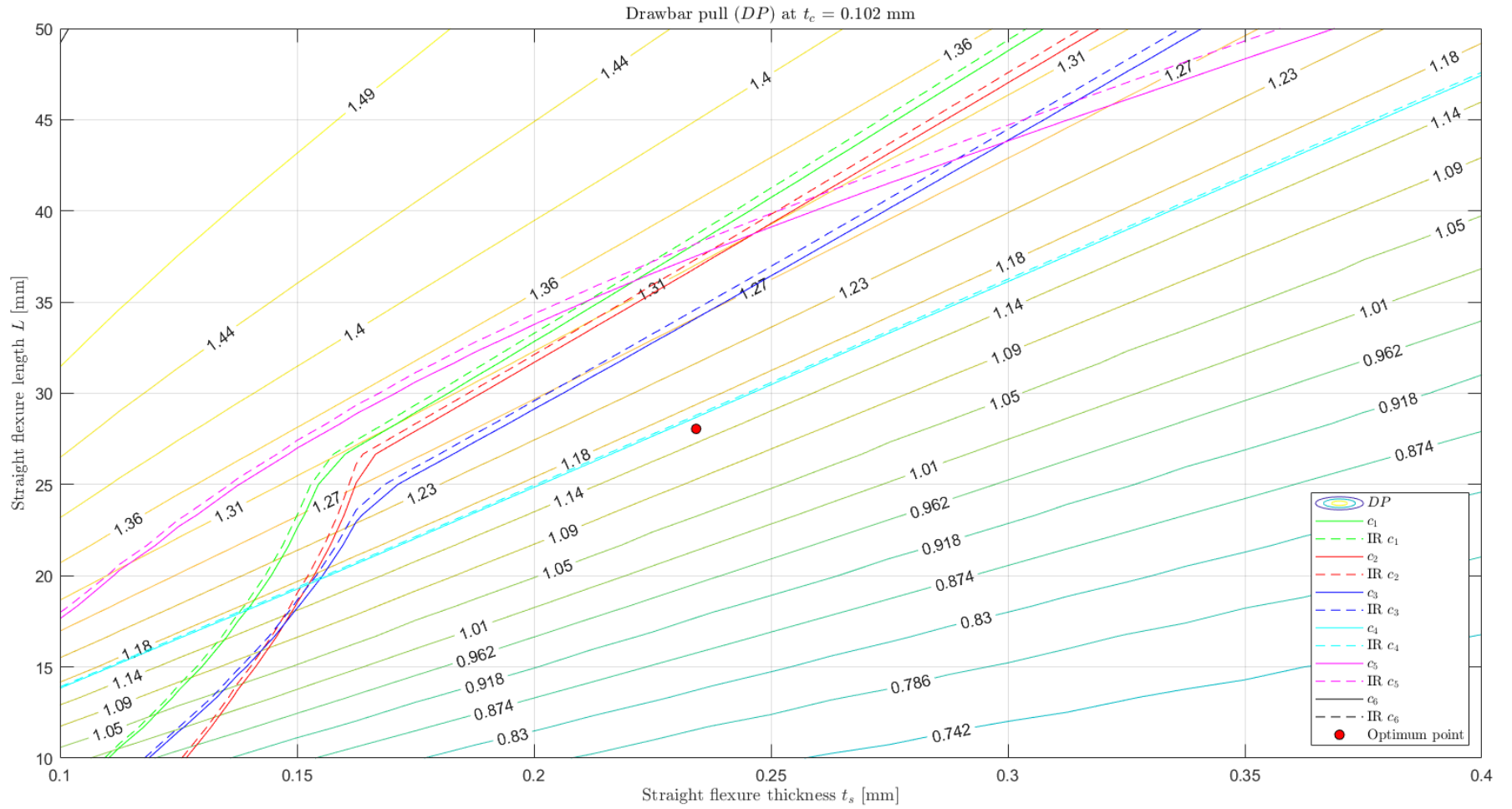


Figure 8.6: Contour plot outer leg drawbar pull DP , t_s vs L at $t_{c,100^\circ C}$, $T = 20^\circ C$

D

Contact surface wear optimisation

D.1. Contact surface wear analysis

The contact surface wear is not taken into account in the scope of the original optimisation, as explained in Section 1.3. But as the results of the optimisation show a low ground contact (curved) flexure thickness is necessary for high tractive performance, especially in the case of the outer leg, concerns can be raised about the abrasive lunar regolith and sharp rocks causing substantial damage to the flexure. In future longer missions, metal fatigue could also be present.

The Martian rover Curiosity has six wheels made out of the same material as the optimised leg, Aluminium 7075. These wheels have a diameter of 500 mm, a width of 400 mm and a tire shell of 0.75 mm thick to support the 900 kg mass of the rover [49]. In its current mission on Mars, the tire shells have suffered damage. This damage can be attributed to single-event punctures due to sharp rocks embedded in bedrock, as well as metal fatigue [50]. Although the Lunar Zebro is significantly lighter in weight, this fact raises concerns. Especially as research of Kalácska et al. [51] in soil simulants shows that "the wear effect of the lunar dusts was considerably higher than Martian ones".

In order to develop a design more resilient to contact surface wear, an optimisation analysis is conducted where the minimum curved flexure thickness is set at 0.25 mm. This analysis is anticipated to yield a design wherein compliance is primarily associated with the straight flexure, with a particular interest in its effect on the remaining tractive performance. The design space is defined as:

$$0.25 \leq t_c \leq 0.40 \text{ mm}, \quad (\text{D.1a})$$

$$0.10 \leq t_s \leq 0.40 \text{ mm}, \quad (\text{D.1b})$$

$$10 \leq L \leq 50 \text{ mm}. \quad (\text{D.1c})$$

D.1.1. Middle leg

The point at which the middle leg achieves optimal tractive performance with an increased ground contact flexure thickness is:

$$\mathbf{x}_{m,CSW} = \begin{bmatrix} t_c \\ t_s \\ L \end{bmatrix} = \begin{bmatrix} 0.250 \\ 0.211 \\ 50.0 \end{bmatrix} \text{ mm}.$$

The optimised middle leg generates a maximum drawbar pull of 1.6198 N. The increased ground contact flexure thickness has led to a 94% improvement in performance compared to the rigid middle leg, while the standard optimised design gave an improvement of 116%. The leg vertically deforms 6.14 mm at the load application point, resulting in a flattened section that measures 52.9 mm. This is a 22% decrease in comparison to the optimal middle leg flattened section length. The critical constraints are c_5 , corresponding to the minimum radius at the end of contact surface, the lower bound of the curved flexure thickness, and the upper bound of the straight flexure length. The constraint values at the optimum point are detailed in Table D.1.

Table D.1: Constraint performance middle leg optimised for contact surface wear

Constraint	Value	Value with safety factor (1.5)	Limiting value
c_1	184 MPa	276 MPa	$\leq 503 \text{ MPa}$
c_2	192 MPa	287 MPa	$\leq 503 \text{ MPa}$
c_3	202 MPa	303 MPa	$\leq 503 \text{ MPa}$
c_4	4.07 mm	-	$\leq 5.00 \text{ mm}$
c_5	58.5 mm	-	$\geq 58.5 \text{ mm}$
c_6	86.3 mm	-	$\geq 55.0 \text{ mm}$

D.1.2. Outer leg

The point at which the outer leg achieves optimal tractive performance with an increased ground contact flexure thickness is:

$$\mathbf{x}_{o,CSW} = \begin{bmatrix} t_c \\ t_s \\ L \end{bmatrix} = \begin{bmatrix} 0.250 \\ 0.122 \\ 50.0 \end{bmatrix} \text{ mm.}$$

The optimised outer leg generates a maximum drawbar pull of 0.905 N. The increased ground contact flexure thickness has led to a 103% improvement in performance compared to the rigid middle leg, while the standard optimised design gave an improvement of 206%. This is a large difference, attributed to the lower normal load exerted on the outer leg compared to the middle leg. Consequently, the generic minimum ground contact flexure thickness is not the ideal solution to contact surface wear, as both the compliance of the design and contact surface wear are dependent on the exerted normal load.

The leg vertically deforms 4.56 mm at the load application point, resulting in a flattened section that measures 45.9 mm. This is a 34% decrease in comparison to the optimal outer leg flattened section length. The critical constraints are the same as the middle leg, with the constraint values at the optimum point being detailed in Table D.2.

Table D.2: Constraint performance outer leg optimised for contact surface wear

Constraint	Value	Value with safety factor (1.5)	Limiting value
c_1	122 MPa	183 MPa	$\leq 503 \text{ MPa}$
c_2	129 MPa	194 MPa	$\leq 503 \text{ MPa}$
c_3	134 MPa	200 MPa	$\leq 503 \text{ MPa}$
c_4	3.33 mm	-	$\leq 5.00 \text{ mm}$
c_5	58.5 mm	-	$\geq 58.5 \text{ mm}$
c_6	88.7 mm	-	$\geq 55.0 \text{ mm}$

E

Finite Element Analysis

E.1. Stress

A Finite Element Analysis (FEA) is performed to verify that the analytical calculations of the compliance and stress give the expected results. This analysis was performed with placeholder variable values before the optimisation process, which showed a good correlation with the analytical calculation. To ensure good compatibility with the optimal designs, this analysis is again performed with the created final middle and outer legs while transmitting the maximum drawbar pull. The analysis is conducted using COMSOL Multiphysics and will specifically focus on the stress encountered in the legs while walking (2D) and while climbing along a sideways gradient (3D). The analysis is modelled with the same assumptions as the analytical calculations, with linear deflections and a single load application point. The lateral force while climbing along a sideways gradient is modelled as an edge load, to ensure that the force is equally spread over the flexure width. The design is fixed around the motor axis, and the material properties of Table C.1 are applied. The maximum stress angle, at which the load application point is located, is defined from the straight flexure onward.

E.1.1. Middle leg

The analytically derived maximum stress values for the straight and curved flexures of the middle leg during both walking and climbing along a sideways gradient are provided in Table E.1, along with the corresponding leg orientation angles at which these maximum stresses occur. The respective maximum stresses obtained through FEA while walking are presented in Figures E.1 and E.2, and while climbing along a sideways gradient in Figures E.3 and E.4.

Table E.1: Analytically derived stress values middle leg at $x_{m,opt}$

Maximum stress	Value	Maximum stress angle
$\sigma_{s,walk}$	230 MPa	35.6°
$\sigma_{c,walk}$	307 MPa	62.9°
$\sigma_{s,side}$	251 MPa	35.6°
$\sigma_{c,side}$	335 MPa	62.9°

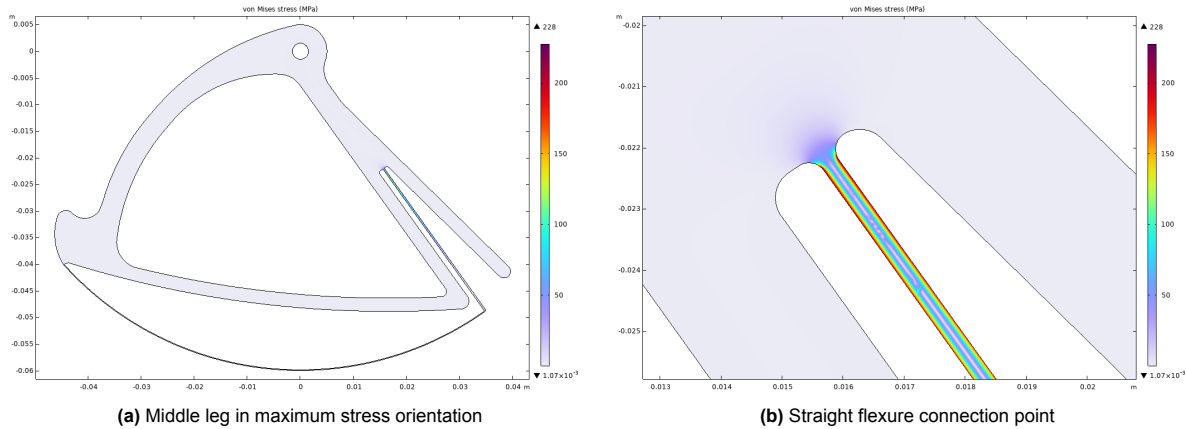


Figure E.1: Maximum stress $\sigma_{s,walk}$ in straight flexure of middle leg while walking

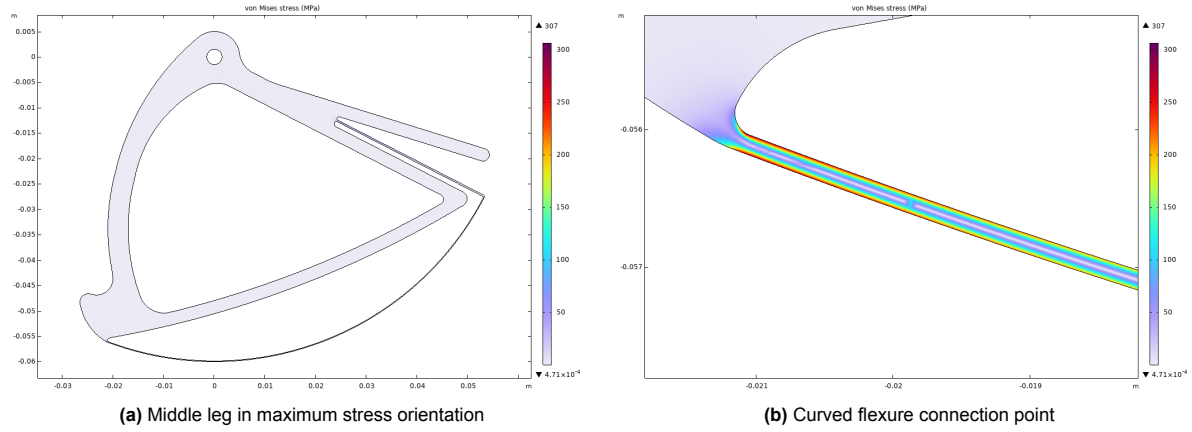


Figure E.2: Maximum stress $\sigma_{c,walk}$ in curved flexure of middle leg while walking

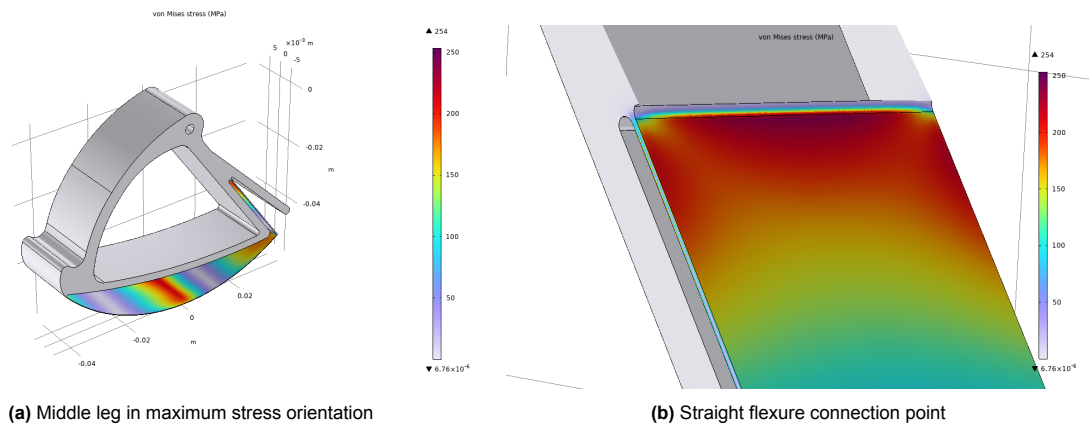


Figure E.3: Maximum stress $\sigma_{s,side}$ in straight flexure of middle leg while climbing along a sideways gradient

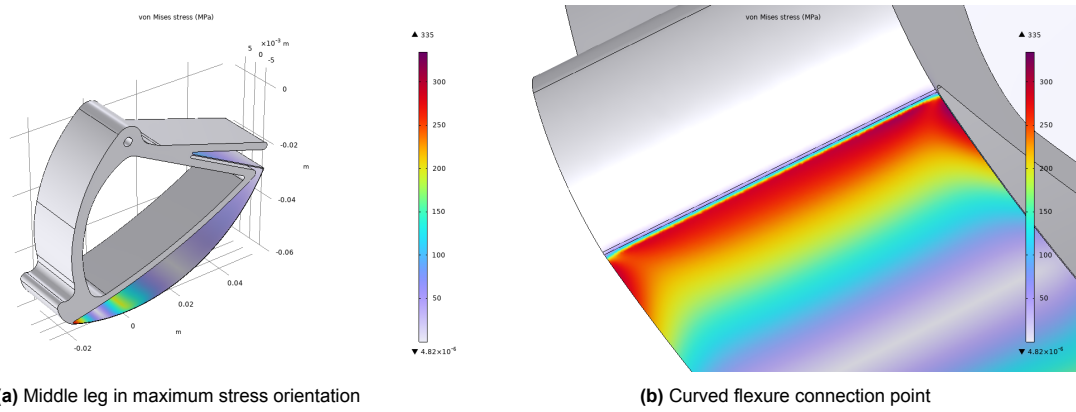


Figure E.4: Maximum stress $\sigma_{c,side}$ in curved flexure of middle leg while climbing along a sideways gradient

E.1.2. Outer leg

The analytically derived maximum stress values for the straight and curved flexures of the outer leg during both walking and climbing along a sideways gradient are provided in Table E.2, along with the corresponding leg orientation angles at which these maximum stresses occur. The respective maximum stresses obtained through FEA while walking are presented in Figures E.5 and E.6, and while climbing along a sideways gradient in Figures E.7 and E.8.

Table E.2: Analytically derived stress values outer leg at $x_{o,opt}$

Maximum stress	Value	Maximum stress angle
$\sigma_{s,walk}$	309 MPa	34.7°
$\sigma_{c,walk}$	291 MPa	62.9°
$\sigma_{s,side}$	335 MPa	34.7°
$\sigma_{c,side}$	317 MPa	62.9°

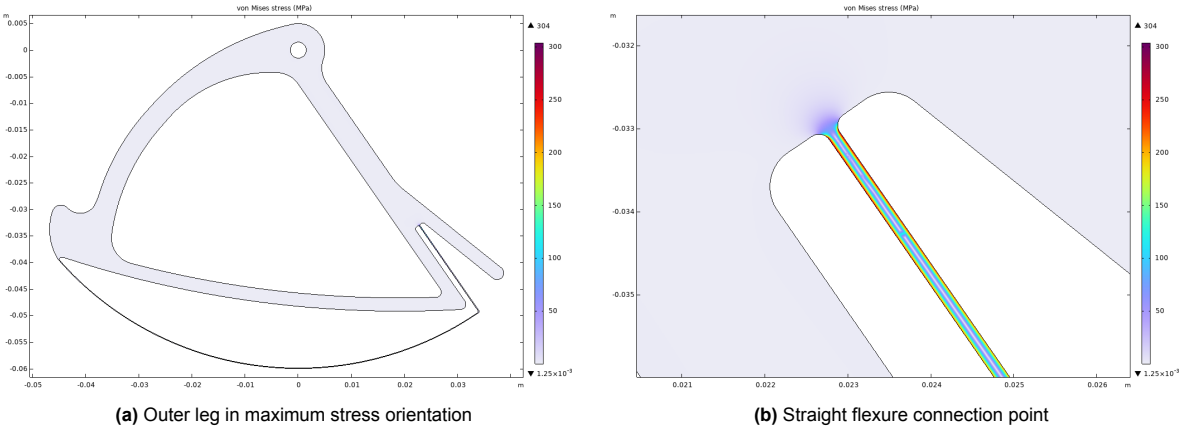


Figure E.5: Maximum stress $\sigma_{s,walk}$ in straight flexure of outer leg while walking

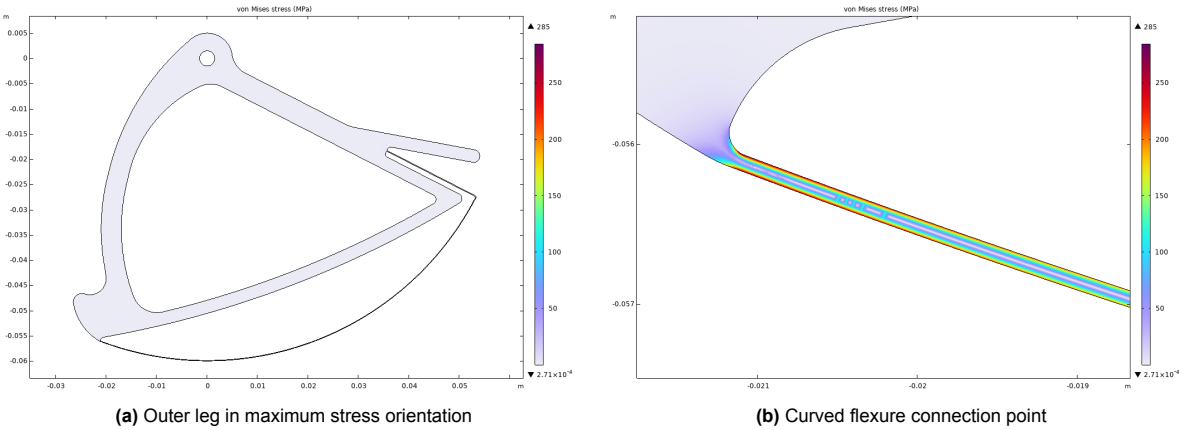


Figure E.6: Maximum stress $\sigma_{c,walk}$ in curved flexure of outer leg while walking

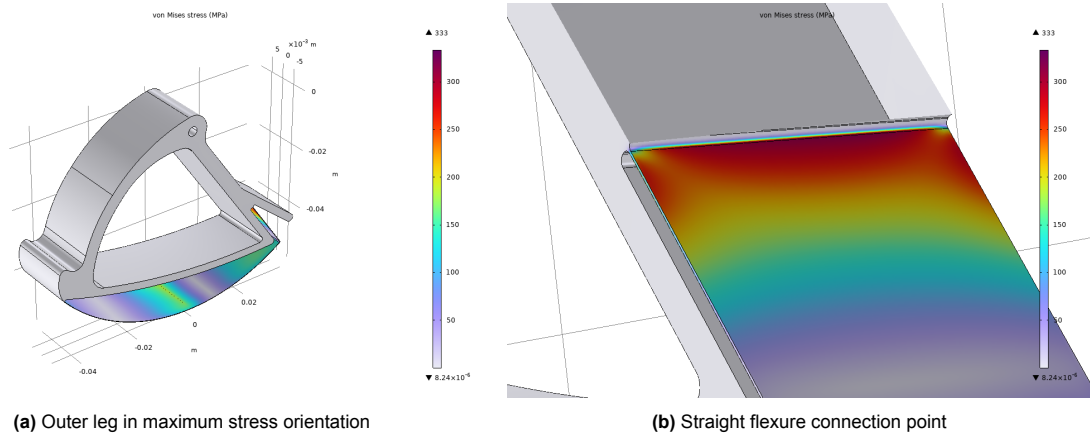


Figure E.7: Maximum stress $\sigma_{s,side}$ in straight flexure of outer leg while climbing along a sideways gradient

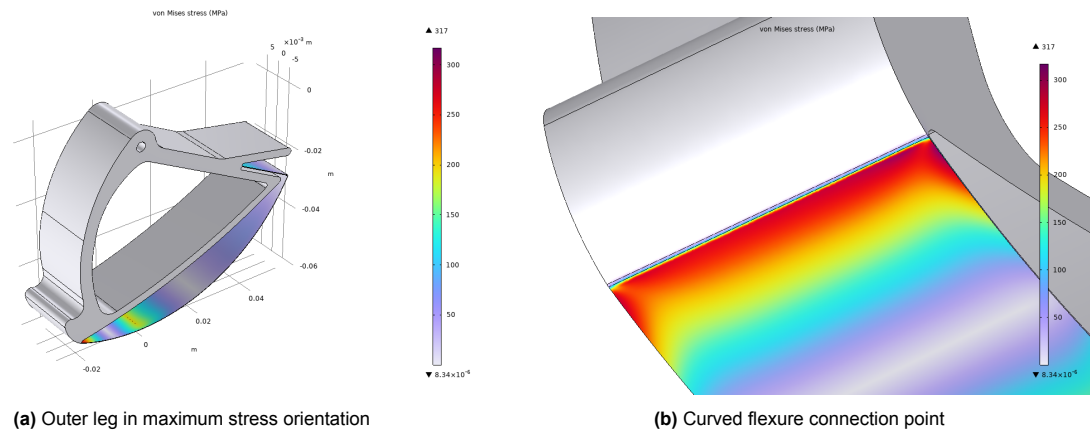


Figure E.8: Maximum stress $\sigma_{c,side}$ in curved flexure of outer leg while climbing along a sideways gradient

E.1.3. Result discussion

The results indicate that the middle leg stress obtained from the FEA closely aligns with the values derived from analytical calculations, thereby successfully validating the analytical compliance and stress calculations. It is important to note that the maximum stress obtained in the FEA can be influenced by variations in the fillet radius of the flexure connection. The simulation and mesh data of the FEA are detailed in Table E.3.

Table E.3: FEA data

Model	Number of elements	DoF
Middle leg $\sigma_{s,walk}$	10754	46899
Middle leg $\sigma_{c,walk}$	10919	47589
Middle leg $\sigma_{s,side}$	753109	4170129
Middle leg $\sigma_{c,side}$	762507	4210947
Outer leg $\sigma_{s,walk}$	11400	50171
Outer leg $\sigma_{c,walk}$	11662	51271
Outer leg $\sigma_{s,side}$	1068887	6070212
Outer leg $\sigma_{c,side}$	1163873	6638340

F

Matlab Code

F.1. Parameters

```

1 %% Middle or outer leg optimisation parameters
2 leg_choice = 'middle'; % Options: 'middle' or 'outer'
3
4 switch leg_choice
5     case 'middle'
6         N = 2; % Leg load factor, middle legs [-]
7         F_x = 1.81; % Longitudinal force at application point used for deflection
            with no vertical force, middle legs [N]
8         F_xside = 1.96; % Longitudinal force at application point when climbing along a
            sideways gradient used for deflection with no vertical force, middle legs [N]
9
10        case 'outer'
11            N = 4; % Leg load factor, outer legs [-]
12            F_x = 1.17; % Longitudinal force at application point used for deflection
                with no vertical force, outer legs [N]
13            F_xside = 1.26; % Longitudinal force at application point when climbing along a
                sideways gradient used for deflection with no vertical force, outer legs [N]
14
15        otherwise
16            error('Invalid leg choice. Use "middle" or "outer".');
17    end
18
19 %% Material parameters
20 % Temperature
21 temp = '20'; % Options: '20', '100' or '-80'
22
23 switch temp
24     case '20' % T = 20 deg C
25         E = 71.7e9; % Young's modulus [Pa]
26         G = 26.9e9; % Shear modulus [Pa]
27         sigma_y = 503e6; % Tensile yield strength [Pa]
28
29     case '100' % T = 100 deg C
30         E = 68.3e9; % Young's modulus [Pa]
31         G = 25.7e9; % Shear modulus [Pa]
32         sigma_y = 448e6; % Tensile yield strength [Pa]
33
34     case '-80' % T = -80 deg C
35         E = 73.8e9; % Young's modulus [Pa]
36         G = 27.7e9; % Shear modulus [Pa]
37         sigma_y = 545e6; % Tensile yield strength [Pa]
38
39     otherwise
40         error('Invalid temperature choice. Use "20", "100" or "-80".');
41 end
42
43 SF = 1.5; % Stress safety factor [-]
44
45 %% Parameters terramechanics
46 kappa = 18e-3; % Shear deformation modulus [m]
47 lambda = 0.1; % Terrain reboundness due to soil elasticity [-]
48 phi_deg = 42; % Internal friction coefficient [deg]
49 c = 520; % Soil cohesion coefficient [Pa]
50 g = 1.62; % Gravitational acceleration [m/s^2]
51 h = 20e-3; % Leg deformable section height [m]
52 k_c = 1400; % Cohesion modulus of soil deformation [Pa/m^{-n1}]
53 k_e = 7; % Parameter related to leg construction [-]
54 k_phi = 820000; % Friction modulus of soil deformation [Pa/m^n]
55 m = 2.5; % Lunar rover mass [kg]
56 n = 1; % Exponent of soil deformation -[]
57 s = 1; % Slip ratio [-]
58
59 % Static equilibrium iteration parameters in Analysis.m and SidewaysGradient.m
60 tolerance = 1e-2; % Tolerance for convergence F_y0 vs. W
61 max_iterations = 500; % Maximum number of iterations to prevent infinite loops
62 update_factor = 0.0001; % Factor to update delta_t
63
64 % Quasi-static equilibrium iteration parameters in Analysis.m and SidewaysGradient.m
65 tolerance2 = 1e-2; % Tolerance for convergence F vs. W

```

```

66 max_iterations2 = 100;          % Maximum number of iterations to prevent infinite loops
67 update_factor2 = 0.0005;      % Factor to update z
68
69 %% Parameters force deflection relationship
70 alpha_angle = deg2rad(41.8);  % Load application angle [rad]
71 beta_angle = deg2rad(83.6);   % Leg flexure angle [rad]
72 R = 60e-3;                    % Leg radius [m]
73 w = 20e-3;                    % Leg width [m]
74
75 %% Parameters skid steering stress constraint
76 mu = 1.2;                     % Shear constant (rectangle) [-]
77
78 %% Parameters climbing sideways gradient constraint
79 gamma_angle = deg2rad(15);    % Sideways gradient LZ needs to be able to ascend [rad]
80 b_LZ = 0.125;                 % Width between outer legs and CoM of Lunar Zebro chassis [m]
81 y_com = 60e-3;                % Height of CoM [m]
82
83 %% Parameters motor torque transmission constraint
84 delta_x_max = 5e-3;           % Maximum longitudinal displacement for torque coupling [m]
85
86 %% Parameters tip displacement next step constraint
87 R_eff_min = 58.5e-3;          % Minimum radius needed to initiate next leg [m]
88
89 %% Parameters climbing height constraint
90 y_c_min = 55e-3;              % Minimal required climbing height [m]
91 y_g = 34.5e-3;                % Height between gripping point and axle [m]

```

F.2. Optimisation

```

1 %% Leg optimisation
2 % Optimisation using fmincon and SQP algorithm
3 % Initialization
4 close all, clear, clc
5
6 % Input parameters
7 Parameters;
8 fprintf('Leg choice: %s\n', leg_choice)
9
10 % Initial design point
11 x0 = [0.15e-3, 0.30e-3, 30e-3];
12
13 % Options for fmincon
14 options = optimoptions('fmincon', 'Algorithm', 'sqp', 'Display', 'iter', 'PlotFcn',
    @optimplotfval);
15
16 % Objective function
17 objfun = @OBJ;
18
19 % Constraint function
20 confun = @CONS;
21
22 tic;
23
24 % Solve using fmincon
25 [x_opt, fval, exitflag, output, lambda_lag, grad, hessian] = fmincon(objfun, x0, [], [], [],
    [], [0.1e-3, 0.1e-3, 10e-3], [0.4e-3, 0.4e-3, 40e-3], confun, options);
26
27 elapsedTime = toc;
28 [eigenvectors, eigenvalues] = eig(hessian);
29
30 %% Display results
31 fprintf('Optimal design variables: t_c = %.5f mm, t_s = %.5f mm, L = %.5f mm\n', x_opt(1)*1e3
    , x_opt(2)*1e3, x_opt(3)*1e3);
32 fprintf('Objective function value (DP): %.5f N\n', -fval);
33 fprintf('Exit flag: %d\n', exitflag);
34 disp('Output structure:');
35 disp(output);
36 disp('Lagrange multipliers:');
37 disp(lambda_lag);
38 fprintf('Elapsed optimisation time: %.2f seconds\n', elapsedTime);
39
40 % Compute values and constraints at optimum point
41 [con_opt, ceq] = CONS(x_opt);
42 [DP, z, T, eta, delta_t, sigma_max_walk, sigma_max_skid, sigma_max_side, delta_x, R_eff, y_c
    ]=Analysis(x_opt(1),x_opt(2),x_opt(3),g,m,k_c,k_phi,n,phi_deg,c,lambda,s,k_e,h,kappa,E,G,
    w,R, alpha_angle,beta_angle,mu,F_x,F_xside,y_g,b_LZ,gamma_angle,y_com,N,tolerance,
    max_iterations,update_factor,tolerance2,max_iterations2,update_factor2);
43 fprintf('Drawbar Pull DP: %.4f N\n', DP);
44 fprintf('Sinkage z: %.4f mm\n', z*1e3);
45 fprintf('Resistance torque T: %.4f N\n', T);
46 fprintf('Tractive efficiency eta: %.4f %\n', eta);
47 fprintf('Vertical deflection of leg delta_t: %.4f mm\n', delta_t*1e3);
48 fprintf('Max. stress in flexure while walking sigma_max_walk: %.4f MPa\n', sigma_max_walk/1e6
    );
49 fprintf('Max. stress in flexure while skid steering sigma_max_skid: %.4f MPa\n',
    sigma_max_skid/1e6);
50 fprintf('Max. stress in flexure while climbing along a sideways gradient sigma_max_side: %.4f
    MPa\n', sigma_max_side/1e6);
51 fprintf('Max. stress in flexure while walking sigma_max_walk with safety factor: %.4f MPa\n',
    SF*sigma_max_walk/1e6);
52 fprintf('Max. stress in flexure while skid steering sigma_max_skid with safety factor: %.4f
    MPa\n', SF*sigma_max_skid/1e6);
53 fprintf('Max. stress in flexure while climbing along a sideways gradient sigma_max_side with
    safety factor: %.4f MPa\n', SF*sigma_max_side/1e6);
54 fprintf('Maximum longitudinal deflection delta_x: %.4f mm\n', delta_x*1e3);
55 fprintf('Effective radius at last 10%% of contact surface: %.4f mm\n', R_eff*1e3);
56 fprintf('Climbing height y_c: %.4f mm\n', y_c*1e3);

```

F.3. Optimisation using GlobalSearch

```

1 %% Leg optimisation Global Search
2 % Optimisation using fmincon and SQP wrapped with GlobalSearch
3
4 % Initialization
5 close all; clear; clc;
6
7 % Input parameters
8 Parameters;
9 fprintf('Leg choice: %s\n', leg_choice)
10
11 % Initial design point
12 x0 = [0.15e-3, 0.30e-3, 30e-3];
13
14 % Lower and upper bounds
15 lb = [0.1e-3, 0.1e-3, 10e-3];
16 ub = [0.4e-3, 0.4e-3, 40e-3];
17
18 % Options for fmincon
19 options = optimoptions('fmincon', ...
20     'Algorithm', 'sqp', ...
21     'Display', 'iter', ...
22     'PlotFcn', @optimplotfval, ...
23     'OptimalityTolerance', 1e-4, ...
24     'StepTolerance', 1e-4, ...
25     'ConstraintTolerance', 1e-4, ...
26     'MaxIterations', 1000);
27
28 % Objective function
29 objfun = @OBJ;
30
31 % Constraint function
32 confun = @CONS;
33
34 % Create problem structure for GlobalSearch
35 problem = createOptimProblem('fmincon', ...
36     'objective', objfun, ...
37     'x0', x0, ...
38     'lb', lb, ...
39     'ub', ub, ...
40     'nonlcon', confun, ...
41     'options', options);
42
43 % Create GlobalSearch object
44 gs = GlobalSearch('Display', 'iter', ...
45     'NumStageOnePoints', 20, ...
46     'NumTrialPoints', 40);
47
48 tic;
49
50 % Run GlobalSearch
51 [x_opt, fval, exitflag, output, solutions] = run(gs, problem);
52
53 elapsedTime = toc;
54
55 % Display results
56 fprintf('Optimal design variables: t_c = %.5f mm, t_s = %.5f mm, L = %.5f mm\n', x_opt(1)*1e3
57     , x_opt(2)*1e3, x_opt(3)*1e3);
58 fprintf('Objective function value (DP): %.5f N\n', -fval);
59 fprintf('Exit flag: %d\n', exitflag);
60 disp('Output structure:');
61 disp(output);
62 disp('Solutions:');
63 disp(solutions);
64 fprintf('Elapsed optimisation time: %.2f seconds\n', elapsedTime);
65
66 % Compute values and constraints at optimum point
67 [con_opt, ceq] = CONS(x_opt);
68 [DP, z, T, eta, delta_t, sigma_max_walk, sigma_max_skid, sigma_max_side, delta_x, R_eff, y_c
69     ]=Analysis(x_opt(1),x_opt(2),x_opt(3),g,m,k_c,k_phi,n,phi_deg,c,lambda,s,k_e,h,kappa,E,G,

```

```

w,R,alpha_angle,beta_angle,mu,F_x,F_xside,y_g,b_LZ,gamma_angle,y_com,N,tolerance,
max_iterations,update_factor,tolerance2,max_iterations2,update_factor2);
68 fprintf('Drawbar Pull DP: %.4f N\n', DP);
69 fprintf('Sinkage z: %.4f mm\n', z*1e3);
70 fprintf('Resistance torque T: %.4f N\n', T);
71 fprintf('Tractive efficiency eta: %.4f %%\n', eta);
72 fprintf('Vertical deflection of leg delta_t: %.4f mm\n', delta_t*1e3);
73 fprintf('Max. stress in flexure while walking sigma_max_walk: %.4f MPa\n', sigma_max_walk/1e6
);
74 fprintf('Max. stress in flexure while skid steering sigma_max_skid: %.4f MPa\n',
sigma_max_skid/1e6);
75 fprintf('Max. stress in flexure while climbing along a sideways gradient sigma_max_side: %.4f
MPa\n', sigma_max_side/1e6);
76 fprintf('Max. stress in flexure while walking sigma_max_walk with safety factor: %.4f MPa\n',
SF*sigma_max_walk/1e6);
77 fprintf('Max. stress in flexure while skid steering sigma_max_skid with safety factor: %.4f
MPa\n', SF*sigma_max_skid/1e6);
78 fprintf('Max. stress in flexure while climbing along a sideways gradient sigma_max_side with
safety factor: %.4f MPa\n', SF*sigma_max_side/1e6);
79 fprintf('Maximum longitudinal deflection delta_x: %.4f mm\n', delta_x*1e3);
80 fprintf('Effective radius at last 10% of contact surface: %.4f mm\n', R_eff*1e3);
81 fprintf('Climbing height y_c: %.4f mm\n', y_c*1e3);

```

F.4. Objective function

```

1 function f = OBJ(x)
2 % Computation of objective function
3 % Input: x: [1x3] row of design variables (t_c, t_s and L)
4 % Output: f: {1x1} scalar of objective function value
5
6 % Assignment of design variables
7 t_c = x(1);
8 t_s = x(2);
9 L = x(3);
10
11 % Input parameters
12 Parameters;
13
14 % Analysis
15 [DP, ~, ~, ~, ~, ~, ~, ~, ~, ~, ~]=...
16 Analysis(t_c,t_s,L,g,m,k_c,k_phi,n,phi_deg,c,lambda,s,k_e,h,kappa,E,G,w,R, ...
17 alpha_angle,beta_angle,mu,F_x,F_xside,y_g,b_LZ,gamma_angle,y_com,N, ...
18 tolerance,max_iterations,update_factor,tolerance2,max_iterations2,update_factor2);
19
20 % Objective function
21 f = -DP; % Objective is maximising DP, thus minimising -DP using fmincon.
22
23 end

```

F.5. Analysis: Terramechanics model

```

1 function [DP, z, T, eta, delta_t, sigma_max_walk, sigma_max_skid, sigma_max_side, delta_x,
   R_eff, y_c]=...
2 Analysis(t_c,t_s,L,g,m,k_c,k_phi,n,phi_deg,c,lambda,s,k_e,h,kappa,E,G,w,R, ...
3 alpha_angle,beta_angle,mu,F_x,F_xside,y_g,b_LZ,gamma_angle,y_com,N, ...
4 tolerance,max_iterations,update_factor,tolerance2,max_iterations2,update_factor2)
5
6 W = (m/N)*g; % Gravitational force on leg axle
7 phi = deg2rad(phi_deg); % Soil friction angle (in radians)
8
9 %% Static equilibrium
10 delta_t = LongitudinalForceDeflection(E, w, t_s, t_c, R, L, alpha_angle, beta_angle, F_x); %
   Initial guess for delta_t, dependent on the deflection by pure longitudinal force F_x.
11
12 for iter = 1:max_iterations
13     % Calculate flattened section length l_t
14     if 2 * R * delta_t > delta_t^2
15         l_t = 2 * sqrt(2 * R * delta_t - delta_t^2);
16     else
17         % warning('Non-physical values for l_t');
18         % fprintf('Last static total vertical force F_y0: %.4f N\n', F_y0);
19         % fprintf('Last leg deflection delta_t: %.4f mm\n', delta_t*10^3)
20
21         if delta_t < 0
22             delta_t = 0;
23             l_t = 0;
24             theta_t0 = 0;
25             z_0 = 0.0005; % Default initial guess
26             % fprintf('Rigid leg considered, thus leg deflection delta_t: %.4f mm\n', delta_t
   *10^3)
27         else
28             % warning('Deflection too big for leg, results are inaccurate. ');
29         end
30         break;
31     end
32
33     % Calculate average ground pressure P_w
34     [F_y, ~] = ForceDeflection(E, w, t_s, t_c, R, L, alpha_angle, beta_angle, F_x, delta_t);
35     P_w = F_y / (w * l_t);
36
37     % Calculate static sinkage z_0
38     if l_t < w
39         z_0 = (P_w / (k_c / l_t + k_phi))^(1/n);
40     else
41         z_0 = (P_w / (k_c / w + k_phi))^(1/n);
42     end
43
44     theta_f0 = acos(1 - (z_0+delta_t)/R); % Static entry angle contact patch
45     theta_t0 = asin(l_t / (2*R)); % Static flattening angle contact patch
46
47     % Calculate total static ground reaction force F_y0
48     sigma_Fs = @(theta) (k_c / w + k_phi) * R^n * (cos(theta) - cos(theta_f0)).^n;
49
50     integrand_Fs = @(theta) sigma_Fs(theta) .* cos(theta);
51     F_s = R * w * integral(integrand_Fs, theta_t0, theta_f0);
52     F_w = P_w * w * l_t;
53     F_y0 = F_w + 2 * F_s;
54
55     % Check if F_y0 is almost equal to vertical load W
56     if abs(F_y0 - W) < tolerance % Converged
57         % Output results
58         % disp('Result static equilibrium:');
59         % fprintf('Converged to correct delta_t value after %d iterations.\n', iter);
60         % fprintf('Leg deflection delta_t: %.4f mm\n', delta_t*10^3);
61         % fprintf('Length flattened section l_t: %.4f mm\n', l_t*10^3);
62         % fprintf('Static sinkage z_0: %.4f mm\n', z_0*10^3);
63         % fprintf('Static entry angle theta_f0 %.4f deg\n', rad2deg(theta_f0))
64         % fprintf('Static flattening angle theta_t0 %.4f deg\n', rad2deg(theta_t0))
65         % fprintf('Static vertical force flattened section F_w: %.4f N\n', F_w);
66         % fprintf('Static vertical force entry & exit section F_s: %.4f N\n', F_s);

```

```

67         % fprintf('Static total vertical force F_y0: %.4f N\n', F_y0);
68         break;
69     else
70         delta_t = delta_t + update_factor*(W-F_y0); % Update delta_t for the next iteration
71     end
72
73     % If maximum iterations reached without convergence, display a warning
74     if iter == max_iterations
75         % warning('Maximum iterations reached without convergence. ');
76         % fprintf('Max. iter. value delta_t: %.4f mm\n', delta_t*10^3);
77         % fprintf('Max. iter. value F_y0: %.4f N\n', F_y0);
78     end
79 end
80
81 theta_t = theta_t0; % Flattening angle considered equal in static and quisi-static state
82
83
84 %% Quisi-static equilibrium
85 z = z_0; % Initial guess for leg sinkage
86 for iter = 1:max_iterations2
87
88     theta_f = acos(1 - (z+delta_t)/R); % Entry angle contact patch
89     theta_r = - acos(1 - lambda * (z+delta_t) / R); % Exit angle contact patch
90     theta_m = (0.4+0.15*s)*theta_f; % Maximum normal stress angle
91
92     theta_t_deg = rad2deg(theta_t);
93     theta_f_deg = rad2deg(theta_f);
94     theta_r_deg = rad2deg(theta_r);
95     theta_m_deg = rad2deg(theta_m);
96
97     % Normal stress sigma(theta) function
98     sigma = @(theta) calculate_sigma(theta, theta_f, theta_r, theta_m, k_c, k_phi, z, R, w, n
99         , l_t, theta_t);
100
101     % Soil deformation j(theta) function
102     j = @(theta) calculate_j_theta(theta, theta_f, theta_t, R, s, delta_t);
103
104     % Shear stress tau(theta) function
105     tau = @(theta) calculate_tau(sigma(theta), c, phi, j(theta), kappa);
106
107     % Vertical ground reaction force F
108     integrand_F1 = @(theta) (sigma(theta) .* cos(theta) + tau(theta) .* sin(theta));
109
110     if l_t < w && l_t ~= 0 % Flattened section normal pressure, as theta_t and l_t are
111         constant and independent of theta.
112         sigma_t = (k_c / l_t + k_phi) * z^n ;
113     else
114         sigma_t = (k_c / w + k_phi) * z^n ;
115     end
116
117     F_AB = R * w * integral(integrand_F1, theta_t, theta_f); % Entry section contribution
118     F_BC = l_t * w * sigma_t; % Flattened section
119     % contribution, as theta_t and l_t are constant independent of theta.
120     F_CD = R * w * integral(integrand_F1, theta_r, -theta_t); % Exit section contribution
121
122     % If flattening angle is bigger than exit angle, ignore exit section contribution
123     if -theta_t <= theta_r
124         F = F_AB + F_BC;
125     else
126         F = F_AB + F_BC + F_CD;
127     end
128
129     % Check if F matches the load W
130     if abs(F - W) < tolerance2 % Converged
131         % disp(' ');
132         % disp('Result dynamic equilibrium:');
133         % fprintf('Converged to correct z value after %d iterations.\n', iter);
134         % fprintf('Final value of sinkage z: %.4f mm\n', z*10^3);
135         % fprintf('Final value of vertical ground reaction force F: %.4f N\n', F);
136         break;
137     else

```



```

135     z = z + update_factor2*(W-F);           % Update z for the next iteration
136 end
137
138 % If maximum iterations reached without convergence, display a warning
139 if iter == max_iterations2
140     % warning('Maximum iterations reached without convergence. ');
141     % fprintf('Max. iter. value of z: %.4f meters\n', z);
142     % fprintf('Max. iter. value of F: %.4f N\n', F);
143     break;
144 end
145 end
146
147 % Calculate thrust H
148 integrand_H_AB = @(theta) tau(theta) .* cos(theta);
149 integrand_H_BC = @(theta) tau(theta) ./ cos(theta).^2;
150 integrand_H_CD = @(theta) (tau(theta) .* cos(theta) - sigma(theta) .* sin(theta));
151 H_AB = R * w * integral(integrand_H_AB, theta_t, theta_f);           % Entry section
152                                     contribution
153 H_BC = (R - delta_t) * w * integral(integrand_H_BC, -theta_t, theta_t); % Flattened
154                                     section contribution
155 H_CD = R * w * integral(integrand_H_CD, theta_r, -theta_t);           % Exit section
156                                     contribution
157
158 % If flattening angle is bigger than exit angle, ignore exit section contribution
159 if -theta_t <= theta_r
160     H = H_AB + H_BC;
161 else
162     H = H_AB + H_BC + H_CD;
163 end
164
165 % Calculate resistance force R_t
166 % Soil compaction resistance R_c
167 integrand_Rc = @(theta) sigma(theta) .* sin(theta);
168 R_c = R * w * integral(integrand_Rc, theta_t, theta_f);
169
170 % Leg deformation resistance R_d
171 epsilon = 1 - exp(-k_e * delta_t / h);
172 if theta_t_deg > 0
173     R_d = (3.581 * w * (2*R)^2 * P_w * epsilon * (0.0349 * theta_t_deg - sind(2*theta_t_deg))
174           ) / (theta_t_deg * (2*R - 2*delta_t));
175 else
176     R_d = 0;           % No leg deformation resistance (Rigid leg)
177 end
178
179 R_t = R_c + R_d;
180
181 % Calculate drawbar pull DP
182 DP = H - R_t;
183
184 % Calculate resistance torque T
185 integrand_T_AB = @(theta) tau(theta);
186 integrand_T_BC = @(theta) (tau(theta) + sigma_t * tan(theta)) ./ cos(theta).^2;
187 integrand_T_CD = @(theta) tau(theta);
188
189 T_AB = R^2 * w * integral(integrand_T_AB, theta_t, theta_f);           % Entry section
190                                     contribution
191 T_BC = (R - delta_t)^2 * w * integral(integrand_T_BC, -theta_t, theta_t); % Flattened
192                                     section contribution
193 T_CD = R^2 * w * integral(integrand_T_CD, theta_r, -theta_t);           % Exit section
194                                     contribution
195
196 % If flattening angle is bigger than exit angle, ignore exit section contribution
197 if -theta_t <= theta_r
198     T = T_AB + T_BC;
199 else
200     T = T_AB + T_BC + T_CD;
201 end
202
203 % Calculate tractive efficiency eta
204 eta = (DP * (1 - s) * R / T) * 100;
205

```

```

199 %% Maximum stress while skid steering constraint
200 % Maximum lateral shear stress
201 tau_z_max = @(theta) (c + sigma(theta) .* tan(phi));
202
203 % Calculate the maximum lateral resistance when skid steering
204 integrand_Rz_AB = @(theta) tau_z_max(theta);
205 integrand_Rz_BC = @(theta) tau_z_max(theta) ./ cos(theta).^2;
206 integrand_Rz_CD = @(theta) tau_z_max(theta);
207
208 Rz_AB = R * w * integral(integrand_Rz_AB, theta_t, theta_f); % Entry section
209 % contribution
210 Rz_BC = (R - delta_t) * w * integral(integrand_Rz_BC, -theta_t, theta_t); % Flattened
211 % section contribution
212 Rz_CD = R * w * integral(integrand_Rz_CD, theta_r, -theta_t); % Exit section
213 % contribution
214
215 if -theta_t <= theta_r
216     Rz_max = Rz_AB + Rz_BC;
217 else
218     Rz_max = Rz_AB + Rz_BC + Rz_CD;
219 end
220
221 %% Constraints
222 if delta_t == 0
223     % If rigid leg is considered, some constraints are not of interest
224     sigma_max_walk = 0;
225     sigma_max_skid = 0;
226     sigma_max_side = 0;
227     delta_x = 0;
228     R_eff = R;
229     [y_c] = ClimbingHeight(R, y_g, z, delta_t);
230 else
231     %% Stress while walking constraint and Motor torque transmission constraint
232     % F_x is the drawbar pull DP
233     % F_y is the vertical gravitational force W
234     [sigma_max_walk, sigma_vm_straight_walk, sigma_vm_curved_walk, delta_x] =
235         MaxStressAndDeflection2D(E, w, t_s, t_c, R, L, beta_angle, DP, W);
236
237     %% Skid steering constraint
238     % F_x is the drawbar pull DP
239     % F_y is the vertical gravitational force W
240     % F_z is the maximum lateral resistance equals Rz_max
241     [sigma_max_skid, sigma_vm_straight_skid, sigma_vm_curved_skid] = MaxStress3D(E, G, w, t_s,
242         t_c, R, L, beta_angle, mu, DP, W, Rz_max);
243
244     %% Side gradient constraint
245     [sigma_max_side, sigma_vm_straight_side, sigma_vm_curved_side] = SidewaysGradient( ...
246         g,m,k_c,k_phi,n,phi_deg,c,lambda,s,k_e,h,kappa, E, G, w, t_s, t_c, R, L, ...
247         alpha_angle, beta_angle, mu, F_xside, b_LZ, gamma_angle, y_com, N, ...
248         tolerance, max_iterations, update_factor, tolerance2, max_iterations2, update_factor2
249     );
250
251     %% End of contact surface constraint
252     % F_x is the drawbar pull DP
253     % F_y is the full gravitational force W, due to small contact surface
254     [R_eff] = MinimumRadiusNextStep(E, w, t_s, t_c, R, L, beta_angle, DP, W);
255
256     %% Climbing height constraint
257     % delta_y is the maximum vertical deflection delta_t
258     [y_c] = ClimbingHeight(R, y_g, z, delta_t);
259 end
260
261 %% Output results
262 % fprintf('Static vertical force Fy: %.4f N\n', F_y);
263 % fprintf('Gravitational force on leg axle W: %.4f N\n', W);
264 % fprintf('Entry angle theta_f: %.4f deg\n', theta_f_deg);
265 % fprintf('Maximum normal pressure angle theta_m: %.4f deg\n', theta_m_deg);
266 % fprintf('Flattened section angle theta_t: %.4f deg\n', theta_t_deg);
267 % fprintf('Exit angle theta_r: %.4f deg\n', theta_r_deg);

```

```

264 % fprintf('Vertical force entry section F_AB: %.4f N\n', F_AB);
265 % fprintf('Vertical force flattened section F_BC: %.4f N\n', F_BC);
266 % fprintf('Vertical force exit section F_CD: %.4f N\n', F_CD);
267 % fprintf('Thrust entry section H_AB: %.4f N\n', H_AB);
268 % fprintf('Thrust flattened section H_BC: %.4f N\n', H_BC);
269 % fprintf('Thrust exit section H_CD: %.4f N\n', H_CD);
270 % fprintf('Compaction resistance R_c: %.4f N\n', R_c);
271 % fprintf('Deformation resistance R_d: %.4f N\n', R_d);
272 % fprintf('Max lateral resistance entry section Rz_AB: %.4f N\n', Rz_AB);
273 % fprintf('Max lateral resistance flattened section Rz_BC: %.4f N\n', Rz_BC);
274 % fprintf('Max lateral resistance exit section Rz_CD: %.4f N\n', Rz_CD);
275 % fprintf('Max lateral resistance Rz_max: %.4f N\n', Rz_max);
276 % fprintf('Slip ratio s: %.4f \n', s);
277 % disp(' ');
278
279 % fprintf('Vertical force F: %.4f N\n', F);
280 % fprintf('Sinkage z: %.4f mm\n', z*10^3);
281 % fprintf('Thrust H: %.4f N\n', H);
282 % fprintf('Resistance R_t: %.4f N\n', R_t);
283 % fprintf('Drawbar Pull DP: %.4f N\n', DP);
284 % fprintf('Resistance torque T: %.4f N\n', T);
285 % fprintf('Tractive efficiency eta: %.4f %%\n', eta);
286 % fprintf('Max. stress in straight flexure while walking sigma_vm_straight_walk: %.4f MPa\n',
    sigma_vm_straight_walk/1e6);
287 % fprintf('Max. stress in curved flexure while walking sigma_vm_curved_walk: %.4f MPa\n',
    sigma_vm_curved_walk/1e6);
288 % fprintf('Max. stress in straight flexure while skid steering sigma_vm_straight_skid: %.4f
    MPa\n', sigma_vm_straight_skid/1e6);
289 % fprintf('Max. stress in curved flexure while skid steering sigma_vm_curved_skid: %.4f MPa\n',
    sigma_vm_curved_skid/1e6);
290 % fprintf('Max. stress in straight flexure while climbing along a sideways gradient
    sigma_vm_straight_side: %.4f MPa\n', sigma_vm_straight_side/1e6);
291 % fprintf('Max. stress in curved flexure while climbing along a sideways gradient
    sigma_vm_curved_side: %.4f MPa\n', sigma_vm_curved_side/1e6);
292
293 %% Functions
294 % Normal pressure sigma(theta)
295 function sigma_theta = calculate_sigma(theta, theta_f, theta_r, theta_m, k_c, k_phi, z, R, w,
    n, l_t, theta_t)
296     if theta_m > theta_t
297         sigma_theta = zeros(size(theta)); % Initialise sigma_theta for all values of theta.
298
299         % Entry section
300         entry_section = (theta >= theta_m) & (theta <= theta_f);
301         sigma_theta(entry_section) = (k_c / w + k_phi) * R^n * (cos(theta(entry_section)) -
            cos(theta_f)).^n;
302
303         % Flattened section (Denoted to calculate H_BC and T_BC)
304         flat_section = ((theta >= -theta_t) & (theta < theta_t));
305         if l_t < w
306             sigma_theta(flat_section) = (k_c / l_t + k_phi) * z^n;
307         else
308             sigma_theta(flat_section) = (k_c / w + k_phi) * z^n;
309         end
310
311         % Exit section and further section
312         exit_section = ((theta >= theta_r) & (theta < -theta_t)) | ((theta >= theta_t) & (
            theta < theta_m));
313         sigma_theta(exit_section) = (k_c / w + k_phi) * R^n * (cos(theta_f - (theta(
            exit_section) - theta_r)*(theta_f - theta_m)/(theta_m - theta_r)) - cos(theta_f))
            .^n;
314
315     else
316         % Condition when theta_m <= theta_t
317         sigma_theta = zeros(size(theta)); % Initialise sigma_theta for all values of theta
318
319         % Entry section
320         entry_section = (theta >= theta_t) & (theta <= theta_f);
321         sigma_theta(entry_section) = (k_c / w + k_phi) * R^n * (cos(theta(entry_section)) -
            cos(theta_f)).^n;
322

```

```

323     % Flattened section (Denoted to calculate H_BC and T_BC)
324     flat_section = ((theta >= -theta_t) & (theta < theta_t));
325     if l_t < w
326         sigma_theta(flat_section) = (k_c / l_t + k_phi) * z^n;
327     else
328         sigma_theta(flat_section) = (k_c / w + k_phi) * z^n;
329     end
330
331     % Exit section
332     exit_section = (theta >= theta_r) & (theta < -theta_t);
333     sigma_theta(exit_section) = (k_c / w + k_phi) * R^n * (cos(theta_f - (theta(
        exit_section) - theta_r)*(theta_f - theta_m)/(theta_m - theta_r)) - cos(theta_f))
        .^n;
334
335     end
336 end
337
338 % Shear stress tau(theta)
339 function tau_theta = calculate_tau(sigma_theta, c, phi, j_theta, kappa)
340     tau_theta = (c + sigma_theta .* tan(phi)) .* (1 - exp(-j_theta ./ kappa));
341 end
342
343 % Soil deformation j(theta)
344 function j_theta = calculate_j_theta(theta, theta_f, theta_t, R, s, delta_t)
345     if abs(theta) >= abs(theta_t)
346         j_theta = R * (theta_f - theta - (1 - s) * (sin(theta_f) - sin(theta)));
347     else
348         j_theta_t = R * (theta_f - theta_t - (1 - s) * (sin(theta_f) - sin(theta_t)));
349         j_theta = j_theta_t + s * (R * sin(theta_t) - (R - delta_t) * tan(theta));
350     end
351 end
352 end

```

F.6. Compliance model

F.6.1. Force-deflection relationship

```

1 function [F_y, delta_x]=...
2 ForceDeflection(E, w, t_s, t_c, R, L, alpha_angle, beta_angle, F_x, delta_y)
3
4 % Moment of inertia and area
5 I_sz = (1/12) * w * t_s^3;
6 I_cz = (1/12) * w * t_c^3;
7 A_s = w * t_s;
8 A_c = w * t_c;
9
10 %% Straight flexure
11 % Deflections in straight flexure
12 delta_Cr_straight = @(F_Cr) (F_Cr * L)/(E*A_s);
13 delta_Ct_straight = @(F_Ct, M_Cz) (M_Cz * L^2)/(2*E*I_sz) + (F_Ct * L^3) / (3*E*I_sz);
14 phi_Cz_straight = @(F_Ct, M_Cz) (M_Cz * L)/(E*I_sz) + (F_Ct * L^2)/(2*E*I_sz);
15
16 %% Curved flexure
17 % Force and moment equilibrium full straight flexure
18 F_Br = @(F_Cr) F_Cr;
19 F_Bt = @(F_Ct) F_Ct;
20 M_Bz = @(F_Ct, M_Cz) F_Ct*L + M_Cz;
21
22 % Moment functions curved flexure
23 Mz1 = @(theta, F_Ct, F_Cr, M_Cz) F_Bt(F_Ct) * R * (1 - cos(theta)) + F_Br(F_Cr) * R * sin(
    theta) - M_Bz(F_Ct, M_Cz);
24 Mz2 = @(theta, F_Ct, F_Cr, M_Cz, F_y) Mz1(theta, F_Ct, F_Cr, M_Cz) - F_x * R * (1 - cos(theta)
    - alpha_angle)) - F_y * R * sin(theta - alpha_angle);
25
26 % Compute partial derivatives
27 partial_Mz1_FCr = @(theta) R * sin(theta);
28 partial_Mz1_FCr = @(theta) R * (1 - cos(theta)) - L;
29 partial_Mz1_MCz = @(theta) -1;
30
31 partial_Mz2_FCr = @(theta) partial_Mz1_FCr(theta);
32 partial_Mz2_FCr = @(theta) partial_Mz1_FCr(theta);
33 partial_Mz2_MCz = @(theta) partial_Mz1_MCz(theta);
34
35 partial_Mz1_Fx = @(theta) 0;
36 partial_Mz2_Fx = @(theta) -R * (1 - cos(theta - alpha_angle));
37
38 partial_Mz1_Fy = @(theta) 0;
39 partial_Mz2_Fy = @(theta) -R * sin(theta - alpha_angle);
40
41 % Deflections in curved flexure
42 delta_Br_curved = @(F_Cr, F_Ct, M_Cz, F_y) ...
43     (R/(E*I_cz)) * (integral(@(theta) Mz1(theta, F_Ct, F_Cr, M_Cz) .* partial_Mz1_FCr(theta),
44         0, alpha_angle, 'RelTol',1e-12,'AbsTol',1e-12) + ...
45         integral(@(theta) Mz2(theta, F_Ct, F_Cr, M_Cz, F_y) .* partial_Mz2_FCr(theta),
46             alpha_angle, beta_angle, 'RelTol',1e-12,'AbsTol',1e-12));
47
48 delta_Bt_curved = @(F_Cr, F_Ct, M_Cz, F_y) ...
49     (R/(E*I_cz)) * (integral(@(theta) Mz1(theta, F_Ct, F_Cr, M_Cz) .* partial_Mz1_FCr(theta),
50         0, alpha_angle, 'RelTol',1e-12,'AbsTol',1e-12) + ...
51         integral(@(theta) Mz2(theta, F_Ct, F_Cr, M_Cz, F_y) .* partial_Mz2_FCr(theta),
52             alpha_angle, beta_angle, 'RelTol',1e-12,'AbsTol',1e-12));
53
54 phi_Bz_curved = @(F_Cr, F_Ct, M_Cz, F_y) ...
55     (R/(E*I_cz)) * (integral(@(theta) Mz1(theta, F_Ct, F_Cr, M_Cz) .* partial_Mz1_MCz(theta),
56         0, alpha_angle, 'RelTol',1e-12,'AbsTol',1e-12) + ...
57         integral(@(theta) Mz2(theta, F_Ct, F_Cr, M_Cz, F_y) .* partial_Mz2_MCz(theta),
58             alpha_angle, beta_angle, 'RelTol',1e-12,'AbsTol',1e-12));
59
60 delta_y_curved = @(F_Cr, F_Ct, M_Cz, F_y) ...
61     (R/(E*I_cz)) * (integral(@(theta) Mz1(theta, F_Ct, F_Cr, M_Cz) .* partial_Mz1_Fy(theta),
62         0, alpha_angle, 'RelTol',1e-12,'AbsTol',1e-12) + ...
63         integral(@(theta) Mz2(theta, F_Ct, F_Cr, M_Cz, F_y) .* partial_Mz2_Fy(theta),
64             alpha_angle, beta_angle, 'RelTol',1e-12,'AbsTol',1e-12));
65
66
67
68
69
70
71
72
73
74
75
76
77
78
79
80
81
82
83
84
85
86
87
88
89
90
91
92
93
94
95
96
97
98
99

```

```

58 %% Solving
59 % Define function for nonlinear solver
60 force_equations = @(F) [
61     delta_Br_curved(F(1), F(2), F(3), F(4)) + delta_Cr_straight(F(1));
62     delta_Bt_curved(F(1), F(2), F(3), F(4)) + delta_Ct_straight(F(2), F(3));
63     phi_Bz_curved(F(1), F(2), F(3), F(4)) + phi_Cz_straight(F(2), F(3));
64     delta_y - delta_y_curved(F(1), F(2), F(3), F(4))
65 ];
66
67 % Improved numerical integration settings
68 opts = optimset('TolFun', 1e-12, 'TolX', 1e-12, 'Display', 'off');
69
70 % Solve
71 F_init = [1,1,0,1];
72 lb = [-Inf, -Inf, -Inf, 0]; % F_y must be >= 0
73 ub = [Inf, Inf, Inf, Inf];
74 F = lsqnonlin(@(F) force_equations(F), F_init, lb, ub, opts);
75
76 F_Cr = F(1);
77 F_Ct = F(2);
78 M_Cz = F(3);
79 F_y = F(4);
80
81 %% Deflection of loading point
82 % Longitudinal deflection loading point
83 delta_x = (R/(E*I_cz)) * (integral(@(theta) Mz1(theta, F_Ct, F_Cr, M_Cz) .* partial_Mz1_Fx(
84     theta), 0, alpha_angle, 'RelTol', 1e-12, 'AbsTol', 1e-12) + ...
85     integral(@(theta) Mz2(theta, F_Ct, F_Cr, M_Cz, F_y) .* partial_Mz2_Fx(theta)
86         , alpha_angle, beta_angle, 'RelTol', 1e-12, 'AbsTol', 1e-12));
87 end

```

F.6.2. Longitudinal force-deflection relationship

```

1 function [delta_y_init]=...
2 LongitudinalForceDeflection(E, w, t_s, t_c, R, L, alpha_angle, beta_angle, F_x)
3
4 % No vertical force
5 F_y = 0;
6
7 % Moment of inertia and area
8 I_sz = (1/12) * w * t_s^3;
9 I_cz = (1/12) * w * t_c^3;
10 A_s = w * t_s;
11
12 %% Straight flexure
13 % Deflections in straight flexure
14 delta_Cr_straight = @(F_Cr) (F_Cr * L)/(E*A_s);
15 delta_Ct_straight = @(F_Ct, M_Cz) (M_Cz * L^2)/(2*E*I_sz) + (F_Ct * L^3) / (3*E*I_sz);
16 phi_Cz_straight = @(F_Ct, M_Cz) (M_Cz * L)/(E*I_sz) + (F_Ct * L^2)/(2*E*I_sz);
17
18 %% Curved flexure
19 % Force and moment equilibrium full straight flexure
20 F_Br = @(F_Cr) F_Cr;
21 F_Bt = @(F_Ct) F_Ct;
22 M_Bz = @(F_Ct, M_Cz) F_Ct*L + M_Cz;
23
24 % Moment functions curved flexure
25 Mz1 = @(theta, F_Ct, F_Cr, M_Cz) F_Bt(F_Ct) * R * (1 - cos(theta)) + F_Br(F_Cr) * R * sin(
    theta) - M_Bz(F_Ct, M_Cz);
26 Mz2 = @(theta, F_Ct, F_Cr, M_Cz) Mz1(theta, F_Ct, F_Cr, M_Cz) - F_x * R * (1 - cos(theta -
    alpha_angle)) - F_y * R * sin(theta - alpha_angle);
27
28 % Compute partial derivatives
29 partial_Mz1_FCr = @(theta) R * sin(theta);
30 partial_Mz1_FCr = @(theta) R * (1 - cos(theta)) - L;
31 partial_Mz1_MCz = @(theta) -1;
32
33 partial_Mz2_FCr = @(theta) partial_Mz1_FCr(theta);
34 partial_Mz2_FCr = @(theta) partial_Mz1_FCr(theta);
35 partial_Mz2_MCz = @(theta) partial_Mz1_MCz(theta);
36
37 partial_Mz1_Fx = @(theta) 0;
38 partial_Mz2_Fx = @(theta) -R * (1 - cos(theta - alpha_angle));
39
40 partial_Mz1_Fy = @(theta) 0;
41 partial_Mz2_Fy = @(theta) -R * sin(theta - alpha_angle);
42
43 % Deflections in curved flexure
44 delta_Br_curved = @(F_Cr, F_Ct, M_Cz) ...
45     (R/(E*I_cz)) * (integral(@(theta) Mz1(theta, F_Ct, F_Cr, M_Cz) .* partial_Mz1_FCr(theta),
46         0, alpha_angle, 'RelTol',1e-12,'AbsTol',1e-12) + ...
47         integral(@(theta) Mz2(theta, F_Ct, F_Cr, M_Cz) .* partial_Mz2_FCr(theta),
48             alpha_angle, beta_angle, 'RelTol',1e-12,'AbsTol',1e-12));
49
50 delta_Bt_curved = @(F_Cr, F_Ct, M_Cz) ...
51     (R/(E*I_cz)) * (integral(@(theta) Mz1(theta, F_Ct, F_Cr, M_Cz) .* partial_Mz1_FCr(theta),
52         0, alpha_angle, 'RelTol',1e-12,'AbsTol',1e-12) + ...
53         integral(@(theta) Mz2(theta, F_Ct, F_Cr, M_Cz) .* partial_Mz2_FCr(theta),
54             alpha_angle, beta_angle, 'RelTol',1e-12,'AbsTol',1e-12));
55
56 phi_Bz_curved = @(F_Cr, F_Ct, M_Cz) ...
57     (R/(E*I_cz)) * (integral(@(theta) Mz1(theta, F_Ct, F_Cr, M_Cz) .* partial_Mz1_MCz(theta),
58         0, alpha_angle, 'RelTol',1e-12,'AbsTol',1e-12) + ...
59         integral(@(theta) Mz2(theta, F_Ct, F_Cr, M_Cz) .* partial_Mz2_MCz(theta),
60             alpha_angle, beta_angle, 'RelTol',1e-12,'AbsTol',1e-12));
61
62 %% Solving
63 % Define function for nonlinear solver
64 force_equations = @(F) [
65     delta_Br_curved(F(1), F(2), F(3)) + delta_Cr_straight(F(1));
66     delta_Bt_curved(F(1), F(2), F(3)) + delta_Ct_straight(F(2), F(3));
67     phi_Bz_curved(F(1), F(2), F(3)) + phi_Cz_straight(F(2), F(3));

```

```

62 ];
63
64 % Improved numerical integration settings
65 opts = optimset('TolFun', 1e-12, 'TolX', 1e-12, 'Display', 'off');
66
67 % Solve
68 F_init = [1,1,0];
69 lb = [-Inf, -Inf, -Inf];
70 ub = [Inf, Inf, Inf];
71 F = lsqnonlin(@(F) force_equations(F), F_init, lb, ub, opts);
72
73 F_Cr = F(1);
74 F_Ct = F(2);
75 M_Cz = F(3);
76
77 %% Deflection of loading point
78 % Longitudinal deflection loading point
79 delta_x_init = (R/(E*I_cz)) * (integral(@(theta) Mz1(theta, F_Ct, F_Cr, M_Cz) .*
    partial_Mz1_Fx(theta), 0, alpha_angle, 'RelTol',1e-12,'AbsTol',1e-12) + ...
80     integral(@(theta) Mz2(theta, F_Ct, F_Cr, M_Cz) .* partial_Mz2_Fx(theta),
    alpha_angle, beta_angle, 'RelTol',1e-12,'AbsTol',1e-12));
81
82 % Vertical deflection loading point
83 delta_y_init = (R/(E*I_cz)) * (integral(@(theta) Mz1(theta, F_Ct, F_Cr, M_Cz) .*
    partial_Mz1_Fy(theta), 0, alpha_angle, 'RelTol',1e-12,'AbsTol',1e-12) + ...
84     integral(@(theta) Mz2(theta, F_Ct, F_Cr, M_Cz) .* partial_Mz2_Fy(theta),
    alpha_angle, beta_angle, 'RelTol',1e-12,'AbsTol',1e-12));
85 end

```


F.7. Constraints

F.7.1. Constraints definition

```

1 function [con, ceq] = CONS(x)
2 % Computation of the constraint function
3 % Input:    x: [1x3] row of design variables (t_c, t_s and L)
4 % Output:   g: {1x6} row of inequality constraint values
5
6 % Assignment of design variables
7 t_c = x(1);
8 t_s = x(2);
9 L = x(3);
10
11 % Input parameters
12 Parameters;
13
14 % Analysis
15 [~, ~, ~, ~, ~, sigma_max_walk, sigma_max_skid, sigma_max_side, delta_x, R_eff, y_c]=...
16     Analysis(t_c,t_s,L,g,m,k_c,k_phi,n,phi_deg,c,lambda,s,k_e,h,kappa,E,G,w,R, ...
17     alpha_angle,beta_angle,mu,F_x,F_xside,y_g,b_LZ,gamma_angle,y_com,N, ...
18     tolerance,max_iterations,update_factor,tolerance2,max_iterations2,update_factor2);
19
20 %% Inequality constraints
21 % Maximum Von Mises stress in flexure due to walking
22 con(1) = SF * sigma_max_walk / sigma_y - 1;
23
24 % Maximum Von Mises stress in flexure due to skid steering
25 con(2) = SF * sigma_max_skid / sigma_y - 1;
26
27 % Maximum Von Mises stress in flexure due to climbing along a sideways gradient
28 con(3) = SF * sigma_max_side / sigma_y - 1;
29
30 % Maximum longitudinal deflection for torque transmission
31 con(4) = delta_x / delta_x_max - 1;
32
33 % Minimum end of contact surface radius
34 con(5) = 1 - R_eff / R_eff_min;
35
36 % Minimum climbing height
37 con(6) = 1 - y_c / y_c_min;
38
39 %% No equality constraints
40 ceq = [];

```

F.7.2. Stress limit while walking & motor torque transmission

```

1 function [sigma_max_vm, sigma_max_vm_straight, sigma_max_vm_curved, delta_x_max]=...
2 MaxStressAndDeflection2D(E, w, t_s, t_c, R, L, beta_angle, F_x, F_y)
3
4 % Initialise arrays for storing results
5 alpha_values = linspace(0, beta_angle-deg2rad(0.1), 90);
6 sigma_straight_values = zeros(size(alpha_values));
7 sigma_curved_values = zeros(size(alpha_values));
8 delta_x_values = zeros(size(alpha_values));
9
10 % Cycle through angles alpha to find maximum stress angle
11 for i = 1:length(alpha_values)
12     alpha_angle = alpha_values(i);
13
14     % Moment of inertia and area
15     I_sz = (1/12) * w * t_s^3;
16     I_cz = (1/12) * w * t_c^3;
17     A_s = w * t_s;
18     A_c = w * t_c;
19
20     %% Straight flexure
21     % Deflections in straight flexure
22     delta_Cr_straight = @(F_Cr) (F_Cr * L)/(E*A_s);
23     delta_Ct_straight = @(F_Ct, M_Cz) (M_Cz * L^2)/(2*E*I_sz) + (F_Ct * L^3) / (3*E*I_sz);
24     phi_Cz_straight = @(F_Ct, M_Cz) (M_Cz * L)/(E*I_sz) + (F_Ct * L^2)/(2*E*I_sz);
25
26     %% Curved flexure
27     % Force and moment equilibrium full straight flexure
28     F_Br = @(F_Cr) F_Cr;
29     F_Bt = @(F_Ct) F_Ct;
30     M_Bz = @(F_Ct, M_Cz) F_Ct*L + M_Cz;
31
32     % Moment functions curved flexure
33     Mz1 = @(theta, F_Ct, F_Cr, M_Cz) F_Bt(F_Ct) * R * (1 - cos(theta)) + F_Br(F_Cr) * R * sin
34         (theta) - M_Bz(F_Ct, M_Cz);
35     Mz2 = @(theta, F_Ct, F_Cr, M_Cz) Mz1(theta, F_Ct, F_Cr, M_Cz) - F_x * R * (1 - cos(theta
36         - alpha_angle)) - F_y * R * sin(theta - alpha_angle);
37
38     % Compute partial derivatives
39     partial_Mz1_FCr = @(theta) R * sin(theta);
40     partial_Mz1_FCr = @(theta) R * (1 - cos(theta)) - L;
41     partial_Mz1_MCz = @(theta) -1;
42
43     partial_Mz2_FCr = @(theta) partial_Mz1_FCr(theta);
44     partial_Mz2_FCr = @(theta) partial_Mz1_FCr(theta);
45     partial_Mz2_MCz = @(theta) partial_Mz1_MCz(theta);
46
47     partial_Mz1_Fx = @(theta) 0;
48     partial_Mz2_Fx = @(theta) -R * (1 - cos(theta - alpha_angle));
49
50     % Deflections in curved flexure
51     delta_Br_curved = @(F_Cr, F_Ct, M_Cz) ...
52         (R/(E*I_cz)) * (integral(@(theta) Mz1(theta, F_Ct, F_Cr, M_Cz) .* partial_Mz1_FCr(
53             theta), 0, alpha_angle, 'RelTol',1e-12,'AbsTol',1e-12) + ...
54             integral(@(theta) Mz2(theta, F_Ct, F_Cr, M_Cz) .* partial_Mz2_FCr(theta),
55                 alpha_angle, beta_angle, 'RelTol',1e-12,'AbsTol',1e-12));
56
57     delta_Bt_curved = @(F_Cr, F_Ct, M_Cz) ...
58         (R/(E*I_cz)) * (integral(@(theta) Mz1(theta, F_Ct, F_Cr, M_Cz) .* partial_Mz1_FCr(
59             theta), 0, alpha_angle, 'RelTol',1e-12,'AbsTol',1e-12) + ...
60             integral(@(theta) Mz2(theta, F_Ct, F_Cr, M_Cz) .* partial_Mz2_FCr(theta),
61                 alpha_angle, beta_angle, 'RelTol',1e-12,'AbsTol',1e-12));
62
63     phi_Bz_curved = @(F_Cr, F_Ct, M_Cz) ...
64         (R/(E*I_cz)) * (integral(@(theta) Mz1(theta, F_Ct, F_Cr, M_Cz) .* partial_Mz1_MCz(
65             theta), 0, alpha_angle, 'RelTol',1e-12,'AbsTol',1e-12) + ...
66             integral(@(theta) Mz2(theta, F_Ct, F_Cr, M_Cz) .* partial_Mz2_MCz(theta),
67                 alpha_angle, beta_angle, 'RelTol',1e-12,'AbsTol',1e-12));
68
69     %% Solving

```

```

62 % Define function for nonlinear solver
63 force_equations = @(F) [
64     delta_Br_curved(F(1), F(2), F(3)) + delta_Cr_straight(F(1));
65     delta_Bt_curved(F(1), F(2), F(3)) + delta_Ct_straight(F(2), F(3));
66     phi_Bz_curved(F(1), F(2), F(3)) + phi_Cz_straight(F(2), F(3));
67 ];
68
69 % Improved numerical integration settings
70 opts = optimset('TolFun', 1e-12, 'TolX', 1e-12, 'Display', 'off');
71
72 % Solve
73 F_init = [0 1 0.01];
74 F = fsolve(force_equations, F_init, opts);
75
76 F_Cr = F(1);
77 F_Ct = F(2);
78 M_Cz = F(3);
79
80 %% Deflection of loading point
81 % Longitudinal deflection loading point
82 delta_x = (R/(E*I_cz)) * (integral(@(theta) Mz1(theta, F_Ct, F_Cr, M_Cz) .*
83     partial_Mz1_Fx(theta), 0, alpha_angle, 'RelTol', 1e-12, 'AbsTol', 1e-12) + ...
84     integral(@(theta) Mz2(theta, F_Ct, F_Cr, M_Cz) .* partial_Mz2_Fx(theta),
85     alpha_angle, beta_angle, 'RelTol', 1e-12, 'AbsTol', 1e-12));
86
87 delta_x_values(i) = delta_x;
88
89 %% Stress straight flexure
90 % Stress at point C
91 sigma_r1 = F_Br(F_Cr) / A_s;
92 sigma_r2 = M_Cz*(t_s/2) / I_sz;
93 sigma_r = sigma_r1 + sigma_r2;
94 tau_rt_straight = (3*F_Bt(F_Ct)) / (2*A_s);
95
96 sigma_vm_straight = sqrt(sigma_r^2 + 3*tau_rt_straight^2);
97 sigma_straight_values(i) = sigma_vm_straight;
98
99 %% Stress curved flexure
100 % Stress at point A
101 r_1 = R-t_c;
102 r_2 = R;
103 R_a = t_c/log(r_2/r_1);
104 R_str = (r_1+r_2)/2;
105 sigma_curved_inner = - Mz2(beta_angle, F_Ct, F_Cr, M_Cz) * (R_a - r_1) / (w*t_c*r_1*(
106     R_str - R_a));
107 sigma_curved_outer = Mz2(beta_angle, F_Ct, F_Cr, M_Cz) * (R_a - r_2) / (w*t_c*r_2*(R_str
108     - R_a));
109 sigma_curved_max = max(abs(sigma_curved_inner), abs(sigma_curved_outer));
110
111 sigma_t1 = F_Bt(F_Ct) / A_c;
112 sigma_t2 = sigma_curved_max;
113 sigma_t = sigma_t1 + sigma_t2;
114 tau_rt_curved = (3*F_Br(F_Cr)) / (2*A_c);
115
116 sigma_vm_curved = sqrt(sigma_t^2 + 3*tau_rt_curved^2);
117 sigma_curved_values(i) = sigma_vm_curved;
118
119 end
120
121 [sigma_max_vm_straight, index1] = max(sigma_straight_values, [], "all", "linear");
122 angle_sigma_max_vm_straight = alpha_values(index1)*180/pi;
123
124 [sigma_max_vm_curved, index2] = max(sigma_curved_values, [], "all", "linear");
125 angle_sigma_max_vm_curved = alpha_values(index2)*180/pi;
126
127 sigma_max_vm = max([sigma_max_vm_straight, sigma_max_vm_curved]);
128
129 [delta_x_max, index3] = max(delta_x_values, [], "all", "linear");
130 angle_delta_x_max = alpha_values(index3)*180/pi;
131 end

```

F.7.3. Stress limit with lateral force

```

1 function [sigma_max_vm, sigma_max_vm_straight, sigma_max_vm_curved]=...
2 MaxStress3D(E, G, w, t_s, t_c, R, L, beta_angle, mu, F_x, F_y, F_z)
3
4 % Initialise arrays for storing results
5 alpha_values = linspace(0, beta_angle-deg2rad(0.1), 90);
6 sigma_straight_values = zeros(size(alpha_values));
7 sigma_curved_values = zeros(size(alpha_values));
8
9 % Cycle through angles alpha to find maximum stress angle
10 for i = 1:length(alpha_values)
11     alpha_angle = alpha_values(i);
12
13     % Moment of inertia and area
14     I_sz = (1/12) * w * t_s^3;
15     I_st = (1/12) * t_s * w^3;
16     J_s = (1/12) * w * t_s * (w^2 + t_s^2);
17     A_s = w * t_s;
18
19     I_cz = (1/12) * w * t_c^3;
20     I_cr = (1/12) * t_c * w^3;
21     J_c = (1/12) * w * t_c * (w^2 + t_c^2);
22     A_c = w * t_c;
23
24     %% Straight flexure
25     % Deflections in straight flexure
26     delta_Cz_straight = @(F_Cz, M_Ct) (M_Ct * L^2)/(2*E*I_st) + (F_Cz * L^3) / (3*E*I_st) + (
27         mu * F_Cz * L) / (G*A_s);
28     delta_Cr_straight = @(F_Cr) (F_Cr * L)/(E*A_s);
29     delta_Ct_straight = @(F_Ct, M_Cz) (M_Cz * L^2)/(2*E*I_sz) + (F_Ct * L^3) / (3*E*I_sz);
30
31     phi_Cz_straight = @(F_Ct, M_Cz) (M_Cz * L)/(E*I_sz) + (F_Ct * L^2)/(2*E*I_sz);
32     phi_Cr_straight = @(M_Cr) (M_Cr * L)/(G*J_s);
33     phi_Ct_straight = @(F_Cz, M_Ct) (M_Ct * L)/(E*I_st) + (F_Cz * L^2)/(2*E*I_st);
34
35     %% Curved flexure
36     % Force and moment equilibrium full straight flexure
37     F_Br = @(F_Cr) F_Cr;
38     F_Bt = @(F_Ct) F_Ct;
39     F_Bz = @(F_Cz) F_Cz;
40     M_Br = @(M_Cr) M_Cr;
41     M_Bt = @(F_Cz, M_Ct) F_Cz*L + M_Ct;
42     M_Bz = @(F_Ct, M_Cz) F_Ct*L + M_Cz;
43
44     % Moment functions curved flexure
45     Mz1 = @(theta, F_Ct, F_Cr, M_Cz) F_Bt(F_Ct) * R * (1 - cos(theta)) + F_Br(F_Cr) * R * sin(
46         theta) - M_Bz(F_Ct, M_Cz);
47     Mz2 = @(theta, F_Ct, F_Cr, M_Cz) Mz1(theta, F_Ct, F_Cr, M_Cz) - F_x * R * (1 - cos(theta
48         - alpha_angle)) - F_y * R * sin(theta - alpha_angle);
49
50     Mr1 = @(theta, F_Cz, M_Cr, M_Ct) -F_Bz(F_Cz) * R * sin(theta) + M_Br(M_Cr) * cos(theta) +
51         M_Bt(F_Cz, M_Ct) * sin(theta);
52     Mr2 = @(theta, F_Cz, M_Cr, M_Ct) Mr1(theta, F_Cz, M_Cr, M_Ct) + F_z * R * sin(theta -
53         alpha_angle);
54
55     Mt1 = @(theta, F_Cz, M_Cr, M_Ct) -F_Bz(F_Cz) * R * (1 - cos(theta)) + M_Br(M_Cr) * sin(
56         theta) - M_Bt(F_Cz, M_Ct) * cos(theta);
57     Mt2 = @(theta, F_Cz, M_Cr, M_Ct) Mt1(theta, F_Cz, M_Cr, M_Ct) + F_z * R * (1 - cos(theta
58         - alpha_angle));
59
60     % Compute partial derivatives
61     partial_Mz1_FCr = @(theta) R * sin(theta);
62     partial_Mz1_FCr = @(theta) R * (1 - cos(theta)) - L;
63     partial_Mz1_MCz = @(theta) -1;
64
65     partial_Mz2_FCr = @(theta) partial_Mz1_FCr(theta);
66     partial_Mz2_FCr = @(theta) partial_Mz1_FCr(theta);
67     partial_Mz2_MCz = @(theta) partial_Mz1_MCz(theta);
68
69     partial_Mr1_FCr = @(theta) -R * sin(theta) + L * sin(theta);

```

```

63 partial_Mr1_MCr = @(theta) cos(theta);
64 partial_Mr1_MCr = @(theta) sin(theta);
65
66 partial_Mr2_FCz = @(theta) partial_Mr1_FCz(theta);
67 partial_Mr2_MCr = @(theta) partial_Mr1_MCr(theta);
68 partial_Mr2_MCr = @(theta) partial_Mr1_MCr(theta);
69
70 partial_Mt1_FCz = @(theta) -R * (1 - cos(theta)) - L * cos(theta);
71 partial_Mt1_MCr = @(theta) sin(theta);
72 partial_Mt1_MCr = @(theta) -cos(theta);
73
74 partial_Mt2_FCz = @(theta) partial_Mt1_FCz(theta);
75 partial_Mt2_MCr = @(theta) partial_Mt1_MCr(theta);
76 partial_Mt2_MCr = @(theta) partial_Mt1_MCr(theta);
77
78 % Deflections in curved flexure
79 delta_Bz_curved = @(F_Cz, M_Cr, M_Ct) ...
80     (R/(E*I_cr)) * (integral(@(theta) Mr1(theta, F_Cz, M_Cr, M_Ct) .* partial_Mr1_FCz(
81         theta), 0, alpha_angle, 'RelTol',1e-12,'AbsTol',1e-12) + ...
82         integral(@(theta) Mr2(theta, F_Cz, M_Cr, M_Ct) .* partial_Mr2_FCz(theta)
83         , alpha_angle, beta_angle, 'RelTol',1e-12,'AbsTol',1e-12)) + ...
84     (R/(G*J_c)) * (integral(@(theta) Mt1(theta, F_Cz, M_Cr, M_Ct) .* partial_Mt1_FCz(
85         theta), 0, alpha_angle, 'RelTol',1e-12,'AbsTol',1e-12) + ...
86         integral(@(theta) Mt2(theta, F_Cz, M_Cr, M_Ct) .* partial_Mt2_FCz(theta)
87         , alpha_angle, beta_angle, 'RelTol',1e-12,'AbsTol',1e-12));
88
89 delta_Br_curved = @(F_Cr, F_Ct, M_Cz) ...
90     (R/(E*I_cz)) * (integral(@(theta) Mz1(theta, F_Ct, F_Cr, M_Cz) .* partial_Mz1_FCr(
91         theta), 0, alpha_angle, 'RelTol',1e-12,'AbsTol',1e-12) + ...
92         integral(@(theta) Mz2(theta, F_Ct, F_Cr, M_Cz) .* partial_Mz2_FCr(theta)
93         , alpha_angle, beta_angle, 'RelTol',1e-12,'AbsTol',1e-12));
94
95 delta_Bt_curved = @(F_Cr, F_Ct, M_Cz) ...
96     (R/(E*I_cz)) * (integral(@(theta) Mz1(theta, F_Ct, F_Cr, M_Cz) .* partial_Mz1_FCr(
97         theta), 0, alpha_angle, 'RelTol',1e-12,'AbsTol',1e-12) + ...
98         integral(@(theta) Mz2(theta, F_Ct, F_Cr, M_Cz) .* partial_Mz2_FCr(theta)
99         , alpha_angle, beta_angle, 'RelTol',1e-12,'AbsTol',1e-12));
100
101 phi_Bz_curved = @(F_Cr, F_Ct, M_Cz) ...
102     (R/(E*I_cz)) * (integral(@(theta) Mz1(theta, F_Ct, F_Cr, M_Cz) .* partial_Mz1_MCr(
103         theta), 0, alpha_angle, 'RelTol',1e-12,'AbsTol',1e-12) + ...
104         integral(@(theta) Mz2(theta, F_Ct, F_Cr, M_Cz) .* partial_Mz2_MCr(theta)
105         , alpha_angle, beta_angle, 'RelTol',1e-12,'AbsTol',1e-12));
106
107 phi_Br_curved = @(F_Cz, M_Cr, M_Ct) ...
108     (R/(E*I_cr)) * (integral(@(theta) Mr1(theta, F_Cz, M_Cr, M_Ct) .* partial_Mr1_MCr(
109         theta), 0, alpha_angle, 'RelTol',1e-12,'AbsTol',1e-12) + ...
110         integral(@(theta) Mr2(theta, F_Cz, M_Cr, M_Ct) .* partial_Mr2_MCr(theta)
111         , alpha_angle, beta_angle, 'RelTol',1e-12,'AbsTol',1e-12)) + ...
112     (R/(G*J_c)) * (integral(@(theta) Mt1(theta, F_Cz, M_Cr, M_Ct) .* partial_Mt1_MCr(
113         theta), 0, alpha_angle, 'RelTol',1e-12,'AbsTol',1e-12) + ...
114         integral(@(theta) Mt2(theta, F_Cz, M_Cr, M_Ct) .* partial_Mt2_MCr(theta)
115         , alpha_angle, beta_angle, 'RelTol',1e-12,'AbsTol',1e-12));
116
117 phi_Bt_curved = @(F_Cz, M_Cr, M_Ct) ...
118     (R/(E*I_cr)) * (integral(@(theta) Mr1(theta, F_Cz, M_Cr, M_Ct) .* partial_Mr1_MCr(
119         theta), 0, alpha_angle, 'RelTol',1e-12,'AbsTol',1e-12) + ...
120         integral(@(theta) Mr2(theta, F_Cz, M_Cr, M_Ct) .* partial_Mr2_MCr(theta)
121         , alpha_angle, beta_angle, 'RelTol',1e-12,'AbsTol',1e-12)) + ...
122     (R/(G*J_c)) * (integral(@(theta) Mt1(theta, F_Cz, M_Cr, M_Ct) .* partial_Mt1_MCr(
123         theta), 0, alpha_angle, 'RelTol',1e-12,'AbsTol',1e-12) + ...
124         integral(@(theta) Mt2(theta, F_Cz, M_Cr, M_Ct) .* partial_Mt2_MCr(theta)
125         , alpha_angle, beta_angle, 'RelTol',1e-12,'AbsTol',1e-12));
126
127 %% Solving
128 % Define function for nonlinear solver
129 force_equations = @(F) [
130     delta_Bz_curved(F(1), F(5), F(6)) + delta_Cz_straight(F(1), F(6));
131     delta_Br_curved(F(2), F(3), F(4)) + delta_Cr_straight(F(2));
132     delta_Bt_curved(F(2), F(3), F(4)) + delta_Ct_straight(F(3), F(4));
133     phi_Bz_curved(F(2), F(3), F(4)) + phi_Cz_straight(F(3), F(4));
134 ];

```

```

116     phi_Br_curved(F(1), F(5), F(6)) + phi_Cr_straight(F(5));
117     phi_Bt_curved(F(1), F(5), F(6)) + phi_Ct_straight(F(1), F(6));
118 ];
119
120 % Improved numerical integration settings
121 opts = optimset('TolFun', 1e-12, 'TolX', 1e-12, 'Display', 'off');
122
123 % Solve
124 F_init = [0 0 2 0 0 0];
125 lb = [-Inf, -Inf, -Inf, -Inf, -Inf, -Inf];
126 ub = [Inf, Inf, Inf, Inf, Inf, Inf];
127 F = lsqnonlin(@(F) force_equations(F), F_init, lb, ub, opts);
128
129 F_Cz = F(1);
130 F_Cr = F(2);
131 F_Ct = F(3);
132 M_Cz = F(4);
133 M_Cr = F(5);
134 M_Ct = F(6);
135
136 %% Stress straight flexure
137 % Stress at point C
138 sigma_r1 = F_Br(F_Cr) / A_s;
139 sigma_r2 = M_Cz*(t_s/2) / I_sz;
140 sigma_r3 = M_Ct*(w/2) / I_st;
141 sigma_r = sigma_r1 + sigma_r2 + sigma_r3;
142 tau_rt_straight = (3*F_Bt(F_Ct)) / (2*A_s);
143 tau_rz_straight = (3*F_Bz(F_Cz)) / (2*L*t_s);
144 tau_tz_straight = (3*M_Cr) / (w*t_s^2);
145
146 sigma_vm_straight = sqrt(sigma_r^2 + 3*(tau_rt_straight^2 + tau_rz_straight^2 +
147     tau_tz_straight^2));
148 sigma_straight_values(i) = sigma_vm_straight;
149
150 %% Stress curved flexure
151 % Stress at point A
152 r_1 = R-t_c;
153 r_2 = R;
154 R_a = t_c/log(r_2/r_1);
155 R_str = (r_1+r_2)/2;
156 sigma_curved_inner = - Mz2(beta_angle, F_Ct, F_Cr, M_Cz) * (R_a - r_1) / (w*t_c*r_1*(
157     R_str - R_a));
158 sigma_curved_outer = Mz2(beta_angle, F_Ct, F_Cr, M_Cz) * (R_a - r_2) / (w*t_c*r_2*(R_str
159     - R_a));
160 sigma_curved_max = max(abs(sigma_curved_inner), abs(sigma_curved_outer));
161
162 sigma_t1 = F_Bt(F_Ct) / A_c;
163 sigma_t2 = sigma_curved_max;
164 sigma_t3 = Mr2(beta_angle, F_Cz, M_Cr, M_Ct)*(w/2) / I_cr;
165 sigma_t = sigma_t1 + sigma_t2 + sigma_t3;
166 tau_rt_curved = (3*F_Br(F_Cr)) / (2*A_c);
167 tau_tz_curved = (3*F_Bz(F_Cz)) / (2*(beta_angle*R)*t_c);
168 tau_rz_curved = 3 * Mt2(beta_angle, F_Cz, M_Cr, M_Ct) / (w * t_c^2);
169
170 sigma_vm_curved = sqrt(sigma_t^2 + 3*(tau_rt_curved^2 + tau_tz_curved^2 + tau_rz_curved
171     ^2));
172 sigma_curved_values(i) = sigma_vm_curved;
173
174 end
175
176 [sigma_max_vm_straight, index1] = max(sigma_straight_values, [], "all", "linear");
177 angle_sigma_max_vm_straight = alpha_values(index1)*180/pi;
178
179 [sigma_max_vm_curved, index2] = max(sigma_curved_values, [], "all", "linear");
180 angle_sigma_max_vm_curved = alpha_values(index2)*180/pi;
181
182 sigma_max_vm = max([sigma_max_vm_straight, sigma_max_vm_curved]);
183 end

```

F.7.4. Sideways gradient

```

1 function [sigma_max_side, sigma_vm_straight_side, sigma_vm_curved_side]=...
2 SidewaysGradient(g,m,k_c,k_phi,n,phi_deg,c,lambda,s,k_e,h, k, E, G, w, t_s, t_c, R, L, ...
3 alpha_angle, beta_angle, mu, F_x, b_LZ, gamma_angle, y_com, N, ...
4 tolerance, max_iterations, update_factor, tolerance2, max_iterations2, update_factor2)
5
6 phi = deg2rad(phi_deg);      % Soil friction angle (in radians)
7
8 %% Force and moment equilibrium
9 F_m = m*g;
10 F_mz = F_m*sin(gamma_angle);
11 F_my = F_m*cos(gamma_angle);
12 F_c1y = (F_mz*y_com + F_my*b_LZ)/(2*b_LZ);
13
14 N_eff = N/2;      % Leg number, middle leg: N_eff=1, outer legs N_eff=2.
15
16 F_c1z = F_c1y*tan(gamma_angle)/N_eff;
17 W = F_c1y / N_eff;
18
19 %% Static equilibrium
20 delta_t = LongitudinalForceDeflection(E, w, t_s, t_c, R, L, alpha_angle, beta_angle, F_x); %
    Initial guess for delta_t, dependent on the deflection by pure longitudinal force F_x.
21
22 for iter = 1:max_iterations
23     % Calculate flattened section length l_t
24     if 2 * R * delta_t > delta_t^2
25         l_t = 2 * sqrt(2 * R * delta_t - delta_t^2);
26     else
27         % warning('Non-physical values for l_t');
28         % fprintf('Last static total vertical force F_y0: %.4f N\n', F_y0);
29         % fprintf('Last leg deflection delta_t: %.4f mm\n', delta_t*10^3)
30
31         if delta_t < 0
32             delta_t = 0;
33             l_t = 0;
34             theta_t0 = 0;
35             z_0 = 0.0005; % Default initial guess
36             % fprintf('Rigid leg considered, thus leg deflection delta_t: %.4f mm\n', delta_t
37                 *10^3)
38         else
39             % warning('Deflection too big for leg, results are inaccurate. ');
40             end
41             break;
42         end
43
44     % Calculate average ground pressure P_w
45     [F_y, ~] = ForceDeflection(E, w, t_s, t_c, R, L, alpha_angle, beta_angle, F_x, delta_t);
46     P_w = F_y / (w * l_t);
47
48     % Calculate static sinkage z_0
49     if l_t < w
50         z_0 = (P_w / (k_c / l_t + k_phi))^(1/n);
51     else
52         z_0 = (P_w / (k_c / w + k_phi))^(1/n);
53     end
54
55     theta_f0 = acos(1 - (z_0+delta_t)/R);      % Static entry angle contact patch
56     theta_t0 = asin(l_t / (2*R));             % Static flattening angle contact patch
57
58     % Calculate total static ground reaction force F_y0
59     sigma_Fs = @(theta) (k_c / w + k_phi) * R^n * (cos(theta) - cos(theta_f0)).^n;
60
61     integrand_Fs = @(theta) sigma_Fs(theta) .* cos(theta);
62     F_s = R * w * integral(integrand_Fs, theta_t0, theta_f0);
63     F_w = P_w * w * l_t;
64     F_y0 = F_w + 2 * F_s;
65
66     % Check if F_y0 is almost equal to vertical load W
67     if abs(F_y0 - W) < tolerance      % Converged
68         % Output results

```

```

68     % disp('Result static equilibrium:');
69     % fprintf('Converged to correct delta_t value after %d iterations.\n', iter);
70     % fprintf('Leg deflection delta_t: %.4f mm\n', delta_t*10^3);
71     % fprintf('Length flattened section l_t: %.4f mm\n', l_t*10^3);
72     % fprintf('Static sinkage z_0: %.4f mm\n', z_0*10^3);
73     % fprintf('Static entry angle theta_f0 %.4f deg\n', rad2deg(theta_f0))
74     % fprintf('Static flattening angle theta_t0 %.4f deg\n', rad2deg(theta_t0))
75     % fprintf('Static vertical force flattened section F_w: %.4f N\n', F_w);
76     % fprintf('Static vertical force entry & exit section F_s: %.4f N\n', F_s);
77     % fprintf('Static total vertical force F_y0: %.4f N\n', F_y0);
78     break;
79 else
80     delta_t = delta_t + update_factor*(W-F_y0); % Update delta_t for the next iteration
81 end
82
83 % If maximum iterations reached without convergence, display a warning
84 if iter == max_iterations
85     % warning('Maximum iterations reached without convergence. ');
86     % fprintf('Max. iter. value delta_t: %.4f mm\n', delta_t*10^3);
87     % fprintf('Max. iter. value F_y0: %.4f N\n', F_y0);
88 end
89 end
90
91 theta_t = theta_t0; % Flattening angle considered equal in static and quasi-static
    situation
92
93
94 %% Quasi-static equilibrium
95 z = z_0; % Initial guess for leg sinkage
96
97 for iter = 1:max_iterations2
98
99     theta_f = acos(1 - (z+delta_t)/R); % Entry angle contact patch
100    theta_r = - acos(1 - lambda * (z+delta_t) / R); % Exit angle contact patch
101    theta_m = (0.4+0.15*s)*theta_f; % Maximum normal stress angle
102
103    theta_t_deg = rad2deg(theta_t);
104    theta_f_deg = rad2deg(theta_f);
105    theta_r_deg = rad2deg(theta_r);
106    theta_m_deg = rad2deg(theta_m);
107
108    % Normal stress sigma(theta) function
109    sigma = @(theta) calculate_sigma(theta, theta_f, theta_r, theta_m, k_c, k_phi, z, R, w, n
        , l_t, theta_t);
110
111    % Soil deformation j(theta) function
112    j = @(theta) calculate_j_theta(theta, theta_f, theta_t, R, s, delta_t);
113
114    % Shear stress tau(theta) function
115    tau = @(theta) calculate_tau(sigma(theta), c, phi, j(theta), k);
116
117    % Vertical force F
118    integrand_F1 = @(theta) (sigma(theta) .* cos(theta) + tau(theta) .* sin(theta));
119
120    if l_t < w && l_t ~= 0 % Flattened section normal pressure, as theta_t and l_t are
        constant and independent of theta.
121        sigma_t = (k_c / l_t + k_phi) * z^n ;
122    else
123        sigma_t = (k_c / w + k_phi) * z^n ;
124    end
125
126    F_AB = R * w * integral(integrand_F1, theta_t, theta_f); % Entry section contribution
127    F_BC = l_t * w * sigma_t; % Flattened section
        contribution, as theta_t and l_t are constant independent of theta.
128    F_CD = R * w * integral(integrand_F1, theta_r, -theta_t); % Exit section contribution
129
130    % If flattening angle is bigger than exit angle, ignore exit section contribution
131    if -theta_t <= theta_r
132        F = F_AB + F_BC;
133    else
134        F = F_AB + F_BC + F_CD;

```



```

135     end
136
137     % Check if F matches the load W
138     if abs(F - W) < tolerance2      % Converged
139         % disp(' ');
140         % disp('Result dynamic equilibrium:');
141         % fprintf('Converged to correct z value after %d iterations.\n', iter);
142         % fprintf('Final value of sinkage z: %.4f mm\n', z*10^3);
143         % fprintf('Final value of F: %.4f N\n', F);
144         break;
145     else
146         z = z + update_factor2*(W-F);      % Update z for the next iteration
147     end
148
149     % If maximum iterations reached without convergence, display a warning
150     if iter == max_iterations2
151         % warning('Maximum iterations reached without convergence.');
```

```

152         % fprintf('Max. iter. value of z: %.4f meters\n', z);
153         % fprintf('Max. iter. value of F: %.4f N\n', F);
154         break;
155     end
156 end
157
158 % Calculate thrust H
159 integrand_H_AB = @(theta) tau(theta) .* cos(theta);
160 integrand_H_BC = @(theta) tau(theta) ./ cos(theta).^2;
161 integrand_H_CD = @(theta) (tau(theta) .* cos(theta) - sigma(theta) .* sin(theta));
162 H_AB = R * w * integral(integrand_H_AB, theta_t, theta_f);      % Entry section
163                                     contribution
164 H_BC = (R - delta_t) * w * integral(integrand_H_BC, -theta_t, theta_t);      % Flattened
165                                     section contribution
166 H_CD = R * w * integral(integrand_H_CD, theta_r, -theta_t);      % Exit section
167                                     contribution
168
169 % If flattening angle is bigger than exit angle, ignore exit section contribution
170 if -theta_t <= theta_r
171     H = H_AB + H_BC;
172 else
173     H = H_AB + H_BC + H_CD;
174 end
175
176 % Calculate resistance force R_t
177 % Soil compaction resistance R_c
178 integrand_Rc = @(theta) sigma(theta) .* sin(theta);
179 R_c = R * w * integral(integrand_Rc, theta_t, theta_f);
180
181 % Leg deformation resistance R_d
182 epsilon = 1 - exp(-k_e * delta_t / h);
183 if theta_t_deg > 0
184     R_d = (3.581 * w * (2*R)^2 * P_w * epsilon * (0.0349 * theta_t_deg - sind(2*theta_t_deg))
185           ) / (theta_t_deg * (2*R - 2*delta_t));
186 else
187     R_d = 0;      % No leg deformation resistance (Rigid leg)
188 end
189
190 R_t = R_c + R_d;
191
192 % Calculate drawbar pull DP
193 DP = H - R_t;
194
195 %% Maximum stress while ascending sideways gradient
196 %% Effectively a lateral force acting on the flexure, thus the same stress calculation.
197 % F_x is the drawbar pull DP
198 % F_y is the vertical gravitational force W
199 % F_z is the lateral force due to gravity F_c1z
200 [sigma_max_side, sigma_vm_straight_side, sigma_vm_curved_side]= MaxStress3D(E, G, w, t_s, t_c
    , R, L, beta_angle, mu, DP, W, F_c1z);

```

```

201 % fprintf('Gravitational force on C_leg axle W: %.4f N\n', W);
202 % fprintf('Entry angle theta_f: %.4f deg\n', theta_f_deg);
203 % fprintf('Maximum normal pressure angle theta_m: %.4f deg\n', theta_m_deg);
204 % fprintf('Flattened section angle theta_t: %.4f deg\n', theta_t_deg);
205 % fprintf('Exit angle theta_r: %.4f deg\n', theta_r_deg);
206 % fprintf('Vertical force entry section F_AB: %.4f N\n', F_AB);
207 % fprintf('Vertical force flattened section F_BC: %.4f N\n', F_BC);
208 % fprintf('Vertical force exit section F_CD: %.4f N\n', F_CD);
209 % fprintf('Thrust entry section H_AB: %.4f N\n', H_AB);
210 % fprintf('Thrust flattened section H_BC: %.4f N\n', H_BC);
211 % fprintf('Thrust exit section H_CD: %.4f N\n', H_CD);
212 % fprintf('Compaction resistance R_c: %.4f N\n', R_c);
213 % fprintf('Deformation resistance R_d: %.4f N\n', R_d);
214 % fprintf('Slip ratio s: %.4f \n', s);
215 % disp(' ');
216 %
217 % fprintf('Vertical force F: %.4f N\n', F);
218 % fprintf('Leg sinkage z: %.4f mm\n', z*10^3);
219 % fprintf('Thrust H: %.4f N\n', H);
220 % fprintf('Resistance R_t: %.4f N\n', R_t);
221 % fprintf('Drawbar Pull DP while climbing along a sideways gradient: %.4f N\n', DP);
222
223 %% Functions
224 % Normal pressure sigma(theta)
225 function sigma_theta = calculate_sigma(theta, theta_f, theta_r, theta_m, k_c, k_phi, z, R, w,
226     n, l_t, theta_t)
227     if theta_m > theta_t
228         sigma_theta = zeros(size(theta)); % Initialise sigma_theta for all values of theta.
229
230         % Entry section
231         entry_section = (theta >= theta_m) & (theta <= theta_f);
232         sigma_theta(entry_section) = (k_c / w + k_phi) * R^n * (cos(theta(entry_section)) -
233             cos(theta_f)).^n;
234
235         % Flattened section (Denoted to calculate H_BC and T_BC)
236         flat_section = ((theta >= -theta_t) & (theta < theta_t));
237         if l_t < w
238             sigma_theta(flat_section) = (k_c / l_t + k_phi) * z^n;
239         else
240             sigma_theta(flat_section) = (k_c / w + k_phi) * z^n;
241         end
242
243         % Exit section and further section
244         exit_section = ((theta >= theta_r) & (theta < -theta_t)) | ((theta >= theta_t) & (
245             theta < theta_m));
246         sigma_theta(exit_section) = (k_c / w + k_phi) * R^n * (cos(theta_f - (theta(
247             exit_section) - theta_r)*(theta_f - theta_m)/(theta_m - theta_r)) - cos(theta_f))
248             .^n;
249
250     else
251         % Condition when theta_m <= theta_t
252         sigma_theta = zeros(size(theta)); % Initialise sigma_theta for all values of theta
253
254         % Entry section
255         entry_section = (theta >= theta_t) & (theta <= theta_f);
256         sigma_theta(entry_section) = (k_c / w + k_phi) * R^n * (cos(theta(entry_section)) -
257             cos(theta_f)).^n;
258
259         % Flattened section (Denoted to calculate H_BC and T_BC)
260         flat_section = ((theta >= -theta_t) & (theta < theta_t));
261         if l_t < w
262             sigma_theta(flat_section) = (k_c / l_t + k_phi) * z^n;
263         else
264             sigma_theta(flat_section) = (k_c / w + k_phi) * z^n;
265         end
266
267         % Exit section
268         exit_section = (theta >= theta_r) & (theta < -theta_t);
269         sigma_theta(exit_section) = (k_c / w + k_phi) * R^n * (cos(theta_f - (theta(
270             exit_section) - theta_r)*(theta_f - theta_m)/(theta_m - theta_r)) - cos(theta_f))
271             .^n;

```

```
264     end
265 end
266
267 % Shear stress tau(theta)
268 function tau_theta = calculate_tau(sigma_theta, c, phi, j_theta, k)
269     tau_theta = (c + sigma_theta .* tan(phi)) .* (1 - exp(-j_theta ./ k));
270 end
271
272 % Soil deformation j(theta)
273 function j_theta = calculate_j_theta(theta, theta_f, theta_t, R, s, delta_t)
274     if abs(theta) >= abs(theta_t)
275         j_theta = R * (theta_f - theta - (1 - s) * (sin(theta_f) - sin(theta)));
276     else
277         j_theta_t = R * (theta_f - theta_t - (1 - s) * (sin(theta_f) - sin(theta_t)));
278         j_theta = j_theta_t + s * (R * sin(theta_t) - (R - delta_t) * tan(theta));
279     end
280 end
281 end
282 end
```

F.7.5. End of contact surface radius for next step

```

1 function [R_eff]=...
2 MinimumRadiusNextStep(E, w, t_s, t_c, R, L, beta_angle, F_x, F_y)
3
4 alpha_end = 0.10*beta_angle;
5
6 % Moment of inertia and area
7 I_sz = (1/12) * w * t_s^3;
8 I_cz = (1/12) * w * t_c^3;
9 A_s = w * t_s;
10
11 %% Straight flexure
12 % Deflections in straight flexure
13 delta_Cr_straight = @(F_Cr) (F_Cr * L)/(E*A_s);
14 delta_Ct_straight = @(F_Ct, M_Cz) (M_Cz * L^2)/(2*E*I_sz) + (F_Ct * L^3) / (3*E*I_sz);
15 phi_Cz_straight = @(F_Ct, M_Cz) (M_Cz * L)/(E*I_sz) + (F_Ct * L^2)/(2*E*I_sz);
16
17 %% Curved flexure
18 % Force and moment equilibrium full straight flexure
19 F_Br = @(F_Cr) F_Cr;
20 F_Bt = @(F_Ct) F_Ct;
21 M_Bz = @(F_Ct, M_Cz) F_Ct*L + M_Cz;
22
23 % Moment functions curved flexure
24 Mz1 = @(theta, F_Ct, F_Cr, M_Cz) F_Bt(F_Ct) * R * (1 - cos(theta)) + F_Br(F_Cr) * R * sin(
    theta) - M_Bz(F_Ct, M_Cz);
25 Mz2 = @(theta, F_Ct, F_Cr, M_Cz) Mz1(theta, F_Ct, F_Cr, M_Cz) - F_x * R * (1 - cos(theta -
    alpha_end)) - F_y * R * sin(theta - alpha_end);
26
27 % Compute partial derivatives
28 partial_Mz1_FCr = @(theta) R * sin(theta);
29 partial_Mz1_FCT = @(theta) R * (1 - cos(theta)) - L;
30 partial_Mz1_MCz = @(theta) -1;
31
32 partial_Mz2_FCr = @(theta) partial_Mz1_FCr(theta);
33 partial_Mz2_FCT = @(theta) partial_Mz1_FCT(theta);
34 partial_Mz2_MCz = @(theta) partial_Mz1_MCz(theta);
35
36 partial_Mz1_Fy = @(theta) 0;
37 partial_Mz2_Fy = @(theta) -R * sin(theta - alpha_end);
38
39 % Deflections in curved flexure
40 delta_Br_curved = @(F_Cr, F_Ct, M_Cz) ...
41 (R/(E*I_cz)) * (integral(@(theta) Mz1(theta, F_Ct, F_Cr, M_Cz) .* partial_Mz1_FCr(theta),
    0, alpha_end, 'RelTol',1e-12,'AbsTol',1e-12) + ...
42 integral(@(theta) Mz2(theta, F_Ct, F_Cr, M_Cz) .* partial_Mz2_FCr(theta),
    alpha_end, beta_angle, 'RelTol',1e-12,'AbsTol',1e-12));
43
44 delta_Bt_curved = @(F_Cr, F_Ct, M_Cz) ...
45 (R/(E*I_cz)) * (integral(@(theta) Mz1(theta, F_Ct, F_Cr, M_Cz) .* partial_Mz1_FCT(theta),
    0, alpha_end, 'RelTol',1e-12,'AbsTol',1e-12) + ...
46 integral(@(theta) Mz2(theta, F_Ct, F_Cr, M_Cz) .* partial_Mz2_FCT(theta),
    alpha_end, beta_angle, 'RelTol',1e-12,'AbsTol',1e-12));
47
48 phi_Bz_curved = @(F_Cr, F_Ct, M_Cz) ...
49 (R/(E*I_cz)) * (integral(@(theta) Mz1(theta, F_Ct, F_Cr, M_Cz) .* partial_Mz1_MCz(theta),
    0, alpha_end, 'RelTol',1e-12,'AbsTol',1e-12) + ...
50 integral(@(theta) Mz2(theta, F_Ct, F_Cr, M_Cz) .* partial_Mz2_MCz(theta),
    alpha_end, beta_angle, 'RelTol',1e-12,'AbsTol',1e-12));
51
52 %% Solving
53 % Define function for nonlinear solver
54 force_equations = @(F) [
55     delta_Br_curved(F(1), F(2), F(3)) + delta_Cr_straight(F(1));
56     delta_Bt_curved(F(1), F(2), F(3)) + delta_Ct_straight(F(2), F(3));
57     phi_Bz_curved(F(1), F(2), F(3)) + phi_Cz_straight(F(2), F(3));
58 ];
59
60 % Improved numerical integration settings
61 opts = optimset('TolFun', 1e-12, 'TolX', 1e-12, 'Display', 'off');

```

```

62
63 % Solve
64 F_init = [0 1 0.01];
65 F = fsolve(force_equations, F_init, opts);
66
67 F_Cr = F(1);
68 F_Ct = F(2);
69 M_Cz = F(3);
70
71 %% Deflection of loading point
72 % Vertical deflection loading point
73 delta_y = (R/(E*I_cz)) * (integral(@(theta) Mz1(theta, F_Ct, F_Cr, M_Cz) .* partial_Mz1_Fy(
74     theta), 0, alpha_end, 'RelTol',1e-12,'AbsTol',1e-12) + ...
75     integral(@(theta) Mz2(theta, F_Ct, F_Cr, M_Cz) .* partial_Mz2_Fy(theta),
76     alpha_end, beta_angle, 'RelTol',1e-12,'AbsTol',1e-12));
77
78 %% Effective radius
79 R_eff = R - delta_y;
80 end

```

F.7.6. Climbing height

```

1 function [y_c]=...
2 ClimbingHeight(R, y_g, z, delta_y)
3
4 % Climbing height y_c
5 y_c = R + y_g - z - delta_y;
6
7 end

```